

Metalorganic Chemical Vapor Deposition of High-Performance GaAs-Based Quantum-Dot Lasers

vorgelegt von
Diplom-Physiker
Roman Sellin
aus Ulm a. d. Donau

von der Fakultät II
– Mathematik und Naturwissenschaften –
der Technischen Universität Berlin
zur Erlangung des akademischen Grades

Doktor der Naturwissenschaften
- Dr. rer. nat. -

genehmigte Dissertation

Arbeit eingereicht am 6. Mai 2003
Tag der wissenschaftlichen Aussprache: 2. Juli 2003
Vorsitzender der Prüfungskommission: Prof. Dr. P. Zimmermann
Berichter: Prof. Dr. D. Bimberg und Prof. Dr. A. Krost

Berlin 2003
D83

Abstract

In this work, Metalorganic Chemical Vapor Deposition (MOCVD) of novel GaAs-based semiconductor laser structures with self-organized InGaAs/GaAs Stranski-Krastanow quantum dots (QDs) as active medium was advanced with regard to the laser characteristics. The three-dimensional morphology of self-organized QDs leads to a significant roughening of thin cap layers on top of QD sheets. Smoother QD cap layers are required, however, to reduce the distance between stacked QD layers and thus to increase the QD volume density for larger modal gain of QD lasers. Hence, the growth of QD lasers was complemented by an in-situ annealing step flattening such corrugated surfaces. The strain of lattice-mismatched self-organized QDs and the untypically low QD deposition temperatures around 500°C lead to dislocations and point defects in QD heterostructures. The density of such defects was strongly reduced by in-situ annealing. Lasers with in-situ annealed QDs exhibit room-temperature transparency current densities around 6 A/cm² per QD sheet at emission wavelengths between 1.14 and 1.16 μm. The internal quantum efficiency was increased to beyond 90 %. Lasers based on 6-fold stacks of such in-situ annealed QDs show room-temperature peak output powers of 11.7 W in quasi-continuous-wave mode and 4.7 W under continuous-wave operation. This was the first demonstration of optical output powers of QD lasers beyond 10 W. The characteristics of such QD lasers did not exhibit significant changes during lifetime measurements of more than 3000 h at 50°C and output powers of 1.0 - 1.5 W.

Arsine, widely used as arsenic precursor in MOCVD, is strongly toxic and was therefore replaced in the course of this work by the alternative precursor tertiarybutylarsine (TBAs). The growth of QDs had to be recalibrated as the physical and chemical properties of TBAs differ from those of arsine. The worldwide first QD laser grown using alternative-precursor MOCVD could be demonstrated. Different techniques to grow QDs emitting at the commercially important data communication wavelength of 1.3 μm were developed and evaluated. Such QD structures were investigated using photoluminescence spectroscopy and transmission electron microscopy. Using InGaAs QDs overgrown with gallium-rich InGaAs quantum films, the room-temperature lasing wavelength could be extended to 1.24 μm. The growth of laser structures for the fabrication of QD-based surface emitting lasers (VCSELs) with Al(Ga)O_x/GaAs oxide mirrors and nine-fold stacks of InGaAs/GaAs QDs as active region was implemented. A VCSEL with a 3.5 μm aperture and four top-DBR pairs exhibited a maximum output power of 0.68 mW at 1.1 μm, a threshold current of 280 μA, and a differential efficiency of 43 %.

Zusammenfassung

Im Rahmen dieser Arbeit wurde eine Verbesserung der metallorganischen Gasphasenepitaxie (MOCVD) neuartiger GaAs-basierter Halbleiter-Laserstrukturen mit selbstorganisierten InGaAs/GaAs Stranski-Krastanow-Quantenpunkten (QPen) als aktivem Medium hinsichtlich der Lasereigenschaften erzielt. Die dreidimensionale QP-Morphologie führt zu einer Aufrauung dünner Bedeckungsschichten auf den Quantenpunkten. Glatte Bedeckungsschichten sind jedoch für kleine Abstände zwischen gestapelten QP-Schichten erforderlich, um die Volumendichte an QPen und damit den modalen Gewinn von QP-Lasern zu erhöhen. Daher wurde ein in-situ Temperverfahren zur Glättung solch rauer Oberflächen eingeführt. Die Verspannung von QP-Strukturen und die niedrigen QP-Wachstumstemperaturen um 500°C führen zu Versetzungen und Punktdefekten. Durch den Tempersschritt wurde die Dichte solcher Defekte drastisch reduziert. Laser mit getemperten QPen zeigen bei Raumtemperatur Transparenzstromdichten um 6 A/cm² pro QP-Schicht bei Emissionswellenlängen zwischen 1.14 und 1.16 µm. Die interne Quanteneffizienz solcher Laser liegt über 90 %. Laserdioden mit Sechsfachstapeln getemperter QPe zeigen Ausgangsleistungen von 11.7 W im Quasi-Dauerstrichbetrieb und 4.7 W im Dauerstrichbetrieb. Damit konnten für QP-Laser erstmalig Ausgangsleistungen von über 10 W erreicht werden. Die Charakteristik solcher Laser blieb während einer über 3000-stündigen Lebensdaueremessung bei 50°C und 1.0-1.5 W optischer Ausgangsleistung unverändert.

Das als Arsen-Vorläufer weit verbreitete Arsin ist hochtoxisch und wurde daher im Laufe dieser Arbeit durch den alternativen Vorläufer Tertiärbutylarsin (TBAs) ersetzt. Das Wachstum von QPen musste daraufhin neu kalibriert werden, da TBAs andere physikalische und chemische Eigenschaften als Arsin besitzt. Weltweit wurden erstmals QP-Laser mit dem alternativen Precursor TBAs hergestellt. Verschiedene Verfahren zum Wachstum von QPen wurden entwickelt, die bei der kommerziell wichtigen Telekommunikations-Wellenlänge von 1.3 µm emittieren. Solche QP-Strukturen wurden mit Photolumineszenzspektroskopie und Transmissions-elektronenmikroskopie untersucht. Mit InGaAs/GaAs QPen, die mit Gallium-reichen InGaAs Quantenfilmen überwachsen wurden, konnte die Raumtemperatur-Lasingwellenlänge zu 1.24 µm ausgedehnt werden. Des weiteren wurden Verfahren zum Wachstum von QP-Strukturen für die Herstellung von oberflächenemittierenden Lasern (VCSEL) mit Al(Ga)O_x/GaAs-Oxidspiegeln entwickelt. Ein VCSEL mit einer 3.5 µm breiten Apertur und vier oberen Spiegelpaaren zeigte eine maximale Ausgangsleistung von 0.68 mW bei 1.1 µm und eine differenzielle Effizienz von 43 %. Der Schwellstrom betrug 280 µA.

Parts of this work have been published in:

R.L. Sellin, I. Kaiander, D. Ouyang, T. Kettler, and D. Bimberg, *Alternative-precursor metalorganic chemical vapor deposition and laser application of self-organized InGaAs/GaAs quantum dots*, Appl. Phys. Lett. **82**, 841 (2003).

A. Lenz, R. Timm, H. Eisele, C. Hennig, S. K. Becker, R.L. Sellin, U.W. Pohl, D. Bimberg, and M. Dähne, *Reversed truncated cone composition distribution of $\text{In}_{0.8}\text{Ga}_{0.2}\text{As}$ quantum dots overgrown by an $\text{In}_{0.1}\text{Ga}_{0.9}\text{As}$ layer in a GaAs matrix*, Appl. Phys. Lett. **81**, 5150 (2002).

R.L. Sellin, C. Ribbat, D. Bimberg, F. Rinner, H. Konstanzer, M.T. Kelemen, and M. Mikulla, *High-reliability MOCVD-grown quantum dot laser*, El. Lett. **38**, 883 (2002).

C. Ribbat and R. Sellin, *High Power Quantum Dot Lasers in Nano-Optoelectronics*, ed. by M. Grundmann (Springer, Berlin, Heidelberg, 2002), p. 353.

R. Sellin, N.N. Ledentsov, D. Bimberg, V.M. Ustinov, and Z.I. Alferov, *Growth and optical characterization of long-wavelength quantum dots for low-threshold current lasers*, Proc. of the 6th Int. Symp. Adv. Phys. Fields, Tsukuba, Japan, March 6-9 (2001), p. 49.

R.L. Sellin, C. Ribbat, M. Grundmann, N.N. Ledentsov, and D. Bimberg, *Close-to-ideal device characteristics of high-power InGaAs/GaAs quantum dot lasers*, Appl. Phys. Lett. **78**, 1207 (2001).

D. Bimberg, M. Grundmann, N.N. Ledentsov, M.H. Mao, C. Ribbat, R. Sellin, V.M. Ustinov, A.E. Zhukov, Z.I. Alferov, and J.A. Lott, *Novel Infrared Quantum Dot Lasers: Theory and Reality*, phys. stat. sol. (b) **224**, 787 (2001).

C. Ribbat, R. Sellin, M. Grundmann, and D. Bimberg, *High Power Quantum Dot Lasers at 1160 nm*, phys. stat. sol. (b) **224**, 819 (2001).

R. Sellin, N.N. Ledentsov, and D. Bimberg, *Verfahren zur Verbesserung der Effizienz von epitaktisch hergestellten Quantenpunkt-Halbleiterbauelementen mit einer oder mehreren Quantenpunktschichten*, patent pending, ref. no. 10044040 (DE) (2000).

R. Sellin, F. Heinrichsdorff, C. Ribbat, M. Grundmann, U.W. Pohl, and D. Bimberg, *Surface flattening during MOCVD of thin GaAs layers covering InGaAs quantum dots*, J. Crystal Growth **221**, 581 (2000).

Further publications (only refereed journals):

C. Ribbat, R. Sellin, I. Kaiander, F. Hopfer, N.N. Ledentsov, D. Bimberg, A.R. Kovsh, V.M. Ustinov, A.E. Zhukov, and M.V. Maximov, *Complete suppression of filamentation and superior beam quality in quantum-dot lasers*, Appl. Phys. Lett. **82**, 952 (2003).

F. Guffarth, R. Heitz, M. Geller, C. Kapteyn, H. Born, R. Sellin, A. Hoffmann, and D. Bimberg, *Radiation hardness of InGaAs/GaAs quantum dots*, Appl. Phys. Lett. **82**, 1941 (2003).

S. Rodt, R. Heitz, A. Schliwa, R. L. Sellin, F. Guffarth, and D. Bimberg, *Repulsive exciton-exciton interaction in quantum dots*, Phys. Rev. B **68**, 035331 (2003).

F. Guffarth, R. Heitz, A. Schliwa, O. Stier, M. Geller, C.M.A. Kapteyn, R. Sellin, and D. Bimberg, *Few-particle interactions in charged InGaAs/GaAs quantum dots*, Phys. Rev. B **67**, 235304 (2003).

L. Müller-Kirsch, N.N. Ledentsov, R. Sellin, U.W. Pohl, D. Bimberg, I. Häusler, H. Kirmse, and W. Neumann, *GaSb quantum dot growth using InAs quantum dot stressors*, J. Crystal Growth **248**, 333 (2003).

P. Borri, W. Langbein, S. Schneider, U. Woggon, R.L. Sellin, D. Ouyang, and D. Bimberg, *Coherent Light-Matter Interaction in InGaAs Quantum Dots: Dephasing Time and Optical Rabi Oscillations*, phys. stat. sol. (b) **233**, 391 (2002).

P. Borri, W. Langbein, S. Schneider, U. Woggon, R.L. Sellin, D. Ouyang, and D. Bimberg, *Temperature-Dependent Time-Resolved Four-Wave Mixing in InGaAs Quantum Dots*, phys. stat. sol. (a) **190**, 517 (2002).

P. Borri, W. Langbein, S. Schneider, U. Woggon, R. Sellin, D. Ouyang, and D. Bimberg, *Relaxation and dephasing of multiexcitons in semiconductor quantum dots*, Phys. Rev. Lett. **89**, 187401 (2002).

P. Borri, W. Langbein, S. Schneider, U. Woggon, R.L. Sellin, D. Ouyang, and D. Bimberg, *Rabi oscillations in the excitonic ground-state transition of InGaAs quantum dots*, Phys. Rev. B **66**, 081306R (2002).

P. Borri, W. Langbein, S. Schneider, U. Woggon, R.L. Sellin, D. Ouyang, and D. Bimberg, *Coherent Light-Matter Interaction in InGaAs Quantum Dots: Dephasing Time and Optical Rabi Oscillations*, phys. stat. sol. (b) **233**, 391 (2002).

V.A. Haisler, F. Hopfer, R.L. Sellin, A. Lochmann, K. Fleischer, N. Esser, W. Richter, N.N. Ledentsov, D. Bimberg, C. Möller, and N. Grote, *Micro-Raman studies of vertical-cavity surface-emitting lasers with Al_xO_y /GaAs distributed Bragg reflectors*, Appl. Phys. Lett. **81**, 2544 (2002).

D. Ouyang, R. Heitz, N.N. Ledentsov, S. Bognár, R.L. Sellin, C. Ribbat, and D. Bimberg, *Lateral-cavity spectral hole burning in quantum dot lasers*, Appl. Phys. Lett. **81**, 1546 (2002).

C. Ribbat, S. Bognár, R.L. Sellin, and D. Bimberg, *Spectral mode dynamics of short cavity quantum-dot lasers*, Appl. Phys. Lett. **81**, 147 (2002).

D.S. Sizov, M.V. Maksimov, A.F. Tsatsul'nikov, N.A. Cherkashin, N.V. Kryzhanovskaya, A.B. Zhukov, N.A. Maleev, S.S. Mikhrin, A.P. Vasil'ev, R. Sellin, V.M. Ustinov, N.N. Ledentsov, D. Bimberg, and Z.I. Alferov, *The Influence of Heat Treatment Conditions on the Evaporation of Defect Regions in Structures with InGaAs Quantum Dots in the GaAs Matrix*, Semiconductors **36**, 1020 (2002).

S. Rodt, A. Schliwa, V. Türc, R. Heitz, O. Stier, R.L. Sellin, M. Strassburg, U.W. Pohl, and D. Bimberg, *Few-particle effects in self-organized quantum dots*, phys. stat. sol. (b) **234**, 354 (2002).

P. Borri, W. Langbein, S. Schneider, U. Woggon, R.L. Sellin, D. Ouyang, and D. Bimberg, *Exciton relaxation and dephasing in quantum-dot amplifiers from room to cryogenic temperature*, J. Sel. Top. Quantum El. **8**, 984 (2002).

S. Bognár, M. Grundmann, O. Stier, D. Ouyang, C. Ribbat, R. Heitz, R. Sellin, and D. Bimberg, *Large Modal Gain of InAs/GaAs Quantum Dot Lasers*, phys. stat. sol. (b) **224**, 823 (2001).

P. Borri, W. Langbein, S. Schneider, U. Woggon, R.L. Sellin, D. Ouyang, and D. Bimberg, *Ultralong Dephasing Time in InGaAs Quantum Dots*, Phys. Rev. Lett. **87**, 157401 (2001).

H.Y. Ryu, Y.H. Lee, R.L. Sellin, and D. Bimberg, *Over 30-fold enhancement of light extraction from free-standing photonic crystal slabs with InGaAs quantum dots at low temperature*, Appl. Phys. Lett. **79**, 3573 (2001).

C. Ribbat, R. Sellin, M. Grundmann, D. Bimberg, N.A. Sobolev, and M.C. Carmo, *Enhanced radiation hardness of quantum dot lasers to high energy proton irradiation*, El. Lett. **37**, 174 (2001).

Acknowledgements

I would like to thank Prof. Dr. Dieter Bimberg who has offered me to work in his group on a very fascinating and challenging topic with increasing importance for applied physics and device research, and for his vivid interest in the progress of my work. Indefatigable fundraising has considerably facilitated the costly business of MOCVD growth. He has given me numerous opportunities to present my work at international conferences. During my work in the management and administration of several third-party-funded projects, I was given the chance to cooperate with very skillful and interesting researchers from all over the world.

Prof. Dr. Marius Grundmann accompanied my work at the beginning, and I would like to thank him for many interesting discussions. Prof. Dr. Nikolai N. Ledentsov provided assistance to my work with many concrete suggestions and an amplex of ideas. I benefited from his large experience with MBE-grown QD lasers. Dr. Frank Heinrichsdorff was my predecessor as an MOCVD quantum-dot device grower, and also my tutor during the first months of my work. During our joint period in the MOCVD laboratory, he conveyed a precious deal of his practical experience to me. I would like to thank Dr. Udo W. Pohl for his commitment in the configuration of the new Aixtron 200/4 MOCVD machine as well as in the establishment of the new MOCVD laboratory. His didactical skills have been a great help in writing manuscripts and in preparing conference abstracts and talks. I want to thank Dr. Robert Heitz for many interesting discussions regarding quantum-dot physics. His personal views and his open critical notes have given me valuable impulses.

Dipl.-Krist. Kathrin Schatke has technically assisted the MOCVD experiments, and I would like to thank her for her unselfish commitment. I would also like to thank Ilona Gründler for her assistance. I have furthermore benefited a lot from the large MOCVD experience of Dr. Armin Dadgar who supported me with numerous tips and tricks. I would like to thank Dr. André Strittmatter for his help on atomic force microscopy and x-ray diffractometry. I am also grateful to Dr. Lutz Müller-Kirsch for many interesting and helpful discussions.

I am particularly indebted to Dipl.-Phys. Ilia Kaiander for the intensive and fruitful cooperation in the field of epitaxy during the last year of my work. I enjoyed the cooperation with Dipl.-Phys. Thorsten Kettler on InGaAsN quantum dots and with Dipl.-Phys. Konstantin Pötschke on InAsSb quantum-dot structures. I want to thank Dipl.-Phys. Florian Guffarth and Dr. Robert Heitz for help and discussions regarding photoluminescence spectroscopy. I am very grateful to Dr. Nikolai Zakharov and Dr. Peter Werner from the Max-Planck Institute of Microstructure Physics, Halle,

Germany, for the steady and speedy supply of numerous transmission electron micrographs. I would like to thank Dr. Christian Ribbat, M.Sc. Dongxun Ouyang, Dipl.-Phys. Oliver Schulz and Dipl.-Phys. Thorsten Kettler for the fabrication and characterization of quantum-dot edge-emitting lasers, and Dipl.-Phys. Friedhelm Hopfer and Dipl.-Phys. Anatol Lochmann for processing and characterizing surface-emitting lasers.

I would like to thank Dipl.-Phys. Sven Rodt for careful proofreading of the manuscript and Prof. Dr. Alois Krost for preparing the second expert opinion on my thesis. I would like to express my gratitude to Dipl.-Phys. Sven Rodt, Dr. Volker Türck and Dr. Armin Dadgar for administering and maintaining a very reliable computer network. I enjoyed sharing my office with Andrei Schliwa, Florian Guffarth and Ilia Kaiander. Parts of this work were funded by the EU project DOTCOM, the German Federal Ministry of Education and Research (bmb+f), and the collaborative research center Sfb 296 of the German Research Foundation (DFG). Last not least I am indebted to Agilent Technologies for a grant within the frame of an external research programme.

Table of contents

1. Introduction	1
2. Lasers and quantum dots	3
2.1. <i>Semiconductor lasers</i>	3
2.2. <i>Quantum dots</i>	6
2.3. <i>Properties of quantum-dot lasers</i>	7
2.4. <i>MOCVD for quantum-dot lasers</i>	10
2.5. <i>Objectives and methods of this work</i>	11
3. Metalorganic chemical vapor deposition	15
3.1. <i>Principle</i>	15
3.2. <i>Conventional and alternative precursors</i>	16
3.2.1 Conventional-precursor MOCVD	17
3.2.2 Alternative-precursor MOCVD	18
3.2.3 Tertiarybutylarsine	20
3.2.3.1 Surface stabilization	22
3.2.3.2 V/III ratios for GaAs and AlGaAs growth	23
3.3. <i>Modular optimization of laser structures</i>	24
3.3.1 Waveguides and distributed Bragg reflectors	25
3.3.1.1 Calibration of growth rate	25
3.3.1.2 Lateral homogeneity of layer thicknesses	27
3.3.1.3 Calibration of oxidation rate for Al(Ga)O _x /GaAs DBRs	30
3.3.2 Optimization of quantum-dot active regions	31
4. Self-organization of quantum dots	35
4.1. <i>The equilibrium crystal shape</i>	35
4.2. <i>Strained heteroepitaxy of thin films</i>	36
4.3. <i>Thermodynamic models of 3D island arrays</i>	37
4.4. <i>Kinetic description of island formation in one dimension</i>	39
4.5. <i>Island size and density</i>	40
4.5.1 Role of temperature	41
4.5.2 Impact of deposition amount	43
4.5.3 Influence of growth interruption	43
4.5.4 Importance of growth rate	43
5. MOCVD of quantum-dot structures for laser diodes	45
5.1. <i>In-situ annealing of QD structures</i>	46
5.1.1 Flattening of the growth front	47
5.1.2 Optical properties of annealed QD structures	52
5.2. <i>Alternative-precursor MOCVD of InGaAs QDs</i>	54

5.3. Redshift of the quantum-dot emission wavelength.....	56
5.3.1 Overgrowth of InGaAs QDs by InGaAs QWs using arsine	57
5.3.1.1 Spectroscopic characterization.....	59
5.3.1.2 Structural characterization	61
5.3.2 Advantage of TBAs for redshifting the QD emission wavelength	67
5.3.3 Wavelength shifting using nitrogen	68
5.3.3.1 Simultaneous deposition of As, Ga, In and N.....	72
5.3.3.2 Nitridation	74
5.3.4 Wavelength shifting using antimony	76
5.3.4.1 Deposition amount	76
5.3.4.2 TESb and TBAs during the growth interruption.....	78
6. Quantum-dot lasers.....	85
6.1. Edge emitters.....	85
6.1.1 Lasers with in-situ annealed quantum-dots.....	85
6.1.1.1 Threshold reduction and increase of efficiency	86
6.1.1.2 High-Power Operation	89
6.1.1.3 Lifetimes	92
6.1.1.4 Characteristic temperature	93
6.1.2 Edge emitters grown with alternative precursors.....	96
6.1.3 Long-wavelength (>1.24 μm) QD lasers	97
6.2. Quantum-dot vertical-cavity surface emitters.....	99
6.2.1 Quantum-well VCSEL	101
6.2.2 Quantum-dot VCSEL.....	105
7. Summary and outlook.....	111
List of acronyms	115
List of figures	117
Bibliography	125

1. Introduction

The importance of semiconductor lasers has increased dramatically during the last decades. In compact disc and DVD players, they have become inherent parts of everyday life. As compared to light emitted by other light sources, laser light is highly monochromatic and by orders of magnitude more intensive. Since laser light can more easily be focused, for example, lasers are particularly suited as signal sources for optical fiber communication. Today, the main application of semiconductor lasers is optical data- and telecommunication¹. Their small size enables, for example, the fabrication of dense laser arrays for wavelength division multiplexing, or space division multiplexing for optical interconnects. For semiconductor lasers with quantum dots² (QDs) as active medium, Arakawa and Sakaki predicted already in 1982 reduced threshold current densities that are far less dependent on operation temperature than conventional quantum well (QW) lasers³. Larger differential gain of QD lasers was foreseen a few years later by Asada et al.⁴, making them attractive as uncooled direct modulators with larger cutoff frequencies.

QDs used as active medium for laser diodes are small coherent three-dimensional semiconductor insertions with a fundamental band gap lower than that of the matrix. They confine trapped carriers in all three spatial directions on a length scale smaller than the exciton Bohr radius and are therefore electronically zero-dimensional. The density of states in QDs is δ -function-like, resulting in atom-like electronic properties. QDs thus combine the advantages of semiconductors (electrical and thermal conductivity, energy gaps in the right range etc.) with those of atoms (spectral purity, symmetric gain spectrum).

An important advantage of QDs is the possibility to extend the emission wavelength on gallium arsenide (GaAs) substrates up to 1.3 μm , a standard telecommunication wavelength. Lasing emission at 1.3 μm is particularly interesting for broadband metropolitan area fiber communication due to a dispersion minimum of conventional glass fibers at 1.3 μm . With conventional QWs, the room-temperature emission wavelength on GaAs substrates is limited to about 1.2 μm ^{5, 6}. The demand of 1.3 μm telecom emitters has so far been satisfied using QW lasers grown on expensive indium phosphide (InP) substrates. Lower fabrication costs of optoelectronic devices grown on GaAs substrates make the replacement of InP-based QW lasers by GaAs-based QD lasers attractive. In addition, GaAs technology opens the possibility to grow highly effective AlAs/GaAs distributed Bragg reflectors (DBRs). This enables the *monolithic* fabrication of vertical-cavity surface-emitting lasers (VCSELs)⁷. AlAs/GaAs heterostructures can selectively be oxidized to obtain AlO_x/GaAs DBRs. Oxide DBRs exhibit higher reflectivities so that less AlO_x/GaAs pairs are needed for a VCSEL mirror.

Layer structures for the fabrication of oxide-DBR VCSELs are thinner and require less epitaxial effort. The combination of telecom wavelengths, GaAs technology and surface-emitting geometry in a monolithic design makes oxide-DBR GaAs-based 1.3 μm QD VCSELs one of the most interesting optoelectronic devices.

QDs for the application in optoelectronic devices are nowadays fabricated using a self-organization concept^{2, 8}: A thin semiconductor film is epitaxially deposited on a substrate having a different lattice constant. Driven by the strain arising from the lattice mismatch, three-dimensional QDs are formed by material redistribution and agglomeration at spontaneously defined nucleation sites on the surface. The discovery of this so-called Stranski-Krastanow (SK) growth mode was a major breakthrough in the development of QD lasers since only self-organized QDs have the crystalline quality required for the realization of the theoretical advantages of QD lasers⁹. Modern technologies of semiconductor crystal growth like Metalorganic Chemical Vapor Deposition (MOCVD) or Molecular Beam Epitaxy (MBE) enable the controlled, reproducible and homogeneous deposition of ultrathin strained semiconductor films required for the fabrication of self-organized QDs. MOCVD is the most important fabrication standard for optoelectronic semiconductor device epitaxy in Europe. Whereas MOCVD-grown QD lasers have been demonstrated in the past^{2, 10-13}, their performance was not yet close to the theoretically predicted limits. The advancements of the MOCVD growth in this work have brought QD lasers further to their theoretical limits: Threshold current densities could be reduced further, internal quantum efficiencies of close to the ideal limit of 100 % have been achieved, output powers of more than 10 W were demonstrated, and lifetime tests of such lasers have proven their high reliability. Different approaches to achieve QD luminescence at 1.3 μm are introduced and discussed, including an extensive characterization of the crystalline and optical properties of the corresponding structures. Whereas MBE-grown GaAs-based QD lasers emitting at 1.3 μm have already been demonstrated (cf. Ref. 14 and references therein), MOCVD-grown QD lasers with emission wavelengths beyond 1.2 μm are presented in this work for the first time¹⁵. MOCVD growth of QD laser structures for vertical light emission was developed within this work and has led to the demonstration of the first MOCVD-grown oxide-DBR QD VCSEL worldwide.

The advancements of MOCVD growth of QD lasers included the substitution of the highly toxic As precursor arsine and the explosive Si precursor silane by alternative organic precursors that are significantly less hazardous and have vapor pressures far below the atmospheric pressure. The successful application of alternative-precursor MOCVD is an important step towards the establishment of a safe and environment-friendly fabrication technology of novel optoelectronic devices.

2. Lasers and quantum dots

The working principle of a laser is *light amplification by stimulated emission of radiation (laser)*. In a laser, the photons are not emitted independently: a photon that is spontaneously generated in the active region of a laser stimulates other photons to be emitted with the same phase and wave vector. In semiconductor lasers, photons are generated by the recombination of electrons in the conduction band with holes in the valence band. Lasing can only set in if sufficient electrons (holes) are located in the conduction (valence) band. This is usually achieved by electrical current injection. In a semiconductor laser, the light-emitting active medium is centered in a resonator waveguide along which the light amplification takes place. Mirrors at both ends of the cavity provide optical feedback and lead to the formation of a stationary light wave. Lasing can only occur if the number of photons generated per length of the resonator is larger than the number of photons lost by absorption and scattering, that is, if the gain overcomes the losses.

Most of today's semiconductor lasers are based on thin low-band-gap semiconductor insertions in the waveguide, such as nanometer-thin QWs in which the carrier recombination takes place. A novel approach is the use of nanometer-sized three-dimensional QDs as light-emitting centers. QD lasers were predicted already in the nineteen-eighties to have superior properties as compared to QW lasers^{3, 4}. A considerable number of these advantages have been demonstrated during the last years. It is the aim of this chapter to give an introduction to the working principle of semiconductor lasers, to the benefits of QDs as light-emitting medium, and to the advancements of the QD laser growth technology achieved during this work.

2.1. Semiconductor lasers

The idea of a current-injection semiconductor laser goes back to a publication by John von Neumann in 1953¹⁶. The first injection lasers were demonstrated in 1962 simultaneously by different groups¹⁷⁻¹⁹ using GaAs *p-n*-junctions as active regions. A further breakthrough in optoelectronics was achieved when the *heterostructure* laser was developed^{20, 21}. Heterostructure lasers differ from the earlier heterojunction lasers by vertical light-wave confinement between two cladding layers that have a refractive index different from the optical-confinement layer. Yet another step towards an improvement of device performance was the separation of charge carrier confinement from optical confinement. In such separate confinement heterostructure (SCH) lasers, carriers are confined within a few nanometer thick low-band-gap semiconductor QW, placed in the optical confinement layer. Quantum-dot lasers are SCH lasers in which the carriers are confined in nanometer-sized, low-band-gap QDs.

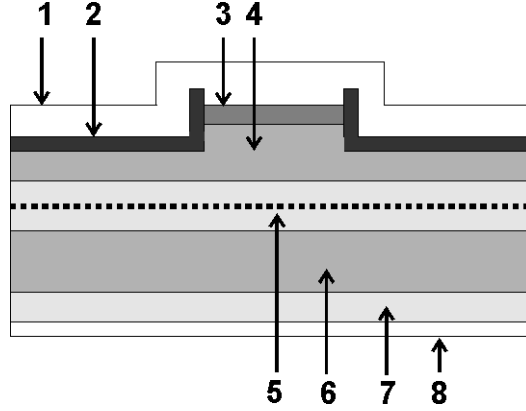


Fig. 1: Schematic diagram of the cross-sectional view on the laser facet of a typical, fully processed edge-emitting laser diode. The different layers are: **1.** Ti/Pt/Au top contact. **2.** SiN_x insulating layer. **3.** p^{++} GaAs contact layer. **4.** p^{+} AlGaAs top cladding. **5.** Undoped optical-confinement GaAs layer with the active region in the center. **6.** n^{+} AlGaAs bottom cladding. **7.** Substrate. **8.** Ni/AuGe bottom contact.

Most important for good laser characteristics are large optical gain and low optical losses. The modal gain g_{mod} of a laser is defined as the negative light absorption coefficient of the resonator waveguide. In the lasing mode, g_{mod} is positive and must compensate optical losses. In current-injection lasers, the lasing threshold is reached if the current passes a certain threshold value. At the lasing threshold, the modal gain g_{mod} provided by the pumped active region equals the optical losses. This is the case if

$$g_{\text{mod}} = \alpha_m + \alpha_i = \alpha_{\text{tot}} \quad (2.1)$$

The total losses α_{tot} consist of the internal losses α_i originating from scattering and free-carrier absorption in the waveguide, and the mirror losses α_m , which depends on the mirror reflectivities R_1 and R_2 , and the cavity length L :

$$\alpha_m = \frac{1}{2L} \ln \left(\frac{1}{R_1 R_2} \right) \quad (2.2)$$

For as-cleaved facets, R_1 and R_2 have the same value. However, R_1 and R_2 can independently be adjusted by facet coatings.

Edge emitters

Edge emitters or Fabry-Perot lasers are obtained if the light wave is guided parallel to the substrate and two cleaved facets act as mirrors. A schematic overview of an edge-emitting laser is given in Fig. 1. The vertical optical confinement is provided by cladding layers that have different optical indices than the waveguide material. Lateral light-wave confinement is

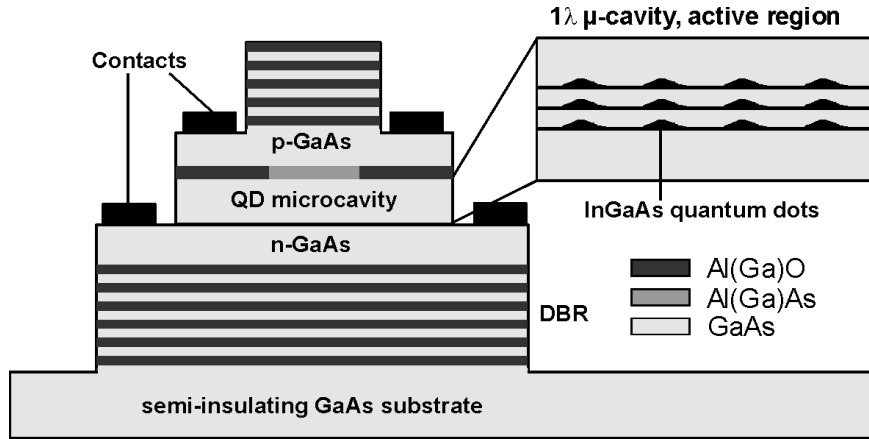


Fig. 2: Layer and structure design of a GaAs-based full-oxide-DBR VCSEL with intracavity *p*- (top) and *n*-contacts (bottom). The active region as shown schematically in the magnification can alternatively consist of a multi QD layer stack or QWs. After Ref. 14.

achieved, for example, by lithographic definition and etching of ridges into the as-grown laser structure. The SiN_x insulation layer as depicted in Fig. 1 restricts current injection to the ridge area.

VCSELs

In VCSELs, the light wave is guided perpendicularly to the substrate. DBRs are used as mirrors. VCSELs enable easy coupling to optical fibers due to their circular beam profile, leading to good mode matching with both multimode and single-mode fibers. VCSELs are considered as the most important devices for optical interconnects, enabling ultra-parallel information transmission in computer systems^{7, 22}.

The working principle of VCSELs is analog to that of edge emitters. However, the emission perpendicular to the growth plane and the ultra short cavity length as compared to edge emitters require a completely different layer design. As can easily be deduced from Eq. 1.2, short cavities require ultra-high mirror reflectivities. In fact, mirror reflectivities of more than 99 % are required for VCSELs. Such reflectivities can only be provided by DBRs. Fig. 2 shows a schematic diagram of a pillar VCSEL. The center of the device is magnified and shows the active layer consisting of QD sheets. Lateral gain guiding is achieved by a top oxide aperture. The oxide of the aperture mainly acts as electrical insulator, allowing pumping of the active medium only below the unoxidized center of the aperture. The diameter of the aperture has a decisive impact on threshold current and lateral mode profile. The active layers are centered in an antinode of the stationary wave so that a maximum overlap of optical wave and active region is achieved.

The n and p intracavity contact layers are placed in nodes of the stationary light wave to minimize free-carrier absorption.

If all-semiconductor AlAs/GaAs DBRs are used, the number of periods for each DBR must be in the order of 30. Using oxide-mirror technology, 5 to 7 Al(Ga)O_x/GaAs DBR pairs yield sufficient reflectivity, depending on the mirror quality and also on the gain of the active medium. Oxide-DBR VCSELs can thus be realized with significantly less epitaxial effort.

2.2. Quantum dots

The use of QDs as active material of semiconductor lasers can lead to superior device characteristics as compared to standard quantum-well based devices. The basic properties of QDs and their impact on laser characteristics are briefly outlined in this section.

Nanometer-sized In(Ga)As QDs in a GaAs matrix represent localization centers for both electrons and holes since the band gap of In(Ga)As is lower than that of the surrounding GaAs matrix and InGaAs/GaAs interfaces are type-I heterojunctions. Self-organized InGaAs/GaAs QDs are typically 2 to 6 nm high and 10-25 nm wide. Carriers trapped by QDs are confined in all three spatial directions and can occupy only discrete energy states. Since the lateral extension of self-organized QDs are comparable to the exciton Bohr radius, the electronic levels of both electron and hole states are substantially determined by the size, shape and chemical composition of the QDs²³. Therefore, QDs have more in common with the electronic structure of atoms than of solids, which have quasi-continuous energy levels.

The original prediction of temperature-independent threshold currents of QD lasers was made for QDs with a single electron (hole) level and infinite potential barriers. Since QDs have typically more than one electron (hole) level, and since the potential barriers are not infinite in real systems, QDs hold the predictions only if the spacing between energy levels is larger than the thermal energy $k_B T$. Otherwise, a significant fraction of carriers are found in higher energy states, or are thermally excited to the GaAs matrix where recombination does not take place at the target wavelength.

The electronic density of states in zero-dimensional objects like QDs is δ -function-like (for $T = 0$):

$$\rho_{0D}(E) = \frac{1}{L_x L_y L_z} \sum_{i=0}^n \delta(E - E_i) \quad (2.3)$$

However, whereas the *density* of states is extremely large for $E = E_i$, the *number* of confined electronic states present in a QD sheet scales with the

QD area density. This value is decisive for the performance of QD lasers. Both threshold current density and modal gain of QD laser diodes increase with the number of QDs.

Due to the δ -function-like density of states, ultra-narrow cathodoluminescence lines of 0.15 meV could be observed for *single* InAs/GaAs QDs at low temperatures²⁴; the value of 0.15 meV was limited by the spectral resolution of the setup. A typical *ensemble* of self-organized QDs, however, exhibits a finite size distribution, leading to an inhomogeneous broadening of the transition line, the full width at half maximum (FWHM) of which typically ranges from 25 meV to 80 meV.

Electron and hole levels in QDs as well as transition probabilities between these levels can be calculated within an 8-band $k\cdot p$ framework²⁵. A decisive difference between QDs and atoms is the lower spatial symmetry of QDs, which are not spherically symmetric. Moreover, the strain in self-organized QDs induces a piezoelectric field, owing to the strain-related relative displacements of the anion and cation sublattices. This further reduces the QD symmetry. None of the transition selection rules valid for atoms exists for QDs, so that transitions from any electron state to any hole state are essentially possible²⁵. The transition matrix elements are in good approximation proportional to the spatial overlap integral of the respective electron and hole wavefunctions.

Whereas the QD electron ground state is two-fold degenerate, the first excited electron state can be occupied by four electrons. Therefore, the modal gain of a QD laser due to exciton recombination from the first excited QD electron state is twice as large. If the ground-state gain of a QD laser cannot overcome losses since, for example, the QD density is not sufficient or a large fraction of the QDs is dislocated, excited-state lasing sets in.

2.3. Properties of quantum-dot lasers

The first QD-like laser was demonstrated in 1982 by applying a strong magnetic field to a QW laser perpendicular to the substrate³. An increase of the characteristic temperature T_0 from 144 K to 313 K was measuredⁱ. Since then, carrier localization was achieved by the fabrication of freestanding QDs via lithographical patterning of QWs. QDs have also been fabricated by selective intermixing using ion implantation or laser annealing. Lateral charge carrier confinement could also be achieved by strain gradients in QWs and also via growth on pre-patterned substrates (cf. Ref. 2 for a review, and references therein). First QD *laser* operation was achieved with QDs realized by lithographic patterning of QWs²⁶. However, lasers based

ⁱ For a definition of T_0 cf. Eq. 6.3.

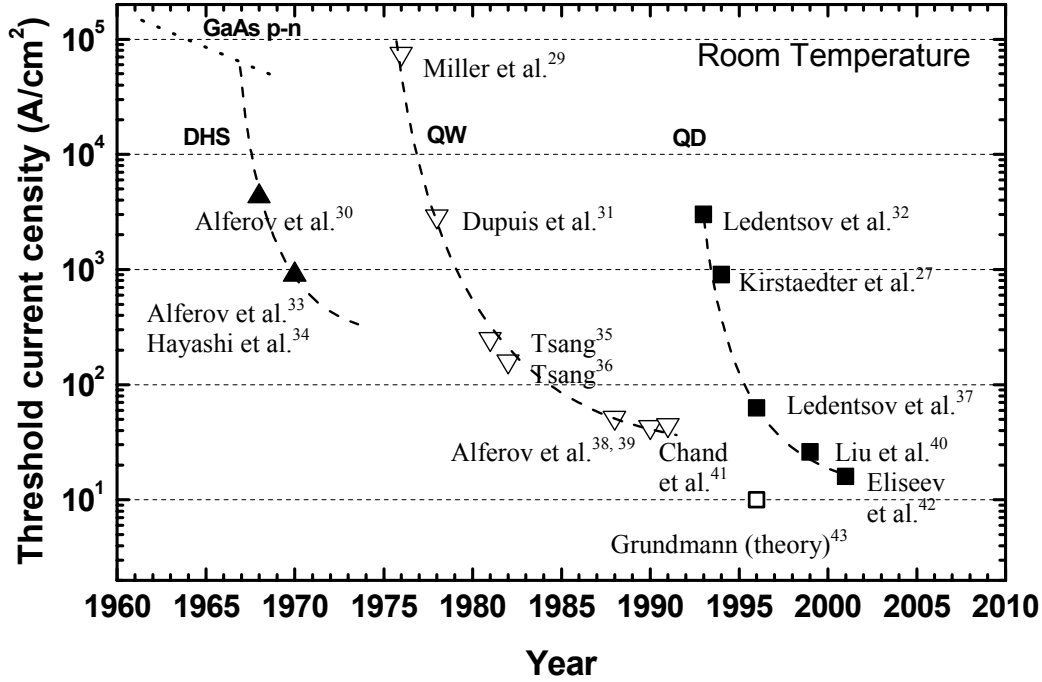


Fig. 3: Lowest threshold current densities reported for double-heterostructure (DHS) lasers, QW lasers, and QD lasers, respectively, versus publication year. After Ref. 28.

on such lithographic QDs were still troubled by extremely high threshold current densities (7.6 kA/cm^2 at 77 K), most likely due to process-induced damages that cause high losses. A new era started in 1994 with the demonstration of the first semiconductor laser based on self-organized QDs²⁷. These devices exhibited significantly lower threshold currents and large T_0 values. No lithographic steps are needed for the fabrication of such QDs so that the danger of process-induced damage drops out. Fig. 3 shows the development of the lowest threshold current densities of different semiconductor laser types with the years. The lasers based on self-organized QDs as active region show the lowest threshold current densities. The reduction of threshold current densities for each of the respective laser types is due to the improvement of growth and process technology.

To date, mostly InP-based optoelectronic components are available in the wavelength regime of 1.3-1.55 μm as required for datacom applications. This lasing wavelength regime can likewise be reached with InGaAsN QWs on GaAs substrates. Threshold current densities of such dilute-nitride lasers are rather high, however. It has been shown that low-threshold lasing in the 1.3-1.55 μm lasing wavelength regime can be reached on GaAs using self-organized QDs^{8, 44}. The wavelength of InGaAs QWs on GaAs, for example, is limited to about 1.2 μm due to the onset of misfit dislocations^{5, 6}. Since

the height of self-organized InGaAs QDs can be larger than the thickness of InGaAs QWs, QDs can exhibit larger emission wavelengths. QD emission wavelengths of more than $1.4\text{ }\mu\text{m}$ at room temperature have been reported⁴⁵. Lateral electronic coupling in dense QD agglomerates can increase the emission wavelength to beyond $1.75\text{ }\mu\text{m}$ ⁴⁶.

The overgrowth of self-organized InAs QDs with a thin Ga-rich InGaAs layer has been demonstrated as an effective approach in MBE to tune the QD ground-state transition up to $1.3\text{ }\mu\text{m}$ ⁴⁷⁻⁴⁹. The overgrowth of InAs QDs with such QWs results in a larger amount of indium located in or around the QDs and to a strain reduction within the overgrown QDs (cf. sect. 5.3.1). As active medium of laser diodes, such QD structures have led to promising characteristics of both edge emitters^{8, 50-52} and VCSELs⁵³ at $1.3\text{ }\mu\text{m}$. Alternatively to *overgrowing* QDs with Ga-rich InGaAs films, InAs QDs have been *inserted* into such QWs to reach room-temperature luminescence and lasing at $1.3\text{ }\mu\text{m}$. This technique is referred to as the DWELL (Dots in a WELL) concept^{40, 42, 48, 54-58}. QWs of about 10 nm thickness and a typical indium fraction of 15 % to 20 % are chosen as matrix for the QDs. Liu et al.⁴⁰ have found that the DWELL concept leads to significantly higher QD densities as compared to direct deposition on GaAs. The lowest transparency current of 13 A/cm^2 ever achieved for a semiconductor laser diode at room temperature was obtained using a single-DWELL as active medium^{42, 58}. For $1.3\text{ }\mu\text{m}$ DWELL lasers, lasing activity at operation temperatures beyond 150°C has been demonstrated⁵⁹.

QD lasers emitting at shorter wavelengths are also in the focus of scientific interest. MOCVD growth of InGaAs/GaAs QD lasers showing ground-state lasing with close to 4 W output power at 1100 nm has been demonstrated¹². Such devices can be used as efficient pump sources for Thulium-doped up-conversion fiber lasers emitting in the blue spectral range^{60, 61}. MBE growth of QD lasers at 980 nm⁶² (pump sources for erbium-doped fiber amplifiers) and 940 nm⁶³ (pump sources for ytterbium-doped yttrium aluminium garnet solid-state lasers and neodymium/erbium-doped fiber lasers) have also been reported. Red-light-emitting InP/InGaP QD lasers have been grown on GaAs substrates using MOCVD^{64, 65}.

Higher differential gain of QD lasers, as foreseen already in 1986 by Asada et al.⁴, implies ultra short gain recovery times⁶⁶, potentially enabling higher cut-off frequencies for directly modulated QD lasers and higher modulation frequencies of QD semiconductor optical amplifiers^{67, 68}. Lower α -factors of QD lasers as compared to QW lasers and lower carrier diffusion in QD sheets lead to suppression of beam filamentation of narrow-stripe lasers⁶⁹. The enhanced beam quality enables to reduce coupling losses to optical fibers.

Whereas the original prediction for QD lasers was a temperature insensitivity of the threshold current at any temperature, the thresholds of *real* QD lasers are still temperature-dependent. This is mainly attributed to thermal excitation of charge carriers from the electron and hole ground states to higher energy states. Ideally, the energy spacing between the discrete QD states is larger than $k_B T$, preventing higher energy states to be significantly populated. This would lead to a complete temperature insensitivity of the threshold current. However, the energy spacing particularly between hole states can be smaller than $k_B T$. QD lasers emitting between 1.1 and 1.2 μm still exhibit temperature sensitivities comparable to those of InP-based QW lasers. This issue is addressed in more detail in sect. 6.1.1.4.

A drawback of QD lasers is the relatively low modal gain g_{mod} per QD sheet. Although QDs exhibit a *material* gain that can exceed the material gain of corresponding QW devices by far⁷⁰, the *modal* gain of a single QD sheet is much lower due to the small optical confinement. g_{mod} is related to the material gain g_{mat} of the light-emitting medium according to

$$g_{\text{mod}} = \Gamma g_{\text{mat}} \quad (2.4)$$

Γ is the optical confinement factor, representing the overlap of the optical wave with the active region. The optical confinement Γ is best expressed as $\Gamma = \Gamma_{\text{xy}} \cdot \Gamma_z$ where Γ_z is the vertical confinement and Γ_{xy} the area coverage with active material. Whereas $\Gamma_{\text{xy}} = 1$ for QWs, it has typical values of only 0.01-0.03 for QD sheets. For a typical QD laser, Γ is in the order of 10^{-4} . This is about ten times lower than a typical optical confinement in QW lasers with comparable waveguide design. To grow QD lasers with high modal gain, both large QD sheet densities and close multiple stacking of QD layers with thin spacer layers are decisive.

2.4. MOCVD for quantum-dot lasers

MOCVD is the most important commercial large-scale fabrication technology for electronic and optoelectronic semiconductor devices in Europe. It is used by leading optoelectronic-device manufacturers like Agilent Technologies, Bookham, Osram Optosemiconductors und JDS Uniphase. Using MOCVD, very high deposition rates can be achieved, and since no UHV is needed like in MBE where extensive baking-out of substrates previous to growth is required, a larger throughput is yielded.

In spite of these advantages, MBE has long been favored among researchers for the development of QD growth technologies as well as for the investigation of QD growth physics. The lasers of which record threshold current densities are shown in Fig. 3 are all grown using MBE. In MBE, growth conditions can very accurately be defined, controlled, and moni-

tored. The reactants can be supplied in elemental form by molecular beams that are directed perpendicularly onto a heated substrate placed in a UHV chamber. The growth process is controlled by substrate temperature and molecular flows only. Reflection high-energy electron diffraction (RHEED) is one of the most important in-situ characterization tools and allows to monitor surface reconstructions, surface smoothness on an atomic scale, surface diffusion lengths and deposition rates. Although QD self-organization has been investigated as long using MOCVD, results on MOCVD-grown QD lasers have hitherto been published only by few research groups⁸. For a couple of reasons, MOCVD growth is more difficult to control. For example, the reactants are supplied as organic or hydride precursors that are thermally cracked by the heated substrate susceptor into growth-reactive species, making the fraction of reactants in the gas phase a function of temperature. Aside from the choice of precursor molecules, total pressure and total gas flow are additional parameters that have to be controlled in contrast to MBE. Since MOCVD is not a UHV technique, in-situ monitoring like RHEED is not available. Only recently, reflectance and reflectance-anisotropy spectrometers were launched as in-situ monitoring tools by Laytec GmbH, Berlin, Germany⁷¹. The promising potential of these techniques for manufacturing QD-based optoelectronic devices is currently being explored.

Another reason for the rare use of MOCVD for the growth of QD lasers might be the observation that MOCVD-grown QDs exhibit an enhanced tendency to form plastically relaxed defect clusters⁷², most likely due to the complex nature of MOCVD precursor molecules, leading to an enhanced mobility of surface adatoms. Parasitic non-radiative recombination occurring in defective QDs drastically reduces optical gain in QD lasers. Whereas enhanced adatom mobilities are beneficial in MOCVD for the fast growth of thick layers and the realization of smooth interfaces, which is particularly important for the realization of low-loss waveguides for edge emitters and high-reflectivity DBRs for VCSELs, MOCVD of QD lasers is still a challenge.

2.5. Objectives and methods of this work

The device characteristics of real QD lasers have not yet been close to the ideal limits outlined by the early predictions. In addition, there have been arrears in the development of MOCVD QD growth due to the larger number of parameters to be controlled with respect to MBE and due to an enhanced tendency of defect formation. This work contributes to advance MOCVD of novel GaAs-based lasers based on self-organized QDs as active medium.

- A technique of high-temperature in-situ annealing was developed to flatten rough growth fronts. This enables a significant reduction of the spacer thickness between stacked QD layers without forfeit of the crystalline quality of the QDs (cf. sect. 5.1.1). The number of QD sheets in a laser waveguide was limited for a given QD sheet density and a given waveguide thickness by the minimum thickness of the *spacing* layers between the QD sheets. *Thinner* GaAs layers on top of QDs typically exhibit corrugated surfaces⁷³, owing to the underlying 3D morphology of the QDs, and to the low growth temperatures around 500°C at which SK QDs are deposited. Such corrugated surfaces are inappropriate for the deposition of subsequent QD sheets.
- Due to the enhanced tendency of defect formation in MOCVD, threshold current densities of MOCVD QD lasers have long been larger than those of MBE-grown lasers. In-situ annealing, initially developed for surface flattening, is shown to improve the crystalline quality of QD structures by reducing the density of non-radiative recombination centers in the matrix (cf. sect. 5.1.2). The enhancement of the crystal quality leads furthermore to an increase of internal quantum efficiencies of QD laser diodes (cf. sect. 6.1.1).
- The origin of the finite temperature stability of QD lasers was investigated (cf. sect. 6.1.1.4). A theoretical approach⁷⁴ assigns the finite temperature stability of threshold currents of state-of-the-art QD lasers to thermal excitation of charge carriers to GaAs matrix states and to subsequent *non-radiative* recombination, owing to low matrix crystal qualities. Radiative recombination efficiencies in the GaAs matrix could significantly be improved in this work by in-situ annealing⁷³. However, the temperature behavior of the threshold currents could not be increased this way. QD lasers were grown in this work with thin AlGaAs diffusion barriers around the QD active region to prevent charge carriers from thermal excitation to the matrix. The results obtained with such structures were compared to *quantum-well* lasers with and without carrier diffusion barriers. The temperature stability of *quantum-well* lasers could be improved. However, diffusion barriers have only a minor influence on the temperature stability of *quantum-dot* lasers. These findings suggest that non-radiative recombination in the matrix is not the primary reason for the finite temperature stability of QD lasers.
- Strongly toxic gaseous hydride precursors such as arsine or explosive hydrides like silane widely used in commercial MOCVD constitute a considerable threat to man and environment. The suitability of the alternative organic precursor tertiarybutylarsine (TBAs) for the growth of QD laser structures was therefore explored (sects. 5.2 and 5.3.2). The changeover to alternative-precursor MOCVD required the adjustment of

MOCVD growth parameters according to the specific precursor properties (sects. 3.2.2 and 3.2.3). The demonstration of QD lasers grown using alternative-precursor MOCVD (sect. 6.1.2) is an important step towards the establishment of a safe and environment-friendly growth technology of QD-based optoelectronic devices.

- In contrast to MBE where 1.3 μm lasers have already been demonstrated, lasing wavelengths of MOCVD-grown QD lasers have not reached 1.3 μm . QDs emitting at this wavelength are rather large and thus contain high strain energies. The danger of defect formation in such strained layers is particularly high in MOCVD. A number of alternative techniques to redshift the QD emission wavelength have been investigated with regard to their suitability for MOCVD-grown long-wavelength QD lasers (sect. 5.3). These techniques comprise the overgrowth of InGaAs QDs with Ga-rich InGaAs QWs (sects. 5.3.1 and 5.3.2). Strain redistribution and increase of the effective QD size lead to a redshift of the QD emission wavelength. This technique is currently used in MBE to grow 1.3 μm QD lasers. In addition, experiments to redshift the emission wavelength by nitrogen (sect. 5.3.3) and antimony insertions (sect. 5.3.4) are carried out and discussed. Nitrogen and antimony were supplied during deposition of InGaAs QDs and/or during the subsequent growth interruption (GRI) that is typically performed after deposition of the QD material in order to allow QD formation and QD size evolution. Long-wavelength QD structures were investigated using photoluminescence (PL) spectroscopy and transmission electron microscopy images (TEM). QD lasers with emission wavelengths beyond 1.2 μm are presented, based on InGaAs QDs overgrown with Ga-rich InGaAs QWs (sect. 6.1.3).
- GaAs-based QD VCSELs at 1.3 μm are particularly attractive optoelectronic devices for data- and telecommunication. An MOCVD growth process for the fabrication of all-oxide DBR QD VCSELs was therefore developed within this work (sect. 6.2). To achieve vertical lasing, large modal gain of the active region and high-reflectivity DBR mirrors are needed. The comparably low modal gain of QD sheets as compared to QW sheets requires dense vertical stacking of QD layers located in the antinodes of the optical wave in the VCSEL cavity. The gallium content of Al-rich AlGaAs layers for the fabrication of AlGaO_x/GaAs DBRs has a strong influence on the oxidation dynamics. The Ga fraction of such AlGaAs layers was calibrated, and parameters for a reproducible growth of such AlGaAs layers were found (sect.3.3.1). The design of thin Ga-rich AlGaAs buffer layers inserted between GaAs and Al-rich AlGaAs layers is decisive for the oxide quality^{75, 76}. The insertion of such buffer layers is related with a roughening of the DBR hetero-interfaces if TBAs is used. The development of

VCSEL growth and the development of the fabrication process took place simultaneously. On the way to the demonstration of a QD VCSEL, a test VCSEL based on a single InGaAs QW as active medium was grown and processed (sect. 6.2.1). Valuable feedback to the ongoing development of both growth and process technology for the QD VCSEL were obtained from this experiment.

3. Metalorganic chemical vapor deposition

3.1. Principle

The growth experiments were initially performed on an Aixtron Aix200 machine, equipped with conventional hydride precursors. Within the course of this work, a new Aix200/4 machine was put into operation. From then on, growth was only carried out on this machine, using weakly toxic alternative precursors.

Both MOCVD machines have horizontal quartz-glass reactors with graphite susceptors and gas-foil rotation of the substrate plate. The graphite susceptors are heated using an radio-frequency (RF) heater (Aix200) and an infrared heater (Aix200/4), respectively. The reactor of the Aix200 enables the growth on 2" wafers. The Aix200/4 has a larger reactor and permits to grow on single 4", 3" and 2" wafers, or on three 2" wafers simultaneously if a satellite-rotation susceptor is used. The structures fabricated within this work were exclusively grown on single 2" wafer.

Fig. 4 shows a simplified schematic of the MOCVD setup, valid for both machines. Highly purified carrier gases (H_2 or N_2) are conducted to the bubblers containing the organic-compound precursors. The bubblers are connected to the machine by 4-way valves. Using such valves, unused bubblers can be bypassed. The bubblers are kept in thermostats filled with a mixture of water and ethylene glycol, and are stabilized at temperatures ranging from $-10^{\circ}C$ to $20^{\circ}C$. The temperature stabilization guarantees constant equilibrium vapor pressures of the precursors inside the bubblers. In addition, the total bubbler pressures (metalorganic + carrier gas) are adjusted by pressure controllers at predefined values larger than the precursor vapor pressure, typically between 200 and 1800 mbar. The carrier gas is conducted through a dip tube to the bottom of the bubbler and ascends through the precursor liquid or granulate. While the carrier gas is conducted through the bubbler, it is saturated with precursor molecules.

The 5/2-way "vent/run" valves conduct the mixture of precursor and carrier gas alternatively to the reactor or to the vent line that bypasses the reactor. This way, stabilized and thus well-defined precursor flows are permanently available, enabling short and reproducible growth sequences. The group-V and group-III precursors are conducted separately to the reactor in order to avoid precursor pre-reactions. In the Aix200, dopants are preferably conducted to the reactor through the group-V line. The Aix200/4 has a separate dopant line that finally meets the reactor few centimeters in front of the reactor gas inlet.

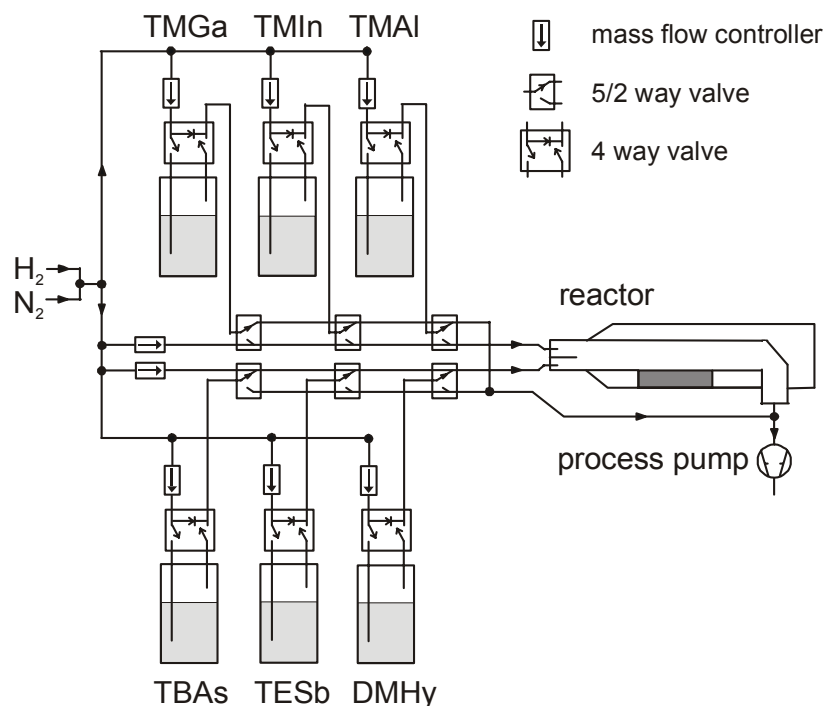


Fig. 4: Simplified schematic of the MOCVD setup of both the Aix200 and Aix200/4 machine. The two kits basically differ by the size of the quartz-glass reactor. The Aix200 disposes of a hydride lines for arsine instead of the TBAs-bubbler line. Dopant lines and pressure controllers are not shown.

The Aix200 was operated at 20 mbar with a total flow (carrier gas + metalorganic precursors + hydrides) of 5.56 standard liters per minuteⁱⁱ (slm). These parameters have been found to yield optimum lateral layer-thickness homogeneity. Moreover, the flow velocity achieved with these parameters allows ultra short reproducible growth sequences with valve opening times of 0.1 s. The situation is different for the larger Aix200/4 machine. The reactor of the Aix200/4 is twice as wide. To obtain sufficient lateral homogeneity for the growth of VCSEL structures, a total gas flow of up to 15.0 slm has to be adjusted. The large gas volumes in reactor and supply pipes require a larger total pressure in order not to overstrain the process pump. A total pressure of 100 mbar is hence used with this machine. The dependence of lateral layer thickness homogeneity on parameters like total pressure, total gas flow as well as the group-V to group-III inlet flow ratio is discussed in detail in section 3.3.1.2.

3.2. Conventional and alternative precursors

In conventional MOCVD of III-V compound semiconductors, only the group-III precursors are supplied in the form of liquid or granular organic

ⁱⁱ Standard conditions are defined as $T = 0^\circ\text{C}$, $p = 1.013 \text{ bar}$.

compound precursors. The group-V elements are usually supplied as gaseous hydrides. The danger connected with the toxicity and the high pressure of hydrides like arsine and phosphine can be overcome if organic group-V compounds such as TBAs and tertiarybutylphosphine are used. The major benefit of alternative precursors for the epitaxy of QD-based optoelectronic devices is their large decomposition efficiency⁷⁷ at low growth temperatures around 500°C required for the formation of SK QDs². On the other hand, the different chemical properties of alternative group-V precursors lead to different layer properties and require other growth parameters, as discussed in the following sections.

3.2.1 Conventional-precursor MOCVD

For conventional-precursor MOCVD on the Aix200 machine, arsine (AsH_3) was used as arsenic precursor. Since arsine hardly decomposes at typical QD growth temperatures of 480-520°C, large V/III ratios must be used. Trimethylgallium (TMGa, $(\text{CH}_3)_3\text{Ga}$), triethylgallium (TEGa, $(\text{C}_2\text{H}_5)_3\text{Ga}$), trimethylaluminium (TMAI, $(\text{CH}_3)_3\text{Al}$) and trimethylindium (TMIn, $(\text{CH}_3)_3\text{In}$) were used as group-III precursors.

Whereas TMGa was used for thick GaAs and AlGaAs layers and also for InGaAs QD sheets and QWs, TEGa was used for the AlGaAs layers of VCSEL structures for the fabrication of oxide DBRs. Reproducible ultra low Ga-fractions of 1 to 4 % are needed in such AlGaAs layers to precisely achieve target oxidation rates (cf. sect. 3.3.1.3). This requires extremely low Ga molar flows between 4×10^{-7} and 1.6×10^{-6} mol/min. Such low TMGa flows could be achieved with a double dilution configuration. However, no such configuration was available for Ga on the Aix200 machine. The problem was solved using TEGa instead of TMGa. TEGa has a much lower vapor pressure than TMGa ($p_{\text{TMGa}}(20^\circ\text{C}) = 243$ mbar, $p_{\text{TEGa}}(20^\circ\text{C}) = 6.7$ mbar) so that larger source flows can be used for the same molar Ga flow, and larger source flows can be controlled more precisely.

For the deposition of ternary InGaAs QDs around 500°C, TMGa was used. It has been reported that the use of TMGa at such growth temperatures leads to strong carbon incorporation and thus to significant intrinsic *p*-doping⁷⁸ which would strongly decrease the radiative efficiency of InGaAs QD layers. Intrinsic *p*-doping is reported not to occur if TEGa is used instead⁷⁸. Therefore, TEGa is sometimes preferred for MOCVD growth at low deposition temperatures, for example for high-quality InGaAsN QWs⁷⁹. A comparative study of InGaAs QDs grown with TMGa and TEGa was undertaken within this work and has shown that the radiative efficiency of the layers grown with TMGa is not inferior to that of TEGa-grown structures.

A mixture of SiH_4 (2 %) and H_2 (98 %) was used as *n*-dopant, conducted through a double dilution configuration. Dimethylzinc (DMZn , $(\text{CH}_3)_2\text{Zn}$) was used as *p*-dopant for the top AlGaAs cladding layers of *pin*-diode structures for edge-emitting lasers. Zn shows strong diffusion in GaAs ^{78, 80}, however, so that for the growth of VCSELs with GaAs intracavity contacts, carbon tetrabromide (CBr_4) was used. With this precursor, *p*-doping levels ranging from 10^{16} to 10^{19} cm^{-3} can be achieved^{81, 82}.

3.2.2 Alternative-precursor MOCVD

For alternative-precursor MOCVD on the Aix200/4 machine, only low-pressure organic-compound precursors were used. Tertiarybutylarsine (TBAs, $(\text{C}_4\text{H}_9)\text{AsH}_2$) was used as substitute for AsH_3 . The most important properties of TBAs as well as the readjustment of growth parameters connected with the use of TBAs are described in more detail in the next section. For the growth of InGaAsN QDs, unsymmetrical dimethylhydrazine⁷⁷ (UDMHy or DMHy, $(\text{H}_2\text{N}-\text{N}(\text{CH}_3)_2)$) was used as nitrogen precursor. DMHy is completely decomposed at 420°C (Ref. 78, p. 258). The decomposition of the standard N precursor ammonia (NH_3), commonly used for the growth of GaN , is only 15 % at 950°C (Ref. 78) and is negligible around 500°C . It has long been difficult to manufacture high-purity UDMHy due to the large reactivity of N, leading to bonds with undesired chemical elements. Today, however, the production of UDMHy with high purity is possible⁷⁷. UDMHy is likewise usable for the growth of GaN ⁸³. For antimony insertions, triethylantimony (TESb) was used.

The same group-III precursors were used on the Aix200/4 as for the Aix200. Instead of using TEGa for the Al-rich AlGaAs layers of VCSEL-DBR structures, however, TMGa was used. A double dilution line for TMGa was available on the new machine, allowing highly reproducible ultra-low Ga molar flows.

N-doping of $\text{Al}_x\text{Ga}_{1-x}\text{As}$ is a general problem since donors like Si or Te form DX centers⁸⁴ in AlGaAs . Depending on the Al fraction x , the donor activation energy is up to 95 meV for Te⁸⁵ and up to 270 meV for Si⁸⁶. Fig. 5 shows the electron concentration in $\text{Al}_x\text{Ga}_{1-x}\text{As}:\text{Te}$ and $\text{Al}_x\text{Ga}_{1-x}\text{As}:\text{Si}$ layers as a function of Al fraction x . The data were taken from two different publications. As one can see for $x = 0$ (pure GaAs) where the donor activation is close to 100 % for both Si and Te, the doping level of the $\text{Al}_x\text{Ga}_{1-x}\text{As}:\text{Te}$ layer is twice as high as the Si doping level of the $\text{Al}_x\text{Ga}_{1-x}\text{As}:\text{Si}$ sample. Between $x = 0.6$ and $x = 0.8$, however, the fraction of ionized Te donors is more than one order of magnitude larger than the fraction of ionized Si donors. At $x = 0.6$, the room-temperature activation of Si donors is roughly 10^{-3} , i.e. a doping level of 10^{20} cm^{-3} would be required

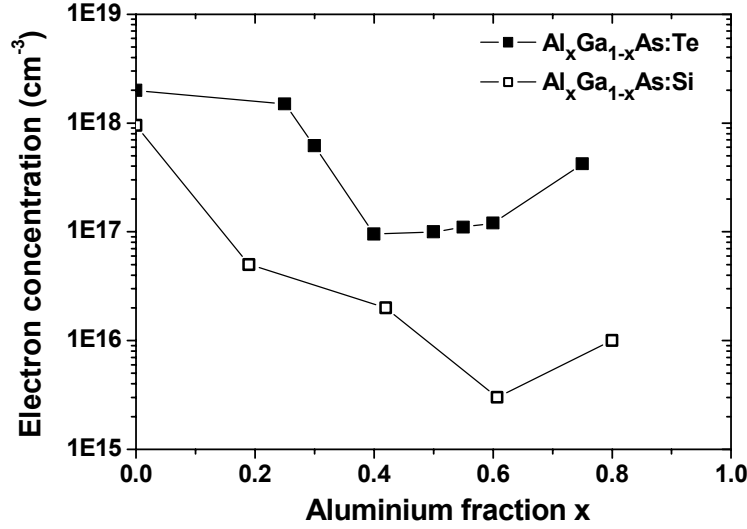


Fig. 5: Electron concentration of $\text{Al}_x\text{Ga}_{1-x}\text{As:Te}$ and $\text{Al}_x\text{Ga}_{1-x}\text{As:Si}$ as functions of the aluminium fraction x , determined by Hall measurements at room temperature. The data for $\text{Al}_x\text{Ga}_{1-x}\text{As:Te}$ were taken from Ref. 87, the data for $\text{Al}_x\text{Ga}_{1-x}\text{As:Si}$ are from Ref. 86.

to achieve an electron concentration of 10^{17} cm^{-3} . Such high doping levels can lead to low crystal qualities and to rough surfaces. Tellurium donors build shallower DX centers in AlGaAs so that their activation is higher and target electron concentrations can be achieved with lower doping levels. Tellurium was therefore preferred to silicon. Diethyltelluride (DETe) was used as tellurium precursor.

Tellurium is reported to be a critical n -dopant due to memory effects: Tellurium, adsorbed by the reactor walls during intentional Te doping, can desorb during the growth of subsequent, nominally undoped layers and lead to unintentional Te doping. Memory effects are, however, not necessarily observed⁸⁷. It was found in this work that memory effects are only significant if, for example, GaAs:Te layers with large electron concentrations of more than 10^{19} cm^{-3} are grown. For Te doping levels leading to electron concentrations in GaAs of 10^{18} cm^{-3} and less, memory effects were not measured. In addition, it could be shown that memory effects after the growth of highly doped layers can be suppressed if GRIs during 5-15 min at 650-700°C are introduced immediately after deposition of the Te-doped layers.

Silicon has no memory effects and should actually be preferred to Te as n -dopant for GaAs. Within the doping experiments carried out in this work using alternative-precursor MOCVD, GaAs could successfully be doped with silicon using the alternative silicon precursor ditertiarybutylsilane⁸⁸.

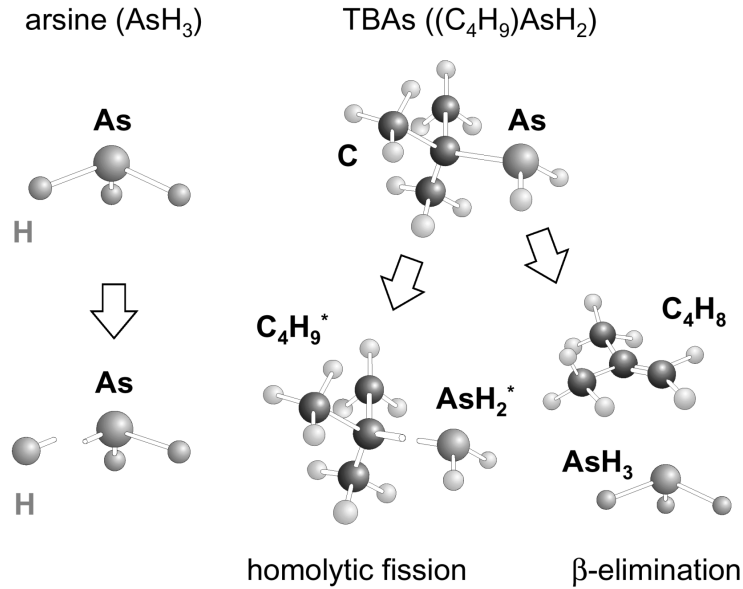


Fig. 6: Schematic diagram of the principal cracking mechanisms of arsine and tertiarybutylarsine (TBAs) during pyrolysis in MOCVD. Homolytic fission and β -elimination are competing decomposition mechanisms of TBAs. Homolytic fission produces a reactive AsH_2 radical. β -elimination generates an arsine molecule and an inert isobutene molecule.

Since the Aix200/4 has only one *n*-dopant line, however, Te was used as *n*-dopant for both AlGaAs and GaAs.

3.2.3 Tertiarybutylarsine

The large hazardous potential of the highly toxic arsine was strongly reduced on the Aix200/4 machine by using the much less toxic organic-compound precursor tertiarybutylarsine (TBAs)⁸⁹. The toxicity of arsenic-containing molecules is essentially due to the number of As-H functions. By replacement of AsH_3 by TBAs, the number of As-H functions per molecule is reduced from 3 to 2 (cf. Fig. 6), so that the toxicity of TBAs is not much lower than that of arsine. A significant reduction of the toxicity is only observed for arsine-*trialkyle* compounds like trimethylarsine (TMAs) or triethylarsine (TEAs)⁸⁹. These molecules do not contain any As-H bonds and would be the optimum solution with regard to toxicity. However, the use of TEAs or TMAs leads to a high carbon incorporation even in GaAs^{78, 90-92}, caused by unsaturated methyl radicals of the group-III sources so that these precursors are applicable only as acceptor dopant sources⁹³.

The decisive advantage of TBAs with regard to safety is its low vapor pressure of 148 mbar at 20°C. The low vapor pressure drastically reduces the risk of spreading in the case of an accidental leak in the MOCVD setup. Since vapor pressure likewise adds to the dangerousness of a precursor,

Stolz and Whitaker defined a safety figure of merit which is given by the LC_{50}^{iii} value divided by the vapor pressure of the chemical at 20°C (Ref. 89). On the scale of this figure of merit, TBAs is by two to three orders of magnitude less dangerous than AsH_3 .

The decomposition of TBAs molecules takes place at high temperatures via two main cracking mechanisms, as shown in the schematic diagram of Fig. 6. In this diagram, the cracking of TBAs is compared to the decomposition of arsine. The homolytic fission of TBAs directly leads to a reactive AsH_2 radical. An isobutene molecule (C_4H_8) and an arsenic-trihydride molecule are obtained after β -elimination. The decomposition of arsine simply occurs by cleavage of one of the hydrogen atoms. Since in the case of β -elimination, a conventional arsine molecule is obtained and since isobutene is a rather inert molecule which is unlikely to participate in later surface processes, the differences between conventional- and alternative-precursor MOCVD is mainly attributed to the homolytic decomposition process. Using quadrupole mass spectroscopy, the β -elimination efficiency of TBAs was estimated to be 55 %. However, Raman measurements of the decomposition products have identified the homolytic fission to be the main decomposition mechanism⁹⁰.

Growth studies of arsenide bulk layers using TBAs showed that crystal qualities equivalent to those of AsH_3 -grown layers is obtained at much lower V/III ratios, owing to the high cracking efficiency of TBAs at low temperatures^{77, 94, 95}. Fig. 7 shows the decomposition efficiencies of arsine and TBAs as a function of reactor temperature. Above 450°C, the decomposition efficiency of TBAs is close to 100 %, whereas the decomposition efficiency of arsine is close to 100 % only beyond 650°C. Particularly at QD deposition temperatures around 500°C, the arsine decomposition efficiency is as low as 10 %.

In contrast to bulk-layer epitaxy, QDs grown in the SK mode are formed by lateral material transport from a strained 2D wetting layer (WL) to coherent 3D islands. Sufficient adatom mobility is hence essential for material migration. Using TBAs, a multitude of bulky organic molecules are adsorbed at the crystal surface during the growth process⁹⁰ which could a priori hinder the QD formation or affect the crystal quality by carbon incorporation. It will be shown later, however, that QDs and QD lasers of high quality can be grown using TBAs.

ⁱⁱⁱ LC_{50} is the concentration of a chemical that is lethal for 50% of a representative animal population after an exposure of typically 4 hours.

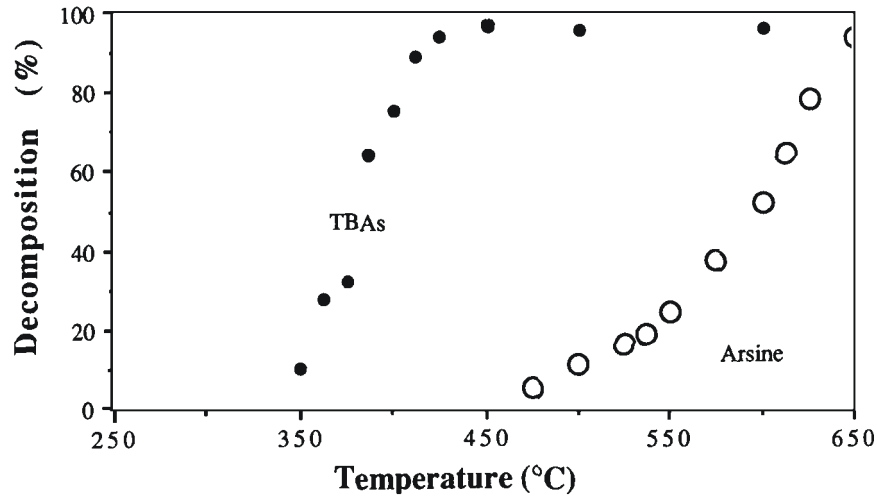


Fig. 7: Comparison of thermal decomposition of TBAs and arsine in an atmospheric pressure reactor. After Stringfellow et al.⁹⁶.

3.2.3.1 Surface stabilization

TBAs ranks among the most expensive consumables in MOCVD growth. First experiments with the new Aix200/4 machine therefore aimed at the minimization of TBAs consumption wherever this is possible, i.e. during heat-up at the beginning of an epitaxy run, cool-down at the end of a run, and during GRIs when the surface is stabilized against As desorption.

In order not to work in the As desorption regime, experiments were conducted with sample pieces that were heated up to 700°C and stabilized under different TBAs flows. The epilayers of these samples are simply 300 nm thick homoepitaxial buffer layers, deposited on semi-insulating (SI) GaAs(001). The heatup procedure is typical at the beginning of every growth run and aims at the removal of the oxide layer and other contaminants from the substrate surface. The substrate pieces were immediately cooled down after the bake-out and measured ex-situ by atomic force microscopy (AFM). The AFM images are shown in Fig. 8. The surface stabilized with the largest TBAs partial pressure of $p_{\text{TBAs}} = 2 \times 10^{-2}$ mbar (A) shows flat monolayer (ML) terraces. The sample stabilized with a lower TBAs partial pressure of $p_{\text{TBAs}} = 2 \times 10^{-3}$ mbar (B) shows ML terraces with small ML-deep holes, presumably owing to congruent desorption of GaAs from these sites. The surface without As stabilization (C) also shows terraces. Here, the terrace planes show small 3D objects, most likely gallium droplets.

For heatup, GRIs and cooldown of further growth experiments, the TBAs partial pressure of Fig. 8 (A) was chosen. This TBAs partial pressure

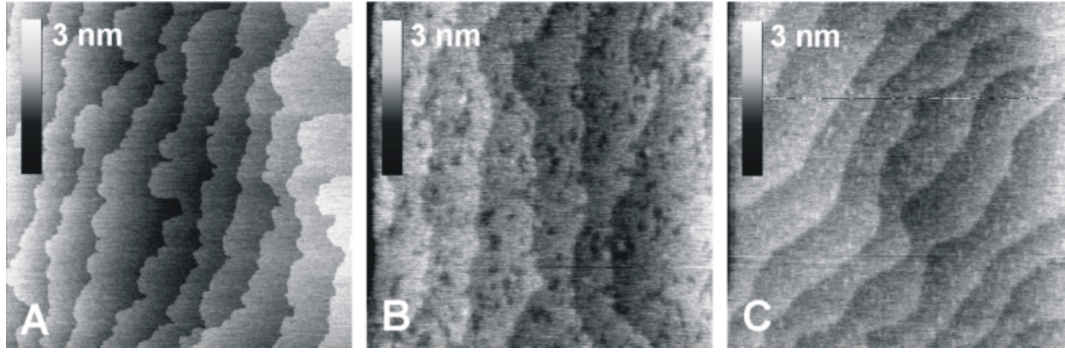


Fig. 8: AFM images ($3 \times 3 \mu\text{m}^2$) of GaAs substrate pieces heated up to 700°C and cooled down under different TBAs partial pressures (A: 2×10^{-2} mbar, B: 2×10^{-3} mbar, C: no stabilization).

is small as compared to the TBAs partial pressure ($p_{\text{TBAs}} = 0.1\text{-}0.3$ mbar) typically used for the growth of high-quality epilayers.

3.2.3.2 V/III ratios for GaAs and AlGaAs growth

If TBAs is used instead of AsH_3 , the V/III ratio during growth of GaAs can be much lower to achieve comparable layer qualities^{77, 95}. This is due to the more efficient pyrolysis of TBAs as compared to AsH_3 (cf. Fig. 7). For GaAs, a V/III ratio of 15 was chosen for the growth of PL test structures. For the growth of devices, it was raised to 20, however. GaAs layers grown with V/III=15 are *n*-type with an electron concentration of only 10^{14} to 10^{15} cm^{-3} .

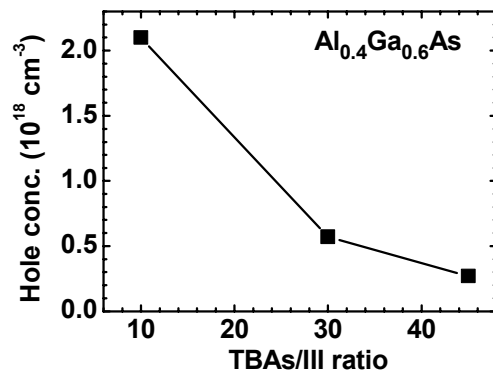


Fig. 9: Hole concentration of $1 \mu\text{m}$ thick, nominally undoped $\text{Al}_{0.4}\text{Ga}_{0.6}\text{As}$ layers as a function of V/III ratio. The hole concentration was measured by the van-der-Pauw method.

Whereas it is possible to grow quasi-SI GaAs with a small V/III ratio, it is shown in sect. 3.3.1.3 that Al-containing layers are highly *p*-doped due to incorporation of carbon from the precursor organyls. Fig. 9 shows the dependence of the hole concentration of $1 \mu\text{m}$ thick $\text{Al}_{0.4}\text{Ga}_{0.6}\text{As}$ layers as a function of V/III ratio. It is inversely proportional to the V/III ratio⁷⁷. Even for a V/III ratio of 45, the hole concentration is as high as $2 \times 10^{17} \text{ cm}^{-3}$. Since carbon atoms in AlGaAs can be passivated by hydrogen atoms^{97, 98}, likely stem-

ming from the carrier gas, the C doping level may be even higher than the hole concentration.

The decrease of carbon incorporation is particularly important for the growth of n -doped AlGaAs layers. Here, the unintentional carbon p -doping must in any case be overcompensated by n -doping. It was found out in this work that values of $n = 5 \times 10^{17} \text{ cm}^{-3}$ needed for bottom AlGaAs cladding layers of edge-emitting lasers can only be achieved with TBAs/III ratios of at least 60.

3.3. Modular optimization of laser structures

Modern semiconductor lasers such as SCH lasers with multi-QD/QW-sheet active regions have rather complex layer structures, as depicted schematically in Fig. 1 and Fig. 2 (sect. 2.1). To work on the performance of such lasers, it is useful to subdivide the laser structure into different modules and to separately optimize these modules using appropriate test structures. The active region, the optical confinement layer, the cladding layers (edge emitters), and DBRs (VCSELs) are the most important modules.

Important for all modules is the lateral homogeneity of the layer thicknesses. Devices processed from different regions of a wafer can only have the same characteristics if their epilayers have the same thicknesses. Such homogeneity is particularly important for the growth of VCSELs where a detuning of the cavity resonance wavelength from the gain maximum of the active region by more than 1 % can make a VCSEL structure unusable. Calibration of growth rates and the adjustment of layer thickness homogeneity are described in the following section.

The QD active region is the most delicate part of a QD laser: the emission wavelength must be calibrated, the crystalline quality has to be optimized to obtain maximum radiative efficiency, and growth surface corrugations related with the presence of three-dimensional QDs must be controlled in order to achieve close vertical QD-layer stacking and also low-loss optical waveguides. A suitable test structure for the optimization of QDs using PL spectroscopy is described in sect. 3.3.2. For the optimization of QD layers, good layer thickness homogeneity is prerequisite. Otherwise, QDs from different parts of the wafer differ in emission wavelength, area density and crystalline quality.

The doping profile within the cladding layers, buffer and contact layers need to be optimized with regard to minimum optical waveguide loss and minimum series resistance. High doping levels mean low series resistance but give rise to large optical losses via free-carrier absorption.

3.3.1 Waveguides and distributed Bragg reflectors

3.3.1.1 Calibration of growth rate

The pyrolysis of MOCVD precursors is a function of temperature. Precursors must be stable at room temperature, whereas at growth temperature, the decomposition should be as efficient as possible. Since the decomposition efficiency varies within a precursor-specific temperature range, growth rates generally depend on temperature. Such dependences are relevant for the growth of lasers since the reactor temperature is varied during the growth run. The choice of growth temperature for a particular layer depends on its vertical position in the laser structure: Layers below QDs can actually be grown at any appropriate temperature. Growth temperatures for layers above the QDs are limited, however, since intermixing of In from the QDs with Ga of the surrounding matrix sets in above 600°C and alters the structural and electronic properties of the QDs⁹⁹⁻¹⁰¹. This leads essentially leading to a blueshift of the QD ground-state emission wavelength¹⁰⁰.

Underneath the QD layers, all GaAs and Al(Ga)As layers can be deposited at optimum growth temperatures. These are 600-650°C for GaAs and 700-750°C for Al(Ga)As layers for the growth with AsH₃. If the deposition temperature for Al(Ga)As layers is too low, carbon and oxygen incorporation increase due to a decrease of the effective V/III ratio¹⁰², related to the strong temperature dependence of the arsine pyrolysis⁷⁸. Large impurity concentrations can effect poor crystal quality. The efficient low-temperature cracking of TBAs enables to grow both GaAs and AlGaAs layers at 625°C with reasonable quality¹⁰³. At this temperature, a good compromise is found between layer quality and TBAs consumption.

Mandatory for the growth rate calibration is a sufficient reproducibility of the layer thicknesses. The run-to-run reproducibility of both MOCVD machines used is better than 1 %. However, growth rate jumps of up to 4 % are observed after regeneration of liner tube, graphite susceptor and substrate plate. The usefulness of a VCSEL structure of which the layer thicknesses deviate from the nominal values by more than 1 % is highly endangered. For a coarse determination of growth rates and their temperature dependence, AlGaAs/GaAs heterostructures were grown in a single sample at different temperatures. A coarse calibration of the thicknesses of GaAs and AlGaAs layers can be performed using cross-sectional AFM, as described in the following subsection. The fine-tuning of the calibration rate is done with optical techniques as described subsequently.

Cross-section Atomic Force Microscopy

Cross-section AFM is very useful to determine growth rates for layers of which the thickness is not so critical for the device characteristics of the laser structure. This applies, for example, to cladding layers and the optical confinement layer of edge emitters or to the thin AlGaAs buffer layers that are inserted between the GaAs and AlGaAs $\lambda/4$ layers of oxide DBRs in VCSEL structures, or to the oxide-aperture layers of VCSELs. If the nominal thicknesses of oxide-aperture layers are not perfectly met, the thickness of undoped GaAs layers during cavity-thickness calibration can be varied.

Cross-sectional Atomic-Force Microscopy allows to get an overview of the temperature dependence of GaAs and Al(Ga)As growth rates for a large number of different temperatures, growth rates and V/III ratios from one sample. To this end, arbitrary sequences of alternating GaAs and Al(Ga)As layers are deposited under different growth conditions. Due to the spatial protrusion of Al-containing layers, owing to the oxidation of Al and swelling of the AlO_x in ambient air, the Al(Ga)As/GaAs interfaces can be identified using cross-sectional AFM on cleaved surfaces. Depending on the Al fraction, the thickness of the natural oxide ranges from few MLs to tenths of nanometers. This permits not only to determine the growth rates of the deposited layers but also their Al fractions^{104, 105}. For the determination of Al fractions, X-ray diffraction spectra of thick AlGaAs reference samples were evaluated in this work. Using this method, Al fractions with errors far below 1 % can be measured¹⁰⁶. GaAs is also subject to oxidation in ambient air. The protrusion due to oxidation is negligible, however. Fig. 10 shows the temperature dependence of GaAs and $\text{Al}_{0.65}\text{Ga}_{0.35}\text{As}$ growth rates, evaluated from cross-sectional AFM measurements.

The accuracy of the AFM method is estimated to be within an error of 5-10 % since the boundaries between different layers are frayed in AFM images. In addition, the geometry of the AFM tip might also falsify the results.

Reflection spectra of AlGaAs-GaAs DBRs

For the growth of Al(Ga)As/GaAs structures for the wet-thermal fabrication of oxide DBRs for VCSELs, the evaluation of optical reflection spectra allows the calibration of layer thicknesses with a precision of better than 0.2 %. Optimum layer thicknesses are important to have the stop band of the oxide DBRs at the gain maximum. For this purpose, the reflection spectrum of such Al(Ga)As/GaAs structures is recorded using a white light source. A transfer matrix method¹⁰⁷ is used to simulate the GaAs and Al(Ga)As layer thicknesses, respectively. The simulations are subsequently fitted to the data.

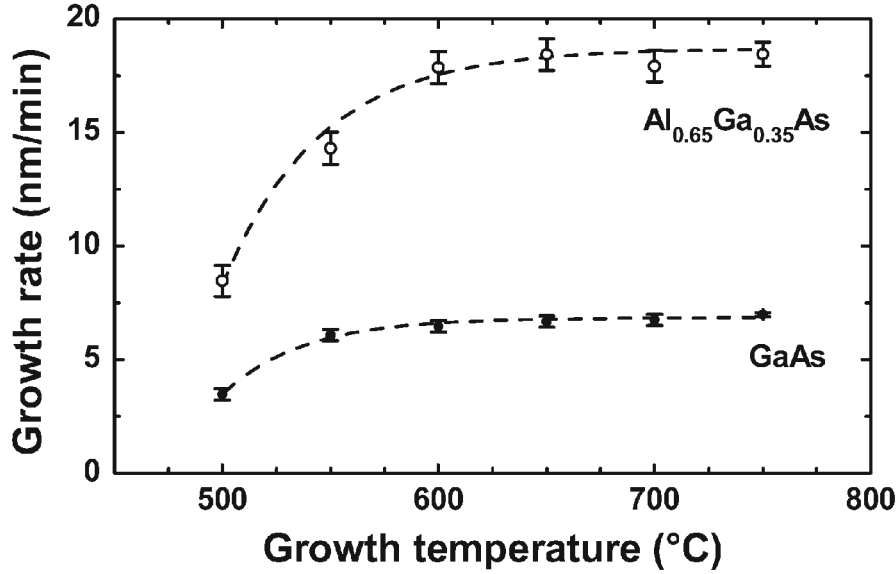


Fig. 10: GaAs and AlGaAs growth rates as determined from cross-sectional AFM images, plotted as a function of growth temperature. The sample consisted of alternating $\text{Al}_x\text{Ga}_{1-x}\text{As}$ /GaAs layers grown at different temperatures, using TMGa, TMAI and AsH_3 as precursors. The TMGa and TMAI flows were 7.4 and 5.8 $\mu\text{mol/min}$, respectively; the V/III ratio was 180 for all layers. Error bars originate from statistical treatment of 10 thickness measurements of each layer; dashed lines are guides to the eye. An Al fraction of $x = 65.1\%$ was determined from an x-ray diffraction spectra of a 1 μm thick AlGaAs epilayer grown at 720°C with the given precursor flows. The Al fraction may slightly change with decreasing growth temperature.

As mentioned earlier, the optical thickness of the cavity is the most delicate issue of a VCSEL structure. For the calibration of the cavity thickness, test structures are grown containing two bottom-DBR pairs, the entire cavity with QDs, contact layers and apertures, and two top-DBR pairs. Oxidation of the DBR layers is not required for the calibration of the cavity thickness. Cavity thickness calibrations are performed previous to each VCSEL growth run. The optical method is also used as quality test of as-grown VCSEL structures. Fig. 11 shows a measured and simulated reflection spectrum of a complete VCSEL structure.

3.3.1.2 Lateral homogeneity of layer thicknesses

The lateral homogeneity of layer-thicknesses of samples grown with the Aix200 machine, achieved with the standard growth parameters used from the very beginning of the experiments, has turned out to be sufficient for the growth of VCSEL structures. The standard parameters are a total pressure of 20 mbar and a total gas flow of 5.56 l/min, equally split over the group-III and group-V gas inlet. The growth experiments on the Aix200 were ini-

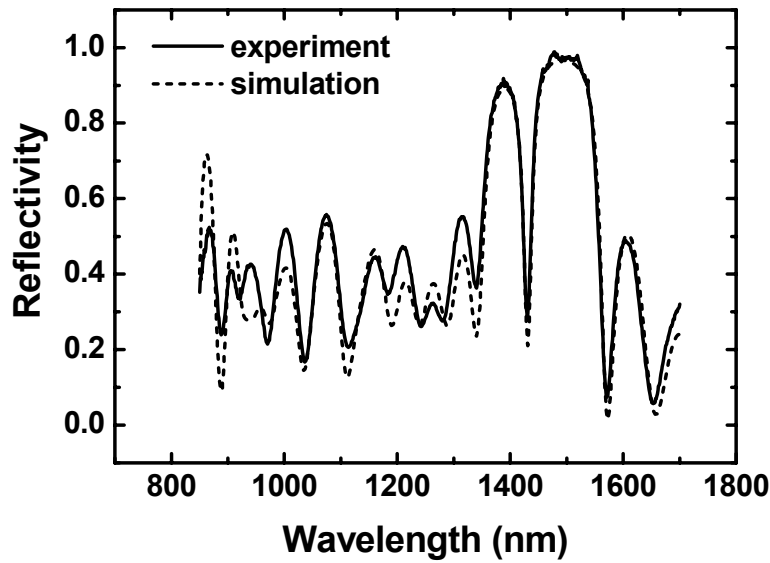


Fig. 11: Reflection spectrum of an unoxidized, as-grown VCSEL structure. The DBRs consist of six periods of GaAs / $\text{Al}_{0.98}\text{Ga}_{0.02}\text{As}^{\text{iv}}$.

tially performed using an infrared lamp heater. In the course of the experimental work, the heater was replaced by an RF heater. This improved the layer-thickness homogeneity further, most likely due to an enhanced homogeneity of the lateral temperature profile.

Since the alternative-precursor-MOCVD growth runs described in this work were the first experiment to be carried out on the new Aix200/4 machine, parameters such as total pressure and total gas flow were to be adjusted first in order to get sufficient layer thickness homogeneity. The main difference of the Aix200/4 with regard to the Aix200 is the width of the reactor. Whereas the 4" reactor of the Aix200/4 is not significantly longer than the 2" reactor of the Aix200, it is twice as wide. This means that the precursors must homogeneously spread to over twice the width on their way from the gas-mixing head to the susceptor. To adjust the layer thickness homogeneity, total pressure, total flow as well as the group-III-line / group-V-line inlet flow ratio ($F_{\text{III}}/F_{\text{V}}$) were varied. A schematic diagram of the position of group-III and group-V inlet in the mixing head is given in Fig. 12.

For the determination of layer thickness homogeneities, similar structures as for the optical measurement of the growth rates (cf. 3.3.1.1) were used. To simplify matters, however, superlattices consisting of only binary AlAs and GaAs layers were grown. Since the area of the circular light spot used for the reflection measurements was less than 1 mm^2 , layer thicknesses could be resolved spatially as a function of lateral position on the wafer.

^{iv} By courtesy of Friedhelm Hopfer.

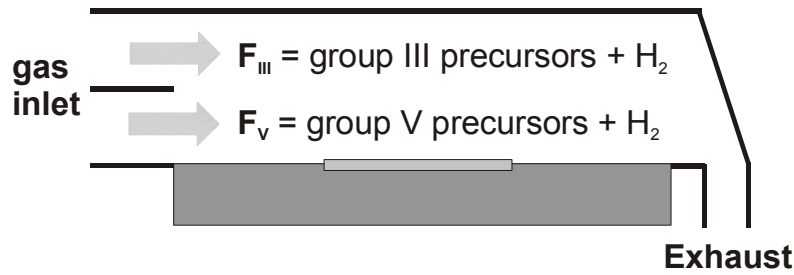


Fig. 12: Strongly simplified gas inlet schematic of the Aix200/4 reactor with susceptor and substrate. Group-V precursor gases are conducted separately from group-III precursors. In order to avoid pre-reactions, they are not mixed before they reach the entrance of the reactor. Dopants are added to the group-III line.

Layer thicknesses of the AlAs layers as a function of distance from the wafer center are shown in Fig. 13 for different total pressures, total gas flows and $F_{\text{III}}/F_{\text{V}}$ ratios. The values for the GaAs layers were omitted as they behave analogous to those of AlAs. The AlAs thicknesses of the samples were normalized to their respective average value. A 1 %-error window in which the thickness values should be contained is also depicted.

The filled circles and triangles in Fig. 13 show the normalized thicknesses of the AlAs layers grown at total pressures of 100 mbar and 50 mbar, respectively, with a total gas flow of 10 slm, equally split over the group-III and group-V inlet. It is obvious that the homogeneity of the sample grown at 50 mbar is worst. This is contradictory to the general belief that the growth rate homogeneity can be improved by lowering the total pressure. For all other growth runs, the total pressure was set to 100 mbar, which is the total pressure recommended by the manufacturer Aixtron. Raising the total pressure to larger values like 200 mbar should in principle increase the homogeneity further. However, the gas velocity in the system is then half if all other parameters are kept constant. This is disadvantageous for the implementation of short growth sequences. Low gas velocities also prevent from quick parameter ramping during the growth of one layer.

For the sample represented by filled squares in Fig. 13, an asymmetric gas inlet was used, keeping a total flow rate of 10 slm. F_{III} was reduced to 3 slm, F_{V} was increased to 7 slm. The asymmetric gas inlet slightly improves the homogeneity. To maintain a reasonable functioning of the machine, however, F_{III} should not be reduced further.

The best result was achieved with $F_{\text{III}} = 3$ slm and $F_{\text{V}} = 12$ slm. As shown by the empty squares in Fig. 13, the homogeneity is better than 1 %. These parameters were used for all following structures. It must be noted that the growth rate for $F_{\text{III}} = 3$ slm and $F_{\text{V}} = 5$ slm is about 30 % lower than for $F_{\text{III}} = F_{\text{V}} = 5$ slm. Using the $3 \times 2''$ satellite configuration, special liner

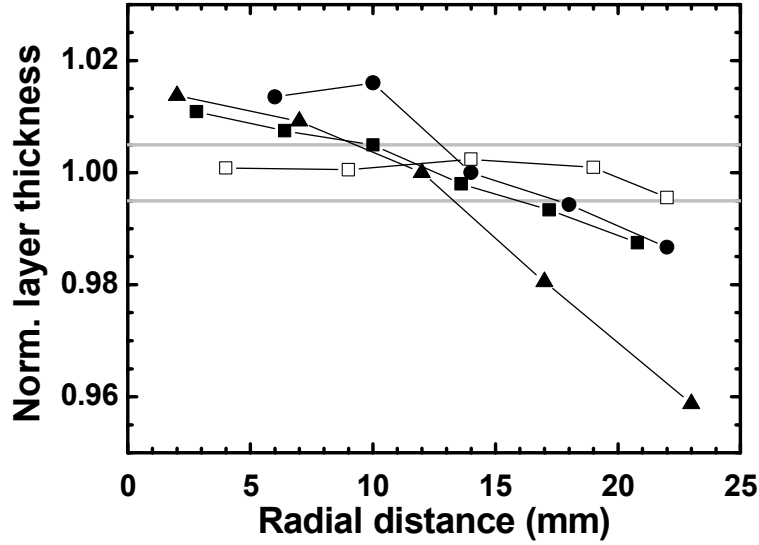


Fig. 13: Thickness of the AlAs layers of AlAs/GaAs superlattices, normalized to 1.0 for a radial distance of 0.5 inch = 12.7 mm. For the sake of clearness, the values for GaAs were omitted. The behavior of GaAs layer thicknesses is analogous to those of AlAs. The AlAs layers were grown with a V/III of 30 at a growth rate of 2 $\mu\text{m/h}$.

(●) $p_{\text{tot}} = 100$ mbar, $F_{\text{III}} = F_{\text{V}} = 5.0$ slm (cf. Fig. 12).

(▲) $p_{\text{tot}} = 50$ mbar, $F_{\text{III}} = F_{\text{V}} = 5.0$ slm.

(■) $p_{\text{tot}} = 100$ mbar, $F_{\text{III}} = 3.0$ slm, $F_{\text{V}} = 7.0$ slm.

(□) $p_{\text{tot}} = 100$ mbar, $F_{\text{III}} = 3.0$ slm, $F_{\text{V}} = 12.0$ slm.

tubes with additional gas deflection plates close to the gas inlet can be used to achieve good lateral thickness homogeneities¹⁰⁸. No experiments with the satellite rotation system were carried out in this work.

3.3.1.3 Calibration of oxidation rate for Al(Ga)O_x/GaAs DBRs

In order to fabricate Al(Ga)O_x/GaAs DBRs for VCSELs, the Al_{1-x}Ga_xAs/GaAs superlattices above and below the microcavity undergo a wet-thermal oxidation process. Fig. 14 shows the oxidation rate at 420°C of a 100 nm thick Al_{1-x}Ga_xAs layer, cladded by 100 nm thick GaAs layers, as a function of the AlAs mole fraction. The oxidation rates of binary AlAs and Al_{0.96}Ga_{0.4}As differ by one order of magnitude, so the oxidation rates in the Al_{1-x}Ga_xAs layers critically depend on the Ga content x . The effect is used to separately adjust the oxidation speeds for VCSEL-DBR mesas of different diameters. This is particularly important for the one-stage oxidation process for the fabrication of QD VCSELs as described in sect. 6.2.2. Here, the oxidation of small top DBRs must be completed within the same time as

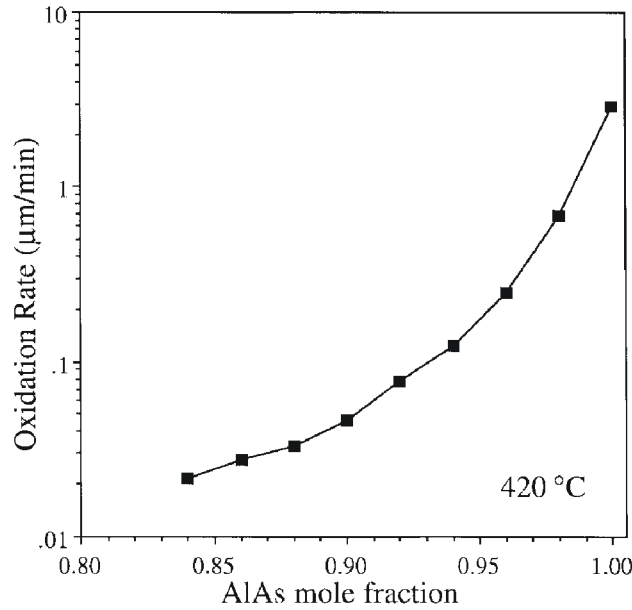


Fig. 14: $\text{Al}_{1-x}\text{Ga}_x\text{As}$ oxidation rate at 420°C versus composition for 100-nm-thick layers cladded by 100 nm thick GaAs layers. From Ref. 109.

the oxidation of the large bottom DBRs. Moreover, the quality of fast-oxidizing binary AlAs layers is very poor: Mesas containing thick binary AlAs layers delaminate along the oxide/semiconductor interfaces¹⁰⁹. The admixture of few percents of Ga considerably enhances the mechanical stability¹¹⁰. This improvement is attributed to the removal of volatile oxidation products such as As and As_2O_3 from the oxidizing layers¹¹¹. The removal of such products is not efficient enough if oxidation rates are as high as for binary AlAs.

Once a parameter window for the oxidation process is determined using test structures with different values of x , the Ga content must be kept as precisely as possible for all subsequent growth runs. This is a challenge to the epitaxy since Ga contents in this range are difficult to control. The problem was solved using TEGa as gallium precursor for growth experiments using the Aix200 machine and TMGa in combination with a double dilution line using the Aix200/4 machine (cf sects. 3.2.1 and 3.2.2).

3.3.2 Optimization of quantum-dot active regions

The most important characterization tool for QD structures is room-temperature PL. PL spectra reveal QD ground- and excited-state emission as well as WL transition wavelengths. PL also enables to assess and compare radiative efficiencies of QD layers. The influence of growth-parameter changes on the properties of the QD layers can fast and comfortably be monitored. Transmission electron microscopy images can reveal QD shapes

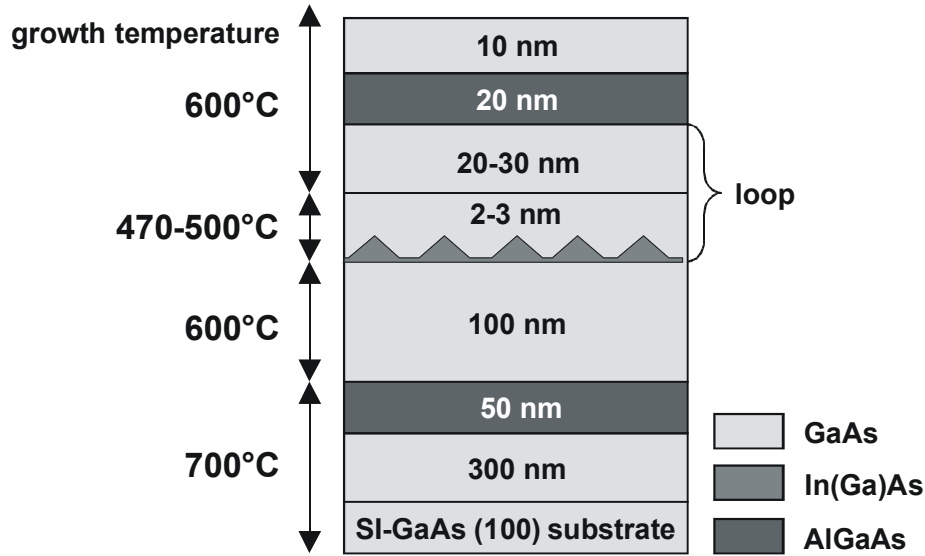


Fig. 15: Typical structure of an undoped sample containing one or more QD layers for PL measurements. AlGaAs diffusion barriers below and above the QDs suppress carrier diffusion to the substrate and to the surface, respectively.

and QD area densities and provide an important feedback during the development of long-wavelength QDs. In contrast to PL, however, sample preparation and processing of TEM images are very time-consuming.

All samples for PL characterization were grown on undoped substrates. The layer schematic of a typical quantum-dot test structure is shown in Fig. 15. After a bake-out of the substrate at 700-750°C during several minutes, a GaAs buffer layer is deposited. The comparably large buffer thickness of 300 nm is chosen to reduce the concentration of contaminants that are present on the substrate surface and show diffusion into GaAs epilayers. A thick AlGaAs layer of typically 60-70 % Al content is subsequently deposited. This layer acts on one side as a final diffusion barrier for contaminants from the substrate. On the other side, it suppresses the diffusion of photo-excited carriers from the vicinity of the QDs to the substrate where the lower crystal quality leads to non-radiative recombination. The QDs are deposited after an intermediate GaAs layer grown at 600°C. After deposition of the QDs, a GRI is applied for the nucleation and the development of the QDs^{12, 37}. The first 2-3 nm of the GaAs cap are deposited at the QD growth temperature. The reactor temperature is then ramped to 600°C. In multilayer QD structures, QD and cap growth are repeated as indicated in the schematic. The last QD cap layer is followed by a thin AlGaAs layer of typically 30-40 % Al content. The low Al content allows growing all layers above the QDs also at the QD deposition temperature. The top AlGaAs layer is finally capped with a thin GaAs film to protect it from oxidation in ambient air.

The samples are excited with the 514.5 nm line of an Ar^+ ion laser, driven at 500 mW output power. The excitation density can be varied with neutral filters from typically 5 W/cm^2 to 5000 W/cm^2 . A LN_2 -cooled Ge detector is used for detection. Low temperature measurements are performed using a closed-cycle cryostat ($T = 8 - 300\text{K}$).

Two room temperature PL spectra are usually taken directly after the sample growth. From the comparison of low ($P_{\text{exc}} = 5 \text{ W/cm}^2$) and high ($P_{\text{exc}} = 5000 \text{ W/cm}^2$) excitation density PL spectra with spectra of other samples, the sample quality can be assessed. At low excitation densities around 5 W/cm^2 , only few electron-hole pairs are generated per unit time, the QDs are only partly filled if the QD density is not too low. For QD area densities $n_{\text{QD}} > 10^{10} \text{ cm}^{-2}$, only QD ground-state luminescence is visible in the setup used. The FWHM of the PL peak is then a probe for the size distribution of the QD ensemble. The integrated QD ground state luminescence is a measure of the crystalline sample quality: if QDs or the surrounding matrix have defects, carriers are trapped faster by these defects and recombine via non-radiative channels.

At high excitation-power density ($P_{\text{exc}} = 5000 \text{ W/cm}^2$), practically all QDs are filled. Saturation of the QD ground state is inferred from the appearance of excited-state transitions in the spectra. Using appropriate reference samples, the peak intensities of the QD ground state luminescence can be used to compare QD area densities. Fig. 22 shows typical examples of low and high excitation PL spectra.

4. Self-organization of quantum dots

Self-organization of QDs can be observed if a thin QW is brought onto a substrate with a different lattice constant. The strain energy of the epilayer related to the lattice mismatch can be reduced if three-dimensional islands are formed. QD formation is only observed if the energy gain connected with the formation of such 3D islands is larger than the energy cost necessary to create island facets and island edges. Self-organized In(Ga)As/GaAs QDs as used in the present work have typical heights of 3-6 nm and lateral dimensions of 15-25 nm. The area density of the QDs ranges between 10^{10} and 10^{11} cm^{-2} .

For a fixed chemical composition, the emission wavelength of a QD ensemble depends on the QD sizes and shapes. Whereas the emission wavelength of QWs can easily be tuned by the QW thickness, QD size and shape are complex functions of growth parameters such as reactor temperature, deposition rate, and V/III ratio. The QD sheet density, likewise depending on the growth conditions, is an additional parameter of QD layers with respect to a QW. Since the gain of QD-based laser diodes directly scales with the number of QDs in the cavity, the sheet density of QDs must pass a certain threshold value to enable laser operation.

The precise shape of SK QDs is still a debated issue. Most likely, the QD shape depends on growth parameters and thus varies. Different shapes of self-organized QDs such as pyramids, truncated pyramids and lens shapes have been reported. A strictly pyramidal shape of InAs/GaAs QDs in both MBE¹¹² and MOCVD¹¹³, a multi-faceted dome structure for MBE-grown InAs islands¹¹⁴ as well as a lens shape for MBE-grown InGaAs QDs^{115, 116} have been reported.

In the following, the basic mechanisms of quantum-dot self-organization with respect to size, shape, and sheet density are described in order to support the understanding of the growth experiments conducted within this work.

4.1. The equilibrium crystal shape

Whereas the energy balance of liquid surfaces is basically determined by the surface tension, a multitude of contributions to the energy balance of crystal surfaces exists. First, crystals are anisotropic. This implies that the energy required to create a crystal surface depends on the surface orientation. Surfaces of different indices can have strongly differing energies. Second, crystal surfaces exhibit intrinsic surface stress even in the absence of lattice mismatch. This is due to the particular coordination of surface atoms in contrast to bulk atoms. Surface stress at edges is analogous to the

Laplace pressure of curved liquids¹¹⁷. For these two reasons, the *equilibrium* crystal surface is not necessarily flat. This is impressively illustrated by the theorem of Herring (1951)¹¹⁸: “If a given macroscopic surface of a crystal does not coincide in orientation with some portion of the boundary of the equilibrium shape, there will always exist a hill-and-valley structure which has a lower free energy than a flat surface, while if the given surface does occur in the equilibrium shape, no hill-and-valley structure can be more stable.” This is in clear contrast to the case of liquids where the surface tension always acts towards the establishment of a flat liquid surface.

Intrinsic surface strain originates from the fact that the equilibrium lattice constant of surface atoms is generally different from that of the bulk since surface atoms have a smaller number of direct neighbors. Being adjusted to the bulk lattice constant, the atoms of the surface layer experience an in-plane surface stress. If the equilibrium surface lattice constant is smaller than in the bulk, the surface exhibits tensile strain, otherwise it is compressively strained. The intrinsic surface stress cannot relax on a flat surface since the surface stress tensor has non-zero elements only in the surface plane. Another situation is given at crystal edges, however, where the surface stress tensor has discontinuities. Here the intrinsic surface strain can partially relax, either by compression or expansion of the near-edge bulk crystal along the direction of the resulting surface stress. Intrinsic-strain relaxation gives a long-range energy contribution $\Delta E_{\text{elastic}}$ to the overall energy.

An illustrative example of the relaxation of intrinsic surface stress is the formation of nanofacets. The minimization of the surface energy leads to an equilibrium period which is much larger than the lattice constant¹¹⁹.

4.2. Strained heteroepitaxy of thin films

If epilayers are regarded that are lattice-*mismatched* to the substrate, two new aspects come into play. Firstly, the interface energy between the two materials enters the energy balance. The values of the surface energy of substrate (σ_S) and epilayer material (σ_E) as well as the interface energy (σ_I) determine if the epilayer wets the surface. If surface wetting takes place and the lattice-mismatch strain is sufficient, QDs can form to reduce the total energy of the system.

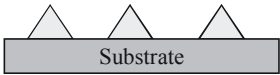
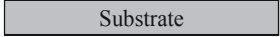
The energy gain per unit area upon deposition of the epilayer is given by

$$\Delta\sigma = \sigma_E + \sigma_I - \sigma_S$$

On a lattice-*matched* substrate, uniform two-dimensional growth takes place if $\Delta\sigma < 0$. This is called the *Frank-van-der-Merve*¹²⁰ growth mode. If

$\Delta\sigma > 0$, three-dimensional coherent crystal islands are formed. This is analogous to the formation of water droplets on oilcloth. This mode is called the *Volmer-Weber*¹²¹ growth.

In the *Stranski-Krastanow* growth mode¹²² as used for the fabrication of QDs in this work, $\Delta\sigma$ is always negative, i.e. the lattice-mismatched epilayer wets the surface. Only above a critical layer thickness, a 2D-3D transition takes place. Coherent islands are formed that grow in size at the expense of the WL thickness. Whereas the WL is pseudomorphically strained by the substrate, the lattice at the top of the QDs is rather relaxed. In the SK mode, the WL can be thinned down to 1 ML by material transport to the 3D islands but usually does not vanish¹²³. An overview of the different growth modes and their dependences on the sign of $\Delta\sigma$ and the lattice mismatch is given in Tab. 1 where the three growth modes are briefly compared with liquids on solid surfaces.

Energy gain	Liquid	Crystal	
$\Delta\sigma > 0$	droplet formation	Volmer - Weber growth	
			
$\Delta\sigma < 0$	wetting of substrate surface	lattice match	Frank-v.d.Merve growth
		lattice mismatch	Stranski-Krastanow growth
			

Tab. 1: Different growth modes of crystal epilayers on lattice-matched and lattice-mismatched substrates compared to the deposition of liquids on solid surfaces. For the Stranski-Krastanow growth, surface wetting and a large lattice mismatch are necessary.

4.3. Thermodynamic models of 3D island arrays

The energy of a strained QW can be reduced by the formation of 3D islands. Following a theoretical model proposed by Shchukin et al.¹¹⁹, the free energy gained by the formation of islands is made up of the elastic strain relaxation, the surface energy related to the augmentation of the overall surface due to the creation of island facets, and the energy required to create island edges. The energy gained by the formation of islands is expressed as

$$\Delta E_{\text{isl}} = \Delta E_{\text{facets}} + E_{\text{edges}} - \Delta E_{\text{elastic}}.$$

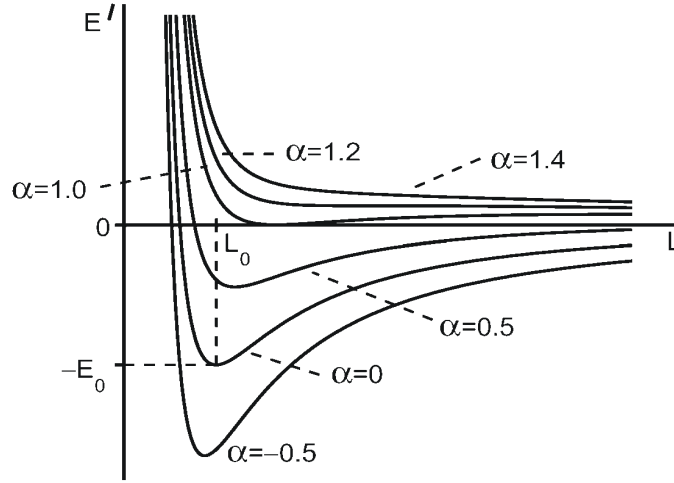


Fig. 16: Free energy gained by the 2D to 3D transition of a pseudomorphically strained WL as a function of island base length. Curves for different values of the parameter α (cf. text) are plotted. From Ref. 119.

The different energy terms on the right are explained as follows.

- ΔE_{facets} describes the change of the surface energy due to the creation of island facets; the total surface of a QD ensemble is larger than that of a plane surface. Moreover, the facet planes have different crystal orientations than the substrate. The surface energy of the facets might differ from that of the substrate due to the general anisotropy of the crystal surface energy.
- E_{edges} is the short-range energy that equals the energy cost necessary to create the islands edges.
- $\Delta E_{\text{elastic}}$ is the energy related to elastic strain relaxation of the islands. This term includes the relaxation of both lattice-mismatch strain *and* intrinsic surface strain, $\Delta E_{\text{elastic}}^{\text{edges}}$, which relaxes at the island edges.

The energy per atom of the strained layer gained by the 2D-to-3D transition is plotted in Fig. 16 as a function of the island base length L for a dilute^v array of islands, and for different values of the parameter α . α is the ratio of the change of *surface energy*, ΔE_{surf} , to the absolute value of the energy contribution of intrinsic-strain relaxation at the island *edges*, $|\Delta E_{\text{elastic}}^{\text{edges}}|$. If $\alpha \leq 1$, an optimum island size L_0 exists, corresponding to a global mini-

^v In a dilute island array, the island area density is low enough that island-island interaction via long-range elastic energies, mediated by wetting layer and substrate, can be disregarded.

mum of the free energy. In case $\alpha > 1$, an equilibrium island size does not exist. The reduction of the free energy corresponds to a continuous increase of the island size. Mass conservation stipulates that the island density decreases. Larger islands grow at the expense of smaller islands. This is referred to as Ostwald ripening¹²⁴.

Whereas the theory by Shchukin is based on continuum elasticity only, calculations by Wang and coworkers¹²⁵ additionally regard *atomistic aspects* using density-functional theory. They found that the energy contribution of edges is too small to be decisive for the existence of an equilibrium island size. In their opinion, the equilibrium island size is rather the result of an energetic balance that governs the material transport between the WL and the islands: They found that the surface energy of the WL, γ_{WL} , is a function of the film thickness: γ_{WL} decreases significantly between 0 and 2 ML and is constant only above 2 ML. The non-zero gradient of γ_{WL} as a function of layer thickness constitutes a force counteracting the thinning of the WL during the 2D-3D transition.

4.4. Kinetic description of island formation in one dimension

The thermodynamic models outlined in the previous section describe the morphology of a thin lattice-mismatched epilayer with the lowest surface energy. The *process* of the 2D-3D transition and the subsequent size increase of the QDs towards an eventual equilibrium size cannot be accounted for within a thermodynamic model. Barabási et al. have introduced an atomistic model in one dimension¹²⁶, describing the process of QD self-organization. Although this model is subject to controversially debated simplifications, such as the restriction to one dimension, a number of basic properties of SK QDs are described which can be observed experimentally.

In the model of Barabási, atoms are successively deposited with a constant deposition rate on a substrate with a smaller lattice constant than the epilayer, thus accounting for compressive strain. The case of a larger lattice constant is not discussed within this model. The hopping probability of an atom to neighboring lattice sites is proportional to $\exp[\mu(x)/k_{\text{B}}T]$ with $\mu(x) \equiv -(nE_{\text{n}} + E_0 - E_{\text{s}}(x))$ being the chemical potential. n is the number of neighboring atoms, E_{n} is the energy of the bonds with nearest atoms, E_0 is the diffusion barrier seen by an isolated atom on a stress-free substrate surface, and $E_{\text{s}}(x)$ is the strain energy of the surface at the position of the considered adatom. The equilibrium position of each lattice atom is iteratively recalculated after each hopping event. Numerical simulations show that for a lattice mismatch above 5 %, an island size distribution with a narrow peak evolves. In Fig. 17, the strain energy of a surface atom as a function of posi-

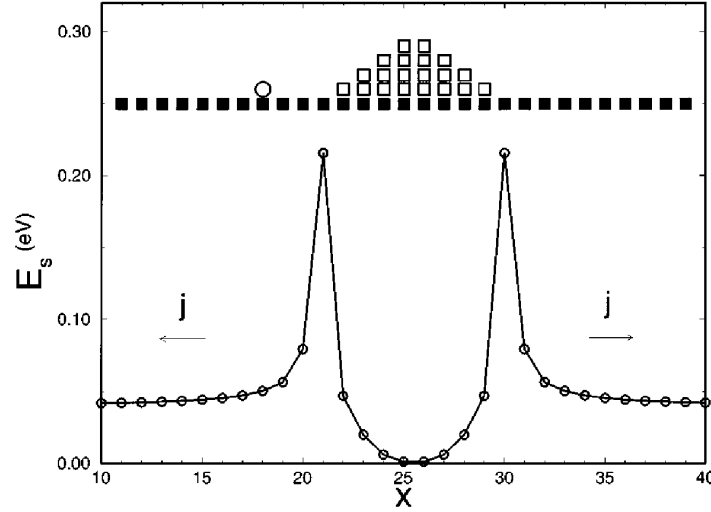


Fig. 17: Strain energy around a spontaneously formed island in a one-dimensional atomistic model by Barabási¹²⁶. E_s is the strain energy of an atom placed on the top of the substrate or on the island. E_s is largest at the island edge. From Ref. 126.

tion x is plotted. The strain energy has a maximum at the island edges, the smallest strain energy value is found at the island top.

Since $\mu(x)$ only depends on the strain energy E_s , a net surface current $j = -\nabla\mu(x)$ is generated, pointing away from the island edge. Since the peak strain energy at the island edges grows with the island size, j increases likewise. The increasing net surface current j suggests a self-limitation of the island size so that a seemingly stable array of equisized islands exists. The model suggests that the size increase of the QDs slows down with their size. An equilibrium size might therefore be assumed asymptotically in time. Whereas QDs form very quickly after the critical layer thickness is reached, they might need a rather long time to achieve equilibrium.

4.5. Island size and density

The right value of the emission wavelength and large modal gain are the most important properties of a QD laser. These properties are directly related to the QD size and QD sheet density, respectively. The models described above do not show how these quantities depend on the growth conditions. The impacts of QD growth temperature as well as of deposition amount, deposition rate and GRI after deposition of the QD material on size evolution and equilibrium sizes are outlined in this section.

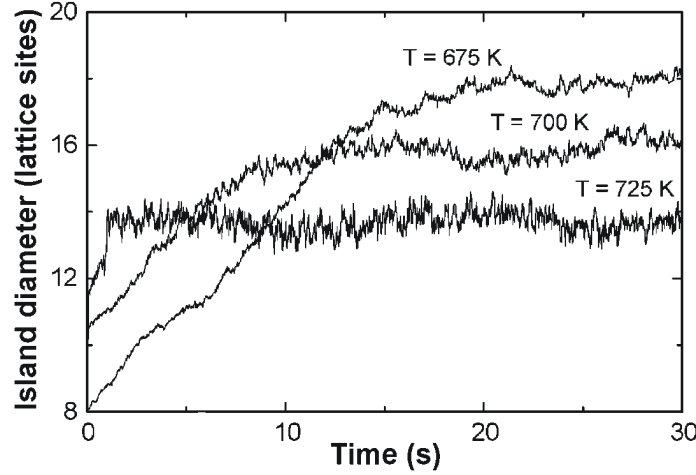


Fig. 18: Monte-Carlo simulations of the temporal evolution of 2D submonolayer islands. A coverage of 4 % was deposited randomly on the surface at a flux of 1 ML/s. Every 0.01 s, a histogram of the island size distribution is recorded. The average island diameter $\langle \sqrt{N} \rangle$ is plotted as a function of GRI duration for different temperatures. The hopping probability p of an adatom is proportional to $\exp[-(E_0 + nE_n - E_s) / k_B T]$ where E_0 is the adatom diffusion barrier, E_n the chemical bond energy to a neighbor atom, n the number of chemically bound neighbors, and E_s the strain energy at the position of the considered adatom. From Ref. 127.

4.5.1 Role of temperature

A two-dimensional Monte-Carlo simulation of compressively strained submonolayer islands introduced by Meixner et al.¹²⁷ reveals the main features of the temperature dependence of island size and density. The results of this simulation are in good agreement with experimental findings for 3D SK QD systems so that the portability of the main aspects of the 2D submonolayer island system to the 3D island system is likely¹²⁸.

Fig. 18 shows the calculated average island diameter as a function of time for deposition temperatures of $T = 675\text{K}$, 700K and 725K . The QD material was deposited within 0.04 s. The average island diameter is calculated from island-size distribution histograms taken at different times during the GRI following the deposition of the island material. It is evident from Fig. 18 that during the first 5 seconds of the GRI, the size distribution is kinetically controlled: Larger islands of a lower density are preferred at higher temperatures since surface diffusion lengths are larger: Adatoms rather attach to already existing islands than form new nuclei. In the kinetically controlled regime where the system is not given enough time to equilibrate, an increase of the temperature thus leads to an increase of the island size, and, due to mass conservation, to a lower island density. For long GRIs where thermodynamics prevails, smaller island sizes and larger island densities are preferred at higher temperatures. At low temperatures,

islands are larger and hence their sheet density is lower. The dependence of island size and island density on temperature in the kinetically controlled regime and in the thermodynamically controlled regime is exactly opposite. During the GRI where the QD system moves towards equilibrium, a cross-over of kinetics and thermodynamics is observed.

The decrease of the island size with temperature was experimentally verified for InAs submonolayer islands (30 % coverage) buried in a GaAs matrix¹²⁹. PL as well as high-resolution TEM images evaluated according to the DALI method¹³⁰ were used as probes. Oshinowo et al.¹¹³ observed an increase of the diameter of MOCVD-grown InGaAs/GaAs QDs from 15 to 20 nm if the QD deposition temperature is raised from 500 to 550°C. The QD sheet density concurrently decreases from 10^{11} cm^{-2} to 10^{10} cm^{-2} . The larger QD density at 500°C can be explained with reduced surface kinetics as compared to $T_{\text{gr}} = 550^\circ\text{C}$. The apparent inconsistency between kinetic theories and thermodynamic predictions occasionally found in literature might simply be attributed to the fact that only time is short for the system under consideration to assume the equilibrium shape, i.e. the crossover region might not have been reached in those cases.

In MOCVD, temperature is not a suitable parameter to tune the QD density since the crystal quality is very sensitive to temperature changes at typical In(Ga)As/GaAs QD deposition temperatures around 500°C. Growth temperatures lower than 500°C would lead to a drastic decrease of the crystal quality. This effect is particularly pronounced in MOCVD where the organic parts of the metalorganic precursors can lead to significant carbon doping. The QD deposition temperature of about 500°C is already very low as compared to temperatures of more than 600°C used for GaAs layers to obtain optimum crystalline quality. Low crystal quality leads to a reduced radiative efficiency of the QDs. At significantly higher temperatures than 500°C, self-organization of QDs in the SK growth mode is not possible due to thermodynamic arguments. In addition, even a slight increase of the temperature may lead to a drastic enhancement of the probability of cluster formation. The temperature window for the fabrication of high-quality QDs is therefore rather small. Particularly in MOCVD of QDs for optoelectronic applications, a compromise between growth temperature, QD crystalline quality and QD size must be found. GRIs are often chosen during which the system might not have enough time to reach the thermodynamically controlled regime.

Within the present work, a QD *equilibrium* size could not be found in any of the described experiments. A steady size increase of uncapped QDs with time was always observed. For kinetic reasons as described in sect. 4.4, the size increase of the QDs slows down with time and would make the assumption of an equilibrium size very time-consuming. Moreover, the time

the system can be given to assume an equilibrium surface morphology is limited by the onset of dislocation-cluster formation setting on few minutes after the deposition of the QD material. The formation of dislocation clusters can be verified using TEM or AFM images.

4.5.2 Impact of deposition amount

It has been shown that the amount of deposited material has a strong influence on the QD density¹³¹⁻¹³⁴. For MOCVD of InGaAs/GaAs using arsine, Leon and coworkers¹³¹ have observed that after the critical layer thickness is reached, the QD density quickly increases and then reaches a saturation density after deposition of about 1.1 times the critical thickness. The QD density does not increase significantly if QD material deposition is continued. The saturation density was found to be larger for smaller V/III ratios. The rapid increase of the area density of MOCVD-grown InGaAs QDs with the amount of deposited material was confirmed within this work: AFM of an In_{0.8}Ga_{0.2}As QD sheet capped with a 2 nm thick GaAs layer previous to cooling shows a QD density of $(2.2 \pm 0.1) \times 10^{10} \text{ cm}^{-2}$. The thickness of the In_{0.8}Ga_{0.2}As deposited was roughly the critical layer thickness. Increasing the deposition amount by only 6 % leads to a QD density of $(3.3 \pm 0.3) \times 10^{10} \text{ cm}^{-2}$, i.e. to a density increase of about 50 %.

4.5.3 Influence of growth interruption

The wavelength of the QD ground-state transition increases with the GRI after the deposition of the QD material. During the GRI, the QDs grow in size at the expense of the WL thickness. This behavior is analogous to the size increase of two-dimensional submonolayer islands as described in sect. 4.5.1, and corresponds also to the one-dimensional model introduced in sect. 4.4.

It is noteworthy that the duration of the GRI after deposition of the QD material was found not to influence the QD density for MOCVD-grown In_{0.8}Ga_{0.2}As QDs using arsine. This finding suggests that kinetic effects dominate the adjustment of the island density during – or shortly after – the deposition of the QD material.

4.5.4 Importance of growth rate

The QD density was furthermore found to depend on the growth rate. This is valid for both the InAs/GaAs^{133, 135} and the InP/GaAs¹³⁶ materials system. A rate equation approach for InP island on GaAs substrates was recently reported¹³⁷ in which both kinetic and thermodynamic properties are

considered. It was found that the nucleus density is higher for larger growth rates.

Experiments were carried out in this work to tune the QD density and also the size dispersion by variation of the growth rate. Unfortunately, the PL efficiency of the QD layers is very sensitive to a variation of this parameter. The QD layers used for the growth of laser diodes were generally optimized to have a maximum radiative efficiency. The influence of the deposition rate on the laser-diode characteristics were not systematically investigated during the optimization procedures. The inhomogeneous luminescence broadening of the QD ensembles used for the growth of the laser diodes is between 60 and 70 meV at room temperature. The QD sheets used in the active region of the laser diode structure with the lowest transparency current density have a FWHM of around 48 meV.

Scanning tunneling microscopy (STM) studies of uncapped MBE-grown InAs/GaAs dots show that QD density and also the QD size dispersion decrease significantly when the growth rate is reduced¹³⁸. PL studies performed on MBE-grown buried InAs/GaAs QD samples show that the emission wavelength increases with decreasing growth rate, reaching a maximum around 1.3 μm with the inhomogeneous broadening decreasing from 44 to 27 meV¹³⁹. For the growth of 1.3 μm QDs, an extremely low growth rate of 0.003 ML/s was used. The low growth rate enables material redistribution towards a very narrow size dispersion. The QD density of these 1.3 μm QDs, however, is clearly below $1 \times 10^{10} \text{ cm}^{-2}$. A very small value of the inhomogeneous line broadening of 26 meV for MBE-grown InAs QDs emitting at 1.25 μm has also been achieved at higher growth rates but with punctuated deposition of the QD material¹⁴⁰.

It can be concluded from these findings that the QD density is highest for large deposition rates. To achieve large QDs with small size dispersions by material agglomeration from the WL and by material redistribution between the islands, the system must be given a certain time. This can be achieved with long-enough GRIs.

5. MOCVD of quantum-dot structures for laser diodes

Although quantum *dot* material gain is known to exceed quantum *well* material gain by far⁷⁰, the low area coverage of QDs leads to lower *modal* gain per QD sheet. For large modal gain of QD lasers, high QD densities are required¹². This makes close stacking of QD layers necessary, thus increasing the QD volume fill factor. Due to the three-dimensional morphology of the QDs and the low temperatures at which QDs and subsequent GaAs capping layers on top of QDs must be grown, GaAs deposited on QD sheets exhibits significant surface corrugations. It is not possible to deposit high-quality QDs on such rough surfaces. Therefore, an in-situ annealing step was developed within this work during which such growth fronts are flattened (cf. sect. 5.1.1).

The threshold currents and quantum efficiencies of MOCVD-grown lasers based on self-organized QDs were not yet close to the ideal limits⁷². This is primarily related to the general difficulty to grow strained heterostructures at low temperatures with high crystalline quality. The strain arising from the lattice mismatch implies the danger of plastic strain relaxation by defect formation. In MOCVD, defect formation is additionally favored by enhanced surface kinetics¹⁴¹ as compared, for example, to MBE. In MBE, the As background pressure for the growth of defect-free InAs QDs at 480°C can be detuned³⁷ by $\pm 50\%$ from the standard value of $p_0^{As} = 2 \times 10^{-6}$ Torr = 2.7×10^{-6} mbar, regardless of the deposition rate. Only for extraordinarily arsenic-rich growth conditions of $p^{As} = 3 \times p_0^{As}$, formation of large defect clusters at the expense of density and size reduction of the remaining QDs is reported.

During MOCVD of QDs, the V/III ratio and also the deposition rate have to be adjusted carefully³⁷. Detuning the V/III ratio by 50 % from the value for optimum luminescence efficiency usually leads to a decrease of the luminescence efficiency by up to an order of magnitude. A possible explanation is based on the fact that MOCVD growth of QDs takes place under comparably arsenic-rich conditions: The AsH₃ partial pressure of typically $1\text{--}3 \times 10^{-1}$ mbar is by five orders of magnitude higher than the typical As pressure in MBE. Although an extremely small cracking efficiency of AsH₃ around 10 % can be assumed at 500°C, the partial pressure of reactive As species is probably still much higher in MOCVD than in MBE. This argument likewise applies to TBAs. The cracking efficiency of TBAs at 500°C is 100 %, i.e. up to 10 times larger than that of AsH₃ (cf. Fig. 7). However, the partial pressure of TBAs supplied is typically 10 times lower than that of AsH₃⁷⁷. The AsH₃ / TBAs partial pressure cannot simply be reduced in MOCVD since high AsH₃ partial pressures are nevertheless mandatory for

the formation of QDs with a reasonable sheet density and sufficient optical quality¹⁴². The enhanced tendency of MOCVD-grown QDs to form defects might also be associated with the reactants used. Particularly, atomic hydrogen stemming from the decomposition of AsH₃ is expected to affect kinetics of QD formation. Hydrogen radicals are known to interact with the surface by breaking bonds due to their high reactivity and thus affect the surface adatom concentration¹⁴¹. Moreover, hydrogen atoms are not the only radicals observed during MOCVD; alkyl radicals formed during pyrolysis of the metalorganic precursor molecules may also play an important role⁹⁰. The in-situ annealing step described in sect. 5.1.1 that has initially been introduced to flatten corrugated growth fronts has a beneficial impact on the crystal quality of QD structures as described in sect. 5.1.2. The threshold current densities of QD lasers could significantly be lowered by in-situ annealing as described later in chapter 6.

Sect. 5.2 reports the fabrication of QD sheets with the alternative arsenic precursor tertiarybutylarsine (TBAs) and works out differences with regard to the growth with arsine.

Lasing emission at 1.3 μm from MOCVD-grown QD lasers has not been reported yet. In sect. 5.3, experiments carried out to increase the QD emission wavelength towards 1.3 μm are presented. Sect. 5.3 comprises a brief review of alternative wavelength shifting techniques. These experiments were carried out using alternative-precursor MOCVD.

5.1. In-situ annealing of QD structures

The growth of GaAs-based SK QDs must take place in a finite temperature window, roughly between 430 and 530°C. At lower temperatures, surface kinetics is insufficient to achieve the 2D-3D transition. At higher temperatures, entropy effects tend to flatten the three-dimensional morphology. Typical growth temperatures of the GaAs material systems, however, are 600°C and more. At QD growth temperatures, surface corrugations are caused by the presence of the underlying three-dimensional QDs. Such corrugations are only slowly planated during the growth of the GaAs cap on top of the QDs. If a sample should contain more than one QD layer, reestablishing a flat growth front of the GaAs matrix before depositing a subsequent QD layer is strongly required. QDs deposited on a corrugated surface show very broad low-intensity PL spectra, indicating a large QD size distribution and the presence of defects. Such QDs are not suited for the deployment in active regions of lasers.

5.1.1 Flattening of the growth front

Several methods were evaluated to flatten the growth front of GaAs cap layers on top of self-organized QDs. For cap thicknesses of more than 50 nm, ML-flat surfaces can be reestablished even if the cap is grown at around 500°C. To increase the QD volume density by close vertical stacking, however, flat surfaces should be achieved for much thinner cap layers. Increasing the growth temperature during growth of the cap significantly enhances the surface flatness. The best results were achieved, however, with GRIs at high temperatures^{73, 143}.

Below the QD sheets, the sample structure used for the flattening experiments is the same as for the PL structures as shown in Fig. 15 (sect. 3.3.2). The $\text{In}_{0.8}\text{Ga}_{0.2}\text{As}$ QDs were deposited at 490-495°C on 100 nm GaAs which was grown at 600°C. Subsequently, a GRI of 60 s without arsine was applied for the nucleation and the development of the QDs^{12, 37}. GaAs caps of 7 nm and 30 nm thickness were deposited on the QDs under different growth conditions. Growth was stopped hereafter and the samples were cooled under As stabilized conditions. The surface morphology was subsequently investigated by contact-mode atomic force microscopy (AFM). In order to avoid degradation of the QDs, the growth temperature was not increased before 3 nm GaAs were deposited on the QDs at the QD growth temperature. A reference sample (A) was grown in which the QD layer was omitted. In this reference sample, 30 nm GaAs were directly deposited at 490°C on 100 nm GaAs grown at 600°C.

Fig. 19 (a) shows a surface AFM image of sample A. The image shows monolayer terraces and a few monolayer-high islands that are elongated in the $\langle 110 \rangle$ direction. Fig. 19 (b) shows a surface AFM image of a QD sample (sample B). In this sample, 30 nm GaAs were deposited at 490°C on a single sheet of QDs that were also grown at 490°C. The surface of sample B exhibits a morphology which differs significantly from that of sample A. Up to 10 nm high and elongated hillocks are visible with mean lateral extensions of $80 \text{ nm} \times 280 \text{ nm}$, all elongated in the $\langle 110 \rangle$ direction. Fig. 19 (c) shows a plan-view TEM image of a sample with a single sheet of QDs buried with GaAs (sample C). The QD density of this sample is $n_{\text{QD}} = 3.4 \times 10^{10} \text{ cm}^{-2}$. The QDs of sample C were deposited under the same growth parameters as those of sample B. Thus the QD density of sample B is also $n_{\text{QD}} = 3.4 \times 10^{10} \text{ cm}^{-2}$.

The hillock density at the surface of sample B amounts to $2.5 \times 10^9 \text{ cm}^{-2}$ which is by a factor of 12.8 lower than the QD density. One hillock thus buries roughly 13 QDs. The hillock height and the QD height (5-10 nm (cf. Ref. 144)) are very similar whereas the lateral extension of the hillocks is about 5 – 10 times larger than that of the QDs. It can be concluded from the

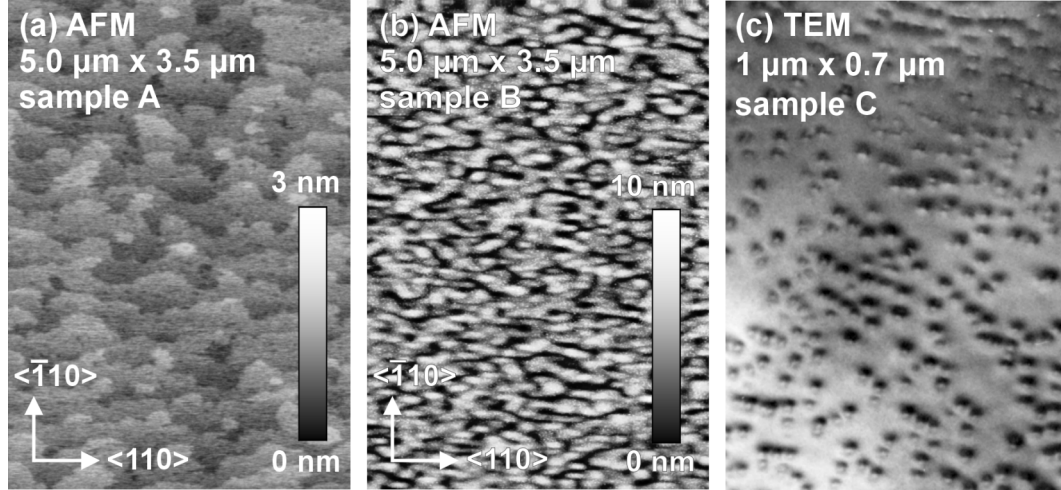


Fig. 19: (a) Reference sample without QDs. A 30 nm thick GaAs layer was directly deposited at 490°C on 100 nm GaAs grown at 600°C. (b) AFM image of a 30 nm thick QD-burying GaAs cap deposited at 490°C on QDs that were also grown at 490°C. The hillock density amounts to $2.5 \times 10^9 \text{ cm}^{-2}$. The picture has been published in Ref. 73 (c) Plan-view TEM image^{vi} of a single-sheet QD sample. The QD density is about $3.4 \times 10^{10} \text{ cm}^{-2}$. The underlying QDs were deposited under the same parameters as those of sample (b).

difference of QD density and hillock density that the hillock morphology is not a continuation of the QD morphology. It is likely that the cap surface morphology is due to the spontaneous formation of nano-facets. Such nano-faceting has been observed by Kasu et al. during MOCVD of GaAs on vicinal GaAs(001) surfaces¹⁴⁵. Although exactly oriented GaAs(001) substrates were used in the present experiments, the QDs lead to local variations of the surface orientation so that nano-faceting can locally take place. At growth temperatures of 600°C and more, nano-faceting in this material system is thermodynamically unfavorable. Facets that have formed at low temperatures blur above 600°C (cf. Ref. 146).

The ML-high islands on top of sample A as well as the large hillocks of sample B are significantly elongated in the $\langle 110 \rangle$ direction. This is likely due to the influence of surface kinetics. Two effects can account for this phenomenon: An anisotropy of the surface diffusion coefficient D_s (for example $D_{s\langle 110 \rangle} > D_{s\langle \bar{1}10 \rangle}$) or an anisotropy of the sticking probability of migrating adatoms to $\langle \bar{1}10 \rangle$ -oriented steps (A-steps) and $\langle 110 \rangle$ -oriented steps (B-steps). Kasu and Kobayashi¹⁴⁷ attributed island elongations similar to those of Fig. 19 (a) and (b) to an anisotropy of the sticking probability of migrating adatoms. They determined the sticking probability to be larger at A-steps than at B-steps. The difference is considered to be

^{vi} By courtesy of N.D. Zakharov and P. Werner, Max-Planck Institute of Micro-structure Physics, Halle, Germany.

due to the anisotropy of the arsenic-rich $c(4\times 4)$ surface reconstruction which is the preferred reconstruction on exactly oriented GaAs(001) surfaces grown under As-rich conditions such as in MOCVD. Calculations by Ito et al.¹⁴⁸ confirm the anisotropy of the sticking probability. Heller and Lagally¹⁴⁹ have investigated MBE-grown GaAs(001) surfaces. In contrast to the case of MOCVD-grown GaAs(001) surfaces, they determined a larger sticking probability to *B-steps* which they attribute to the anisotropy of the (2×4) reconstruction they determined using STM. Employing first-principles total-energy calculations, Kley et al.¹⁵⁰ have reported a lower adatom diffusion barrier in the $\langle \bar{1}10 \rangle$ direction than in the $\langle 110 \rangle$ -direction for the MBE-typical $\beta 2(2\times 4)$ surface reconstruction. According to their calculations, the adatom diffusion is faster parallel to the As dimers of the $\beta 2(2\times 4)$ unit cell, favoring nucleus elongation in the $\langle \bar{1}10 \rangle$ direction. The references cited in this paragraph refer to ML-high nuclei as one can see in Fig. 19 (a). However, the above considerations are likely to be valid also for the case of elongated hillocks such as in Fig. 19 (b).

A first step towards reestablishing a flat growth front was to enhance the surface mobility of adatoms of the cap surface by increasing the growth temperature. However, before increasing the temperature for the growth of the cap layer, the QDs were covered by 2-3 nm GaAs at the QD growth temperature. An earlier rise of the temperature results in a decreased PL signal from the sample, presumably due to defect formation in the QD layer. The growth temperature was kept below 600°C to avoid intermixing effects of In from the QDs with Ga of the matrix. This would result in an undesired blueshift¹⁰⁰ of the QD emission wavelength.

The surface morphology of a sample for which the growth temperature of the cap was ramped to 590°C is shown in Fig. 20 (a). It is completely different from that of sample B. It exhibits a ML step landscape showing terraces and ML islands. As compared to sample A (Fig. 19 (a)), the terraces are significantly frayed, however, and the ML island density of $2.8 \times 10^8 \text{ cm}^{-2}$ is about five times larger. A sample grown at the intermediate temperature of 535°C exhibits a surface similar to sample B but with half the hillock height.

It was also tried to improve the result shown in Fig. 20 (a) by insertion of a short-period GaAs/AlGaAs superlattice. Similar AlGaAs/GaAs superlattices are typically used in MBE of GaAs-based edge emitting lasers with AlGaAs cladding layers of high aluminium content to reduce surface corrugations related with the thick AlGaAs layers. In such layer structures, short-period superlattices are grown directly below and above each cladding layer. A QD sample was grown within this work which differs from that shown in Fig. 20 (a) by the insertion of 3 periods of a GaAs (2.7 nm) / AlGaAs (1.8 nm) superlattice, keeping an overall cap thickness of 30 nm. The

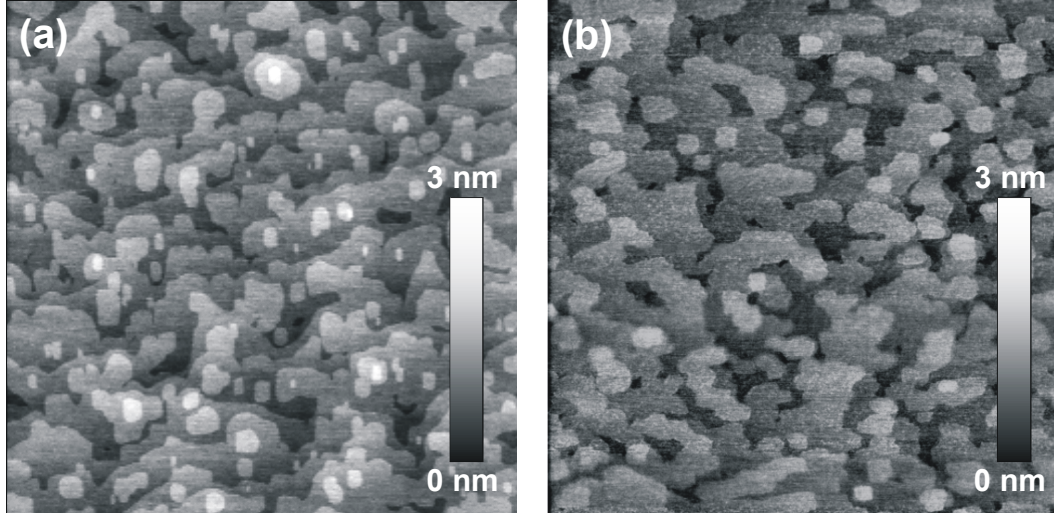


Fig. 20: (a) AFM surface image of a sample where the growth temperature of the 30 nm thick GaAs cap was ramped in-situ to 590°C. The picture has been published in Ref. 73. (b) AFM surface image of a sample where the QDs were capped with 7 nm GaAs. Subsequently, the surface was annealed during 10 min at 600°C under As stabilization.

temperature was ramped to 590°C before the growth of the superlattice. AFM of the surface was performed revealing an insignificant reduction of the ML island density by 14 % to $2.4 \times 10^8 \text{ cm}^{-2}$, and an increase of the average ML island area by 40 % to $3.3 \times 10^4 \text{ nm}^2$. So the insertion of an $\text{Al}_{0.65}\text{Ga}_{0.35}\text{As}/\text{GaAs}$ superlattice does not lead to an improvement of the surface flatness which is considered relevant for the subsequent deposition of QDs.

The most efficient flattening is achieved if the growth is stopped after the deposition of the cap and if GRIs of several minutes are applied subsequently at 600°C. This method is very efficient even for only 7 nm thick caps. In the experiment, the first 2-3 nm of the GaAs caps were grown at the QD deposition temperature. The growth temperature was then ramped to 600°C during the last 4-5 nm. Three samples were grown with GRIs of 0, 10, and 20 min. The samples were weakly arsenic-stabilized during the GRIs with an AsH_3 partial pressure of $5.4 \times 10^{-2} \text{ mbar}$. For the as-grown case (GRI = 0), the surface shows hillocks with an average height of 4 nm and a hillock density of $8.2 \times 10^8 \text{ cm}^{-2}$, similar to sample B. However, these hillocks have an atomically flat top of which the average area amounts to $2.0 \times 10^4 \text{ nm}^2$. Fig. 20 (a) shows an AFM image of the surface annealed during 10 min. The surface exhibits ML steps again, the ML island density is as low as $1.5 \times 10^8 \text{ cm}^{-2}$ and the average island area amounts to $8.5 \times 10^4 \text{ nm}^2$. These values are not significantly improved for 20-30 min annealing.

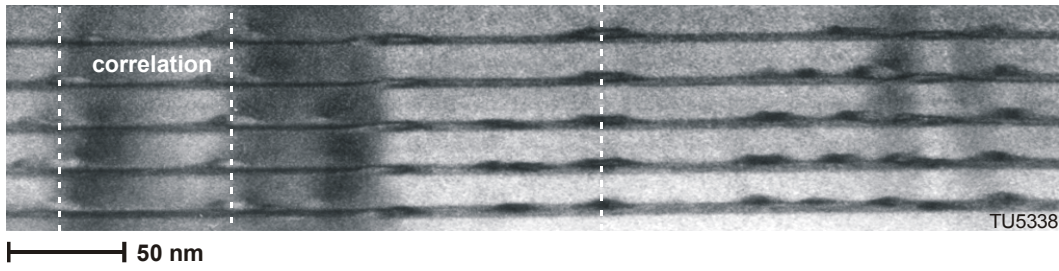


Fig. 21: Cross-sectional dark-field TEM image^{vii} of a five-fold $\text{In}_{0.8}\text{Ga}_{0.2}\text{As}$ QD stack grown with in-situ annealing after each QD layer was capped by 7 nm GaAs. The vertical sheet-to-sheet distance is 18-20 nm.

The surface of the sample with a 7 nm thick cap annealed during 10 min (Fig. 20 (b)) is comparable to the surface of the 30 nm thick cap shown in Fig. 20 (a). The decisive advantage of the annealing step as compared to simple temperature ramps or the integration of a superlattice is the extremely small thickness of the cap for which a ML-step surface profile can be reestablished. This has a strong impact on the layer qualities in dense QD stacks.

Fig. 21 shows a cross-sectional dark-field TEM image of a five-fold $\text{In}_{0.8}\text{Ga}_{0.2}\text{As}$ QD stack grown with 10 min in-situ annealing at 600°C after each QD layer was capped with 7 nm GaAs. The vertical sheet-to-sheet distance is about 18-20 nm. For such thin GaAs spacers, the strain fields generated by the lattice-mismatched QDs lead to vertical QD coupling. The vertically correlated QDs marked with dashed white lines in Fig. 21 broaden from layer to layer. The vertical correlation is due to a minimum of the elastic-energy density on the spacing-layer surface exactly above buried QDs¹⁵¹. This minimum exhibits a fine structure of four shallow minima arranged in cloverleaf geometry above the strained QDs as shown in Fig. 1 of Ref. 151. This fine structure can possibly account for the increase of the QD widths from sheet to sheet.

PL spectra from such vertically correlated stacked QD sheets show very broad transition lines, most likely due to the size increase of the QDs from sheet to sheet. This is disadvantageous for laser diodes where gain is to be maximized within a narrow spectral region. For the application as active medium in lasers, the spacer of such QD layers is increased until correlation is completely lost. Then the QDs of all layers have similar sizes and shapes and the inhomogeneous broadening decreases. The occurrence of vertical QD correlation which is a function of the QD size, the QD strain and the sheet-to-sheet distance limits the number of QD sheets that can be used in an optical confinement layer of a given thickness.

^{vii} by courtesy of N.D. Zakharov and P. Werner, Max-Planck Institute of Microstructure Physics, Halle, Germany.

To conclude, a strong reduction of growth front corrugations of the GaAs cap layer on top of InGaAs QDs and the reestablishment of a smooth surface were demonstrated. An elevated overgrowth temperature which can be adjusted after the QDs are covered by 2-3 nm of GaAs is essential. The best results were obtained for a cap layer thickness of only 7 nm with subsequent annealing during 10 min at 600°C.

5.1.2 Optical properties of annealed QD structures

The influence of the annealing step on the optical properties of the QDs was also investigated. For this purpose, samples were grown as described in the previous section. The samples were additionally capped with 20 nm of $\text{Al}_{0.33}\text{Ga}_{0.67}\text{As}$, however, acting as a charge-carrier diffusion barrier to suppress non-radiative surface recombination. The measurements were carried out at room temperature. Low excitation densities were used to probe the emission wavelength and the optical quality of the QDs. High excitation densities where both QD and WL states are saturated were used to investigate the radiative recombination in the GaAs matrix.

Fig. 22 shows PL spectra of undoped test structures for four different annealing times ($t_A = 0, 10, 20, 30$ min) taken at low (a) and high (b) excitation density. The low-excitation spectra show a blueshift of the QD emission wavelength and a slight reduction of the peak intensity for annealing during 10 min. The blueshift is attributed to some In-Ga intermixing¹⁰⁰. The decrease of the peak intensity, however, cannot be explained using this argument. When the annealing time is extended to 30 min, a monotonic increase of the peak intensity of the QD luminescence is observed which is attributed to a reduction of defect-related non-radiative recombination channels¹⁵². The high-excitation spectra of Fig. 22 (b) show that the GaAs matrix intensity increases by a factor of about two upon annealing for 10 and 20 min. A GRI of 30 min, however, leads to a reduction of the PL-intensity of the GaAs matrix. In the high-excitation spectra, the saturated PL intensity from the QDs remains quasi unchanged for all GRI durations.

As an explanation for the increase of the GaAs luminescence, a reduction of two different kinds of defects is suggested that are both related to the growth of the QD layers. First, misfit dislocations might be formed in a very small fraction of the QDs, most likely in very large ones³⁷. These dislocations proceed into the GaAs on top of them and strongly reduce the GaAs luminescence, acting as non-radiative recombination centers. In contrast to Ref. 6 where the dislocation density is enhanced upon post-growth annealing, an in-situ annealing step with the surface being very close to the spatial origin of the dislocations enables strong reduction of the number of dislocations, as demonstrated in Ref. 152 by deep level transient spectroscopy.

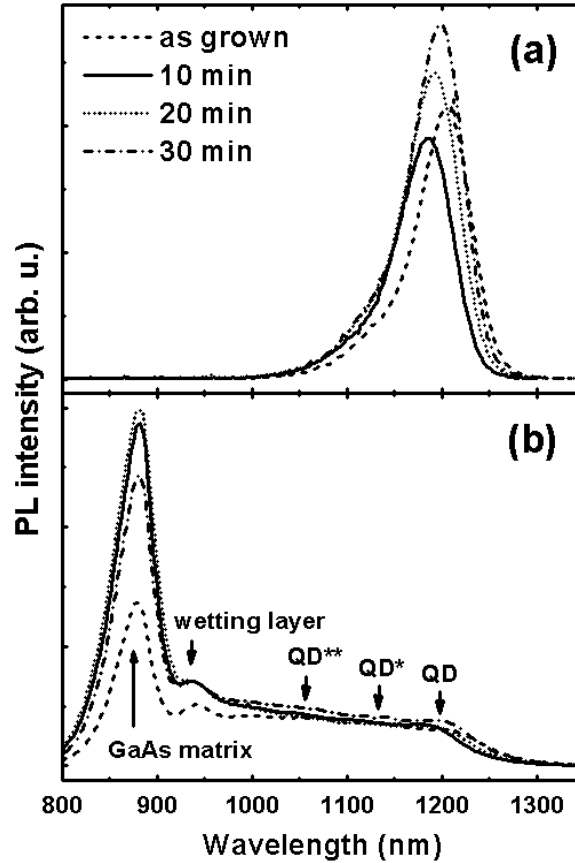


Fig. 22: Room-temperature PL spectra of annealed QD samples at low excitation density (a) (5 W/cm^2) and at high excitation density (b) (5 kW/cm^2). In (a), recombination occurs essentially on the QD ground state. Luminescence from the WL and the matrix is not visible. In (b), radiative recombination mainly takes place in the GaAs matrix. The stars denote transitions from the excited QD states. This figure has been published in Ref. 73.

copy. However, as the number of dislocation-containing or -inducing QDs is small compared to the number of QDs in which recombination occurs radiatively, no significant improvement of the QD luminescence is observed upon annealing. It is therefore assumed that the QDs are of high crystalline quality even without annealing. Secondly, point defects in the first 2-3 nm of the low-temperature GaAs grown at 490°C immediately on top of the QDs may act as non-radiative recombination centers. Typical MOCVD growth temperatures for low-defect-density bulk GaAs are in the range of 600 to 650°C (Ref. 153). GaAs grown at lower temperatures tends to build non-equilibrium point defects.

The annealing step described here is also useful to eliminate large dislocated clusters from MOCVD-grown QDs emitting at 1300 nm ¹⁵⁴. In this case an improvement of the QD PL intensity by a factor of two was found. The selective deposition of AlAs on defect-free regions of cluster-

containing InGaAs surfaces enables the selective evaporation of such defect-containing sites if annealing is applied subsequently¹⁵⁵.

5.2. Alternative-precursor MOCVD of InGaAs QDs

It will be shown here that QDs grown using TBAs in a suitable growth regime also have excellent optical properties, very similar to QDs grown using AsH₃. Conclusive evidence of the high quality of self-organized QDs grown with alternative-precursor MOCVD is supplied by the realization of QD lasers as reported in sect. 6.1.2, proving the general suitability of this QD growth process also for other optoelectronic devices.

For PL studies, undoped structures containing only a single In_{0.67}Ga_{0.33}As/GaAs QD sheet were grown under various growth conditions, applying a GRI of 60 s after deposition of the QD material. The In fraction of $x = 0.67$ was determined using x-ray diffraction of a ten-fold InGaAs QW stack. The QWs of this stack were deposited under the same growth parameters as the QDs but the QW thickness was kept below the critical value for the formation of SK QDs. Room-temperature PL spectra of an InGaAs QD test structure grown at 485°C using a V/III ratio of 1.5 are shown in Fig. 23. For high excitation power, emission from the QD ground state and first excited state as well as transitions from the WL and the matrix is clearly visible. At low excitation power, PL mainly originates from the QD ground state, the inhomogeneous broadening being 70 nm (65 meV). A very large QD density of $9.6 \times 10^{10} \text{ cm}^{-2}$ is determined from the plan-view transmission electron micrograph shown in the inset of Fig. 23. Both PL and transmission electron micrograph show a unimodal coherent QD growth without defect clusters. These results are comparable to data of QDs grown using AsH₃ and used as active medium for high-power lasers^{156, 157}.

Using AsH₃, V/III ratio and deposition temperature are crucial growth parameters for good optical and structural properties of InGaAs QDs¹⁴². Therefore, the peak wavelength of the ground-state transition of In_{0.67}Ga_{0.33}As QDs grown with TBAs as a function of these parameters is studied using low-excitation-density PL (Fig. 24). An increase of the V/III ratio leads to a pronounced redshift of the peak wavelength, indicating an increased size of the QDs. Similar observations were reported for MOCVD of InGaAs QDs using AsH₃¹⁵⁸ and for MBE of InAs QDs³⁷, indicating a general behavior which is independent of growth technology and chemistry of the As precursor. The dependence can be explained by considering the surface energy: Calculations show that an increase of the arsenic pressure leads to a decrease of the surface energies of both GaAs(001)¹⁵⁹ and InAs(001)¹⁶⁰. It is natural to assume that a strained InGaAs WL on

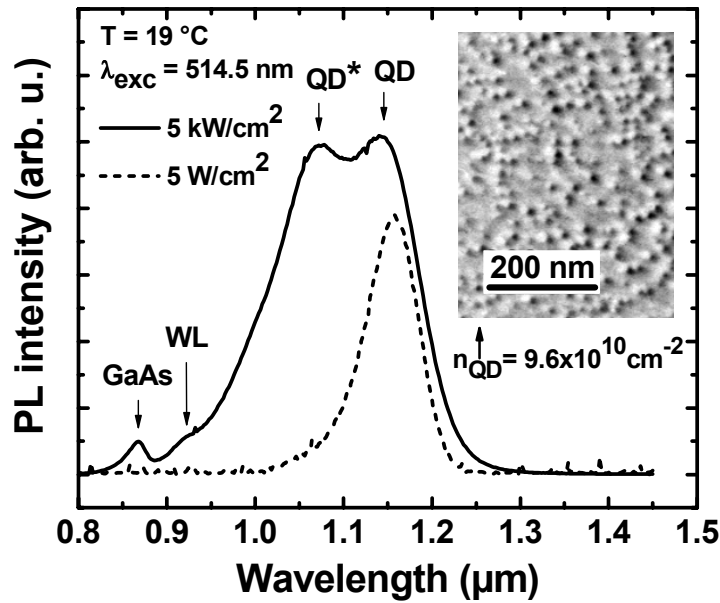


Fig. 23: PL spectra of $\text{In}_{0.67}\text{Ga}_{0.33}\text{As}$ QDs, deposited at 485°C . “QD”, “QD*”, and “WL” denote transitions from the QD ground state, the first excited QD state, and the WL, respectively. Inset: Plan-view dark-field transmission electron micrograph of the same QD layer. This figure has been published in Ref. 161.

GaAs(001) shows a similar tendency. Calculations of the thermodynamics of QD formation indicate that the QD equilibrium size rises if the surface energy of the WL is reduced¹¹⁹.

In contrast to the dependence on the V/III ratio, the variation of temperature has different impacts on the emission wavelength of QDs grown using either AsH_3 or TBAs. The PL of TBAs-grown QDs shows a slight blueshift with increasing temperature above 485°C (Fig. 24). For AsH_3 -grown InGaAs QDs a strong *redshift* of the QD ground-state transition is always observed¹⁴² if the temperature is increased. This is most likely related to an increase of the QD size. The equilibrium size of SK QDs has been predicted to decrease with temperature, using thermodynamic equilibrium arguments¹¹⁹. Actual growth processes, however, usually imply too short time intervals for formation and overgrowth of such QDs for reaching an equilibrium size. This applies particularly for lower growth temperatures at which the equilibrium size is large and the adatom mobility is low, as it is the case for the sample in Fig. 24 grown at 470°C . The emission wavelength of this sample is expected to be further in the red as compared to the other samples. Thus, decrease *and* increase of QD size with temperature may occur, depending on the balance between thermodynamics and kinetics¹²⁷.

Using AsH_3 , however, only a *redshift* of the emission peak with increasing temperature was observed. This particularity is likely related to the

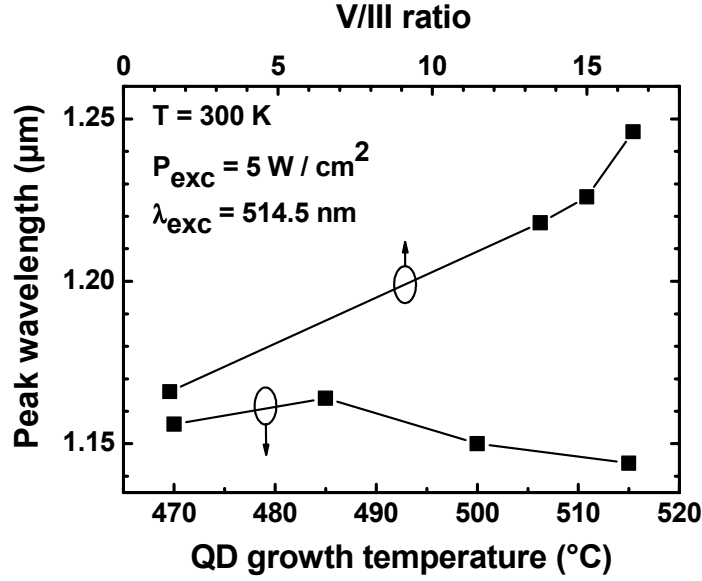


Fig. 24: PL peak emission wavelengths of the ground-state transitions of $\text{In}_{0.67}\text{Ga}_{0.33}\text{As}$ QDs as a function of growth temperature and V/III ratio. QDs of the V/III series were deposited at 485°C , the V/III ratio of the temperature series was kept at 1.5. The reproducibility of the peak positions is within 10 nm. This figure has been published in Ref. 161.

strong temperature dependence of the AsH_3 pyrolysis between 450°C and 650°C (cf. Fig. 7 on p. 22). Increasing the temperature leads to a larger fraction of reactive As species. The V/III ratio hence rises and causes an increase of the QD size via lowering the surface energy, as described above. For the QDs grown using TBAs, this effect is not observed since the cracking efficiency of TBAs is nearly 100 % at 500°C (cf. Fig. 7 on p. 22). The use of TBAs thus allows a nearly independent tuning of the growth parameters temperature and V/III ratio. As compared to AsH_3 , the growth of QDs using TBAs is less dependent on the chemical properties of the arsenic precursor.

5.3. Redshift of the quantum-dot emission wavelength

As shown in the previous section, the emission wavelength of TBAs-grown InGaAs QDs can easily be tuned to above 1200 nm just by increasing the V/III ratio during deposition of the QD material (cf. Fig. 24). InGaAs QDs grown using conventional AsH_3 at high V/III ratios and elevated temperatures emitting even beyond $1.3\text{ }\mu\text{m}$ have been demonstrated^{viii}. Wavelengths close to $1.3\text{ }\mu\text{m}$ can also be achieved using MBE of large InAs QDs⁴⁹. Unfortunately, all these long-wavelength QDs have low sheet densities and are therefore unsuited for the application in laser diodes. Achieving

^{viii} Frank Heinrichsdorff, unpublished.

sufficient QD sheet densities at 1.3 μm poses a general problem. This is in agreement with the general observation that QD sheet densities decrease with increasing QD size. To obtain QD ground-state lasing, however, large QD densities are required. Different techniques were explored within this work to redshift the emission wavelength of high-density QDs without forfeit of their number.

Approaches to obtain QD luminescence at 1.3 μm and beyond generally make use of high-density short-wavelength (1.1 – 1.2 μm) In(Ga)As stressor QDs. The density of these stressors is typically in the upper 10^{10} cm^{-2} regime. To achieve 1.3 μm luminescence, such stressors are subsequently capped with thin films of a material having a lower band gap than GaAs. These materials can be lattice-matched to GaAs like $\text{In}_x\text{Ga}_{1-x}\text{As}_y\text{N}_{1-y}$ with corresponding fractions x and y , or exhibit smaller ($\text{GaAs}_x\text{N}_{1-x}$) or larger lattice constants ($\text{In}_x\text{Ga}_{1-x}\text{As}$) than GaAs. QD emission at 1.3 μm has been demonstrated, for example, by overgrowing InAs QDs with 40 nm $\text{In}_{0.03}\text{Ga}_{0.97}\text{As}_{0.99}\text{N}_{0.01}$ using MBE¹⁶². Due to the large band gap bowing of dilute nitrides¹⁶³, the band gap of the $\text{In}_{0.03}\text{Ga}_{0.97}\text{As}_{0.99}\text{N}_{0.01}$ is about 1.2 eV (1033 nm) at room temperature. Therefore, the confinement of the electron wavefunction is lower for the quaternary barrier than for GaAs, leading to lower exciton recombination energies. Overgrowth of InGaAs QDs with GaAsN is expected to have a similar effect. In addition, the tensile strain of GaAsN^{164, 165} in a GaAs matrix would lead to a reduction of the overall strain of the QD structure. An overview of the different techniques is given in the flow chart of Fig. 25. The admixture of Sb could possibly further increase the emission wavelength. The DWELL concept described in sect. 2.3 has turned out to lead to a comparably large decrease of the luminescence efficiency in MOCVD and was therefore not pursued within this work.

Three approaches to shift the QD emission to longer wavelengths will be discussed in this section. InGaAs QDs overgrown with Ga-rich QWs are described in sect. 5.3.1. This technique has turned out to be very successful for the fabrication of 1.3 μm QD lasers in MBE. The admixture of nitrogen (sect. 5.3.3) and antimony (sect. 5.3.4) to InGaAs QDs has been explored as other means to redshift the emission wavelength.

5.3.1 Overgrowth of InGaAs QDs by InGaAs QWs using arsine

In this section, the overgrowth of short-wavelength InGaAs stressors with Ga-rich InGaAs layers using conventional precursors is discussed as an approach to redshift the QD emission wavelength to 1.3 μm . This technique has previously been explored in MBE and is referred to as Activated Alloy Phase Separation (AAPS)⁴⁹. The increase of the strain energy related to this technique enhances the danger of plastic relaxation by formation of

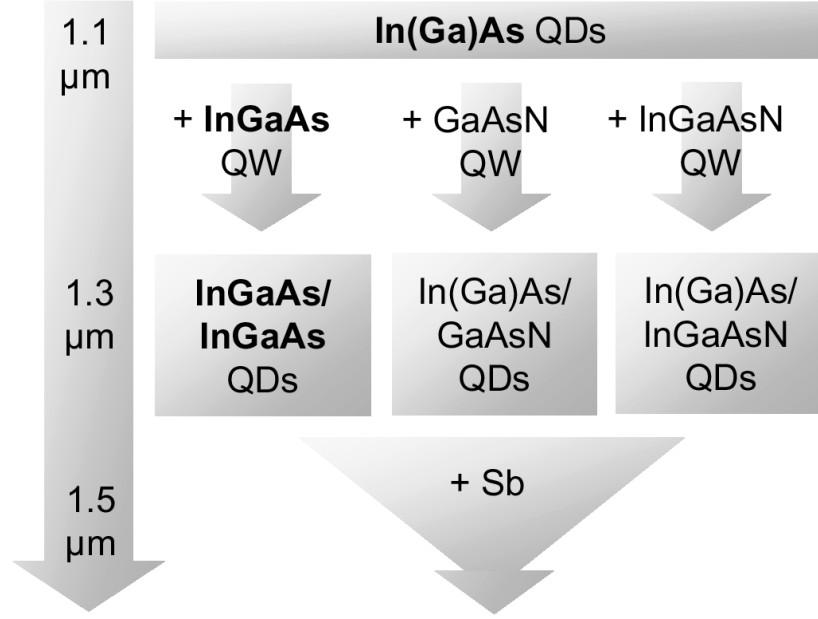


Fig. 25: Flow chart of different approaches to achieve lasing emission at 1.3 μm and beyond by overgrowing small In(Ga)As QDs. Structures in bold scripture were grown and characterized within this work.

dislocations and precipitates so that a careful choice of the stressor QD size and the indium fraction of the overgrown QW is required^{49, 166}. The advantage of TBAs with regard to AsH_3 for the deposition of such compound structures is outlined in sect. 5.3.2.

The $\text{In}_{0.8}\text{Ga}_{0.2}\text{As}$ stressor QDs used here were grown with conventional-precursor MOCVD. They have a lateral density of about $5 \times 10^{10} \text{ cm}^{-2}$ and have proven their crystalline quality as active medium of laser diodes¹⁵⁶. These devices exhibit differential efficiencies of almost 100 %, and the threshold currents are exceptionally low (more details are given in sect. 6.1.1). The InGaAs stressor dots used for the overgrowth experiments were deposited under the same growth conditions as the QDs of the laser diodes. They were eventually overgrown with gallium-rich InGaAs QWs of varying thickness and composition and finally capped with GaAs.

Depending on thickness and composition of the QW, the overgrowth leads to a distinct redshift of the QD emission wavelength. This is ascribed to changes of the electronic properties of the InGaAs stressor QDs. Two main effects come into consideration to explain these changes:

1. The overgrown $\text{In}_x\text{Ga}_{1-x}\text{As}$ cap layer causes a strain redistribution that leads to a partial strain relaxation of the stressor dots^{167, 168}. The band gap of the InGaAs stressor dots decreases. This is discussed in sect. 5.3.1.1.

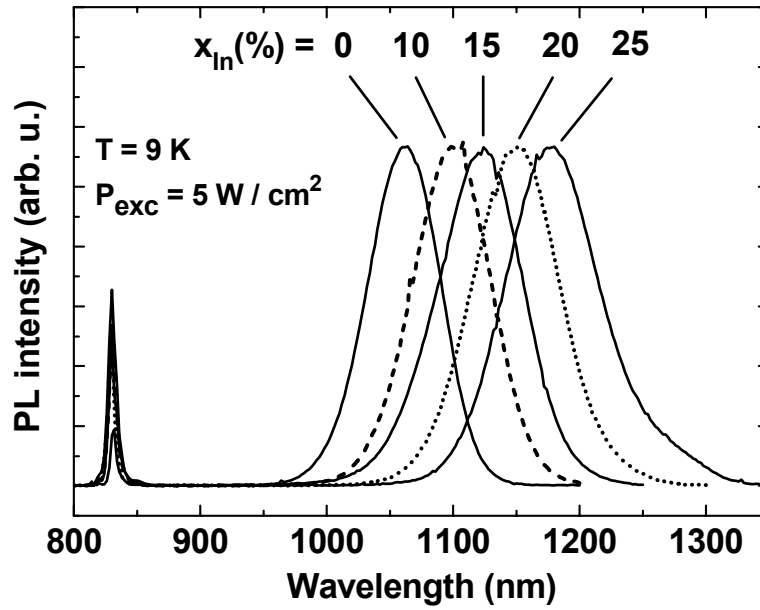


Fig. 26: Low-temperature PL spectra of single $\text{In}_{0.8}\text{Ga}_{0.2}\text{As}$ QD layers overgrown with 5 nm $\text{In}_x\text{Ga}_{1-x}\text{As}$ QWs of varying indium fraction x . The spectra were normalized to equal peak intensities.

2. Strain-driven surface kinetics leads to the decomposition of the $\text{In}_x\text{Ga}_{1-x}\text{As}$ QW during growth^{55, 169, 170} due to preferential agglomeration of indium at already existing stressors, thus increasing the effective QD size. The structural changes of the QDs upon overgrowth are described in sect. 5.3.1.2.

The overgrown QD structures were investigated using PL, TEM, and cross-section scanning tunneling microscopy (XSTM).

5.3.1.1 Spectroscopic characterization

Fig. 26 shows PL spectra of overgrown $\text{In}_{0.8}\text{Ga}_{0.2}\text{As}$ QDs, recorded at 9 K. The stressors were overgrown with 5 nm thick $\text{In}_x\text{Ga}_{1-x}\text{As}$ QWs with indium fractions x ranging from 0 to 25 % (the In fraction was calibrated using x-ray diffraction of ten-fold InGaAs QWs). The spectra were normalized to equal peak intensities in order to facilitate the comparison of the respective line shapes.

The emission wavelength of the QD structures shifts monotonously into the red with increasing x_{In} . QDs consisting of lattice-mismatched InGaAs are considerably strained. The hydrostatic strain of the QDs strongly raises the QD-material band gap as compared to unstrained InGaAs. If an additional InGaAs QW is inserted between QDs and GaAs matrix on top of the

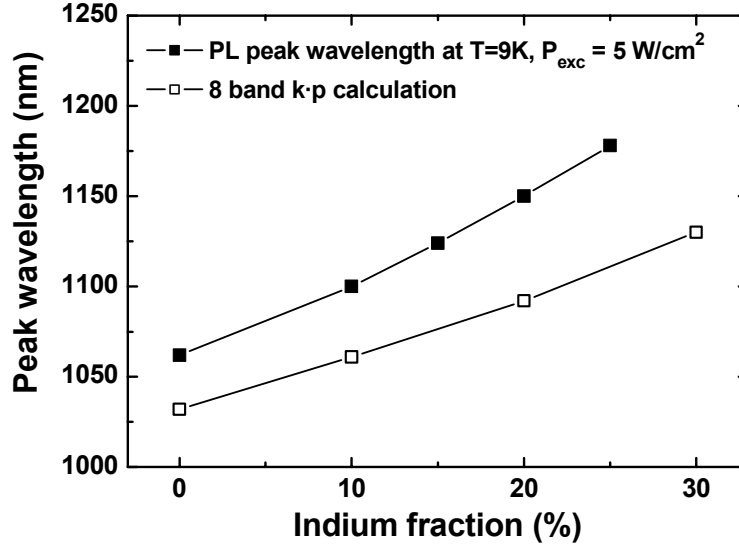


Fig. 27: Full squares: PL peak wavelength of $\text{In}_{0.8}\text{Ga}_{0.2}\text{As}$ QDs overgrown with 5 nm $\text{In}_x\text{Ga}_{1-x}\text{As}$ of denoted indium fraction x , recorded at 9 K. From TEM images, the QDs are estimated to be 3-5 nm high and 20-25 nm wide. Hollow squares: Ground-state transition wavelengths of a 2.6 nm high truncated-pyramid-shaped InAs QD overgrown with an $\text{In}_x\text{Ga}_{1-x}\text{As}$ QW of denoted indium fraction x , calculated within an eight-band $k\cdot p$ framework.

dots, the strain of QDs decreases in growth direction. The strain redistribution of a similar QD structure was calculated in the framework of continuum mechanics, using a finite-differences method¹⁶⁷. It is shown in Ref. 167 that the hydrostatic strain of the QW increases with increasing indium concentration, whereas the strain of the QDs decreases. This leads to a lowering of the confining potential, following the strain dependence of the InGaAs band gap, and leads to a reduction of the exciton recombination energy.

Up to $x = 15\%$, the PL lines of Fig. 26 exhibit rather symmetric shapes as expected for mono-dispersed ensembles of self-organized QDs at low temperatures¹⁷¹. The sample with $x = 25\%$ shows a shoulder on the long-wavelength side, suggesting that a number of larger QDs have formed that might lead to a bimodal size distribution if x is raised further.

The peak wavelengths of the spectra in Fig. 26 are plotted in Fig. 27 as a function of the indium fraction x of the overgrown $\text{In}_x\text{Ga}_{1-x}\text{As}$ QW. Calculated values¹⁶⁷ of transition wavelengths previously obtained for comparable structures are likewise plotted. In these calculations, truncated InAs pyramids capped with a 4 nm thick $\text{In}_x\text{Ga}_{1-x}\text{As}$ layer of varying composition were used. These QDs were assumed to be on top of a 0.36 nm thick InAs WL and to have $\{101\}$ -type side facets and a base length / height of

11.3 nm / 2.6 nm. The localized electron and hole states in these QDs were then calculated within an eight-band k - p framework. Exciton formation is treated self-consistently in the Hartree approximation. Calculations for truncated-pyramid QDs are described in Ref. 167, calculations for pyramidal InAs/GaAs QDs can be found in Ref. 172.

Fig. 27 indicates that the measured emission wavelengths are larger than the calculated ones. A deviation of the experimental data from the calculated values is not surprising since the respective QD structures are slightly different. Whereas ternary $\text{In}_{0.8}\text{Ga}_{0.2}\text{As}$ QDs were overgrown with 5 nm $\text{In}_x\text{Ga}_{1-x}\text{As}$, the calculations are based on binary InAs QDs capped with only 4 nm $\text{In}_x\text{Ga}_{1-x}\text{As}$. Binary InAs is nevertheless a good approximation for QDs formed upon deposition of $\text{In}_{0.8}\text{Ga}_{0.2}\text{As}$ since it has been shown that the In fraction of SK QDs formed upon deposition of $\text{In}_x\text{Ga}_{1-x}\text{As}$ QDs is usually much larger than the nominal fraction x of the 2D layer¹⁷³. This effect is attributed to lateral decomposition of the ternary InGaAs driven by strain effects. From TEM images not shown here, the shape of the $\text{In}_{0.8}\text{Ga}_{0.2}\text{As}$ stressor QDs cannot be determined in detail: A possible lens shape and a truncated-pyramid shape can hardly be distinguished. However, lens-shaped QDs and truncated-pyramid QDs of comparable spatial dimensions have similar electron and hole levels.

In addition to the vertical offset of the experimental data from the theoretical values in Fig. 27, a superproportional increase of the emission wavelength with increasing indium fraction is observed. This observation gives reason to assume that an additional phase separation of the InGaAs QW has taken place, additionally pushing the emission wavelength of the QD structure further into the red. A structural investigation of such AAPS structures is given in the next section.

5.3.1.2 Structural characterization

Structural investigations of AAPS structures were carried out using high-resolution cross-section TEM and XSTM. TEM images were processed from a series of samples that contain single $\text{In}_{0.8}\text{Ga}_{0.2}\text{As}$ stressor sheets overgrown with $d = 0, 1, 2$ and 3 nm of $\text{In}_{0.25}\text{Ga}_{0.75}\text{As}$. The samples were grown using conventional precursors. Fig. 28 shows low-excitation room-temperature PL spectra of these QD structures. The QD emission wavelength shifts from below 1200 nm ($d = 0$ nm) to beyond 1300 nm ($d = 3$ nm). This qualitatively corresponds to the overgrowth experiments using InGaAs QWs of constant thickness but varying composition. The FWHM of the QD ground-state transition line increases from 60 meV to more than 80 meV, indicating a broadening of the QD size distribution. The integrated PL intensity decreases by a factor of two. This is evidence of an increase of

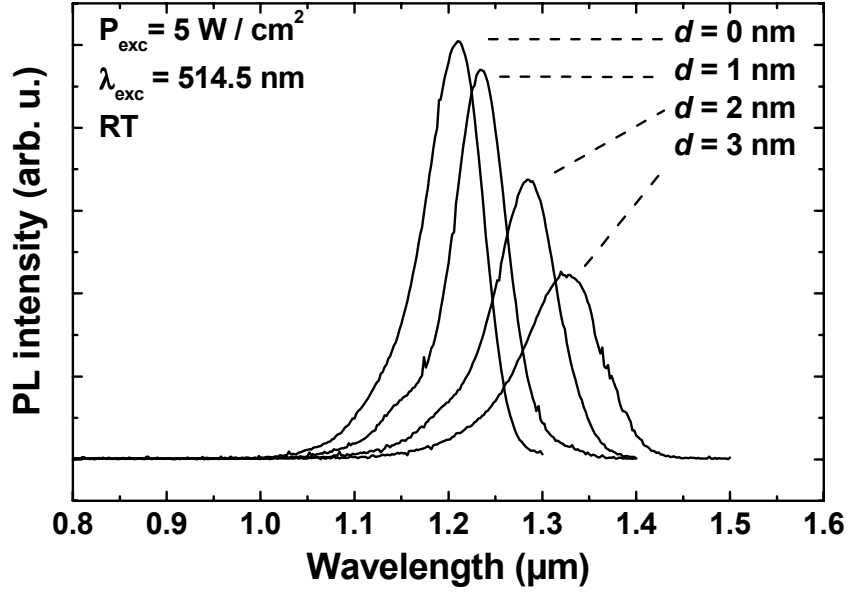


Fig. 28: Room-temperature PL spectra of $\text{In}_{0.8}\text{Ga}_{0.2}\text{As}$ QDs overgrown with $\text{In}_{0.25}\text{Ga}_{0.75}\text{As}$ QWs of varying thickness d .

the defect density upon overgrowth. Although the target wavelength has been reached, defects must still be reduced in these structures to obtain QD structures with sufficient quality for the application in devices.

Fig. 29 shows Fourier-filtered high-resolution TEM images of the structures in cross-sectional geometry. QDs with a representative size were chosen for the TEM analysis. Plan-view TEM images of these structures do not show any plastically relaxed clusters. The dotted white lines depict the boundary between InGaAs and GaAs. These boundaries were determined according to the reversal of the In-As and Ga-As image contrast, occurring at an indium fraction of about 15 %^{174, 175}. The TEM images indicate that the QD height increases with the thickness of the overgrown InGaAs QW. The plateaus of the truncated pyramids become wider. The layer on both sides of the QDs, now consisting of the original WL and the overgrown InGaAs QW, also gains in thickness. Interestingly, the width of the QDs hardly varies.

The different states of overgrowth are depicted schematically in Fig. 30. An as-grown, freestanding InGaAs QD is depicted in (a). During overgrowth (b), In atoms are assumed to attach preferably at the InGaAs islands, whereas Ga atoms prefer the pseudomorphically strained WL regions between the QDs¹⁷⁶. A similar observation has been made in MBE during overgrowth of InAs QDs by binary GaAs: gallium atoms were shown to migrate away from the QDs towards the pseudomorphically strained WL regions between the QDs that have an in-plane local lattice constant equal

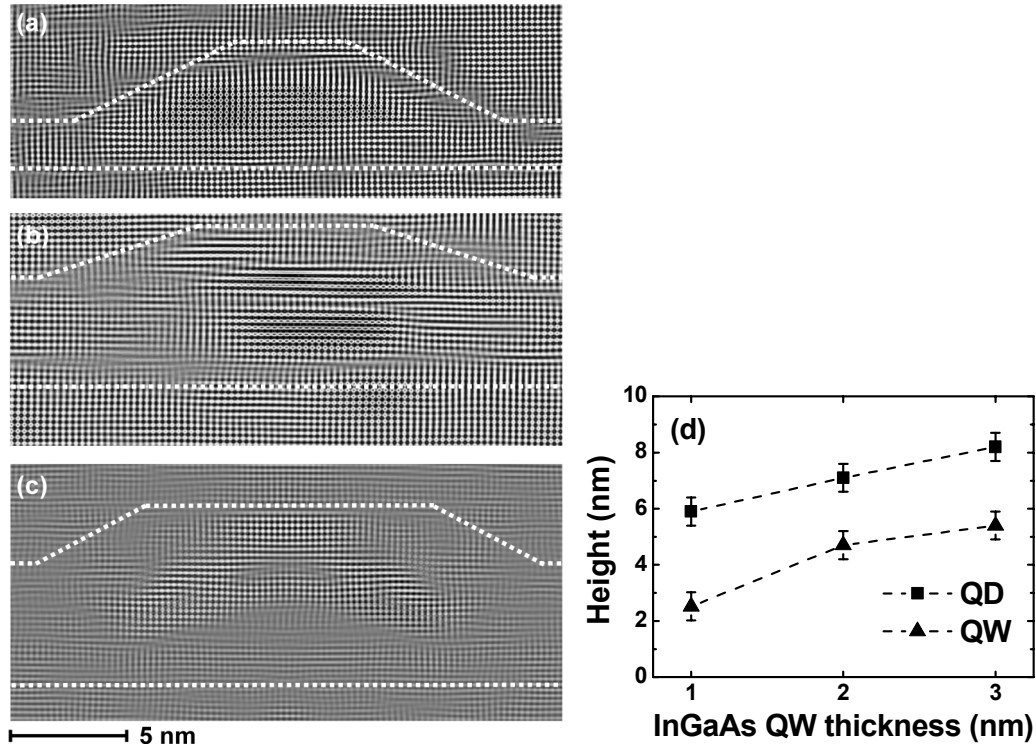


Fig. 29: (a)-(c) Fourier-filtered cross-sectional high-resolution TEM images of $\text{In}_{0.8}\text{Ga}_{0.2}\text{As}$ QDs covered with (a) 1 nm, (b) 2 nm, and (c) 3 nm $\text{In}_{0.25}\text{Ga}_{0.75}\text{As}$. The dotted white lines depict the boundary between InGaAs and GaAs. The boundaries were determined after the reversal of the In-As and Ga-As image contrast, occurring at an indium fraction of about 15 %. (d) Heights of the QDs and the QW near the QD bases. A generous error of 1 nm is assumed for each value, taking uncertainties of the determination of the InGaAs/GaAs boundary into account.

to that of unstrained GaAs¹⁷⁷. Fig. 30 (c) shows the complete GaAs-capped structure.

As suggested by the TEM images of Fig. 29, the In-enriched material grows both on top and on the facets of the QDs. It is likely that the In-Ga phase separation along the QD facets is stronger at the upper part of the QDs, close to the plateau. It is known from strain calculations¹⁷⁸ that the strain of uncapped pyramidal InAs QDs is minimum at the pyramid tip. This means that at the QD bases, the local lattice constant is equal to that of GaAs and increases towards the apex of the island, approaching the lattice constant of unstrained InAs. The strain situation of truncated-pyramid islands is qualitatively the same; compositionally homogeneous truncated InGaAs pyramids should have the largest lattice constant on their plateaus. Therefore, the upper part of such an island is most attractive for In attachment. The increase of the alloy separation efficiency is reflected by the cuneiform shape of the dark-grey shaded region at the QD facets in Fig. 30 (b)

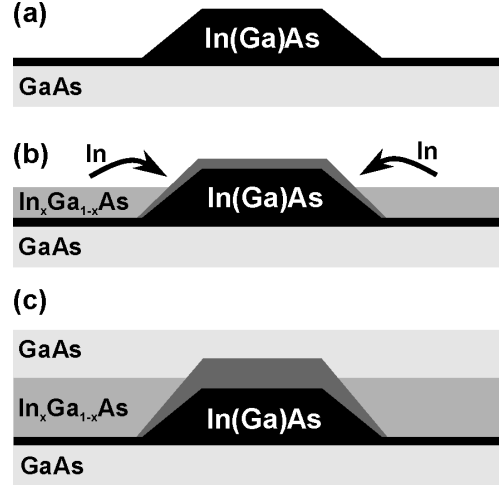


Fig. 30: Schematic diagrams illustrating the separation of a ternary InGaAs alloy into indium-rich and gallium-rich phases, activated by the strain-relaxed surface of an underlying In(Ga)As stressor QD. (a) Initial In(Ga)As stressor QD, assumed to have the shape of a truncated pyramid. (b) Partial decomposition of the InGaAs alloy into indium-rich and gallium-rich regions. (c) Final structure, buried by GaAs.

and (c), depicting In-enriched InGaAs stemming from the overgrown QW. The slowly increasing base widths of the overgrown QD structures (cf. Fig. 29) can be explained by a *reduced* phase-separation efficiency at the QD bases.

In addition to the stressor-induced separation of the InGaAs QW into In-rich and In-depleted regions, a net material transport from the QW to the QDs can be observed, so that for all thicknesses of the overgrown QW, the QD plateaus significantly loom over the QW/WL compound. The strength of net material transport is likely to depend on the In fraction of the overgrown QW. For an indium fraction of only 15 %, the effect has been shown to be negligible: Fig. 31 shows a cross-sectional dark-field TEM image of InAs QDs formed upon MBE of 2 ML InAs at 485°C. These QDs were subsequently overgrown with 5 nm In_{0.15}Ga_{0.85}As and eventually capped with GaAs. The three dark regions in the QW are strain contrasts due to the QDs. The image shows a significant increase of the effective QD height from usually 4-5 nm for GaAs-capped dots to about 10 nm. However, the QDs do not loom over the compound of WL and overgrown InGaAs QW. The room-temperature emission wavelength of this QD structure is 1.3 μm .

The QD increase of the effective height of the MBE-grown InAs QDs capped with In_{0.15}Ga_{0.85}As is analogous to the MOCVD-grown sample where the indium fraction of the QW was 25 %. However, the interface between QD structure and subsequent GaAs cap is not as smooth as for the MBE QDs (Fig. 31). A net material transport in the MBE-grown sample

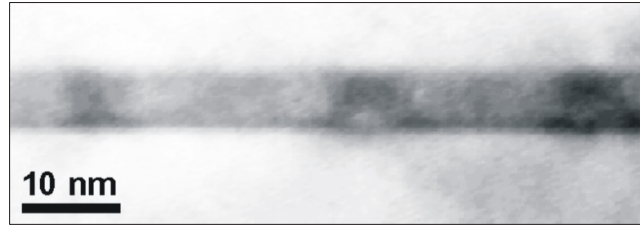


Fig. 31: Cross-sectional dark-field TEM image of QDs formed upon MBE of 2 ML InAs at 485°C, overgrown with 5 nm $\text{In}_{0.15}\text{Ga}_{0.85}\text{As}$. From Ref. 169.

can therefore be excluded. In the limit of *binary* InAs used for overgrowth of InAs QDs, the QW material *entirely* attaches at the stressors, as has been demonstrated in MBE¹⁴⁰.

Quantitative statements about the indium distribution inside QDs and WL cannot be made from the TEM images of Fig. 29. The enhanced image contrast inside the QD only suggests that the indium fraction is larger in the center of the QD than in the QW region, as one expects due to the large difference between the nominal In fraction of 80 % for the QDs and 25 % for the InGaAs QW. This is also consistent with Fig. 31.

Cross-sectional scanning tunneling microscopy (XSTM) was used to obtain quantitative information on the In distribution of $\text{In}_{0.8}\text{Ga}_{0.2}\text{As}$ QDs overgrown with 3 nm $\text{In}_{0.1}\text{Ga}_{0.9}\text{As}$ ¹⁷⁹. XSTM is a method to obtain direct structural and chemical information of buried QDs¹⁸⁰⁻¹⁸³. Fig. 32 shows an empty-state XSTM image of a QD representative for the dots of the ensemble, taken at a bias voltage of $V_S = +2.1$ V. For zinc-blende type III-V semiconductors, it has been shown that at positive sample bias voltages V_S , the empty states of the group-III atoms are imaged^{184, 185}. Fig. 32 shows such an XSTM image. The height of the QD amounts to 5 nm and the width to about 16 nm. The image contrast is partly an In-Ga selective chemical contrast. Strain relaxation out of the cleavage plane, however, also contributes to the image contrast. In order to separate the chemical and topographic contrast and to determine the local In concentration quantitatively, the lateral distances between neighboring zigzag chains is evaluated¹⁸⁶. A maximum In concentration of 60 % inside the QD is concluded. The data from strained InGaAs QWs were used to gauge the In concentration. Since QDs are stronger strained than QWs, however, the maximum In concentration is assumed to be higher. This is consistent with the nominal In concentration of 80 %.

Evaluation of the atom chains in the center of the dot (Fig. 32 (a)) shows that the center of weight of the In distribution is located at the upper part of the QD, close to the truncated-pyramid plateau. According to the schematic of Fig. 30 (c), however, a maximum of the In distribution is rather expected

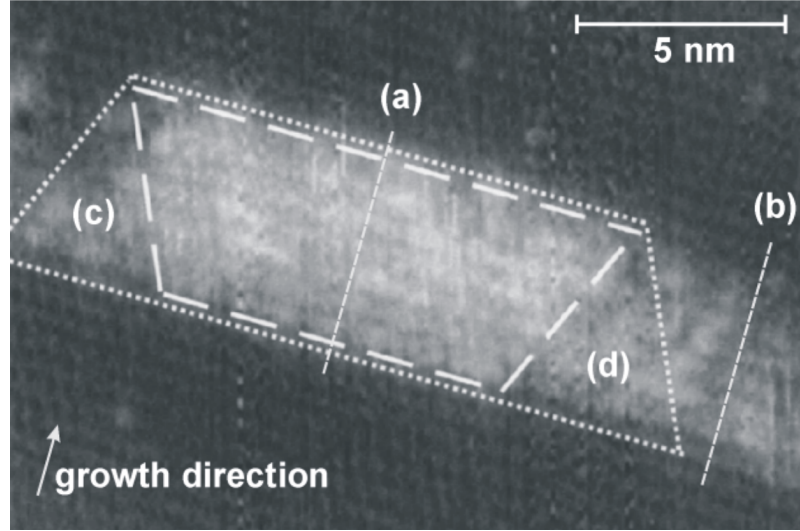


Fig. 32: Empty-state XSTM image taken at $V_S = +2.1$ V. The contours of the dot are indicated by dotted lines, and those of its In-rich zone by dashed lines. The In distribution was evaluated along the intersection lines (a) and (b) by evaluation of atom-chain distances (cf. text). After Lenz et al.¹⁷⁹.

to be located in the *lower* region of the QD. It is conceivable that during overgrowth of the $\text{In}_{0.8}\text{Ga}_{0.2}\text{As}$ QDs, kinetic effects lead to a redistribution of In and to an In segregation to the upper part of the QDs^{173, 187}. An analysis¹⁷⁹ of the indium distribution of the 4 nm thick InGaAs compound layer (Fig. 32 (b)) reveals that the weight of the In distribution is located at the bottom of the structure, close to the lower GaAs/InGaAs interface. The In fraction starts at 40 % and decreases linearly to about 15 %. From In segregation effects as observed for InGaAs QWs, the opposite behavior is expected^{188, 189}. This inverse behavior is ascribed to the decomposition of the ternary InGaAs alloy of the overgrown QW where In atoms are attracted by the QD stressors, leaving a Ga-rich phase.

The reverse truncated cone shape of the In-rich QD center is the most remarkable feature of Fig. 32. XSTM studies of InAs QDs and InGaAs QDs capped with GaAs have also revealed inhomogeneous In composition profiles^{186, 190-192}. An inverse-pyramid shaped indium distribution inside MBE-grown $\text{In}_{0.5}\text{Ga}_{0.5}\text{As}$ QDs is reported in Ref. 193. It is surprising that a similar result is obtained for QDs overgrown with a rather thick InGaAs QW of only 10 % indium fraction. It is conceivable that an initially truncated-pyramid-shaped InGaAs QD was transformed to the inverted truncated-pyramid shape as in Fig. 32 by indium depletion near the baselines of the initial dot. In that case, the depleted region would correspond to the triangular areas (c) and (d) in Fig. 32. Refs. 194 and 195 report models of the electronic structure of such inverted pyramid QDs. An inverted electron-hole alignment is found with respect to a pyramidal QD.

To conclude, overgrowing In(Ga)As QDs with Ga-rich InGaAs QWs enables to redshift the QD emission wavelength to more than 1.3 μm at room temperature. Calculations show that renormalization of the band gap inside the stressor QDs by strain redistribution via the overgrown InGaAs can account for this redshift. Structural analyses using cross-sectional TEM and STM images reveal that alloy phase separation of the overgrown QW as well as segregation of the indium *within* the QDs takes place, leading to an inverse truncated pyramid structure of the indium-rich QD core. From comparison with other growth experiments, the strength of this material redistribution effects is assumed to increase with the indium composition of the overgrown QW. The decrease of the luminescence efficiency upon overgrowth with InGaAs requires defect reduction (cf. sect. 5.1) to obtain device-quality 1.3 μm QD structures. Lasing from InGaAs QDs overgrown with a Ga-rich InGaAs QW at 1.24 μm is reported in sect. 6.1.3.

5.3.2 Advantage of TBAs for redshifting the QD emission wavelength

It was shown in sect. 5.2 that due to the different decomposition mechanisms of TBAs with respect to AsH_3 , the QD formation using TBAs as arsenic precursor leads to different dependences on the growth parameters. Optical in-situ investigations on the formation of InAs QDs have shown¹⁴¹ that the danger of dislocation formation is enhanced for AsH_3 , probably due to a larger number of hydrogen radicals.

The properties of QD ensembles as a function of the V/III ratio were investigated using PL. Fig. 33 shows room-temperature PL measurement for two sample series. The samples in (a) were grown using AsH_3 ¹⁴²; the samples in (b) were deposited using TBAs as arsenic precursor. From the dependence of the PL spectra on increasing V/III ratio, it can be concluded that increasing AsH_3 partial pressure leads to a bimodal size distribution. Whereas the crystal quality for V/III = 40 is worst due to a lack of As species on the surface, and probably no QDs were formed, the spectrum for V/III = 80 is dominated by small QDs emitting around 1200 nm. With further increased V/III ratio, QDs with a larger size are created, so-called high QDs¹⁴², emitting around 1300 nm. The formation of such QDs is accompanied by large dislocated clusters as one can see on plan-view TEM images not shown here. The QDs grown using TBAs show a mono-dispersed size distribution for all V/III ratios. One is tempted to argue that all TBAs/III ratios are lower than the AsH_3 /III ratios and that, if the same V/III ratios were used in both cases, the same results would be obtained. At typical QD deposition temperatures of 500°C, however, the cracking efficiencies of the two precursors strongly (cf. Fig. 7 and Ref. 77). Moreover, the PL excitation densities are different. Whereas a rather high excitation density was used to

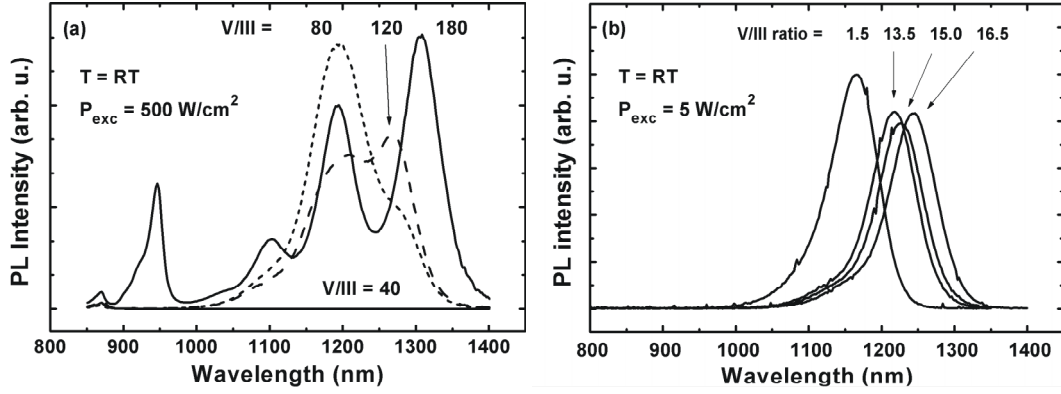


Fig. 33: Room-temperature PL spectra of InGaAs QDs grown with (a) AsH₃ (from Ref. 142) and (b) TBAs, deposited around 500°C. The respective V/III ratios are marked in the viewgraphs.

excite the AsH₃-grown samples, the TBAs-grown QD structures were excited at a much lower level. Spectra obtained from the TBAs-grown QDs with higher excitation density, however, do not show the formation of a second QD size.

Using TBAs, the V/III ratio can thus be tuned within one order of magnitude without changing the unimodal character of the size distribution. The formation of a second size mode using AsH₃ has also been observed when the temperature is raised¹⁴². A temperature increase apparently has the same effect as the increase of the AsH₃/III ratio. Using TBAs, the QD size increase is attributed to a decrease of the surface energy. This results in an increase of the QD size due to thermodynamic arguments¹¹⁹. No dislocated clusters were observed on TEM images of QD sheets grown with TBAs/III = 16.5. These findings are promising for low defect densities of 1.3 μ m QD structures grown using alternative-precursor MOCVD.

5.3.3 Wavelength shifting using nitrogen

Dilute nitrides such as Ga(In)AsN attract growing interest since they exhibit much smaller band gaps than N-free Ga(In)As alloys, even for N fractions of only a few percents. Self-organized GaInAsN QDs could therefore have longer emission wavelengths than InGaAs QDs. Ga(In)AsN/GaAs QWs emitting around 1.3 μ m are currently attractive for telecom lasers since the incorporation of N strongly reduces the lattice constant with respect to N-free Ga(In)As^{164, 165} so that low-band-gap InGaAsN layers lattice-matched to GaAs can be grown¹⁹⁶. High-quality InGaAsN/GaAs QWs are used as active layers in low-threshold 1.3 μ m lasers in both edge-emitting^{197, 198} and vertically emitting geometry¹⁹⁹. Fig. 34 shows a flow chart of different approaches to achieve QD emission at 1.3 μ m and beyond

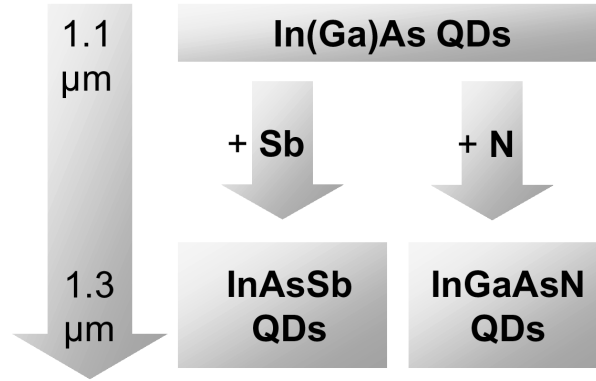


Fig. 34: Flow chart of different approaches to achieve QD emission at 1.3 μm by addition of antimony and nitrogen to In(Ga)As QDs or InGaAs QWs.

using nitrogen (and also antimony) insertions in In(Ga)As QDs that initially emit around 1.1 μm . Structures as shown in Fig. 34 were grown and characterized; the experiments carried out using antimony are described in sect. 5.3.4.

If two binary III-V materials AB and AC are mixed, the band gap of the alloy $\text{AB}_{1-x}\text{C}_x$ follows the formula^{200, 201}

$$E_{\text{gap}}(x) = (1-x) \cdot E_{\text{gap}}^{\text{AB}} + x \cdot E_{\text{gap}}^{\text{AC}} - b \cdot x \cdot (1-x) \quad (5.1)$$

where b is the so-called *bowing parameter*^{ix}. In case b is small, the composition dependence of the band gap can be approximated by linear interpolation between $E_{\text{gap}}^{\text{AB}}$ and $E_{\text{gap}}^{\text{AC}}$. For larger bowing parameters, the composition dependence of the band gap follows a parabola. The band gaps of $\text{GaAs}_{1-y}\text{N}_y$ and $\text{In}_{0.47}\text{Ga}_{0.53}\text{As}_{1-y}\text{N}_y$ as functions of the lattice parameter are depicted in Fig. 35. A recent publication reports a bowing parameter of 40 eV for $\text{GaAs}_x\text{N}_{1-x}$. The bowing parameters of nitrogen-free III-V compound semiconductors is much smaller ($\text{In}_x\text{Ga}_{1-x}\text{As}$ ²⁰²: $b_{\Gamma} = 0.32\text{-}0.6$ eV; $\text{Al}_x\text{Ga}_{1-x}\text{As}$ ²⁰²: $b_{\Gamma} = 0.14$ to 0.66 eV).

The large bowing parameter of dilute nitrides is ascribed to microscopic interactions of the nitrogen atoms with the matrix. It has been shown that doping of conventional group III-V semiconductors with low, impurity-like concentrations of nitrogen introduces highly localized acceptor levels²⁰³. Although a reduction of the band gap by more than 100 meV per atomic percentage was observed in InGaNs alloys, the electronic band structure of the host crystal is actually not affected by such low nitrogen concentrations, owing to the highly localized nature of the nitrogen perturbations.

^{ix} The formula actually applies only to ternary alloys. It is applicable to InGaAsN if $A = \text{In}_y\text{Ga}_{1-y}$, $B = \text{As}$, and $C = \text{N}$ are chosen.

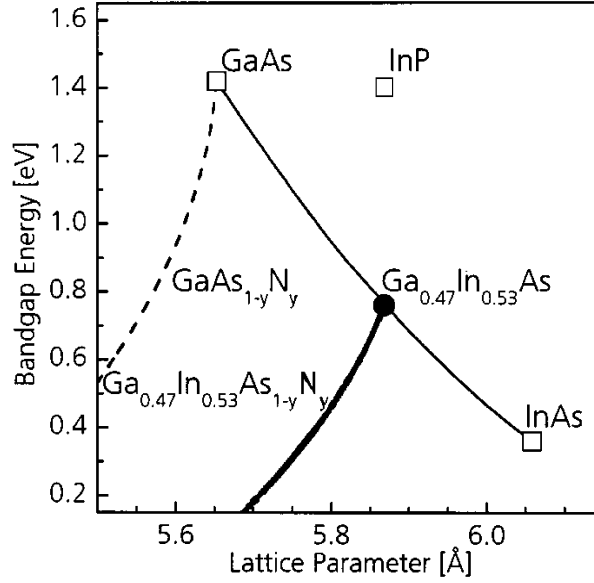


Fig. 35: Band gap energy versus lattice parameter of GaAsN, InGaAs, and $\text{In}_{0.53}\text{Ga}_{0.47}\text{As}_{1-y}\text{N}_y$. From Ref. 205.

The band gap decrease is rather attributed to a strong interaction between the conduction band and a narrow resonant band formed by the nitrogen states. This results in a splitting of the conduction band and thus to an effective reduction of the fundamental band gap²⁰⁴.

The principal difficulty about growing N-containing alloys is that the small covalent radius of N implies extremely low solubilities, leading to large mixing enthalpies ΔH . The free energy F of an alloy with composition x and temperature T is given by

$$F(x, T) = \Delta H(x) - T \cdot S(x) \quad (5.2)$$

where S is the configuration entropy. $F(x)$ is plotted for a hypothetical semiconductor alloy at fixed temperature in Fig. 36 (a). It exhibits a composition range with a large upward bowing. In this region, the second derivative of F is below zero. If a hypothetical alloy of composition x_a is assumed, the system can reduce its free energy by Δ_1 if this alloy decomposes into two phases b and c. x_b and x_c are interdependent since due to mass conservation, the average composition must be constant. The phase separation will continue until it stops to be energetically favorable. Points C and D are the deflection points of F ($\partial^2 F / \partial x^2 = 0$) and are called *spinodal* points. Alloys with x between the spinodal points are unstable; this composition range is called *miscibility gap*. Outside the miscibility gap, $\partial^2 F / \partial x^2$ is positive. A spontaneous alloy phase separation will not occur outside the miscibility gap since F would then increase: If alloy d decomposes into phases e and f, for example, F would increase by Δ_2 . Alloys outside the miscibility gap are

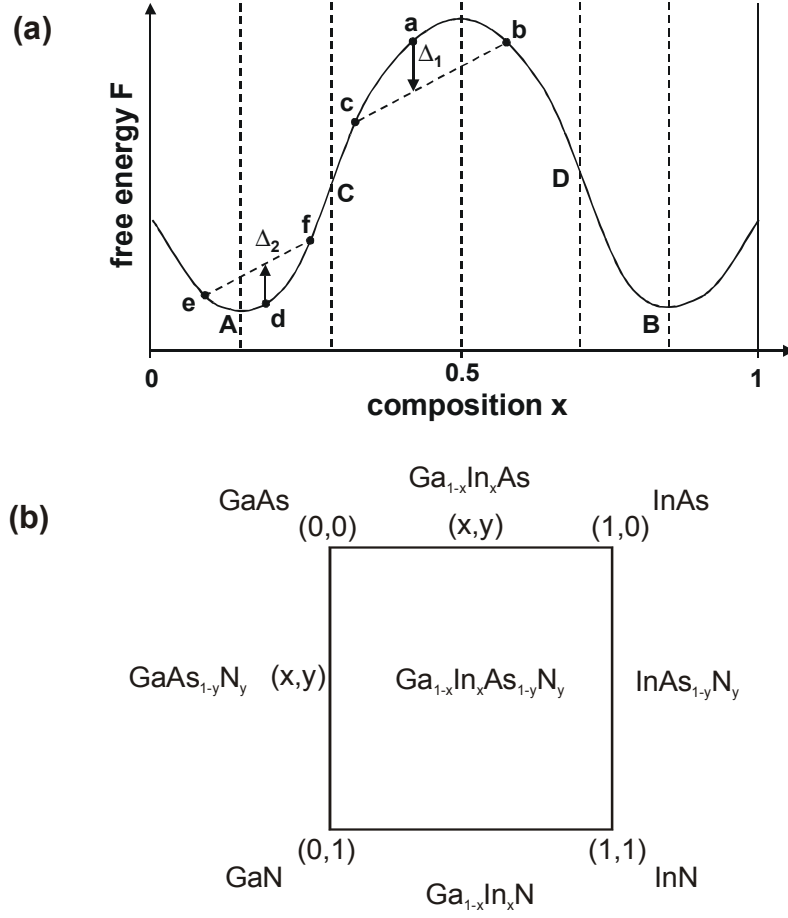


Fig. 36: (a) Free energy F versus solid composition for a hypothetical semiconductor alloy with a large positive mixing enthalpy H . The points labelled A and B are the *binodal* points, the inflection points C and D are the *spinodal* points. The miscibility gap is the composition range between x_C and x_D . (b) The fabrication of $\text{In}_x\text{Ga}_{1-x}\text{As}_y\text{N}_{1-y}$ can be achieved by separately mixing Ga and In on the group-III sublattice with parameter x , and As and N on the group-V sublattice with parameter y .

stable even if they do not coincide with the binodal points A and B, which are the two local minima of F . The growth of quaternary InGaAsN can be understood as a combined alloying of In and Ga on the group-III sublattice, and of As and N on the group-V sublattice, as depicted schematically in Fig. 36 (b).

With increasing temperature, the miscibility gap shrinks due to the entropy contribution to the free energy (Eq. 5.2), and vanishes above a critical temperature T_c . All III-V compound semiconductors have positive mixing enthalpies, so any III-V semiconductor is thermodynamically unstable at $T = 0$. If $\Delta H(x)$ is sufficiently small for a given pair of semiconductor materials to be mixed, however, the critical temperature T_c is below the growth temperature range, and any composition x is stable. Miscibility can – in

principle - be overcome by raising the growth temperature to beyond T_c . However, this would require extremely high growth temperatures. Instead, particularly low growth temperatures are commonly chosen to grow dilute nitrides, allowing to kinetically freeze alloys with thermodynamically unstable compositions.

The high indium fraction of the $\text{In}_{0.8}\text{Ga}_{0.2}\text{As}$ QDs makes the nitrogen incorporation very difficult. For ternary GaAsN, a maximum N fraction of 6.7 % was reached²⁰⁶. The maximum N fractions reported for InGaAsN QWs are much lower: InGaAsN QW emitting at 1.3 μm usually have indium contents around 40 % and N fractions of typically 1 %¹⁴². However, the minimum indium fraction needed for the growth of InGaAs QDs in the SK mode is 40 %¹⁴². Upon N incorporation, this fraction must even be higher since N incorporation leads to a decrease of the lattice constant, counteracting the driving force for SK growth of QDs. Due to the high indium fraction, arsenic is more easily incorporated than N. This means that the N/As ratio must be very high in the gas phase. To avoid As vacancies, however, the partial pressure of reactive As species must not fall below a certain value. To achieve large N/As ratios at the same time, huge flows of DMHy have to be provided. To reduce the effect of the miscibility gap, low temperatures and high growth rates are used for the growth experiments as described in the following. Low temperatures reduce the adatom mobility and large growth rates shorten the available time for decomposition and diffusion processes.

5.3.3.1 Simultaneous deposition of As, Ga, In and N

The first experiments to fabricate InGaAsN QDs aimed at the simultaneous deposition of the four constituting elements In, Ga, As, and N. For these experiments, an InGaAs QD sample was used as reference and starting point. In order to obtain InGaAsN QDs, the same growth parameters as for the reference sample were used. All samples of this series were grown at 500°C with a nominal growth rate of 1 $\mu\text{m}/\text{h}$. The TBAs/III ratio was constantly 1.5. The reference sample exhibits a QD density of $2.2 \times 10^{10} \text{ cm}^{-2}$ and a QD ground-state PL at 1208 nm at room temperature. The TMIn/TMGa ratio was 2.5, corresponding to an In fraction of 70-80 % in the InGaAs reference sample. During the deposition of the InGaAs QD material, however, different flows of DMHy were added to the gas phase. The $p_{\text{DMHy}}/p_{\text{TBAs}}$ ratio was varied from 0 to 360, larger DMHy flows were not supported by the DMHy bubbler for technical reasons. After the deposition of InGaAsN, a GRI of 60 s was performed during which all precursors were switched off.

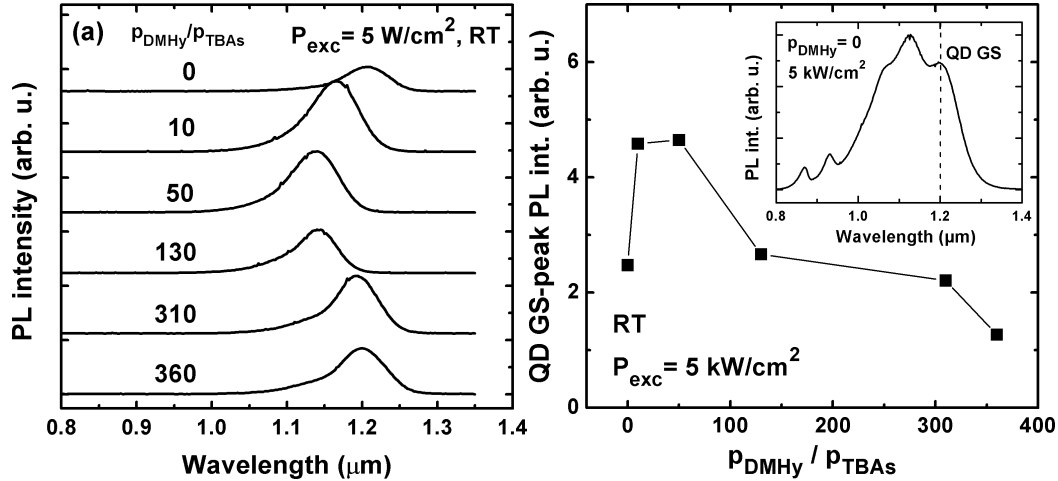


Fig. 37: (a) Room-temperature low-excitation spectra of undoped samples with single InGaAsN QD sheets. (b) PL peak intensities of the QD ground-state (GS) PL, plotted as a function of $p_{\text{DMHy}}/p_{\text{TBAs}}$. A power density of 5 kW/cm^2 was used for excitation. The inset shows the spectra belonging to the first data point at $p_{\text{DMHy}}/p_{\text{TBAs}} = 0$.

Fig. 37 (a) shows low-excitation PL spectra of the sample series, recorded at room temperature. Fig. 37 (b) shows the peak intensities of the QD ground-state transitions. PL spectra obtained under a very high excitation power density of 5 kW/cm^2 (not shown here) were used for this evaluation. The high excitation power leads to a complete saturation of the QD ground-state PL. The peak intensities then scale with the QD density and can thus be used for relative estimation of the latter.

The topmost curve shows the PL of the reference sample. The position of the peak is at 1208 nm, the FWHM is 63 meV. If DMHy is now switched on and successively increased during the deposition of the InGaAs, a blueshift of the PL peak by 86 nm can be observed up to a $p_{\text{DMHy}}/p_{\text{TBAs}}$ ratio of 50. This blueshift is accompanied by a significant increase of the low-excitation PL (a), and also by a strong increase of the QD density, possibly by a factor of two, as suggested by Fig. 37 (b). The presence of DMHy in this range apparently leads to the formation of a much larger density of QDs that are smaller than those of the reference sample. With further increasing $p_{\text{DMHy}}/p_{\text{TBAs}}$, a redshift of the PL peak sets in, the PL intensity is reduced and the QD density drops. A plan-view TEM image of the sample grown with $\text{DMHy/TBAs}=360$ shows a QD density of $4.9 \times 10^9 \text{ cm}^{-2}$ which is by a factor of 4.5 lower than that of the reference sample.

The following explanations can be given for these effects:

- As described in sect. 4.5, the QD density is strongly determined by kinetic effects. It is conceivable that the presence of DMHy reduces

the surface mobility so that a larger number of nuclei are formed. The smaller QD size can then be explained with mass conservation.

- Using thermodynamic arguments, the reduced QD size could also be explained by an increase of the surface energy¹¹⁹, leading to a smaller equilibrium size. In this case, N would act as anti-surfactant.

A reduction of the QD size and an increase of the QD density upon N supply has also been observed during chemical-beam epitaxy of InGaAsN QDs^{207, 208}: The QDs had a nominal N content of 1 %, roughly estimated using the N₂ flow rate and the growth rate, and exhibited a height / base length of 4 (30) nm as compared to a height (base) length of 6 (45) nm of the reference sample. An increase of the QD density by a factor of 3 was measured. Upon a further increase of the N₂ flow, the QD size increased again and the QD density dropped.

The only publication of InGaAsN QDs grown using MBE reports a lower QD density if nitrogen is switched on. The QDs are reported to keep their height if N is supplied²⁰⁹. The emission wavelength, however, increased immediately and could be extended to 1.52 μm . The PL intensity decreased strongly during the redshift. The In fraction of the QDs was 70 %, and an N fraction of 4 % is reported. This high value was not measured, but estimated from InGaAsN QWs deposited under similar growth conditions.

Alternatively to the use of InGaAs QDs as starting point to grow InGaAsN as described in this section, compressively strained long-wavelength emitting InGaAsN QWs could be grown and used for QD self-organization. Upon deposition of a supercritical thickness of this strained material, self-assembly of SK dots *may* set in. As mentioned earlier, the approach is problematic with regard to the strain situation of InGaAsN: InGaAsN QWs emitting at 1.3 μm usually have a maximum indium fraction of around 40 %. For larger In fractions, the N incorporation efficiency is most likely not large enough to achieve this wavelength. It is known from the growth of SK QDs, however, that at least 40 % of indium are required to obtain SK QDs (cf. p. 63 of Ref. 142).

5.3.3.2 Nitridation

As an alternative to the simultaneous deposition of all four elements, ternary InGaAs QDs were grown with a subsequently performed N/As exchange reaction. Ternary InGaAs QDs are fabricated by deposition of a supercritically thick InGaAs QW and a subsequent GRI of 1 min without TBAs stabilization. Different DMHy flows were now applied during the GRI. Fig. 38 shows PL spectra of such InGaAsN-QD test structures for

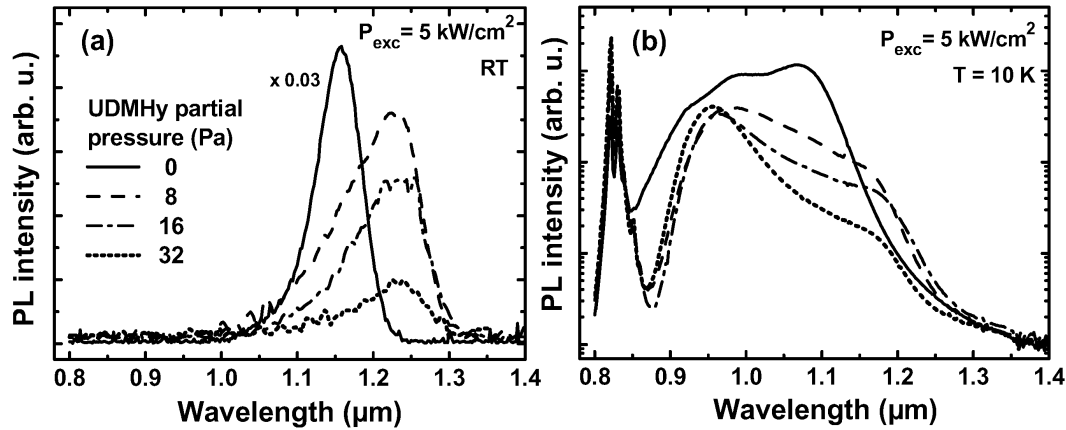


Fig. 38: PL spectra of InGaAsN QD samples. The InGaAs QD samples were nitrified by adjusting the denoted DMHy partial pressures in the reactor chamber during a GRI of 1 min after deposition of the InGaAs QD material. (a) Low-excitation room-temperature PL spectra. The spectra of the nitrified samples are smoothed. (b) High-excitation low-temperature spectra of the same samples, logarithmically plotted.

which different DMHy partial pressures were used. Fig. 38 (a) shows that a partial pressure of 8 Pa DMHy during the GRI leads to a wavelength shift from 1150 nm (InGaAs QDs) to 1226 nm (InGaAsN QDs). This shift is larger than the maximum redshift achieved by simultaneous deposition of quaternary InGaAsN (cf. sect. 5.3.3.1).

The most noticeable feature of the PL spectra of Fig. 38 (a) is the tremendous loss of PL intensity associated with the supply of DMHy. This phenomenon is known for both GaAsN²¹⁰ and InGaAsN^{211, 212} QWs. It is attributed to the deterioration of the crystal quality due to the small size and the high reactivity of atomic nitrogen. Fig. 38 (b) shows a strong decrease of the QD ground-state PL peak intensity, indicating also a decrease of the QD density. The PL intensity can be improved by post-growth annealing treatments that partially eliminate the N-induced crystal defects in both InGaAsN^{213, 214} and GaAsN²¹⁰ layers. Annealing was not applied to the present samples in order to maintain the comparability to ternary InGaAs QDs. In view of the large intensity loss observed for the InGaAsN QDs obtained via As/N exchange reaction, it is remarkable that the PL intensity of simultaneously deposited QDs as described in sect. 5.3.3.1 hardly decreases. Although the method of simultaneous deposition is not as effective with respect to the extension of the emission wavelength, the crystalline quality is almost maintained.

5.3.4 Wavelength shifting using antimony

Experiments were conducted to grow long-wavelength QDs by reducing the band gap of InAs QDs via Sb insertions. The growth of InAsSb QDs via Sb supply during the deposition of InAs QDs was explored. The investigations were carried out similarly to the experiments on N incorporation into InGaAs QDs, as described in the previous section. Undoped test structures containing single InAs(Sb) QD sheets were grown and investigated using PL, PL-excitation spectroscopy (PLE) and high-resolution TEM.

The impact of Sb supply during deposition and/or GRI on the structural and optical properties of the QDs was investigated on the basis of two sample series. For the samples of the first series (sect. 5.3.4.1), In, As and Sb were supplied simultaneously. Then a GRI after deposition of the QD material was applied to allow QD formation. These samples are compared to an analogous series of InAs QD reference samples. In the second sample series (sect. 5.3.4.2), pure InAs QDs were deposited. Different TESb flows were supplied during a GRI after deposition of the InAs QDs.

5.3.4.1 Deposition amount

A series of samples with InAsSb layers with thicknesses between 1.6 and 2.0 ML was grown at 485°C. The TBAs/III ratio was kept at 1.5, the TESb / (TBAs+TESb) ratio was 0.3. The QD material was deposited at a growth rate of 0.4 ML/s. The TESb flow of 4.4 $\mu\text{mol/min}$ supplied during QD deposition was also kept during the GRI of 5 s. PL spectra of these samples are compared to a reference series of InAs QDs in Fig. 39.

The deposition amount of the InAs QD samples was varied between 1.5 and 2.1 ML. In the case of binary InAs, the critical layer thickness is between 1.5 and 1.7 ML as one can see in Fig. 39 (a). This agrees well with published values^{132, 215}. The wavelength right above the critical layer thickness is 1.12 μm and shifts to almost 1.2 μm with increasing deposition amount. For the sample with 2.1 ML InAs, a low energy shoulder emerges at about 1.27 μm . This shoulder is ascribed to large coherent QDs occurring in a low density, suggesting the formation of a bimodal size distribution. The maximum PL signal comes from the sample with 1.8 ML, most likely due to a high density of coherent InAs QDs and a low density of defects. For larger deposition amounts, the signal decreases, most likely due to an increase of the defect density. Disregarding the low-energy shoulder of the 2.1 ML sample, the emission wavelength of InAs could not be extended to beyond 1.2 μm at room temperature. At 485°C, the maximum emission wavelength of InAs QDs is widely unaffected by a variation of the V/III ratio.

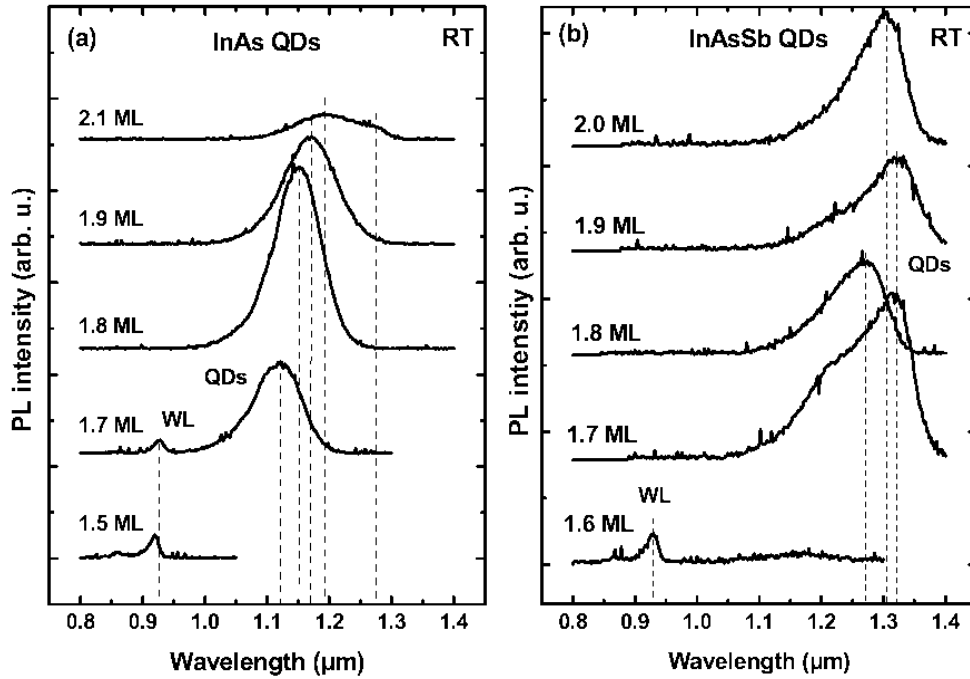


Fig. 39: Room-temperature PL spectra of (a) InAs QDs and (b) InAsSb QD sheets. In both cases, the deposition amount was varied over the same range. Both InAs and InAsSb QDs were grown at $T_{\text{gr}} = 485^\circ\text{C}$. A GRI of 5 s was introduced after deposition of the QD material to allow QD formation. The InAsSb QDs were deposited with an additional TESb flow of $4.4 \mu\text{mol/min}$ during deposition and the subsequent GRI. The excitation power density was 5 W/cm^2 .

The QD sample series with TESb supply during deposition and GRI shows a 2D-3D transition between 1.6 and 1.7 ML, i.e. in the same regime as for the InAs QDs. The behavior of the PL emission lines with increasing deposition amount is completely different as compared to the binary InAs QDs, as one can see in Fig. 39 (b). After the onset of the 2D-3D transition, the emission wavelength immediately shifts to values around $1.3 \mu\text{m}$ and beyond. The PL signal does not decrease as in the case of the InAs samples. However, the average peak intensity of the InAsSb samples is by a factor of 4 lower than for the InAs QDs. The QD density in the sample with 1.7 ML is probably very low, leading to a saturation of the QD ground-state transition and to a contribution of the first excited state, leading to the shoulder on the high-energy side. The peak emission wavelength oscillates around $1.3 \mu\text{m}$. This behavior suggests a minor reproducibility within the series.

It can be concluded from the comparison of Fig. 39 (a) and (b) that the critical layer thicknesses for both InAs and InAsSb layers are comparable. This means that the strain in both materials is similar, so that the fraction of incorporated Sb is likely to be very low. For this reason, it is all the more remarkable that the emission wavelength is strongly redshifted by about 160 meV with regard to the binary InAs QDs. In cross-sectional high-

resolution TEM images not shown here, diffraction contrast from Sb atoms could not be detected. These findings indicate that Sb incorporation cannot be the principal reason for the strong redshift. However, Sb incorporation into InAs in the range of few percents has been reported elsewhere⁷⁸. As described below, the presence of Sb mainly *accelerates* the size increase of the InAs QDs during the GRI, accounting for the longer emission wavelengths of the QDs grown with Sb supply.

5.3.4.2 TESb and TBAs during the growth interruption

Experiments to grow InAsSb QDs with TESb supplied *only* during the GRI after deposition of the QDs surprisingly revealed that a similarly strong redshift as described for the simultaneous deposition of In, As, and Sb can be obtained. A sample series of InAs QDs with constant deposition amount was grown. The InAs was again deposited at 485°C at a growth rate of 0.4 ML/s, using a TBAs/III ratio of 1.5. Various flows of TESb ranging from 2.2 to 8.8 $\mu\text{mol/min}$ were supplied during the subsequent GRI of 5 s.

Fig. 40 shows a PLE contour plot of such a QD layer, grown with a TESb flux of 8.8 $\mu\text{mol/min}$. The bold curve is a PL spectrum of the same sample (cf. also Fig. 43). Both PL and PLE spectra were recorded at 7K. The PL spectrum shows a large number of peaks. Since the QD density is in the 10^{10} cm^{-2} range as deduced from TEM images, and the excitation power is very low, the high-energy peaks are unlikely due to excited-state transitions. The PLE contour plot helps to identify the origin of this multiplet. In a PLE contour plot, both excitation and detection energies are varied. For every detection energy value, the excitation energy is varied from the detection energy to beyond the GaAs band gap energy. Vertical cuts show QD-size selective PLE spectra. Signal from excited QD states is maximum at a given detection energy if the excitation energy is resonant with the respective QD transition energy. In this case, the signal additionally scales with the *number* of QDs of which the ground-state transition matches the detection energy.

One can see on the PLE contour plot that the PLE signal originating from the first excited QD states oscillates with the detection energy. It can thus be concluded that the size distribution of QDs is multimodal. From the geometry of the experimental setup, it can be ruled out that these peaks are Fabry-Perot oscillations. The PL peak multiplet can neither be ascribed to multiphonon relaxation of localized carriers since the energetic distances between the peaks do not coherently match the GaAs LO-phonon energy of 36 meV (the energetic distances between the respective peaks as marked with numbers 1 to 6 in Fig. 40 are $\Delta E_{12} = 34 \text{ meV}$, $\Delta E_{23} = 42 \text{ meV}$, $\Delta E_{34} = 44 \text{ meV}$, $\Delta E_{45} = 44 \text{ meV}$, and $\Delta E_{56} = 34 \text{ meV}$).

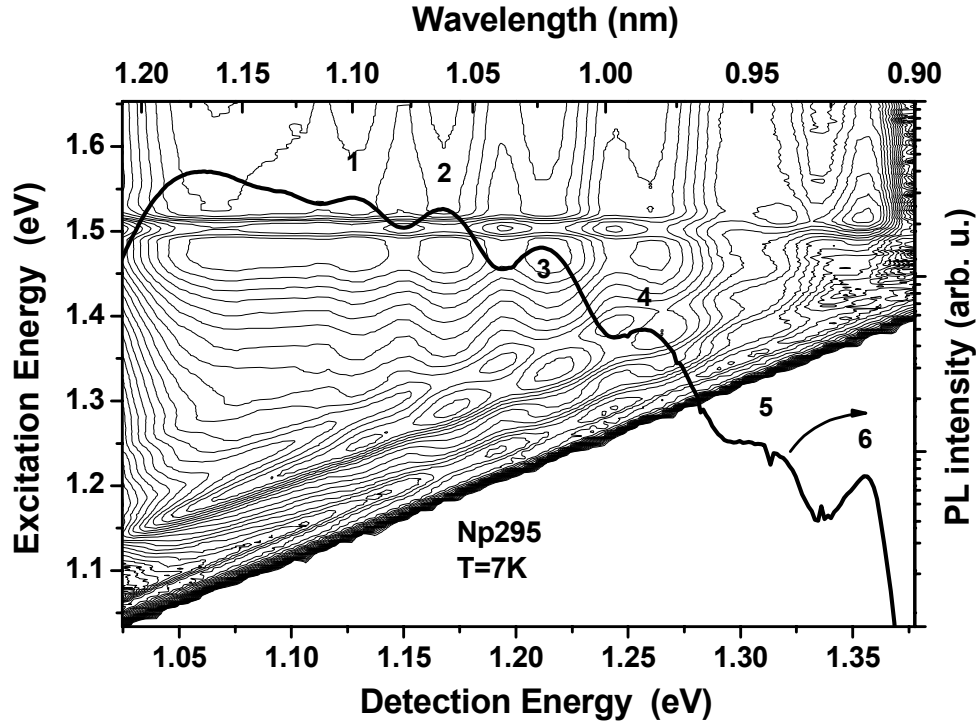


Fig. 40: Low-temperature PLE contour plot of an InAs sample with a TESb flow of $8.8 \mu\text{mol/min}$ during the GRI of 5 s, subsequent to the InAs deposition (compare to Fig. 43). PL was excited using a white-light source and a double monochromator. The excitation density is below 5 mW/cm^2 . The intensity is plotted on a logarithmic scale, the thin lines are equi-intensity lines. The bold black curve shows a PL spectrum, excited at 514.5 nm and an excitation power density of 5 W/cm^2 . The logarithmic scale of the PL intensity is given on the right. The peaks of the PL spectrum are partially numbered^x.

Fig. 41 shows a cross-sectional high-resolution TEM image of the QD structure. Flat, truncated-pyramid islands with sharp interfaces between GaAs and WL and also between island top and matrix can be identified. The white lines were drawn along the regions of group-V- / group-III-atom contrast reversal. The contrast reversal of $\text{In}_x\text{Ga}_{1-x}\text{As}$ occurs at around $x = 0.15$ as mentioned earlier. The TEM image suggests that the islands have well-defined heights of integer numbers of atomic MLs. It is likely that the discrete nature of island heights is the reason for the multiplet visible in the PL and PLE spectra of Fig. 40. The single lines of the multiplet are rather broad since the transition energies of the islands are not solely determined by the height of the QDs. The lateral carrier confinement, being a function of the QD *width*, likewise contributes to the transition energy. Since the lateral extension of the islands is large, the contribution of lateral confinement is rather weak, however.

^x PL and PLE measurements by courtesy of Florian Guffarth and Robert Heitz.

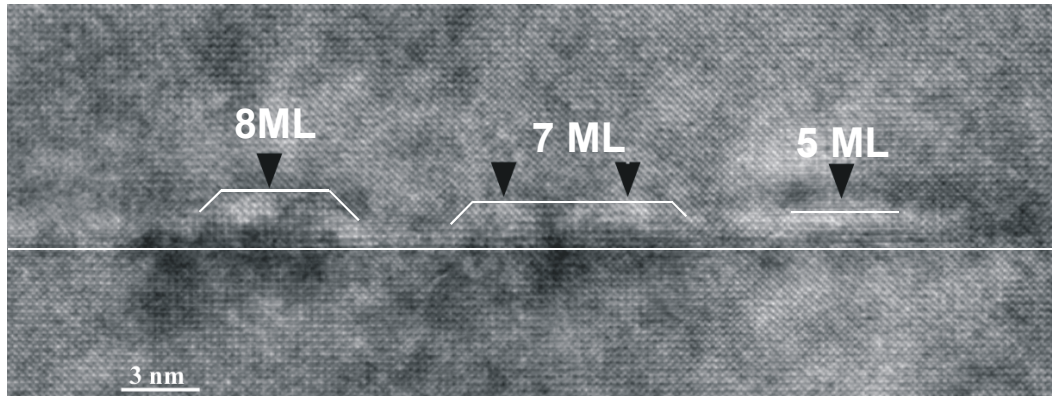


Fig. 41: High-resolution cross-section transmission micrograph of a single InAs QDs sheet grown at 500°C. A GRI of 5 s under TESb flux of 8.8 $\mu\text{mol}/\text{min}$ was performed after the deposition of the InAs. The lower InAs/GaAs interface as well as the top interfaces of the truncated-pyramidal InAs islands are depicted with thin white lines. The boundaries are determined according to the reversal of the group-III/group-V-atom contrast, occurring at an indium fraction x of about 15 % for $\text{In}_x\text{Ga}_{1-x}\text{As}$.^{xi}

An 8-band $k\cdot p$ calculation qualitatively illustrates the relation between QD height and transition energy. Fig. 42 shows QD ground-state transition energies for truncated pyramids as a function of their respective height. A constant QD base width of 13.6 nm and a facet angle of 45° were assumed for all simulated islands. It is shown that the ground-state transition energy monotonously decreases with increasing island height. The calculations further show that the energetic distance between neighbored ground-state transition energies decreases with increasing aspect ratio. A similar observation is made for the present samples, indicating that the aspect ratios of islands with lower emission energies are higher.

In the following, the dependence of the QD-layer morphology on the amount of TESb supply during the GRI is studied. In addition, the influence of TBAs during the GRI is compared to that of TESb. Fig. 43 shows low-temperature low-excitation PL spectra of InAs QD samples with varying TBAs (a) and TESb supply (b). The right curve of Fig. 43 (a) shows the PL spectra of an InAs QD sample without any precursor flow during the GRI. Supply of the same TBAs flow during the GRI as used for the deposition of InAs ($Q_{\text{TBAs}} = 20.7 \mu\text{mol}/\text{min}$) leads to a redshift of all transition energies. The multiplet structure disappears, indicating an increase of the average aspect ratio: The islands gain in height and the size distribution becomes narrower. Fig. 43 (b) shows PL spectra of InAs QD samples for which different TESb flows are supplied during the GRI. With increasing TESb flow,

^{xi} TEM image by courtesy of N.D. Zakharov and P. Werner, Max-Planck Institute of Microstructure Physics, Halle, Germany.

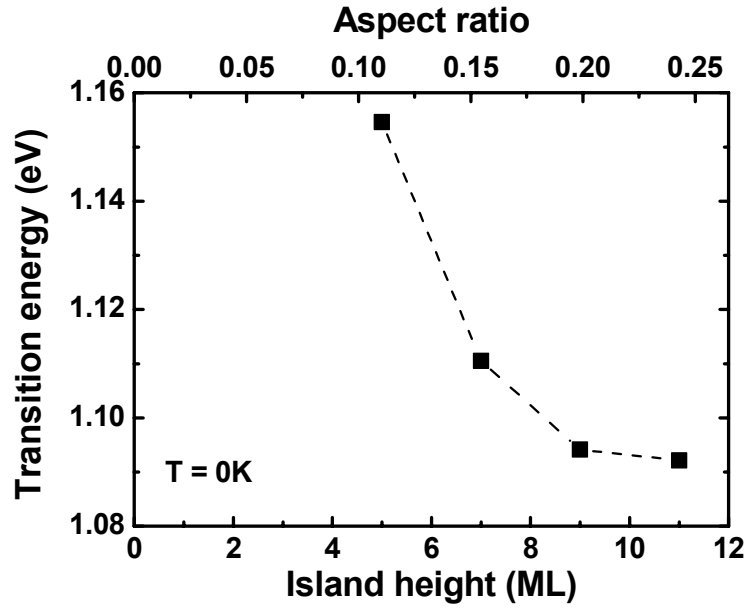


Fig. 42: Transition energies of truncated-pyramidal InAs islands as a function of island height, calculated using 8-band k - p -theory. The InAs islands have constant base length of 13.6 nm and 45° facets. With increasing island height, the shape changes from a truncated pyramid towards a complete pyramid. The aspect ratio of a complete pyramid with 45° facet angle is 0.5^{xii} .

the PL peak of the largest QDs strongly shifts to longer wavelengths. In contrast to the supply of TBAs, however, the size distribution does not become narrower. On the contrary, the ML splitting of the ground-state transitions becomes far more pronounced.

Under the influence of both TBAs and TESb, the QDs exhibit an accelerated ripening behavior, suggesting that surface diffusion of In atoms is enhanced. In addition, the size of the largest QDs of an ensemble is increased. The increase of the average QD size upon supply of group-V precursors during the GRI can also be taken as a sign of a larger equilibrium size of the QD ensemble. Thermodynamical calculations show that the equilibrium size of a QD ensemble is a function of the surface energy¹¹⁹. If the surface energy is lowered, the equilibrium size is increased. The reason for an enhanced QD size after TESb / TBAs supply can be an enhanced equilibrium QD size, suggesting that both TBAs and TESb act as surfactants and lower the surface energy. The redshift during TBAs supply is not as strong as in the TESb case but the ensemble width decreases. TESb is more effective with regard to the QD size increase of the largest QDs. The size distribution broadens, however, and the PL intensity decreases strongly, most likely due to the formation of defects.

^{xii} Calculations by Oliver Stier and Andrei Schliwa.

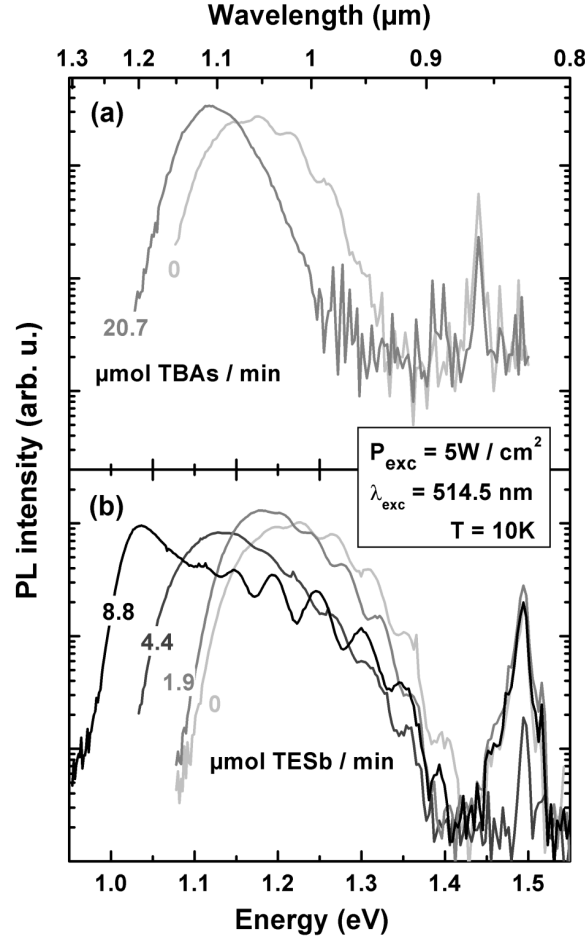


Fig. 43: Low-temperature low-excitation PL spectra of undoped test structures, each containing a single QD sheet. 1.7 ML InAs were deposited at 485°C with a V/III ratio of 1.5. During the subsequent GRI of 5s, different precursors (TBAs and TESb) were switched on. The impact of TBAs supply is shown in (a), the influence of TESb during the GRI is shown in (b). The rightmost curves in (a) and (b) are reference InAs samples, grown without any precursor flow during the GRI. They are slightly different in (a) and (b) since they stem from different growth series. The nominal deposition parameters are the same, however.

From the above findings, it can be concluded that the strong redshift of InAs QDs upon supply of Sb in the GRI is rather due to a size increase than due to a change of the band gap of the QD material, related to Sb insertions. Supply of TESb during the GRI causes a pronounced redshift of the QD PL, but the size distribution of the islands and thus the spectral width of the ground-state transition PL strongly increases. An acceleration of the QD size increase during the GRI can be inferred from the fact that the duration of the GRI applied after QD deposition was the same for all QD samples of this series. It is conceivable that Sb acts as surfactant²¹⁶, lowering the energy of the InAs surface. A lower surface energy leads to larger equilibrium islands size in the SK growth mode, following thermodynamic arguments by Shchukin et al.¹¹⁹.

The 1.3 μm QDs of which PL is shown in Fig. 43 (b) are not suitable for the application as active medium in 1.3 μm lasers. A narrower QD size distribution is prerequisite for large modal gain, low threshold current densities and high efficiencies. Other approaches such as the growth of an alternating layer sequence of InAs and GaSb QWs are conceivable to obtain high-density defect-free InGaAsSb QDs emitting at 1.3 μm with a small size dispersion. Although the thickness of each InAs and GaSb is below the critical value for QD formation, the overall strain of the superlattice can exceed the critical value and SK QD formation sets in. A similar observation has been made for an alternating sequence of $\text{In}_{0.5}\text{Ga}_{0.5}\text{As}$ and GaAs layers in MOCVD²¹⁷, leading to large self-organized InGaAs QDs.

6. Quantum-dot lasers

In this chapter, the growth of edge-emitting and vertically emitting injection laser diodes with stacks of QDs as active medium is described. The layer structures of the edge-emitting diodes follow the state-of-the-art design of separate-confinement double heterostructures with multilayer active regions. In sect. 6.1.1, the improvement of laser characteristics of edge emitters upon in-situ annealing of QDs is described. These devices were grown with conventional-precursor MOCVD. The growth of QD devices with alternative precursors is described in sect. 6.1.2. Room-temperature lasing at wavelengths beyond 1.24 μm from QD lasers grown using alternative-precursor MOCVD is reported in sect. 6.1.3. Sect. 6.2 reports growth and characterization of QD VCSEL structures. In sect. 6.2.1 a preliminary study of an InGaAs QW VCSEL is reported. The first MOCVD-grown QD VCSEL world-wide has been demonstrated and is described in sect. 6.2.2.

Standard techniques were applied to process broad-area ridge-waveguide lasers. Although processing of the laser structures is briefly described and device characteristics are presented and discussed, processing and characterization of the lasers were not part of this work. Processing of the edge emitters is described in detail in Ref. 218. The lasers described in sects. 6.1.1.2 and 6.1.1.3 were processed and characterized at the Fraunhofer Institute of Applied Solid State Physics in Freiburg, Germany. All other edge emitters were processed at the Technical University of Berlin. Design, modeling and processing of the oxide-DBR VCSELs as described in sect. 6.2 were carried out at the Technical University of Berlin and are the subject of a forthcoming Ph.D. thesis by F. Hopfer⁷⁶.

6.1. Edge emitters

6.1.1 Lasers with in-situ annealed quantum-dots

The characteristics of previous devices grown using MOCVD were not yet close to the ideal limits of low threshold and high quantum efficiency as expected theoretically^{2-4, 11} and reported for a few exceptional MBE-grown devices^{42, 58}. Drastic improvements of the QD laser characteristics are reported here, based on in-situ annealing of QD layers. The impact of annealing on surface morphology and QD PL is described in sect. 5.1. The influence of this technological step on the performance of laser diodes is discussed in the following sections. In-situ annealing of QD structures is considered to have general importance for the optimization of QD lasers¹⁴³.

6.1.1.1 Threshold reduction and increase of efficiency

The impact of in-situ annealing of QD lasers on threshold current and quantum efficiency was investigated using a series of annealed laser structures grown using AsH₃. The results are compared to QD lasers grown without the annealing step.

Laser structures based on triple stacks of In_{0.8}Ga_{0.2}As QDs were grown on *n*-GaAs(001) substrates using conventional-precursor MOCVD. The GaAs below the QDs was grown at 600°C. Before deposition of the InGaAs QDs, a sufficiently long GRI of 90 s was performed to reach thermal equilibrium and a very smooth GaAs surface at the QD growth temperature of 490°C. After deposition of the QD material, a GRI of 60 s was performed in order to achieve the desired emission wavelength¹². From TEM images of comparable QDs, an area density of $n_{\text{QD}} \approx 10^{11} \text{ cm}^{-2}$ is estimated. Subsequent to the QD formation, the QDs were covered by 7 nm of GaAs. The first 2-3 nm of the GaAs cap were grown at the QD deposition temperature of 490°C. Then the temperature was ramped to 600°C. This value was reached after about 60 s, just when the growth of the 7 nm GaAs cap was completed. Ramping the temperature to 600°C *before* starting the growth of the GaAs cap results in structural degradation of the QDs. After deposition of the cap, GRIs of varying duration ($t_{\text{A}} = 0, 10, 20, 30 \text{ min}$) were performed under As-stabilized conditions ($p_{\text{AsH}_3} = 7.2 \times 10^{-2} \text{ Torr} = 9.6 \times 10^{-2} \text{ mbar}$). Then the GaAs cap growth was resumed. The active medium of the present lasers eventually consists of three layers of In_{0.8}Ga_{0.2}As QDs, separated by 35 nm GaAs, each grown by the described procedure. 1.1 μm thick Al_{0.66}Ga_{0.34}As layers were used as cladding layers.

Ridge-waveguide lasers as depicted schematically in Fig. 1 were processed as follows: Broad area mesas are defined by optical lithography, the 300 nm thick contact layer and the 1200 nm thick top cladding are etched down on both sides of the ridge to about 200 nm above the interface between optical confinement layer and top cladding. 100-150 nm dielectric medium is subsequently sputtered on the surface except on top of the ridge. Afterwards, the Ti/Pt/Au *p*-contact is brought onto the structure by vacuum deposition. The wafer is thinned from originally 450-500 μm to 100-150 μm . Finally, the Ni/AuGe *n*-contact is deposited on the back side of the structure. For characterization of the laser structures, ridge-waveguides of 75, 100 and 200 μm width were processed in the present case. For widths larger than 50 μm , current spreading hardly alters the threshold / transparency currents. Below this value, the threshold currents become dependent on the etch depth and the quality of the interface between top cladding and dielectric medium. Facets were fabricated by cleaving and were not coated.

From the slope of the light-current (L - I) curve $P_{\text{opt}}(I)$ above threshold, the differential quantum efficiencies η_d (also called external or slope efficiencies η_{ext}) were calculated for different cavity lengths. η_d represents the change of the number of photons emitted on both facets upon a variation of the number of injected electrons in the lasing regime:

$$\eta_d = \frac{q}{\hbar \omega} \frac{P_{\text{opt}}}{(I - I_{\text{th}})} \quad (6.1)$$

The differential quantum efficiency is affected by optical losses and thus changes with cavity length and facet coating. The *internal* quantum efficiency η_i is independent from optical losses. It is as related to η_d via

$$\frac{1}{\eta_d} = \frac{2\alpha_i}{\eta_i \ln\left(\frac{1}{R_1 R_2}\right)} L + \frac{1}{\eta_i} \quad (6.2)$$

If the inverse differential quantum efficiency $1/\eta_d$ is plotted as a function of the device length, extrapolation to $L = 0$ yields the inverse internal quantum efficiency $1/\eta_i$. The internal loss α_i can be determined from the slope of $1/\eta_d$ as a function of L . Transparency current density, internal optical losses and internal quantum efficiency are the most important parameters giving access the quality of a laser structure.

Fig. 44 shows the L - I -characteristics of a 200 μm wide and 1.3 mm long device. A maximum output power of 3.7 W is achieved in pulsed mode (1 kHz, duty cycle 1:1250). Threshold current density and slope efficiency η_d are 110 A/cm^2 and 85 %, respectively. In undoped test structures, single sheets of QDs deposited under the same conditions as for the present lasers showed a PL maximum around 1190 nm. During the growth of the upper cladding layer of the laser structures, which is typically performed at 620°C, the emission wavelength of such QDs is blue-shifted to 1150 nm (cf. inset of Fig. 44, EL-spectrum). The inset of Fig. 44 shows that the lasing modes emerge on the high-energy flank of the QD ground-state emission. This wavelength shift is attributed to gain contributions from first excited QD states²¹⁹. For longer cavity lengths fabricated from the same wafer, lasing occurs at 1160 nm²²⁰. Fig. 45 depicts the threshold current density versus the total optical loss (cf. Eq. 1.1).

Transparency currents of 17 A/cm^2 and 20 A/cm^2 for the devices with $t_A = 10$ min were extrapolated. The stripe widths are 75 μm and 100 μm , respectively; the samples are from different growth runs. These values correspond to a transparency current density of about 6 A/cm^2 per QD sheet. This is the smallest value ever reported for a semiconductor laser emitting around 1100 nm. Annealing during 30 min increases the transparency cur-

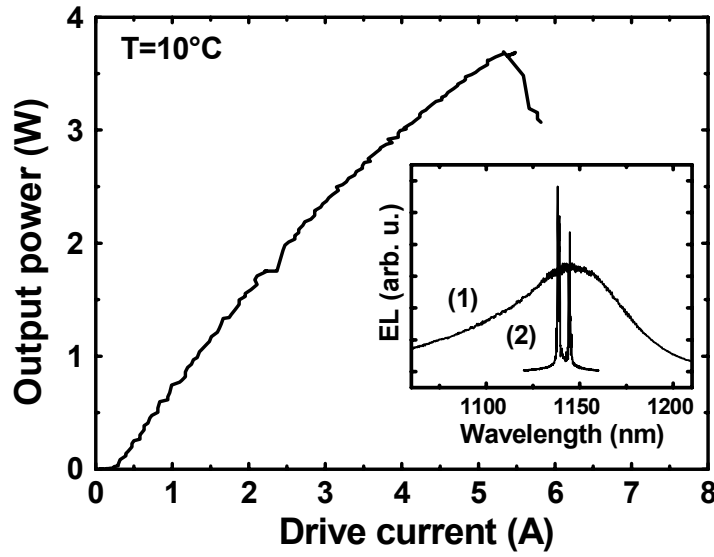


Fig. 44: Output power (two facets) of a QD laser (10 min annealing step) versus injection current (pulsed). **Inset:** electroluminescence of a laser-structure at $0.9 \times j_{th}$ (1) and $1.01 \times j_{th}$ (2). The stripe width of the device is $200 \mu m$, the cavity length is $1.3 mm$. The threshold current density and slope efficiency are $110 A/cm^2$ and 85% , respectively.

rent significantly. This is consistent with the decrease of the PL intensity of the GaAs matrix (Fig. 22 (b)). The inset of Fig. 45 shows the L - I curves of lasers grown with $t_A = 0, 10$, and 30 min. The annealing step leads to a reduction of the threshold current by a factor of about 2.6 for $t_A = 10$ min with regard to $t_A = 0$ min, indicating an increase of the quantum efficiency of spontaneous recombination below threshold.

Fig. 46 depicts $1/\eta_d$ as a function of the cavity length for $t_A = 0, 10$, and 30 min. Internal quantum efficiencies of $\eta_i = 47 \%$ (0 min), $\eta_i = 92 \%$ (10 min), and $\eta_i = 62 \%$ (30 min) are obtained in correlation with the GaAs matrix PL signal in Fig. 22 (b). η_i is strongly enhanced up to 92% for $t_A = 10$ min. The internal losses α_i derived from the slope of the fits are $2.1 \pm 0.5 cm^{-1}$ (0 min), $1.5 \pm 0.3 cm^{-1}$ (10 min), and $2.1 \pm 0.4 cm^{-1}$ (30 min).

To conclude, the introduction of in-situ surface annealing has shown to drastically reduce the transparency current densities of QD lasers and to increase the internal quantum efficiency to nearly 100% . Device structures with the lowest transparency currents ever reported for MOCVD-grown QD lasers were demonstrated. As compared to QD lasers grown using conventional-precursor MOCVD without QD annealing¹², the threshold currents were reduced by more than a factor of two. These improvements in the device characteristics are attributed to a strong reduction of non-radiative recombination centers in the GaAs matrix near the QDs.

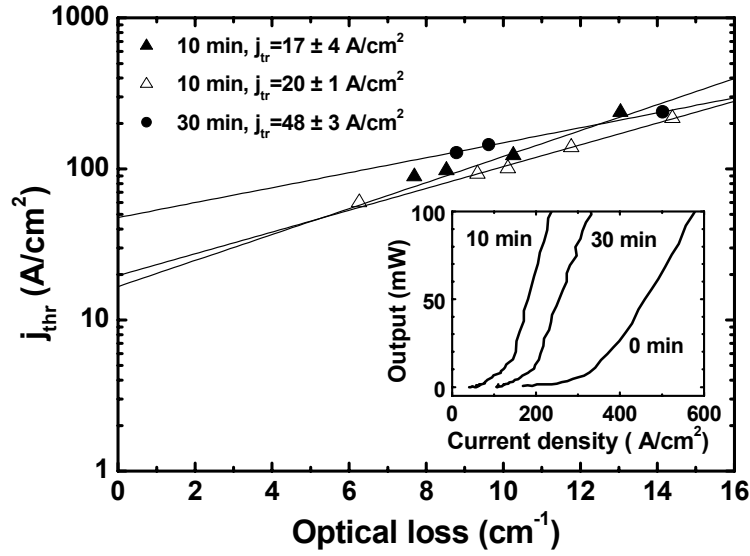


Fig. 45: Threshold current density versus optical loss for devices with 10 min and 30 min annealing and stripe-width of 75 μm . Triangles show data for a laser with QDs annealed during 10 min. Filled and empty triangles are data from the same laser structure but from different growth runs. The stripe width is 100 μm for these lasers. Straight lines are exponential fits. The stated errors are from the numeric regression fit only, a general error of 10 % for the measurements can additionally be assumed, however. **Inset:** L - I -characteristics of devices grown with annealing durations of $t_A = 0$ min ($j_{th} = 340$ A/cm²), 10 min ($j_{th} = 130$ A/cm²), and 30 min ($j_{th} = 180$ A/cm²). Stripe widths are 75 μm , cavity lengths are 1.4 mm ($t_A = 0$ min) and 1.3 mm ($t_A = 10, 30$ min). This figure has been published in Ref. 156.

6.1.1.2 High-Power Operation

Concern has been raised about the potential of QD lasers for high-power emission because of their small volume filling factor, leading to lower modal gain than for conventional QW devices. In addition, refill times were conjectured to be high due to slow intra-dot carrier relaxation, owing to the phonon bottleneck effect^{221, 222}. However, the first QD laser with an output power beyond 10 W¹⁵⁷ and very promising lifetime data recorded under high-power operation at elevated temperatures is demonstrated and described below.

The n - i - p type laser structure was grown on n -GaAs (001) substrate using conventional precursors. The active region inside the 0.4 μm thick SI GaAs waveguide consists of six layers of self-organized $\text{In}_{0.7}\text{Ga}_{0.3}\text{As}$ QDs, grown at 485°C and separated by 30 nm GaAs. A more detailed description of the QD growth is found in Ref. 156. Bottom and top cladding layers consist of n - and p -doped $\text{Al}_{0.3}\text{Ga}_{0.7}\text{As}$, respectively. All layers were grown at 600°C, except for the QDs and the bottom cladding that was deposited at 720°C. Broad area devices with 150 μm wide ridges were processed using

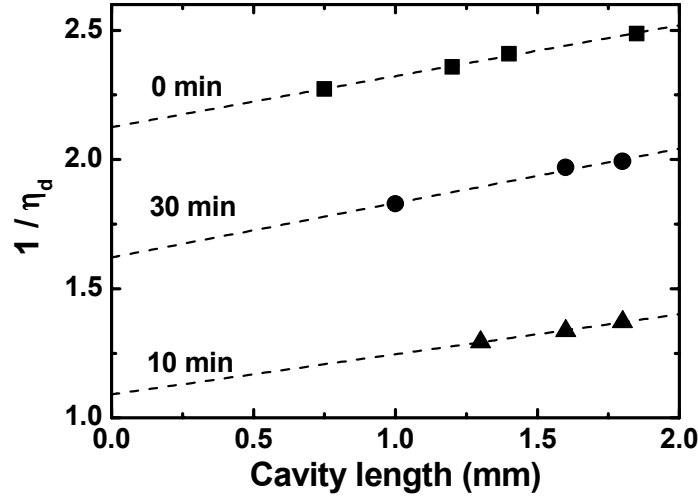


Fig. 46: Inverse differential quantum efficiency as a function of cavity length for different annealing durations. Dashed lines are linear fits. Stripe widths are 75 μm . An estimated error of about 10 % can be assumed. This figure has been published in Ref. 156.

standard etching and metallization techniques. 2 mm long devices were cleaved from the laser bars. The facets of the devices were high-reflection (HR) and anti-reflection (AR) coated, leading to reflectivities of 95 % and 1 %, respectively. The laser diodes were finally mounted *p*-side down on copper heat sinks using indium solder.

Output power versus injection current is depicted in Fig. 47 for two representative broad area lasers emitting at 1135 nm for a stripe geometry of 2 mm \times 150 μm . Device A shows an output power of 4.7 W in continuous-wave (CW) operation at a heat sink temperature of 20°C. The lasing threshold of this device is 650 mA (216 A/cm²), the maximum differential efficiency equals 57 %, and the maximum optical power density at the front facet is 7.5 MW/cm². Device B was driven in quasi-CW (50 μs pulses with 50 Hz repetition frequency) at a heat sink temperature of 20°C. A maximum output power of 11.7 W was observed for the same stripe geometry. Device B passes the lasing threshold at 478 mA (159 A/cm²) and exhibits a maximum differential efficiency of 62 %. The optical power density of the front facet reaches 19.5 MW/cm². These are the highest CW output powers of quantum-dot lasers reported to date. Both lasers fail due to catastrophic optical mirror damage (COMD), attested by optical interference contrast microscopy. Device A reaches the COMD level earlier since it is driven in CW mode and thus heats stronger. Due to the finite temperature sensitivity of the devices, a larger fraction of the drive current is converted to heat as compared to quasi-CW operation. Values of the characteristic temperature

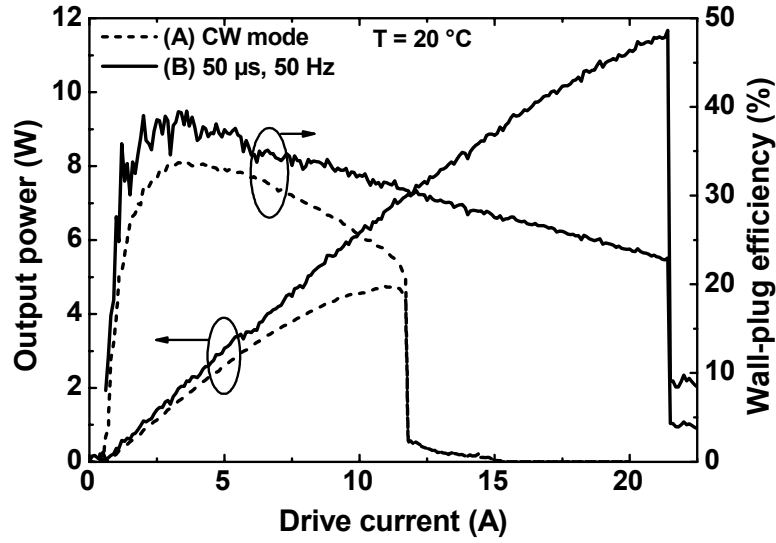


Fig. 47: Front facet output power of two different devices, driven in CW (A) and quasi-CW mode (B), respectively. The stripe geometry is $2 \text{ mm} \times 150 \text{ } \mu\text{m}$. The heat sink temperature was stabilized at 20°C . Device (A) shows CW operation up to 4.7 W. Device (B) was driven up to 11.7 W in quasi-CW mode with $50 \text{ } \mu\text{s}$ pulses and 50 Hz repetition frequency. This figure has been published in Ref. 157.

for both devices are $T_0 = (73 \pm 2) \text{ K}$ between 20 and 50°C and $T_0 = (53 \pm 1) \text{ K}$ between 50 and 80°C .

The COMD level of about 19.5 MW/cm^2 ranks among the highest values reported for QD semiconductor laser diodes and is comparable to the best values reported for conventional QW laser diodes grown on GaAs substrates. For Al-free lasers with InGaP claddings, 20 MW/cm^2 have been reported for as-cleaved facets and QDs as gain medium ($T_{\text{heatsink}} = 20^\circ\text{C}$)¹². 18.5 MW/cm^2 have been observed for a QW as active layer and passivated facets ($T_{\text{heatsink}} = 10^\circ\text{C}$)²²³. 19 MW/cm^2 were achieved with an InGaAs QW as gain medium, AlGaAs claddings and AR/HR coatings ($T_{\text{heatsink}} = 10^\circ\text{C}$)²²⁴. 20 MW/cm^2 is probably close to an upper limit for COMD of conventionally mounted laser diodes with stabilized *heat sink* temperature. The COMD level of an InGaAs/AlGaAs QW laser could be extended to beyond 30 MW/cm^2 using a special mounting technique combined with temperature stabilization of the *laser chip*²²⁵.

In conclusion, a maximum output power of 4.7 W was obtained in CW mode, 11.7 W were achieved in quasi-CW operation. The output power of these lasers is larger than the output power of the lasers described in sect. 6.1.1.1. This is attributed to the active region of the present lasers, consisting of a six-fold QD stack. The devices presented in sect. 6.1.1.1 have only three QD layers as active medium. The output power of the present lasers

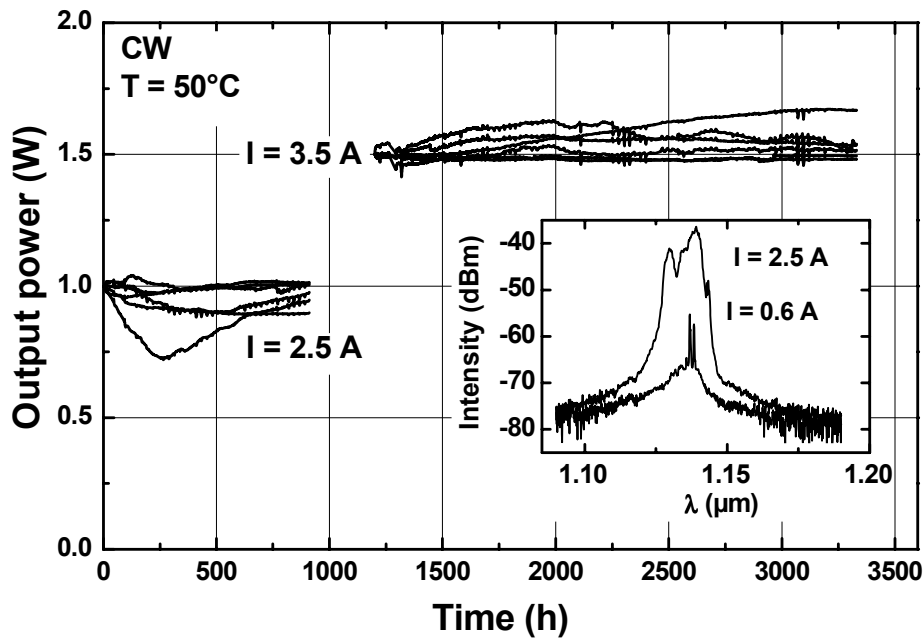


Fig. 48: Lifetime measurements of six 2 mm long and 150 μm wide laser stripes, driven in CW mode at a heat sink temperature of 50°C at two different drive currents. The measurement was interrupted after 910 hours. The depiction of the temporal offset between both measurements is arbitrary. The inset shows lasing spectra near threshold at 0.6 A, and at 2.5 A. This figure has been published in Ref. 157.

was limited by catastrophic optical mirror damage, occurring at a power density of about 19.5 MW/cm² on the front facet.

6.1.1.3 Lifetimes

Lifetime measurements of lasers with six-fold QD stacks in the active region were performed. Growth and characteristics of these devices are described in the previous section. The laser facets were passivated with AR and HR coatings. Lifetime measurements during 3040 h at 50°C are shown in Fig. 48 and give evidence of the high reliability of InGaAs / GaAs QD lasers.

The measurements were started at 1.0 W output power. After 910 h, the lasers were examined for changes of the device characteristics. No significant changes were found. The measurements were resumed at 1.5 W output power. No significant changes of the conversion efficiency are observable during the second measurement period, either. A maximum output power of 9 nW/QD in quasi-CW mode was calculated. This corresponds to an upper limit of 19.5 ps for the refill time. These values are comparable to numbers previously published for an MOCVD-grown laser diode based on a three-

fold stack of comparable InGaAs QDs¹², indicating that carrier capture is not influenced when the number of QD layers is doubled.

6.1.1.4 Characteristic temperature

Temperature insensitivity of the threshold currents of ideal QD lasers has been predicted³ assuming a zero-dimensional density of states in the QDs (Eq. 2.3), QD confinement energies larger than $k_B T$ at room temperature and single confined electron and hole levels. This is in contrast to threshold currents of QW lasers that increase exponentially with temperature. For temperatures up to 150 K, the prediction of such a temperature insensitivity holds indeed. Even a decrease of the threshold current with temperature is observed for QD lasers up to typically 150 K. This is due to the transition from a non-equilibrium to an equilibrium carrier distribution function⁴³ within the QD ensemble.

In the case of more than one electron and hole level per QD and small energetic distances between these levels in *real* QDs, the threshold current becomes temperature-sensitive above 150 K. The energy separation between the electron ground state and the first excited state in QDs is typically between 50¹⁰¹ and 100 meV^{226, 227}, depending on size, shape and chemical composition of the QDs. The separation between the discrete hole levels, however, is estimated to be in the order of 10 meV only²²⁸ so that at room temperature, thermal spreading of the holes over closely lying hole states within the QDs can dominate the gain characteristics at room temperature²²⁹. In the temperature-sensitive regime, the threshold current of a QD laser therefore increases with temperature and can be approximated by

$$j_{\text{th}}(T) \propto \exp(T/T_0) \quad (6.3)$$

where T_0 is the so-called characteristic temperature and is used as a general measure of the temperature stability of the threshold currents of laser diodes.

It is conceivable that charge carriers are thermally excited to higher-lying electronic levels from which *non-radiative* recombination takes place. Non-radiative recombination might particularly occur via matrix states. The carrier density in the matrix increases with temperature, and if a radiative efficiency of, e.g., only 5 % is assumed in the matrix, a T_0 value of 54 K is obtained theoretically⁷⁴. This value is in the range of typical T_0 values of QD lasers emitting around 1.1-1.2 μm .

It should be noted in this context that laser diodes with exceptionally high threshold currents usually exhibit high characteristic temperatures. This does not necessarily mean, however, that the effect of thermal excitation of carriers does not occur or that the radiative efficiency in the matrix

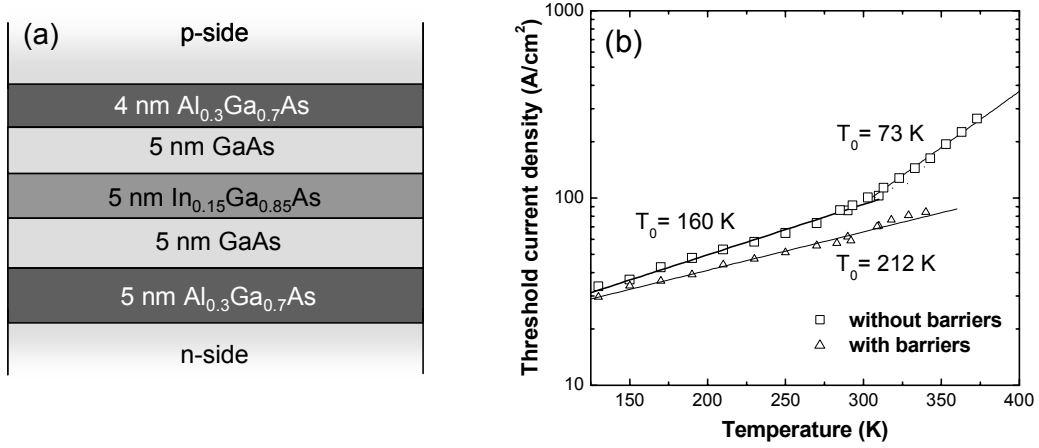


Fig. 49: (a) Schematic diagram of a double-barrier DHS QW injection laser. (b) Temperature dependence of the threshold current of a QW laser with and without double-barrier design.

is especially large. On the contrary, this effect is more likely due to leakage currents that are slowly varying functions of temperature. If leakage currents are large as compared to the current needed for inversion of the laser active medium, the threshold current increases much less with temperature.

In order to assess the contribution of non-radiative recombination in the matrix to the low T_0 values, QD lasers with and without $\text{Al}_{0.3}\text{Ga}_{0.7}\text{As}$ carrier diffusion barriers close to the active region were grown and characterized. These barriers prevent carriers to escape from the active material to matrix states. In addition, single *quantum well* lasers with and without diffusion barriers were grown as reference. The design of such a double-barrier active region goes back to an idea of Tsang et al.²³⁰ who demonstrated an improved characteristic temperature of double-barrier QW lasers.

Fig. 49 (a) shows a schematic diagram of the center of such a double-barrier single-QW laser structure, emitting around 1050 nm at room temperature. The barrier below the InGaAs QW is 5 nm thick, the *p*-side barrier has a thickness of only 4 nm, taking smaller tunnel rates due to the larger effective mass of the holes into account. The layer sequences as well as the temperature ramps of QD and QW laser structures were exactly the same. In contrast to the design of Tsang, a distance of 5 nm was kept between the barriers and the active layers since PL experiments have shown that if the AlGaAs barriers are grown too close to the active layer, the radiative efficiency drops by orders of magnitude. This is ascribed to contaminations at the GaAs/AlGaAs interfaces. The non-radiative recombination efficiency related to these contaminants increases strongly with decreasing distance between InGaAs and AlGaAs.

Lasers with 75 μm wide ridges and as-cleaved facets were processed from these 4 laser structures; the cavities were 1.8 mm long. All measurements were performed in pulsed mode operation. T_0 measurements of the single-QW-laser with and without barriers are shown in Fig. 49 (b). The given temperatures are those of the copper heat sink. One can see that between 150 K and room temperature, the T_0 values of the devices with and without barriers are 212 K and 160 K, respectively. Above room temperature, the T_0 value of the barrier-free QW laser drops to 73 K whereas the device with the barriers keeps the large T_0 value up to an operation temperature of 330 K. From the influence of the barriers on the T_0 of QW lasers, it can be concluded that non-radiative recombination in the GaAs matrix does indeed impact the temperature dependence.

In contrast to the QW laser, the impact of the double barrier on the T_0 of QD lasers is negligible. T_0 of the triple-stack QD laser without barriers is 60 K at room temperature. The device with the diffusion barriers showed a T_0 of about 70 K. The threshold current of this device is slightly larger, however, most likely due to impurities at the $\text{Al}_{0.3}\text{Ga}_{0.7}\text{As}/\text{GaAs}$ interfaces. It can be concluded from these findings that the improvement of the characteristic temperature due to the presence of the barriers is negligible, indicating that other mechanisms dominate the high temperature sensitivity of QD lasers. It is likely that this temperature sensitivity is related to the close energetic hole spacing of the QDs. Long-wavelength QD lasers with larger carrier confinement and larger inter-sublevel spacing of electron and hole states show better temperature stabilities²³¹.

Experiments on *p*-type modulation doping near the QD layers of laser diodes have shown that T_0 can significantly be increased by an excess hole population of the QDs^{229, 232}. This way, the number of hole states that can be populated by current injection is strongly reduced. The holes available for radiative recombination are thus concentrated in a narrower energy window. With *p*-doping levels between $5 \times 10^{17} \text{ cm}^{-3}$ and $1.5 \times 10^{18} \text{ cm}^{-3}$, characteristic temperatures above 160 K between 0°C and 80°C were achieved at reasonably low threshold currents for a twofold QD stack as active medium²³². The ground-state gain of this structure could be increased from 9 cm^{-1} to maximum values of 18 cm^{-1} . A similar problem of closely spaced hole subbands exists in planar QWs. *P*-type modulation doping could also increase the characteristic temperature of QW lasers. However, the level of *p*-doping needed for QWs is nearly one order of magnitude larger²²⁹. In the *p*-doping range required for such QW lasers, doping-related optical loss mechanisms such as free-carrier absorption would worsen the device performance significantly.

6.1.2 Edge emitters grown with alternative precursors

MOCVD of QD laser diodes with close-to-ideal characteristics and high output power has been demonstrated using conventional precursors only^{12, 156, 157} (cf. also sect. 6.1.1). QD laser diodes with equivalently outstanding performance exclusively grown using alternative precursors are demonstrated here. This is all the more remarkable since no in-situ annealing was applied during growth of the lasers presented in this section. Only during growth of the 1.24 μm lasers described in section 6.1.3, in-situ annealing led to a significant improvement of the device characteristics. The demonstration of lasers grown using alternative precursors is decisive for the propagation of MOCVD as laser fabrication technology in regions with high safety standards where strongly toxic hydrides cannot be used.

The *n-i-p* type laser-diode structure was grown on an *n*-GaAs:Si (001) substrate. The active medium consists of three $\text{In}_{0.5}\text{Ga}_{0.5}\text{As}$ QD layers, stacked with a distance of 35 nm in the center of a 300 nm thick undoped GaAs optical-confinement layer. The QDs were deposited at 500°C with a growth rate of about 0.4 ML/s. All precursor flows were switched off hereafter for 30 s to allow QD formation. The first 5 nm of GaAs on top of the QDs were also grown at 500°C. The reactor temperature was then ramped to 600°C. The deposition temperature of layers underneath the QDs was 650°C. All layers on top of the QDs were grown at 600°C. 1 μm thick $\text{Al}_{0.65}\text{Ga}_{0.35}\text{As}:\text{Te}$ and $\text{Al}_{0.7}\text{Ga}_{0.3}\text{As}:\text{C}$ layers were used as bottom and top cladding layers, respectively. 100 μm wide ridge-waveguide lasers were processed using standard techniques, facets were left uncoated.

Fig. 50 shows room-temperature electroluminescence spectra of such a ridge-waveguide QD laser as a function of drive current. The PL spectrum of an undoped PL structure containing *one* QD layer grown under the same conditions as the laser structure is also plotted. The wavelength of the PL peak coincides almost perfectly with the lasing wavelength, indicating that lasing occurs via the QD ground state. The evaluation of the *L-I* curves of four devices with different cavity lengths is shown in Fig. 51. A transparency current as low as $29.7 \pm 0.3 \text{ A/cm}^2$ is derived. The internal quantum efficiency is $91.4 \pm 3.0 \%$ and the internal optical loss is $2.2 \pm 0.2 \text{ cm}^{-1}$ (cf. inset). These numbers are close to the best values ever achieved with QD lasers grown by MOCVD using AsH_3 ¹⁵⁶, although no spacer annealing was applied here.

The outstanding characteristics of the first QD laser grown with alternative-precursor MOCVD gives evidence of the high optical quality of QDs grown using TBAs.

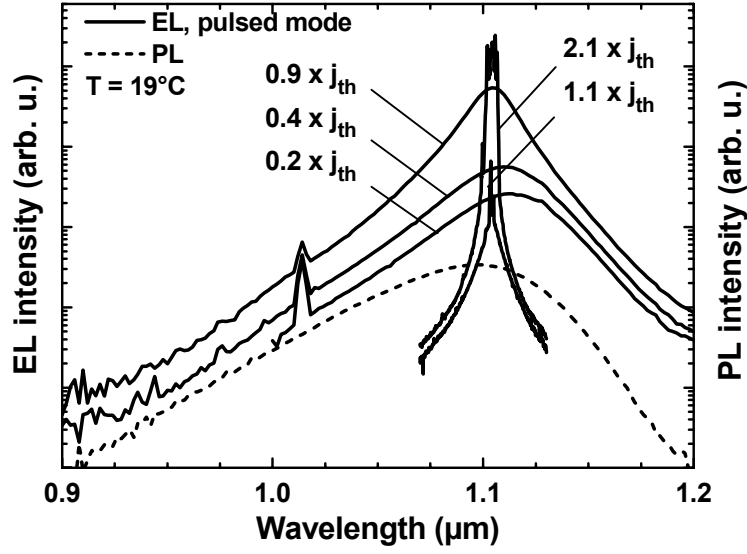


Fig. 50: Electroluminescence spectra of a $100\ \mu\text{m} \times 2\ \text{mm}$ ridge-waveguide laser with a threshold current density of $60\ \text{A}/\text{cm}^2$, driven in pulsed mode (500 ns, 5 kHz). The laser structure was grown with alternative precursors only. Laser spectra were recorded with monochromator slit widths reduced from 1 to 0.1 mm, leading to a signal decrease by about 100. Peaks at $1.01\ \mu\text{m}$ stem from the laboratory lighting. Dotted line: PL of a single QD layer excited with $5\ \text{W}/\text{cm}^2$ at $514.5\ \text{nm}$. This figure has been published in Ref. 161.

6.1.3 Long-wavelength ($>1.24\ \mu\text{m}$) QD lasers

Using alternative-precursor MOCVD, an edge-emitting laser structure with long-wavelength QDs as active region was grown, processed and characterized¹⁵. To achieve long-wavelength emission, ternary InGaAs QDs were overgrown with Ga-rich InGaAs QWs. Spectroscopic and structural studies of such long-wavelength QDs were described earlier in sect. 5.3.1 and 5.3.2. In this section, room-temperature *lasing* activity at wavelengths beyond $1.24\ \mu\text{m}$ is reported. This is the worldwide first demonstration of lasing beyond $1.24\ \mu\text{m}$ reported for MOCVD-grown GaAs-based QD lasers.

The laser structure was grown on a Si-doped GaAs(001) substrate. The active region consists of 10 sheets of $\text{In}_{0.65}\text{Ga}_{0.35}\text{As}/\text{In}_{0.2}\text{Ga}_{0.8}\text{As}/\text{GaAs}$ long-wavelength QDs, separated by $40\ \text{nm}$ GaAs. The QD stack was centered in a $480\ \text{nm}$ thick undoped GaAs optical confinement layer, sandwiched by n - and p -doped $1.1\ \mu\text{m}$ $\text{Al}_{0.6}\text{Ga}_{0.4}\text{As}$ cladding layers. A $350\ \text{nm}$ thick p^{++} contact layer was deposited on top. The bottom cladding layer was grown at 650°C ; waveguide, top cladding layer and contact layer were grown at only 600°C to avoid any In-Ga intermixing of the QDs. The QDs were grown as follows: 2.7ML of $\text{In}_{0.65}\text{Ga}_{0.35}\text{As}$ were deposited at 500°C . A GRI of $1\ \text{min}$

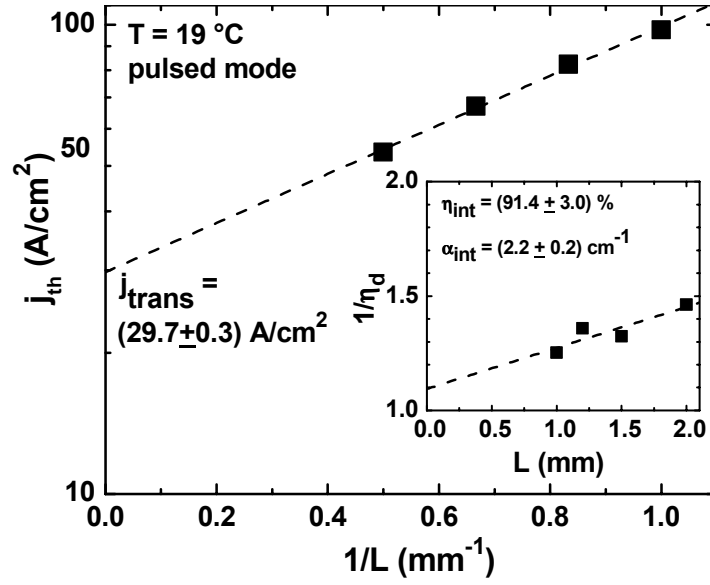


Fig. 51: Threshold current densities of 100 μm wide ridge-waveguide lasers as a function of inverse cavity length. The dashed line shows a linear fit of the decadal logarithm of j_{th} . **Inset:** inverse differential quantum efficiency η_d as a function of cavity length. The devices were driven with 500 ns long current pulses at a repetition frequency of 5 kHz. This figure has been published in Ref. 161.

was introduced to allow QD formation. All precursors were switched off during the GRI, including TBAs. 5 nm of $\text{In}_{0.2}\text{Ga}_{0.8}\text{As}$ were subsequently deposited directly on top of the QDs. Overgrowth of $\text{In}_{0.65}\text{Ga}_{0.35}\text{As}$ QDs with such a QW does not lead to a significant decrease of the integrated PL efficiency, while the redshift of the QD luminescence is considerable. As estimated from TEM images, the QD density is about $2.6 \times 10^{10} \text{ cm}^{-2}$. After deposition of the InGaAs QW, GaAs growth was resumed. First, 2 nm GaAs were deposited at the QD growth temperature. Then the growth was again interrupted for in-situ annealing at 600°C during 3 min (cf. also sect. 5.1). The remaining part of the GaAs spacer is grown at 600°C. A comparison of PL spectra of test structures with single QD sheets grown with and without in-situ annealing shows that upon in-situ annealing, the PL intensity is significantly higher. The spectral width (FWHM) of the PL emission is reduced by the annealing step from 72 meV to 64 meV.

Ridge-waveguide lasers with 50 μm ridge width were processed using standard techniques. Laser facets were left uncoated. The devices were mounted p -side up and were driven in pulsed mode with a pulse width of 800 ns at 1 kHz repetition rate. Fig. 52 shows the dependence of threshold current on the cavity length at room temperature. The lowest threshold current was measured as 220 A/cm^2 for the 2.9 mm long device. The extrapolation of a logarithmic fit of the threshold current densities as a function of cavity length yields a transparency current density of 139 A/cm^2 . Fig. 52

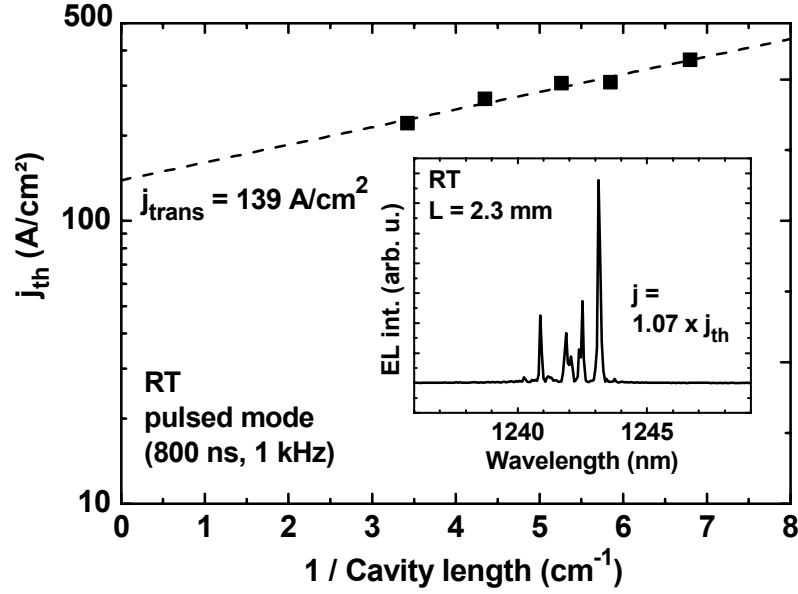


Fig. 52: Threshold current vs. inverse cavity length of a laser diodes based on a 10-fold stack of $\text{In}_{0.65}\text{Ga}_{0.35}\text{As}/\text{In}_{0.2}\text{Ga}_{0.8}\text{As}/\text{GaAs}$ QD sheets. The stripe width is $50\text{ }\mu\text{m}$. The inset shows a lasing spectrum of a 2.3 mm long and $50\text{ }\mu\text{m}$ wide device at room temperature. This figure has been published in Ref. 15.

shows the lasing spectrum of a 2.3 mm long and $50\text{ }\mu\text{m}$ wide laser stripe with for $j = 1.07 \times j_{\text{th}}$. The internal efficiency and the internal optical losses are $(47 \pm 5)\%$ and $(4.0 \pm 0.4)\text{ cm}^{-1}$, respectively. A transparency current density of 139 A/cm^2 corresponds to a transparency current density per QD sheet of about 14 A/cm^2 . This is roughly twice the current as for the laser diodes reported in sect. 6.1.1.

The relatively low internal quantum efficiency points to a yet significant rate of non-radiative recombination. This points to a large density of defects that are still present in the QD sheets. The internal efficiency is potentially increased by optimizing the in-situ annealing step. For a further redshifting of the lasing emission wavelength, the use of binary InAs stressors might be advantageous. Due to the larger strain of such stressors, the alloy phase separation can be enhanced. Previous to the use of such InAs stressors, however, the large inhomogeneous broadening (cf. sect. 5.3.4) must be controlled.

6.2. Quantum-dot vertical-cavity surface emitters

As outlined in sect. 2.1, vertical emitters are very attractive devices, e.g. because of the possibility to fabricate monolithic arrays for parallel data transmission; the circular beam profile of VCSELs allows high coupling efficiencies into optical fibers. The fabrication of VCSELs, however, represents an enormous challenge to both device epitaxy and device processing:

The resonance wavelength of the cavity must exactly match the gain maximum of the active medium, and mirror reflectivities must be high at this wavelength.

Whereas for edge-emitting devices, cavity lengths ranging from several 100 μm to few millimeters can arbitrarily be chosen by ex-situ cleavage, the cavity length of a VCSEL is fixed during growth by choice of the cavity-layer thickness. The longitudinal mode spacing of edge emitters is much smaller than the inhomogeneous broadening of the QD ground-state transition so that exact matching of the cavity length to longitudinal modes is not required. The longitudinal mode spacing of VCSELs, however, is much larger than the typical inhomogeneous broadening of the QD ground state transition. This is because of the short cavity height of only a few λ . Therefore, exact matching of the cavity height of VCSELs to the desired longitudinal mode within 1 % is mandatory. If the thickness of a 300 nm thick GaAs cavity as used for a VCSEL structure emitting at 1.0 μm is changed by 1 %, for example, the cavity resonance wavelength is altered by about 10 nm. This can have a dramatic impact on the device performance.

The short cavity length of a few λ requires extremely large mirror reflectivities in order to keep total optical losses below the gain maximum of the active region (cf. Eq. 2.1). Such reflectivities of more than 99 % can only be provided by DBRs. On GaAs substrates, Al(Ga)As/GaAs DBRs can be used. GaAs-based optoelectronic devices benefit from the unique incidence that AlAs is almost lattice-matched to GaAs. Due to the large difference of optical indices between GaAs and AlAs, such AlAs/GaAs DBRs are highly efficient. In other material systems, DBRs are much less efficient. The efficiency of InP/InGaAsP DBRs as used for the growth of monolithic VCSELs on InP substrates²³³, for example, is much lower so that around 50 InP/InGaAsP pairs are required for each DBR. For GaAs-based VCSELs, 30 pairs of AlAs/GaAs are usually sufficient. The large penetration depth of the light wave into the Bragg mirrors makes high demands on the layer quality.

Although AlAs/GaAs DBRs are very efficient, Al(Ga)O_x/GaAs *oxide* DBRs were used as mirrors for the VCSELs grown within this work. The difference of the optical indices of GaAs and Al(Ga)O_x is much larger so that only 7 and 6 Al(Ga)O_x/GaAs pairs are needed for bottom and top mirrors at 1.1 μm emission wavelength, respectively. This reduces growth times drastically and saves expensive precursor material as compared to all-semiconductor AlAs/GaAs DBRs. Another great advantage of oxide DBRs is the wide stop band, enabling comparably large tolerances of the DBR layer thicknesses. The processing of oxide-DBR VCSELs, however, requires a sophisticated wet-thermal oxidation technique^{234, 235} as outlined in the following section.

Since QD VCSELs are very sensitive to optical losses and low mirror reflectivities, owing to the low modal gain of QDs, the development of a QD VCSEL took place in two steps. As a first step, a QW VCSEL was designed which helped to assess the quality of the different device modules, as described in the following section. A two step oxidation process was applied for the fabrication of the QW VCSELs. Previous to the deployment of QDs as active medium, drawbacks could be eliminated (cf. sect. 6.2.2). The QD VCSELs were fabricated using a one-step oxidation process, as described in sect. 6.2.2.

6.2.1 Quantum-well VCSEL

As a first step towards the fabrication of a QD VCSEL, a single-*quantum-well* VCSEL structure was grown, processed and characterized. Detailed information on the quality of the different parts of a VCSEL can only be accessed by laser parameters such as threshold current densities and efficiencies. Therefore, it is particularly important to achieve lasing with such a VCSEL test structure. A single QW was hence chosen as active medium for this device since the modal gain of QDs might have been too low to obtain lasing, potentially due to non-optimized layer design.

The single-InGaAs-QW VCSEL structure with Al(Ga)As/GaAs layers for subsequent wet-thermal oxidation of Al(Ga)O_x/GaAs DBRs was grown on the Aix200 machine using conventional precursors. The InGaAs QW in the active region was deposited at 490°C. It has a thickness of 5 nm and shows maximum room-temperature PL at 1050 nm. The bottom DBR structure was grown at 720°C, the top DBR was deposited at 600°C. All other layers were deposited at 600°C. In contrast to In-rich QDs, the effect of In-Ga intermixing in Ga-rich InGaAs QWs is rather low so that a larger deposition temperature could have been chosen for the top DBR. It was the aim of this growth experiment, however, to optimize a VCSEL structure that can eventually be used for *quantum dots* as active material. The deposition temperature for layers above QDs should not be increased to more than 600°C. To increase the mechanical stability of the oxide DBRs, 10 nm thick Al_xGa_{1-x}As buffer layers were inserted between the GaAs layers and the Al_{0.98}Ga_{0.02}As layers of the bottom and top DBR. The aluminium fraction x was ramped digitally within these buffer layers from 0.3 to 0.9, with the low Al-fraction sides oriented towards the GaAs layers. Such Ga-rich Al-GaAs layers oxidize very slowly and prevent the GaAs layers from vertical oxidation⁷⁵.

The design of the VCSEL is shown schematically in Fig. 2. The structure has 7 bottom and 6 top DBR pairs and two oxide apertures on both sides of the active region. The design was optimized for minimum optical losses,

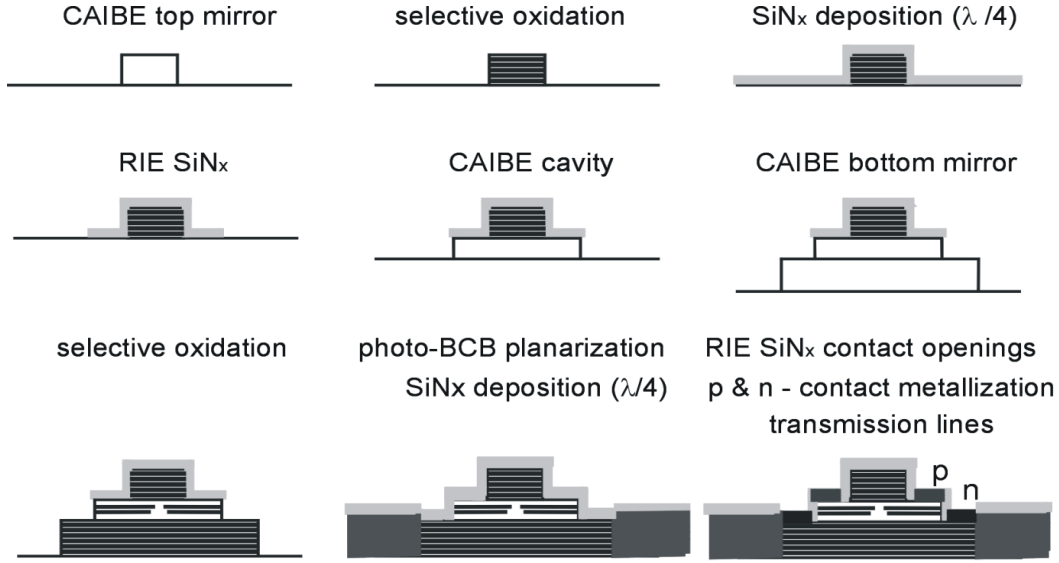


Fig. 53: Schematic overview of the two-step oxidation process used for the fabrication of single-QW VCSELs with oxide aperture and all-oxide DBRs (cf. text). After Ref. 76.

taking into account low modal gain of QD sheets, which are deployed later as active region. Low optical losses were realized using the lowest possible doping levels for the contact layers. n - and p -doping levels of $1 \times 10^{18} \text{ cm}^{-3}$ were chosen for the n - and p -contact layers, respectively. This is close to the minimum values needed to achieve Ohmic contacts.

Fig. 53 shows a schematic overview of the process steps applied for oxide-DBR VCSELs with intra-cavity contacts. The process starts with Chemically-Assisted Ion-Beam Etching (CAIBE) of the top-mirror mesas down to the top interface of the p -contact layer. The process outlined schematically in Fig. 53 includes two separate oxidation steps. First, top DBR and the apertures are selectively oxidized. A $\lambda/4$ thick SiN_x layer is then deposited onto the structure to protect the top oxide DBR from degradation during the second oxidation step. The SiN_x is structured using Reactive-Ion Etching (RIE). The same photoresist mask is used for the subsequent CAIBE etching of the middle mesa down to the top interface of the n -contact layer, while a new mask is required previous to CAIBE etching of the bottom-DBR mesas. After the following simultaneous selective oxidation of the apertures and the bottom DBR, the pillars are partly planarized using photo-bencocyclobutene. A second $\lambda/4$ layer of SiN_x is deposited onto the whole structure to protect the oxide layers during the subsequent lithography steps for the electrical contacts. This has turned out to be necessary since all developing solutions used for the definition of electrical contacts have shown to strongly etch AlO_x . Now the SiN_x layer has a thickness

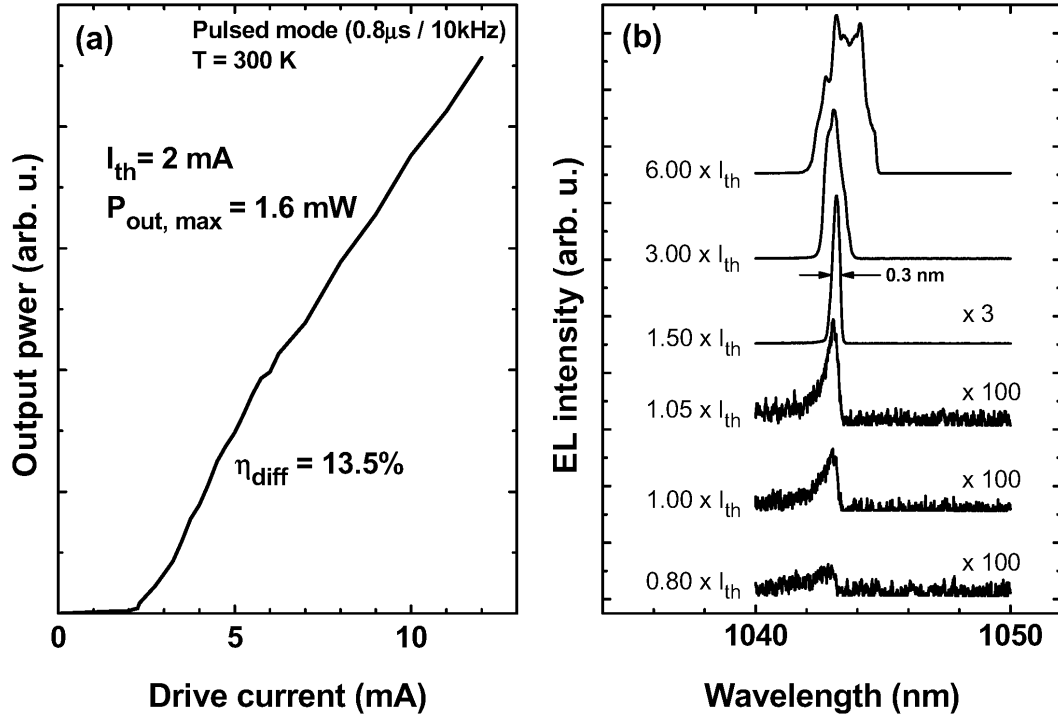


Fig. 54: (a) L - I -characteristics and (b) spectra below and above lasing threshold of a QW VCSEL with an aperture diameter of 25 μ m. The threshold current density is 400 A/cm².

of $\lambda/2$ and consequently does not alter the reflectivity of the structure at the design wavelength. The last step is the metallization of the p - and n -contacts.

Lasing in pulsed mode was achieved for different mesa sizes. The low doping levels of the contact layers imply high series resistances that would lead to extensive heat development if the devices were driven in (a) shows the L - I -curve for a device with a 25 μ m wide circular aperture. The threshold current is 2 mA, corresponding to a threshold current density of 400 A/cm², and the slope amounts to 0.16 W/A (corresponding to 13.5 % differential efficiency). A maximum output power of 1.6 mW CW mode. Immediate thermal rollover and device degradation would be the consequences. Fig. 54 could be achieved. Fig. 54 (b) shows spectra closely below and above threshold. For $I = 1.5 \times I_{th}$, the electroluminescence peak exhibits a FWHM of 0.3 nm. A device with an aperture diameter of 12 μ m showed lasing with a threshold current of 1 mA (900 A/cm²) at a bias of 8 V. The onset voltage of this device is 3.5 V in agreement with previously calculated values.

Fig. 55 (a) shows a reflection and a lasing spectrum of a device with a 25 μ m aperture. A weak cavity dip is visible at the lasing wavelength. It has a width of 1-2 nm, which is comparable to the resolution of the measure-

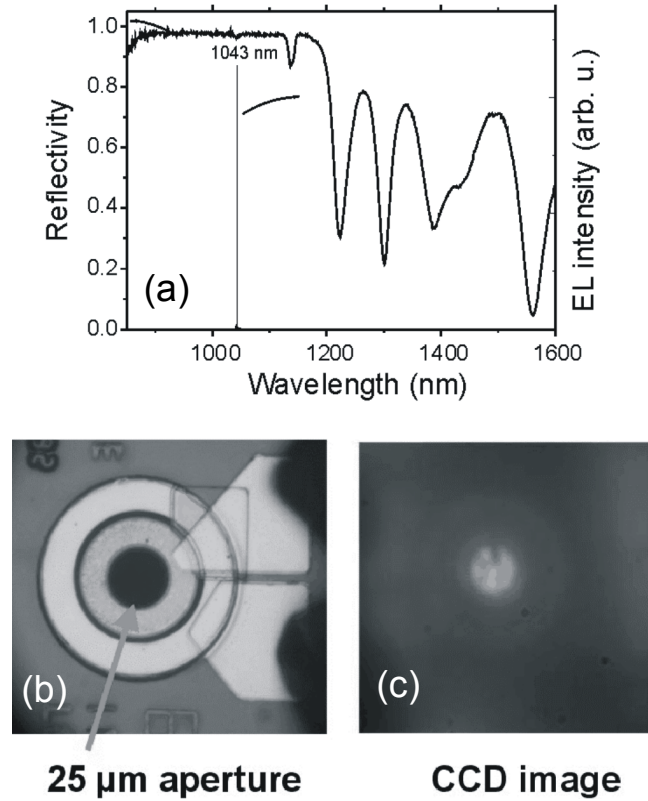


Fig. 55: (a) Reflection spectra and EL spectra of a single-InGaAs-QW oxide-DBR VCSEL with a 25 μm aperture. The reflection shows a weak cavity dip. (b) Microscopic image of an oxide-DBR QW VCSEL with a 25 μm aperture. (c) Near-field distribution of the same device at an averaged output power of 13 μW (duty cycle: 0.8 %). The nearfield was recorded using a Si-CCD camera having a rather low sensitivity at 1050 nm.

ment setup. The visibility of the cavity dip indicates a non-perfect top mirror. The image of a QW-VCSEL with a 25 μm aperture as well as its near-field distribution under pulsed-mode operation are shown in Fig. 55 (b) and (c), respectively. For an aperture diameter as large as 25 μm , a very inhomogeneous current injection with current maxima near the boundary of the aperture is expected (current crowding). In this case, lasing is expected only at the boundary regions of the aperture. However, the CCD image also shows intensity maxima in the center of the aperture. Since the cavity between the contact layers is undoped, the current probably spreads over the whole aperture, which leads to sufficient gain also in the center of the optical mode.

The aperture of the 25 μm VCSEL has the same diameter as the top mirror. In that case, huge optical losses are expected. The threshold current density of this device is nevertheless rather good. This indicates low optical losses *inside* the cavity. The device with the smaller aperture diameter of 12 μm exhibits a significantly larger threshold current density. This effect is

ascribed to a lower quality of the top oxide-DBR in the center region: Although all top mirrors were covered with more than 200 nm SiN_x to prevent them from degradation during the oxidation of the bottom DBRs, a slight degradation could not be avoided. Smaller top DBRs with a larger perimeter-to-area ratio are more sensitive to degradation, and their quality and thus reflectivity are lower, requiring stronger pumping to reach the laser threshold.

The InGaAs-QW oxide-DBR test VCSEL gives evidence of the control of both VCSEL growth technology and wet-thermal oxidation of DBRs. This is an important result with regard to the implementation of a QD active region where mirror reflectivities and doping levels are more critical to the device performance because of the low modal gain of QD layers. For the processing of *quantum-dot* VCSELs, a one-stage oxidation process was therefore developed which circumvents the problem of mirror degradation and leads to a larger top-DBR reflectivity.

6.2.2 Quantum-dot VCSEL

A QD full-oxide-DBR VCSEL structure was grown with alternative precursors using the Aix200/4 machine. The structure was fabricated using a one-stage oxidation process. This way, the danger of over-oxidizing the top oxide DBR is eliminated. On the other hand, the oxidation rates for top-DBR oxide, bottom-DBR oxide and aperture have to be calibrated within 10 % (cf. also sect. 3.3.1.3). Room-temperature lasing was observed around 1100 nm on the QD ground state. This is the worldwide first demonstration of an MOCVD-grown electrically pumped QD VCSEL.

The refractive-index profile of the VCSEL structure is depicted in Fig. 56. The graph shows the active region, the contact layers, and also the intensity distribution of the optical wave. As active medium, 9 $\text{In}_{0.5}\text{Ga}_{0.5}\text{As}$ QD layers were used in 3 stacks. Details of the QD growth are described in sect. 5.2. These QDs have a sheet density of $4\text{--}5 \times 10^{10} \text{ cm}^{-2}$. QDs deposited under the same growth conditions were previously used as 3-fold stacks in edge-emitting lasers, as described in sect. 6.1.2.

As inferred from the characteristics of the QW test VCSEL described in the previous section, a two-stage oxidation process leads to a poor quality of the top DBR. Excess oxidation of the top-DBR oxide during the second oxidation step reduces its optical quality and increases strain in the device⁷⁵. Since high mirror reflectivities are highly needed in QD VCSELs, however, a *one-stage* oxidation process was developed during which top DBR, bottom DBR and apertures are oxidized simultaneously. Due to the pillar design of the present VCSELs with three different mesa sizes for top DBR, cavity with aperture, and bottom DBR, three different oxidation lengths

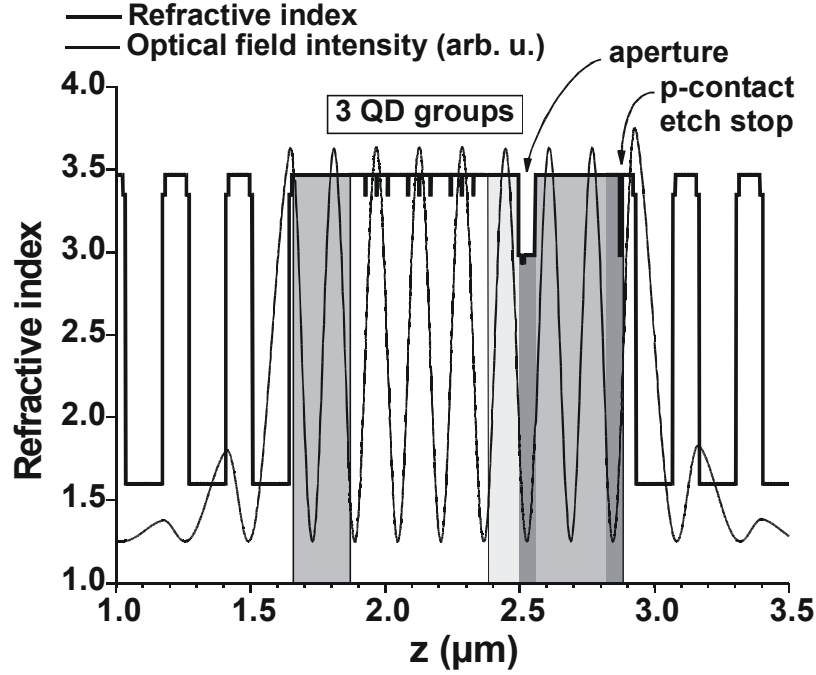


Fig. 56: Vertical refractive-index profile of the oxide-DBR quantum-dot VCSEL. The active region consists of 3 stacks of 3 QD layers each. The bold line denotes the refractive index, the thin line depicts the intensity of the optical field. The cavity is cladded by the bottom oxide DBR (left side, 7 pairs) and top oxide DBR (right side, 6 pairs) and contains the n -contact, the active region, the aperture, the p contact and an AlGaAs p -contact etch stop. The contact layers are marked by grey-shaded regions (cf. text).

have to be controlled in one oxidation step. For the larger mesas, higher oxidation rates are thus required. The oxidation rates of bottom and top DBR are adjusted by calibrating the Ga fraction of the respective Al(Ga)As layers, as described in sect. 3.3.1.3. For well-calibrated oxidation rates, top and bottom DBR oxidation is completed when the target oxidation length of the aperture is reached.

The grey-shaded areas in Fig. 56 depict the different doping levels of the contact layers. The 200 nm thick n -contact layer below the active medium is doped at $n = 1 \times 10^{18} \text{ cm}^{-3}$; the 300 nm thick p -contact layer above the aperture is doped at $p = 1 \times 10^{18} \text{ cm}^{-3}$ (medium grey). The topmost 50 nm of the p -contact layer (dark grey) are doped at $3 \times 10^{18} \text{ cm}^{-3}$, however, to obtain better p contacts. The differential electrical resistance of the VCSELs critically depends on the doping level of the aperture. The aperture is strongly doped with $p = 3 \times 10^{18} \text{ cm}^{-3}$. For a lower series resistance of the cavity, the 150 nm GaAs immediately below the aperture are additionally p -doped at a level of $p = 1 \times 10^{17} \text{ cm}^{-3}$.

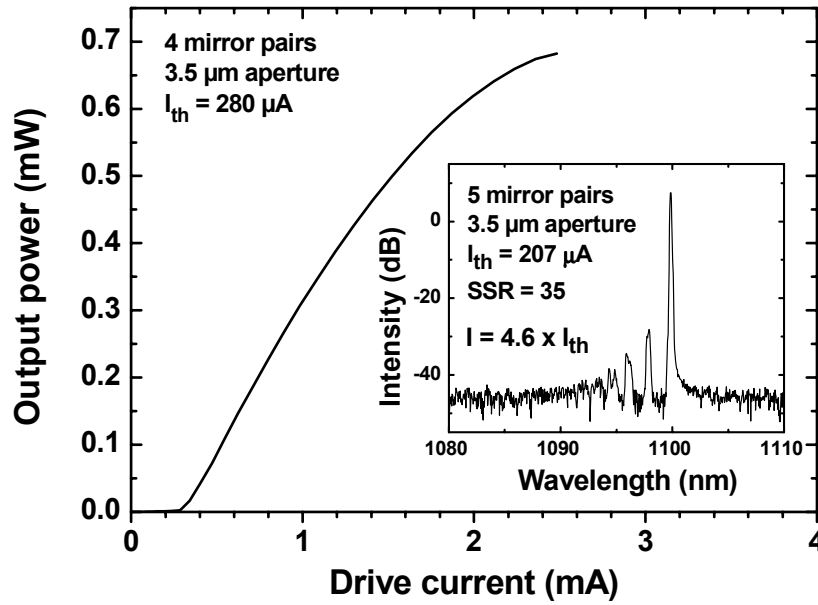


Fig. 57: L - I curve of a 3.5 μm aperture VCSEL with 4 top-mirror pairs. The threshold current is 280 μA at a bias voltage of 2.5 V, the maximum slope efficiency is 43 %, and the maximum output power amounts to 0.68 mW. **Inset:** Spectrum of a QD VCSEL with 5 top DBR pairs and a 3.5 μm aperture. Since the aperture is placed in a node of the optical wave, multimode operation can be observed even for such small apertures. The side-mode suppression ratio (SSR) is 35 dB.

The layer thickness homogeneity across the as-grown wafer was 0.3 %, excluding 8 mm of the wafer edge. Whereas the layer thickness homogeneity of the as-grown VCSEL structure was excellent, large inhomogeneities were caused during the wet-thermal oxidation. Oxidation rates are very temperature-sensitive, and the oxidation temperature strongly varied across the susceptor of the used setup. Nevertheless, all of the 200 characterized VCSELs with aperture diameters smaller than the top DBRs showed lasing. The unusually high yield is ascribed to the large tolerance of the wide QD gain spectrum to variations of the optical cavity thickness. The VCSEL structure was grown with 7 bottom and 6 top DBR pairs. From some wafer pieces, one and two top DBR pairs were selectively removed during the process, so that VCSELs with 6, 5 and 4 top DBR pairs could be characterized.

Fig. 57 shows the L - I -curve of a 3.5 μm aperture VCSEL with 4 top DBR pairs. The maximum output power of this device is 0.68 mW. Lasing sets on at 280 μA at a bias voltage of 2.5 V. The maximum differential efficiency is 43 %. The inset of Fig. 57 shows a spectrum of a VCSEL with a 3.5- μm aperture and 5 top DBR pairs. Single-mode operation is observed for this aperture diameter with a side-mode suppression ratio of 35 dB. A

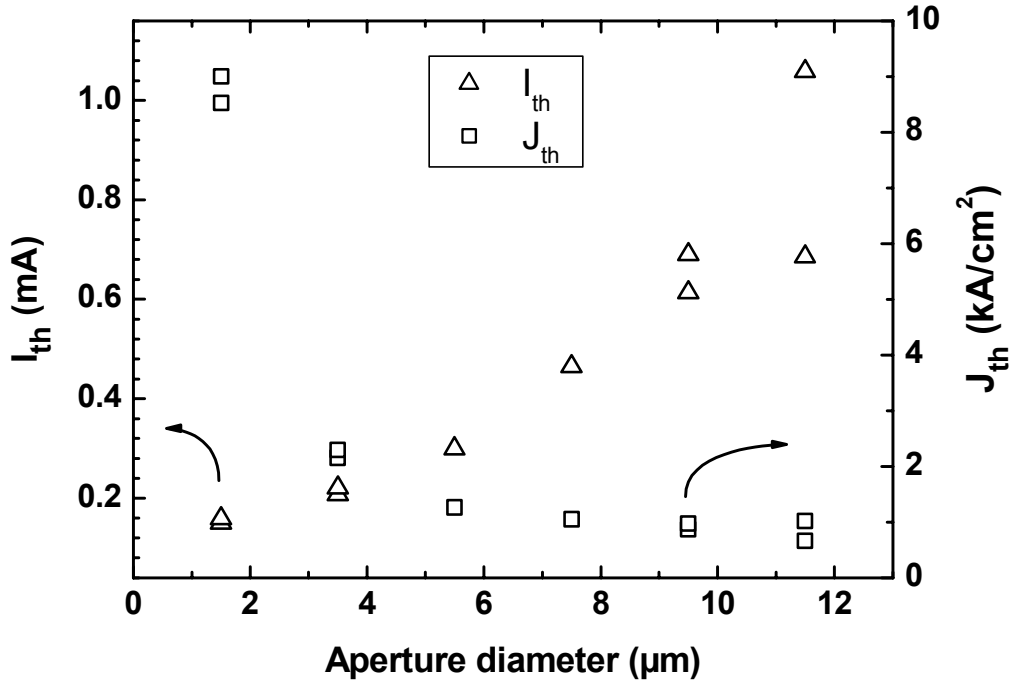


Fig. 58: Threshold current densities of QD VCSELs with 5 top DBR pairs as a function of aperture diameter. For small apertures, current spreading is significant. The threshold current density therefore increases with decreasing aperture diameter.

lower maximum output power of 0.14 mW was observed for this device, owing to the larger top mirror reflectivity.

Threshold currents and threshold current densities of QD VCSELs with 5 top DBR pairs are plotted in Fig. 58 as a function of aperture diameter. The threshold currents are lowest for the smallest apertures. The behavior of the threshold current densities is opposite, however; threshold current densities are lowest for the largest apertures and increase significantly with decreasing aperture diameter. The increase of the threshold current with increasing aperture size is expected since more and more QDs are pumped. If the lateral extension of the pumped gain medium coincided with the aperture area for all aperture diameters, a threshold current density independent from the aperture size would result. The deviation from this ideal behavior is on one side due to current spreading to regions below the aperture oxide, and on the other side due to current crowding near the aperture edge. Thus the injection current density in the middle of a VCSEL decreases significantly with increasing aperture size.

The aperture is placed in a node of the optical wave. This means that the lateral spreading of the optical wave is significant for small apertures. Current spreading is likewise considerable for small apertures. It is estimated that the inverted gain medium of VCSELs with 1.5 μm wide apertures is at

least 3 μm . As a consequence of these two effects, the lateral overlap of the pumped gain medium with the optical wave is best for the smallest apertures. The differential efficiency is therefore highest for the smallest apertures. For an aperture diameter of 3.5 μm , the maximum differential efficiency amounts to 9.8 %. Due to the increasing importance of current crowding for larger apertures, VCSELs with 11.5 μm wide apertures show differential efficiencies below 2 %.

7. Summary and outlook

Within the present work, metalorganic chemical vapor deposition (MOCVD) of novel GaAs-based semiconductor laser structures based on self-organized InGaAs quantum dots (QDs) grown in the Stranski-Krastanow mode was advanced with regard to device performance. The characteristics of such devices had not been close to the earlier predicted theoretical limits before. The characteristics of laser diodes processed from QD structures grown within this work have approached these limits considerably.

The previously established QD growth technology was complemented by an in-situ annealing step that leads to a reduction of defects and to a smoothening of the growth front which is roughened by the deposition of three-dimensional islands. Lasers based on such QDs were demonstrated and exhibit transparency current densities around 6 A/cm^2 per QD sheet for emission wavelengths between 1.1 and $1.2 \mu\text{m}$ at room temperature. Using in-situ annealing, the internal quantum efficiency was increased from previously 50 % to above 90 %. The flattening of the growth front allows to reduce the distance between vertically stacked QD layers and thus helps to increase the QD volume density. In the early stages of QD device research, concern was raised about the reliability of QD lasers due to their highly strained active regions. However, lasers based on 6-fold stacks of in-situ annealed QDs as active medium show room-temperature peak output powers of 11.7 W in quasi-CW mode and 4.7 W under CW operation at emission wavelengths around $1.14 \mu\text{m}$. This was the first demonstration of optical output powers of more than 10 W for QD lasers. It was found during lifetime measurements at 50°C and output powers of 1.0 -1.5 W that the device characteristics remain unchanged for more than 3000 h. This supplies conclusive evidence of the high reliability of QD lasers.

In MOCVD of III-V semiconductors, strongly toxic hydrides such as AsH_3 are typically used as group-V precursors. In the course of this work, MOCVD was changed over to alternative precursors. The organic-compound precursor tertiarybutylarsine (TBAs) was used as substitute for AsH_3 . Since the physical and chemical properties of TBAs are different from those of AsH_3 , epitaxy of all layer structures needed for the growth of QD lasers was to be recalibrated. The worldwide first QD laser grown using TBAs was demonstrated. This is a major breakthrough in the development of a more environment-friendly epitaxy method.

Using self-organized QDs, the emission wavelength of GaAs-based lasers can be tuned to the $1.3 \mu\text{m}$ wavelength regime which is important for datacom applications. In contrast to $1.3 \mu\text{m}$ InGaAsN/GaAs quantum well (QW) lasers, QD lasers exhibit much lower threshold currents and larger

quantum efficiencies. Different techniques to grow $1.3\ \mu\text{m}$ QDs using MOCVD were experimentally explored and evaluated in this work. These included the overgrowth of InGaAs stressors with gallium-rich InGaAs QWs and the admixture of nitrogen and antimony to InGaAs QDs. Undoped test structures containing such QD layers were investigated by photoluminescence spectra and transmission electron microscopy. Using the overgrowth concept, lasing at $1.24\ \mu\text{m}$ was achieved. This is the first demonstration of an MOCVD-grown QD laser emitting beyond $1.2\ \mu\text{m}$ at room temperature. The growth of laser structures for the fabrication of QD vertical-cavity surface-emitting lasers (VCSELs) with all-oxide distributed Bragg reflectors (DBRs) and nine-fold stack of InGaAs/GaAs QDs as active region was implemented. VCSELs with a room-temperature emission at $1.1\ \mu\text{m}$ were processed from these structures. A VCSEL with a $3.5\ \mu\text{m}$ aperture and four top DBR pairs exhibits a maximum output power of $0.68\ \text{mW}$, a differential efficiency of $43\ \%$ at a threshold current of $280\ \mu\text{A}$ at $2.5\ \text{V}$.

The demonstration of MOCVD-grown QD-based all-oxide DBR VCSELs on GaAs substrates as well as edge-emitting QD lasers emitting close to $1.3\ \mu\text{m}$ are major advances towards the commercialization of $1.3\ \mu\text{m}$ QD VCSELs. MOCVD is an important fabrication standard of optoelectronic devices since it is cost-efficient and scalable. It is thus well suited for the commercial growth of such VCSEL structures. However, there are still some tasks to fulfill before such devices can be launched: First of all, the emission wavelength must be extended to the dispersion minimum of glass fibers at $1.31\ \mu\text{m}$. The current $1.24\ \mu\text{m}$ laser is based on InGaAs stressor QDs overgrown with gallium-rich QWs. InGaAs stressor QDs are preferred in MOCVD since they are more stable with regard to defect formation than binary InAs^{45, 142}. The redshift upon overgrowth with Ga-rich QWs can be larger, however, if binary InAs stressors are used, since these exhibit larger strain, favoring the alloy decomposition within the overgrown QW. Using InAs stressors, probably larger effective QD sizes will be achieved in such structures⁴⁹. In contrast to ternary InGaAs QDs, the InAs QDs grown with alternative precursors presented in this work have very low aspect ratios and exhibit a large size distribution. The increase of the aspect ratio of such stressors and the reduction of the QD size distribution will allow to grow QDs with longer emission wavelengths and lower defect densities.

Alternatively to gallium-rich InGaAs QWs as used to overgrow InAs or InGaAs stressor QDs, the use of low-band-gap dilute nitrides such as GaAsN or InGaAsN will allow to achieve longer emission wavelengths than with InGaAs QWs. If dilute nitride QWs are used, $1.3\ \mu\text{m}$ room-temperature lasing might likewise be achieved with ternary InGaAs stressors. QD structures containing dilute nitrides may suffer, however, from ni-

tride-related defects²¹³ which might require special post-growth annealing techniques²¹⁰. The extension of the QD lasing wavelength to even larger values than 1.3 μm is essentially driven by the demand of lasers for long-haul optical datacom, taking place at the attenuation minimum of conventional glass fibers at 1.55 μm . At present, dilute nitrides are indispensable to achieve lasing at this wavelength on GaAs substrates. Luminescence studies of nitride-containing QD heterostructures at 1.55 μm are presently carried out using MBE²³⁶.

Self-organized long-wavelength QDs are very large and highly strained. In sheets of such large QDs, dislocated defect clusters are often formed. This requires an appropriate defect reduction technique if the density of such clusters is high. The annealing step reported in this work has been developed for defect reduction in QD sheets that are *free* of dislocated clusters. Defect reduction in long-wavelength QD sheets must additionally be capable of *cluster* elimination, similar to annealing procedures reported for long-wavelength QD growth using MBE²³⁷. Here, the thickness of the cap deposited previous to the annealing step is chosen only to cover coherent QDs. Clusters are larger than coherent QDs and emerge from the surface of the thin cap. During a high-temperature growth interruption (GRI), such clusters can be evaporated²³⁷. The holes that are left behind in the thin GaAs cap are filled with either GaAs or AlAs. In addition to GRIs at high temperatures in MOVCD, in-situ etching using tertiarybutylchloride^{238, 239} (TBCl) might help to remove clusters and to reestablish smooth surfaces.

If large, long-wavelength QDs are densely stacked, the vertical strain fields of successive QD sheets can overlap, depending on the thickness of the spacer layer. The strain field of an underlying QD layer can influence the formation of QDs in a subsequent layer. This has two disadvantages: First, vertical correlation can result (cf. Fig. 21), potentially leading to larger QDs than in the preceding layer; secondly, the danger of cluster formation might be enhanced due to accumulated strain from buried QD sheets. To avoid these two effects in highly strained QD stacks, strain-compensating Ga(PAs) layers might be useful. GaPAs has a smaller lattice constant than GaAs, compressive strain from indium-containing layers can be compensated by the tensile strain of GaPAs. GaPAs layers have been used to for strain compensation in edge-emitting InGaAs(N)/GaAs-QW edge emitters^{197, 240} and InGaAs(N)-QW VCSELs^{241, 242} with comparably low threshold currents.

List of acronyms

Chemical elements

Al	aluminium
Ar	argon
As	arsenic
C	carbon
Ga	gallium
Ge	germanium
H	hydrogen
In	indium
N	nitrogen
O	oxygen
P	phosphorus
Sb	antimony
Si	silicon
Te	tellurium

Precursors

AsH ₃	arsine / arsenic hydride / arsenic trihydride
CBr ₄	carbon tetrabromide
DETe	diethyltelluride
DMHy	(unsymmetric) dimethylhydrazine
DMZn	dimethylzinc
NH ₃	ammonia
TBAs	tertiarybutylarsine
TBCl	tertiarybutylchloride
TEAs	triethylarsine
TEGa	triethylgallium
TESb	triethylantimony
TMAI	trimethylaluminium
TMA _s	trimethylarsine
TMGa	trimethylgallium
TMIn	trimethylindium
UDMH _y	unsymmetric dimethylhydrazine

Abbreviations

AAPS	activated alloy phase separation
AFM	atomic force microscopy
AR	anti reflection
COMD	catastrophic optical mirror damage

CW	continuous-wave
DBR	distributed Bragg reflector
DHS	double heterostructure
GRI	growth interruption
HR	high reflection
<i>L-I</i>	light-current
MBE	molecular beam epitaxy
MFC	mass-flow controller
ML	monolayer
MOCVD	metalorganic chemical vapor deposition
PL	photoluminescence
PLE	photoluminescence excitation (spectroscopy)
QD(s)	quantum dot(s)
QW(s)	quantum well(s)
RHEED	reflection high-energy electron diffraction
RIE	reactive-ion etching
SCH	separate-confinement heterostructure
SI	semi-insulating
SK	Stranski-Krastanow
slm	standard ($T = 0^{\circ}\text{C}$, $p = 1.013$ bar) liters per minute
STM	scanning tunneling microscopy
TEM	transmission electron microscopy
VCSEL	vertical-cavity surface-emitting laser
WL	wetting layer
XSTM	cross-section scanning tunneling microscopy

Physical quantities

E	energy	(J)
F	free energy	(J)
H	free enthalpy	(J)
j	current density	(A/cm ²)
p	pressure	(bar, Pa, Torr) ^{xiii}
S	entropy	(J/K)
σ	surface energy	(J/cm ²)
t	time	(s)
T	temperature	(K or $^{\circ}\text{C}$)

Physical constant

k_B	Boltzmann's constant ($1.3806503 \cdot 10^{-23}$ J/K)
-------	--

^{xiii} 1 bar = 10^5 Pa \approx 750 Torr

List of figures

- Fig. 1: Schematic diagram of the cross-sectional view on the laser facet of a typical, fully processed edge-emitting laser diode. The different layers are: 1. Ti/Pt/Au top contact. 2. SiN_x insulating layer. 3. p^{++} GaAs contact layer. 4. p^+ AlGaAs top cladding. 5. Undoped optical-confinement GaAs layer with the active region in the center. 6. n^+ AlGaAs bottom cladding. 7. Substrate. 8. Ni/AuGe bottom contact..... 4
- Fig. 2: Layer and structure design of a GaAs-based full-oxide-DBR VCSEL with intracavity p - (top) and n -contacts (bottom). The active region as shown schematically in the magnification can alternatively consist of a multi QD layer stack or QWs. After Ref. 14. 5
- Fig. 3: Lowest threshold current densities reported for double-heterostructure (DHS) lasers, QW lasers, and QD lasers, respectively, versus publication year. After Ref. 28. 8
- Fig. 4: Simplified schematic of the MOCVD setup of both the Aix200 and Aix200/4 machine. The two kits basically differ by the size of the quartz-glass reactor. The Aix200 disposes of a hydride lines for arsine instead of the TBAs-bubbler line. Dopant lines and pressure controllers are not shown. 16
- Fig. 5: Electron concentration of Al_xGa_{1-x}As:Te and Al_xGa_{1-x}As:Si as functions of the aluminium fraction x , determined by Hall measurements at room temperature. The data for Al_xGa_{1-x}As:Te were taken from Ref. 87, the data for Al_xGa_{1-x}As:Si are from Ref. 86. 19
- Fig. 6: Schematic diagram of the principal cracking mechanisms of arsine and tertiarybutylarsine (TBAs) during pyrolysis in MOCVD. Homolytic fission and β -elimination are competing decomposition mechanisms of TBAs. Homolytic fission produces a reactive AsH₂ radical. β -elimination generates an arsine molecule and an inert isobutene molecule..... 20
- Fig. 7: Comparison of thermal decomposition of TBAs and arsine in an atmospheric pressure reactor. After Stringfellow et al.⁹⁶ 22
- Fig. 8: AFM images ($3 \times 3 \mu\text{m}^2$) of GaAs substrate pieces heated up to 700°C and cooled down under different TBAs partial pressures (A: 2×10^{-2} mbar, B: 2×10^{-3} mbar, C: no stabilization)..... 23
- Fig. 9: Hole concentration of 1 μm thick, nominally undoped Al_{0.4}Ga_{0.6}As layers as a function of V/III ratio. The hole concentration was measured by the van-der-Pauw method. 23
- Fig. 10: GaAs and AlGaAs growth rates as determined from cross-sectional AFM images, plotted as a function of growth temperature. The sample consisted of alternating Al_xGa_{1-x}As/GaAs layers grown at different temperatures, using TMGa, TMAI and AsH₃ as precursors. The TMGa

- and TMAI flows were 7.4 and 5.8 $\mu\text{mol/min}$, respectively; the V/III ratio was 180 for all layers. Error bars originate from statistical treatment of 10 thickness measurements of each layer; dashed lines are guides to the eye. An Al fraction of $x = 65.1\%$ was determined from an x-ray diffraction spectra of a 1 μm thick AlGaAs epilayer grown at 720°C with the given precursor flows. The Al fraction may slightly change with decreasing growth temperature..... 27
- Fig. 11: Reflection spectrum of an unoxidized, as-grown VCSEL structure. The DBRs consist of six periods of GaAs / $\text{Al}_{0.98}\text{Ga}_{0.02}\text{As}$ 28
- Fig. 12: Strongly simplified gas inlet schematic of the Aix200/4 reactor with susceptor and substrate. Group-V precursor gases are conducted separately from group-III precursors. In order to avoid prereactions, they are not mixed before they reach the entrance of the reactor. Dopants are added to the group-III line. 29
- Fig. 13: Thickness of the AlAs layers of AlAs/GaAs superlattices, normalized to 1.0 for a radial distance of 0.5 inch = 12.7 mm. For the sake of clearness, the values for GaAs were omitted. The behavior of GaAs layer thicknesses is analogous to those of AlAs. The AlAs layers were grown with a V/III of 30 at a growth rate of 2 $\mu\text{m/h}$ 30
- Fig. 14: $\text{Al}_{1-x}\text{Ga}_x\text{As}$ oxidation rate at 420°C versus composition for 100-nm-thick layers cladded by 100 nm thick GaAs layers. From Ref. 109. ... 31
- Fig. 15: Typical structure of an undoped sample containing one or more QD layers for PL measurements. AlGaAs diffusion barriers below and above the QDs suppress carrier diffusion to the substrate and to the surface, respectively. 32
- Fig. 16: Free energy gained by the 2D to 3D transition of a pseudomorphically strained WL as a function of island base length. Curves for different values of the paramter α (cf. text) are plotted. From Ref. 119. 38
- Fig. 17: Strain energy around a spontaneously formed island in a one-dimensional atomistic model by Barabási¹²⁶. E_s is the strain energy of an atom placed on the top of the substrate or on the island. E_s is largest at the island edge. From Ref. 126. 40
- Fig. 18: Monte-Carlo simulations of the temporal evolution of 2D submonolayer islands. A coverage of 4 % was deposited randomly on the surface at a flux of 1 ML/s. Every 0.01s, a histogram of the island size distribution is recorded. The average island diameter $\langle\sqrt{N}\rangle$ is plotted as a function of GRI duration for different temperatures. The hopping probability p of an adatom is proportional to $\exp[-(E_0 + nE_n - E_s) / k_B T]$ where E_0 is the adatom diffusion barrier, E_n the chemical bond energy to a neighbor atom, n the number of chemically bound neighbors, and E_s the strain energy at the position of the considered adatom. From Ref. 127. 41

- Fig. 19: (a) Reference sample without QDs. A 30 nm thick GaAs layer was directly deposited at 490°C on 100 nm GaAs grown at 600°C. (b) AFM image of a 30 nm thick QD-burying GaAs cap deposited at 490°C on QDs that were also grown at 490°C. The hillock density amounts to $2.5 \times 10^9 \text{ cm}^{-2}$. The picture has been published in Ref. 73 (c) Plan-view TEM image of a single-sheet QD sample. The QD density is about $3.4 \times 10^{10} \text{ cm}^{-2}$. The underlying QDs were deposited under the same parameters as those of sample (b). 48
- Fig. 20: (a) AFM surface image of a sample where the growth temperature of the 30 nm thick GaAs cap was ramped in-situ to 590°C. The picture has been published in Ref. 73. (b) AFM surface image of a sample where the QDs were capped with 7 nm GaAs. Subsequently, the surface was annealed during 10 min at 600°C under As stabilization. 50
- Fig. 21: Cross-sectional dark-field TEM image of a five-fold $\text{In}_{0.8}\text{Ga}_{0.2}\text{As}$ QD stack grown with in-situ annealing after each QD layer was capped by 7 nm GaAs. The vertical sheet-to-sheet distance is 18-20 nm. 51
- Fig. 22: Room-temperature PL spectra of annealed QD samples at low excitation density (a) (5 W/cm^2) and at high excitation density (b) (5 kW/cm^2). In (a), recombination occurs essentially on the QD ground state. Luminescence from the WL and the matrix is not visible. In (b), radiative recombination mainly takes place in the GaAs matrix. The stars denote transitions from the excited QD states. This figure has been published in Ref. 73. 53
- Fig. 23: PL spectra of $\text{In}_{0.67}\text{Ga}_{0.33}\text{As}$ QDs, deposited at 485°C. “QD”, “QD*”, and “WL” denote transitions from the QD ground state, the first excited QD state, and the WL, respectively. Inset: Plan-view dark-field transmission electron micrograph of the same QD layer. This figure has been published in Ref. 161. 55
- Fig. 24: PL peak emission wavelengths of the ground-state transitions of $\text{In}_{0.67}\text{Ga}_{0.33}\text{As}$ QDs as a function of growth temperature and V/III ratio. QDs of the V/III series were deposited at 485°C, the V/III ratio of the temperature series was kept at 1.5. The reproducibility of the peak positions is within 10 nm. This figure has been published in Ref. 161. 56
- Fig. 25: Flow chart of different approaches to achieve lasing emission at 1.3 μm and beyond by overgrowing small In(Ga)As QDs. Structures in bold scripture were grown and characterized within this work. 58
- Fig. 26: Low-temperature PL spectra of single $\text{In}_{0.8}\text{Ga}_{0.2}\text{As}$ QD layers overgrown with 5 nm $\text{In}_x\text{Ga}_{1-x}\text{As}$ QWs of varying indium fraction x. The spectra were normalized to equal peak intensities. 59
- Fig. 27: Full squares: PL peak wavelength of $\text{In}_{0.8}\text{Ga}_{0.2}\text{As}$ QDs overgrown with 5 nm $\text{In}_x\text{Ga}_{1-x}\text{As}$ of denoted indium fraction x, recorded at 9 K. From TEM images, the QDs are estimated to be 3-5 nm high and 20-

- 25 nm wide. Hollow squares: Ground-state transition wavelengths of a 2.6 nm high truncated-pyramid-shaped InAs QD overgrown with an $\text{In}_x\text{Ga}_{1-x}\text{As}$ QW of denoted indium fraction x , calculated within an eight-band $k\cdot p$ framework. 60
- Fig. 28: Room-temperature PL spectra of $\text{In}_{0.8}\text{Ga}_{0.2}\text{As}$ QDs overgrown with $\text{In}_{0.25}\text{Ga}_{0.75}\text{As}$ QWs of varying thickness d 62
- Fig. 29: (a)-(c) Fourier-filtered cross-sectional high-resolution TEM images of $\text{In}_{0.8}\text{Ga}_{0.2}\text{As}$ QDs covered with (a) 1 nm, (b) 2 nm, and (c) 3 nm $\text{In}_{0.25}\text{Ga}_{0.75}\text{As}$. The dotted white lines depict the boundary between InGaAs and GaAs. The boundaries were determined after the reversal of the In-As and Ga-As image contrast, occurring at an indium fraction of about 15 %. (d) Heights of the QDs and the QW near the QD bases. A generous error of 1 nm is assumed for each value, taking uncertainties of the determination of the InGaAs/GaAs boundary into account. 63
- Fig. 30: Schematic diagrams illustrating the separation of a ternary InGaAs alloy into indium-rich and gallium-rich phases, activated by the strain-relaxed surface of an underlying In(Ga)As stressor QD. (a) Initial In(Ga)As stressor QD, assumed to have the shape of a truncated pyramid. (b) Partial decomposition of the InGaAs alloy into indium-rich and gallium-rich regions. (c) Final structure, buried by GaAs. 64
- Fig. 31: Cross-sectional dark-field TEM image of QDs formed upon MBE of 2 ML InAs at 485°C, overgrown with 5 nm $\text{In}_{0.15}\text{Ga}_{0.85}\text{As}$. From Ref. 169. 65
- Fig. 32: Empty-state XSTM image taken at $V_s = +2.1$ V. The contours of the dot are indicated by dotted lines, and those of its In-rich zone by dashed lines. The In distribution was evaluated along the intersection lines (a) and (b) by evaluation of atom-chain distances (cf. text). After Lenz et al.¹⁷⁹ 66
- Fig. 33: Room-temperature PL spectra of InGaAs QDs grown with (a) AsH_3 (from Ref. 142) and (b) TBAs, deposited around 500°C. The respective V/III ratios are marked in the viewgraphs. 68
- Fig. 34: Flow chart of different approaches to achieve QD emission at 1.3 μm by addition of antimony and nitrogen to In(Ga)As QDs or InGaAs QWs. 69
- Fig. 35: Band gap energy versus lattice parameter of GaAsN, InGaAs, and $\text{In}_{0.53}\text{Ga}_{0.47}\text{As}_{1-y}\text{N}_y$. From Ref. 205. 70
- Fig. 36: (a) Free energy F versus solid composition for a hypothetical semiconductor alloy with a large positive mixing enthalpy H . The points labelled A and B are the *binodal* points, the inflection points C and D are the *spinodal* points. The miscibility gap is the composition range between x_C and x_D . (b) The fabrication of $\text{In}_x\text{Ga}_{1-x}\text{As}_y\text{N}_{1-y}$ can be achieved by separately mixing Ga and In on the group-III sublattice

- with parameter x , and As and N on the group-V sublattice with parameter y 71
- Fig. 37: (a) Room-temperature low-excitation spectra of undoped samples with single InGaAsN QD sheets. (b) PL peak intensities of the QD ground-state (GS) PL, plotted as a function of $p_{\text{DMHy}}/p_{\text{TBAAs}}$. A power density of 5 kW/cm^2 was used for excitation. The inset shows the spectra belonging to the first data point at $p_{\text{DMHy}}/p_{\text{TBAAs}} = 0$ 73
- Fig. 38: PL spectra of InGaAsN QD samples. The InGaAs QD samples were nitrided by adjusting the denoted DMHy partial pressures in the reactor chamber during a GRI of 1 min after deposition of the InGaAs QD material. (a) Low-excitation room-temperature PL spectra. The spectra of the nitrided samples are smoothed. (b) High-excitation low-temperature spectra of the same samples, logarithmically plotted. 75
- Fig. 39: Room-temperature PL spectra of (a) InAs QDs and (b) InAsSb QD sheets. In both cases, the deposition amount was varied over the same range. Both InAs and InAsSb QDs were grown at $T_{\text{gr}} = 485^\circ\text{C}$. A GRI of 5 s was introduced after deposition of the QD material to allow QD formation. The InAsSb QDs were deposited with an additional TESb flow of $4.4 \text{ }\mu\text{mol/min}$ during deposition and the subsequent GRI. The excitation power density was 5 W/cm^2 77
- Fig. 40: Low-temperature PLE contour plot of an InAs sample with a TESb flow of $8.8 \text{ }\mu\text{mol/min}$ during the GRI of 5 s, subsequent to the InAs deposition (compare to Fig. 43). PL was excited using a white-light source and a double monochromator. The excitation density is below 5 mW/cm^2 . The intensity is plotted on a logarithmic scale, the thin lines are equi-intensity lines. The bold black curve shows a PL spectrum, excited at 514.5 nm and an excitation power density of 5 W/cm^2 . The logarithmic scale of the PL intensity is given on the right. The peaks of the PL spectrum are partially numbered..... 79
- Fig. 41: High-resolution cross-section transmission micrograph of a single InAs QDs sheet grown at 500°C . A GRI of 5 s under TESb flux of $8.8 \text{ }\mu\text{mol/min}$ was performed after the deposition of the InAs. The lower InAs/GaAs interface as well as the top interfaces of the truncated-pyramidal InAs islands are depicted with thin white lines. The boundaries are determined according to the reversal of the group-III/group-V-atom contrast, occurring at an indium fraction x of about 15 % for $\text{In}_x\text{Ga}_{1-x}\text{As}$ 80
- Fig. 42: Transition energies of truncated-pyramidal InAs islands as a function of island height, calculated using 8-band $k\cdot p$ -theory. The InAs islands have constant base length of 13.6 nm and 45° facets. With increasing island height, the shape changes from a truncated pyramid towards a complete pyramid. The aspect ratio of a complete pyramid with 45° facet angle is 0.5..... 81

- Fig. 43: Low-temperature low-excitation PL spectra of undoped test structures, each containing a single QD sheet. 1.7 ML InAs were deposited at 485°C with a V/III ratio of 1.5. During the subsequent GRI of 5s, different precursors (TBAs and TESb) were switched on. The impact of TBAs supply is shown in (a), the influence of TESb during the GRI is shown in (b). The rightmost curves in (a) and (b) are reference InAs samples, grown without any precursor flow during the GRI. They are slightly different in (a) and (b) since they stem from different growth series. The nominal deposition parameters are the same, however..... 82
- Fig. 44: Output power (two facets) of a QD laser (10 min annealing step) versus injection current (pulsed). Inset: electroluminescence of a laser-structure at $0.9 \times j_{th}$ (1) and $1.01 \times j_{th}$ (2). The stripe width of the device is 200 μm , the cavity length is 1.3 mm. The threshold current density and slope efficiency are 110 A/cm² and 85 %, respectively..... 88
- Fig. 45: Threshold current density versus optical loss for devices with 10 min and 30 min annealing and stripe-width of 75 μm . Triangles show data for a laser with QDs annealed during 10 min. Filled and empty triangles are data from nominally the same laser structure but from different growth runs. The stripe width is 100 μm for these lasers. Straight lines are exponential fits. The stated errors are from the numeric regression fit only, a general error of 10 % for the measurements can additionally be assumed, however. Inset: L - I -characteristics of devices grown with annealing durations of $t_A = 0$ min ($j_{th} = 340$ A/cm²), 10 min ($j_{th} = 130$ A/cm²), and 30 min ($j_{th} = 180$ A/cm²). Stripe widths are 75 μm , cavity lengths are 1.4 mm ($t_A = 0$ min) and 1.3 mm ($t_A = 10, 30$ min). This figure has been published in Ref. 156. 89
- Fig. 46: Inverse differential quantum efficiency as a function of cavity length for different annealing durations. Dashed lines are linear fits. Stripe widths are 75 μm . An estimated error of about 10 % can be assumed. This figure has been published in Ref. 156..... 90
- Fig. 47: Front facet output power of two different devices, driven in CW (A) and quasi-CW mode (B), respectively. The stripe geometry is 2 mm \times 150 μm . The heat sink temperature was stabilized at 20°C. Device (A) shows CW operation up to 4.7 W. Device (B) was driven up to 11.7 W in quasi-CW mode with 50 μs pulses and 50 Hz repetition frequency. This figure has been published in Ref. 157. 91
- Fig. 48: Lifetime measurements of six 2 mm long and 150 μm wide laser stripes, driven in CW mode at a heat sink temperature of 50°C at two different drive currents. The measurement was interrupted after 910 hours. The depiction of the temporal offset between both measurements is arbitrary. The inset shows lasing spectra near

- threshold at 0.6 A, and at 2.5 A. This figure has been published in Ref. 157..... 92
- Fig. 49: (a) Schematic diagram of a double-barrier DHS QW injection laser. (b) Temperature dependence of the threshold current of a QW laser with and without double-barrier design. 94
- Fig. 50: Electroluminescence spectra of a $100\text{ }\mu\text{m} \times 2\text{ mm}$ ridge-waveguide laser with a threshold current density of 60 A/cm^2 , driven in pulsed mode (500 ns, 5 kHz). The laser structure was grown with alternative precursors only. Laser spectra were recorded with monochromator slit widths reduced from 1 to 0.1 mm, leading to a signal decrease by about 100. Peaks at $1.01\text{ }\mu\text{m}$ stem from the laboratory lighting. Dotted line: PL of a single QD layer excited with 5 W/cm^2 at 514.5 nm . This figure has been published in Ref. 161. 97
- Fig. 51: Threshold current densities of $100\text{ }\mu\text{m}$ wide ridge-waveguide lasers as a function of inverse cavity length. The dashed line shows a linear fit of the decadal logarithm of j_{th} . Inset: inverse differential quantum efficiency η_d as a function of cavity length. The devices were driven with 500 ns long current pulses at a repetition frequency of 5 kHz. This figure has been published in Ref. 161..... 98
- Fig. 52: Threshold current vs. inverse cavity length of a laser diodes based on a 10-fold stack of $\text{In}_{0.65}\text{Ga}_{0.35}\text{As}/\text{In}_{0.2}\text{Ga}_{0.8}\text{As}/\text{GaAs}$ QD sheets. The stripe width is $50\text{ }\mu\text{m}$. The inset shows a lasing spectrum of a 2.3 mm long and $50\text{ }\mu\text{m}$ wide device at room temperature. This figure has been published in Ref. 15. 99
- Fig. 53: Schematic overview of the two-step oxidation process used for the fabrication of single-QW VCSELs with oxide aperture and all-oxide DBRs (cf. text). After Ref. {Hopfer, #947}..... 102
- Fig. 54: (a) L - I -characteristics and (b) spectra below and above lasing threshold of a QW VCSEL with an aperture diameter of $25\text{ }\mu\text{m}$. The threshold current density is 400 A/cm^2 103
- Fig. 55: (a) Reflection spectra and EL spectra of a single-InGaAs-QW oxide-DBR VCSEL with a $25\text{ }\mu\text{m}$ aperture. The reflection shows a weak cavity dip. (b) Microscopic image of an oxide-DBR QW VCSEL with a $25\text{ }\mu\text{m}$ aperture. (c) Nearfield distribution of the same device at an averaged output power of $13\text{ }\mu\text{W}$ (duty cycle: 0.8 %). The nearfield was recorded using a Si-CCD camera having a rather low sensitivity at 1050 nm 104
- Fig. 56: Vertical refractive-index profile of the oxide-DBR quantum-dot VCSEL. The active region consists of 3 stacks of 3 QD layers each. The bold line denotes the refractive index, the thin line depicts the intensity of the optical field. The cavity is cladded by the bottom oxide DBR (left side, 7 pairs) and top oxide DBR (right side, 6 pairs) and contains the n -contact, the active region, the aperture, the p contact and

- an AlGaAs *p*-contact etch stop. The contact layers are marked by grey-shaded regions (cf. text)..... 106
- Fig. 57: *L-I* curve of a 3.5 μm aperture VCSEL with 4 top-mirror pairs. The threshold current is 280 μA at a bias voltage of 2.5 V, the maximum slope efficiency is 43 %, and the maximum output power amounts to 0.68 mW. Inset: Spectrum of a QD VCSEL with 5 top DBR pairs and a 3.5 μm aperture. Since the aperture is placed in a node of the optical wave, multimode operation can be observed even for such small apertures. The side-mode suppression ratio (SSR) is 35 dB..... 107
- Fig. 58: Threshold current densities of QD VCSELs with 5 top DBR pairs as a function of aperture diameter. For small apertures, current spreading is significant. The threshold current density therefore increases with decreasing aperture diameter..... 108

Bibliography

- ¹ R. V. Steele, *Semiconductor Laser Market Review and Forecast*, Proc. of the Laser Focus World Marketplace Seminar, San Jose, California, January 21 (2002).
- ² D. Bimberg, M. Grundmann, and N. N. Ledentsov, *Quantum Dot Heterostructures* (John Wiley & Sons, Chichester, 1998).
- ³ Y. Arakawa and H. Sakaki, *Multidimensional quantum well laser and temperature dependence of its threshold current*, Appl. Phys. Lett. **40**, 939 (1982).
- ⁴ M. Asada, Y. Miyamoto, and Y. Suematsu, *Gain and the threshold of three dimensional quantum-box lasers*, J. Quantum El. **QE-22**, 1915 (1986).
- ⁵ T. Takeuchi, Y.-L. Chang, A. Tandon, D. Bour, S. Corzine, R. Twist, M. Tan, and H.-C. Luan, *Low threshold 1.2 μm InGaAs quantum well lasers grown under low As/III ratio*, Appl. Phys. Lett. **80**, 2445 (2002).
- ⁶ X. W. Liu, A. A. Hopgood, B. F. Usher, H. Wang, and N. S. J. Braithwaite, *Formation of misfit dislocations during growth of $\text{In}_x\text{Ga}_{1-x}\text{As}/\text{GaAs}$ strained-layer heterostructures*, Semicond. Sci. Technol. **14**, 1154 (1999).
- ⁷ H. E. Li and K. Iga (Ed.), *Vertical-Cavity Surface-Emitting Laser Devices* (Springer, 2002).
- ⁸ N. N. Ledentsov, D. Bimberg, V. M. Ustinov, Z. I. Alferov, and J. A. Lott, *Self-Organized InGaAs Quantum Dots for Advanced Applications in Optoelectronics*, Jpn. J. Appl. Phys. (1) **41**, 949 (2002).
- ⁹ D. Bimberg, *Quantum Dots: Lasers and Amplifiers*, Proc. of the 28th International Symposium on Compound Semiconductors, Tokyo, Japan, 1-4 Oct (2001), p. 485.
- ¹⁰ D. Bimberg, M. Grundmann, F. Heinrichsdorff, N. N. Ledentsov, V. M. Ustinov, A. E. Zhukov, A. R. Kovsh, M. V. Maximov, Y. M. Shernyakov, B. V. Volovik, A. F. Tsatsul'nikov, P. S. Kop'ev, and Z. I. Alferov, *Quantum dot lasers: breakthrough in optoelectronics*, Thin Solid Films **376**, 235 (2000).
- ¹¹ M. Grundmann, *The present status of quantum dot lasers*, Physica E **5**, 167 (2000).
- ¹² F. Heinrichsdorff, C. Ribbat, M. Grundmann, and D. Bimberg, *High-power quantum-dot lasers at 1100 nm*, Appl. Phys. Lett. **76**, 556 (2000).
- ¹³ F. Heinrichsdorff, M.-H. Mao, N. Kirstaedter, A. Krost, D. Bimberg, A. O. Kosogov, and P. Werner, *Room-temperature continuous-wave*

- lasing from stacked InAs/GaAs quantum dots grown by metalorganic chemical vapor deposition*, Appl. Phys. Lett. **71**, 22 (1997).
- 14 N. N. Ledentsov, *Long-wavelength quantum-dot lasers on GaAs substrates: from media to device concepts*, J. Sel. Top. Quantum El. **8**, 1015 (2002).
 - 15 I. N. Kaiander, R. L. Sellin, T. Kettler, N. N. Ledentsov, and D. Bimberg, *Long Wavelength ($<1.24\ \mu\text{m}$) InGaAs/GaAs Quantum Dot Laser Grown by Alternative Precursor MOCVD*, subm. to Appl. Phys. Lett. (2003).
 - 16 J. von Neumann, *Collected Works* (Pergamon Press, Oxford, 1963), Vol. 5.
 - 17 R. N. Hall, G. E. Fenner, J. D. Kingsley, T. J. Soltys, and R. O. Carlson, *Coherent Light Emission From GaAs Junctions*, Phys. Rev. Lett. **9**, 366 (1962).
 - 18 N. Holonyak and S. F. Bevacqua, *Coherent (visible) light emission from Ga(As_{1-x}P_x) junctions*, Appl. Phys. Lett. **1**, 82 (1962).
 - 19 M. I. Nathan, W. P. Dumke, G. Burns, F. H. Dill, and G. I. Lasher, *Stimulated emission of radiation from GaAs p-n junctions*, Appl. Phys. Lett. **1**, 62 (1962).
 - 20 Z. I. Alferov and R. F. Kazarinov, *Semiconductor laser with electrical pumping*, Patent No. 181737 (1963).
 - 21 H. Kroemer, *Semiconductor laser with electrical pumping*, Patent No. 3309553 (1967).
 - 22 C. W. Wilmsen, H. Temkin, and L. A. Coldren (Ed.), *Vertical-Cavity Surface-Emitting Lasers* (Cambridge University Press, 1999).
 - 23 M. Grundmann, N. N. Ledentsov, O. Stier, J. Böhrer, D. Bimberg, V. M. Ustinov, P. S. Kop'ev, and Z. I. Alferov, *Nature of optical transitions in self-organized InAs/GaAs quantum dots*, Phys. Rev. B **53**, R10509 (1996).
 - 24 M. Grundmann, J. Christen, N. N. Ledentsov, J. Böhrer, D. Bimberg, S. S. Ruvimov, P. Werner, U. Richter, U. Gösele, J. Heydenreich, V. M. Ustinov, A. Y. Egorov, A. E. Zhukov, P. S. Kop'ev, and Z. I. Alferov, *Ultrannarrow Luminescence Lines from Single Quantum Dots*, Phys. Rev. Lett. **74**, 4043 (1995).
 - 25 O. Stier, *Electronic and Optical Properties of Quantum Dots and Wires in Berlin Studies in Solid State Physics*, ed. by C. Thomsen, D. Bimberg, M. Dähne, and W. Richter (Wissenschaft & Technik Verlag, Berlin, 2001), Vol. 7.
 - 26 Y. Miyamoto, *Light emission from a quantum-box structure by current injection*, Jpn. J. Appl. Phys. (2) **26**, L225 (1987).
 - 27 N. Kirstaedter, N. N. Ledentsov, M. Grundmann, D. Bimberg, V. M. Ustinov, S. S. Ruvimov, M. V. Maximov, P. S. Kop'ev, Z. I. Alferov,

- U. Richter, P. Werner, U. Gösele, and J. Heydenreich, *Low threshold, large T_0 injection laser emission from (InGa)As quantum dots*, *El. Lett.* **30**, 1416 (1994).
- ²⁸ N. N. Ledentsov, M. Grundmann, F. Heinrichsdorff, D. Bimberg, V. M. Ustinov, A. E. Zhukov, M. V. Maximov, Z. I. Alferov, and J. A. Lott, *Quantum-dot heterostructure lasers*, *J. Sel. Top. Quantum El.* **6**, 439 (2000).
- ²⁹ R. C. Miller, R. Dingle, A. C. Gossard, R. A. Logan, W. A. Nordland, and W. Wiegman, *Laser oscillation with optically pumped very thin GaAs-Al_xGa_{1-x}As multilayer structures and conventional double heterostructures*, *J. Appl. Phys.* **47**, 4509 (1976).
- ³⁰ Z. I. Alferov, V. M. Andreev, E. L. Portnoi, and M. K. Trukan, *AlAs-GaAs heterojunction injection lasers with a low room-temperature threshold*, *Fiz. Tverd. Tela* **9**, 279 (1969).
- ³¹ R. D. Dupuis, P. D. Dapkus, N. Holonyak, E. A. Rezek, and R. Chin, *Room-temperature laser operation of quantum-well Ga_(1-x)Al_xAs-GaAs laser diodes grown by metalorganic chemical vapor deposition*, *Appl. Phys. Lett.* **32**, 295 (1978).
- ³² N. N. Ledentsov, V. M. Ustinov, A. Y. Egorov, A. E. Zhukov, M. V. Maximov, I. G. Tabatadze, and P. S. Kop'ev, *Optical properties of heterostructures with InGaAs-GaAs quantum clusters*, *Fiz. i Tekn. Poluprovodn.* **28**, 1484 (1993).
- ³³ Z. I. Alferov, V. M. Andreev, D. Z. Garbuzov, Y. V. Zhilyaev, E. P. Morozov, E. L. Portnoi, and V. G. Trofim, *Effect of heterostructure parameters on the laser threshold current and the realization of continuous generation at room temperature*, *Sov. Phys. Semicond.* **4**, 1573 (1970).
- ³⁴ I. Hayashi, M. B. Panish, P. W. Foy, and S. Sumski, *Junction lasers which operate continuously at room temperature*, *Appl. Phys. Lett.* **17**, 109 (1970).
- ³⁵ W. T. Tsang, *Extremely low threshold (Al,Ga)As modified multi-quantum well heterostructure lasers grown by molecular beam epitaxy*, *Appl. Phys. Lett.* **39**, 786 (1981).
- ³⁶ W. T. Tsang, *Extremely low threshold (Al,Ga)As graded-index waveguide separate confinement heterostructure lasers grown by molecular beam epitaxy*, *Appl. Phys. Lett.* **40**, 217 (1982).
- ³⁷ N. N. Ledentsov, M. Grundmann, N. Kirstaedter, O. Schmidt, R. Heitz, J. Böhrer, D. Bimberg, V. M. Ustinov, V. A. Shchukin, A. Y. Egorov, A. E. Zhukov, S. Zaitsev, P. S. Kop'ev, Z. I. Alferov, S. S. Ruvimov, A. O. Kosogov, P. Werner, U. Gösele, and J. Heydenreich, *Ordered Arrays of Quantum Dots: Formation, Electronic Spectra, Relaxation Phenomena, Lasing*, *Sol. St. Electron.* **40**, 785 (1996).

- 38 Z. I. Alferov, A. M. Vasiliev, S. V. Ivanov, P. S. Kop'ev, N. N. Ledentsov, B. Y. Meltser, and V. M. Ustinov, *Reduction of the threshold current density (52 A/cm^2 , 300K) in SCH GaAs-AlGaAs lasers by using a quantum well confined by a variable-step short-period superlattice*, Sov. Phys. Techn. Phys. Lett. **14**, 782 (1988).
- 39 Z. I. Alferov, S. V. Ivanov, P. S. Kop'ev, N. N. Ledentsov, M. E. Lutsenko, M. I. Nemenov, B. Y. Meltser, V. M. Ustinov, and S. V. Shaposhnikov, *Spreading and surface recombination in quantum well (Al,Ga)As double heterostructure separate confinement lasers with a broad stripe*, Sov. Phys. Semicond. **24**, 92 (1990).
- 40 G. T. Liu, H. Li, K. J. Malloy, and L. F. Lester, *Extremely low room-temperature threshold current density diode lasers using InAs dots in $\text{In}_{0.15}\text{Ga}_{0.85}\text{As}$ quantum well*, El. Lett. **35**, 1163 (1999).
- 41 N. Chand, E. E. Becker, J. P. van der Ziel, S. N. G. Chu, and N. K. Dutta, *Excellent uniformity and very low ($<50 \text{ A/cm}^2$) threshold current density strained InGaAs quantum well diode lasers on GaAs substrate*, Appl. Phys. Lett. **58**, 1704 (1991).
- 42 P. G. Eliseev, H. Li, A. Stintz, G. T. Liu, T. C. Newell, K. J. Malloy, and L. F. Lester, *Transition dipole moment of InAs/InGaAs quantum dots from experiments on ultralow-threshold laser diodes*, Appl. Phys. Lett. **77**, 262 (2000).
- 43 M. Grundmann and D. Bimberg, *Gain and Threshold of Quantum Dot Lasers: Theory and Comparison to Experiments*, Jpn. J. Appl. Phys. (1) **36**, 4181 (1997).
- 44 N. N. Ledentsov, A. E. Zhukov, A. R. Kovsh, N. A. Maleev, S. S. Mikhlin, A. P. Vasile'ev, E. S. Semenova, M. V. Maximov, Y. M. Shernyakov, N. V. Kryzhanovskaya, V. M. Ustinov, and D. Bimberg, *High performance quantum dot lasers on GaAs substrates operating in the $1.5 \mu\text{m}$ range*, El. Lett. **39**, 1126 (2003).
- 45 A. Passaseo, G. Maruccio, M. D. Vittorio, R. Rinaldi, and R. Cingolani, *Wavelength control from 1.25 to $1.4 \mu\text{m}$ in $\text{In}_x\text{Ga}_{1-x}\text{As}$ quantum dot structures grown by metal organic chemical vapor deposition*, Appl. Phys. Lett. **78**, 1382 (2001).
- 46 V. M. Ustinov, A. Y. Egorov, A. E. Zhukov, A. R. Kovsh, N. N. Ledentsov, M. V. Maximov, B. V. Volovik, A. F. Tsatsul'nikov, P. S. Kop'ev, Z. I. Alferov, I. P. Soshnikov, N. Zakharov, P. Werner, and D. Bimberg, *$1.75 \mu\text{m}$ emission from self-organized InAs quantum dots on GaAs*, J. Crystal Growth **201/202**, 1143 (1999).
- 47 Y. M. Shernyakov, D. A. Bedarev, E. Y. Kondrat'eva, P. S. Kop'ev, A. R. Kovsh, N. A. Maleev, M. V. Maximov, S. S. Mikhlin, A. F. Tsatsul'nikov, V. M. Ustinov, B. V. Volovik, A. E. Zhukov, Z. I. Alferov, N. N. Ledentsov, and D. Bimberg, *$1.3 \mu\text{m}$ GaAs-based laser us-*

- ing quantum dots obtained by activated spinodal decomposition, *El. Lett.* **35**, 898 (1999).
- 48 A. E. Zhukov, A. R. Kovsh, A. Y. Egorov, N. A. Maleev, V. M. Ustinov, B. V. Volovik, M. V. Maksimov, A. F. Tsatsul'nikov, N. N. Ledentsov, Y. M. Shernyakov, A. V. Luniv, Y. G. Musikhin, N. A. Bert, P. S. Kop'ev, and Z. I. Alferov, *Photo- and electroluminescence in the 1.3 μm wavelength range from quantum-dot structures grown on GaAs substrates*, *Semiconductors* **33**, 153 (1999).
- 49 M. V. Maximov, A. F. Tsatsul'nikov, B. V. Volovik, D. S. Sizov, Y. M. Shernyakov, I. N. Kaiander, A. E. Zhukov, A. R. Kovsh, S. S. Mikhrin, V. M. Ustinov, and Z. I. Alferov, *Tuning quantum dot properties by activated phase separation of an InGa(Al)As alloy grown on InAs stressors*, *Phys. Rev. B* **62**, 16671 (2000).
- 50 Y. Arakawa, *Progress in Self-Assembled Quantum Dots for Optoelectronic Device Application*, *IEICE Trans. El.* **E85-C**, 37 (2002).
- 51 N. A. Maleev, A. R. Kovsh, A. E. Zhukov, S. S. Mikhrin, A. P. Vasil'ev, Y. M. Shernyakov, D. A. Livshits, M. V. Maximov, V. M. Ustinov, and Z. I. Alferov, *High-performance long-wavelength QD diode lasers on GaAs substrates*, *Proc. of the 18th International Conference on Semiconductor Lasers*, Garmisch, Germany, Sept 30 - Oct 3, 2002 (2002), Vol. 1, p. 153.
- 52 G. Park, O. B. Shchekin, S. Csutak, D. L. Huffaker, and D. G. Deppe, *Room-temperature continuous-wave operation of a single-layered 1.3 μm quantum dot laser*, *Appl. Phys. Lett.* **75**, 3267 (1999).
- 53 J. A. Lott, N. N. Ledentsov, V. M. Ustinov, Z. I. Alferov, and D. Bimberg, *Continuous wave 1.3 μm InAs-InGaAs quantum dot VCSELs on GaAs substrates*, *Proc. of the 13th Int. Conf. Ind. Phosph. Rel. Mat. (IPRM)* (2001), p. 137.
- 54 H. Y. Liu, M. Hopkinson, C. N. Harrison, M. J. Steer, R. Frith, I. R. Sellers, D. J. Mowbray, and M. S. Skolnick, *Optimizing the growth of 1.3 μm InAs/InGaAs dots-in-a-well structure*, *J. Appl. Phys.* **93**, 2931 (2003).
- 55 K. Nishi, H. Saito, S. Sugou, and J.-S. Lee, *A narrow photoluminescence linewidth of 21 meV at 1.35 μm from strain-reduced InAs quantum dots covered by In_{0.2}Ga_{0.8}As grown on GaAs substrates*, *Appl. Phys. Lett.* **74**, 1111 (1999).
- 56 L. F. Lester, A. Stintz, H. Li, T. C. Newell, E. A. Pease, B. A. Fuchs, and K. J. Malloy, *Optical characteristics of 1.24- μm InAs quantum-dot laser diodes*, *Phot. Techn. Lett.* **11**, 931 (1999).
- 57 V. M. Ustinov, N. A. Maleev, A. E. Zhukov, A. R. Kovsh, A. Y. Egorov, A. V. Lunev, B. V. Volovik, I. L. Krestnikov, Y. G. Musikhin, N. A. Bert, P. S. Kop'ev, Z. I. Alferov, N. N. Ledentsov,

- and D. Bimberg, *InAs/InGaAs quantum dot structures on GaAs substrates emitting at 1.3 μm* , Appl. Phys. Lett. **74**, 2815 (1999).
- ⁵⁸ P. G. Eliseev, H. Li, G. T. Liu, A. Stintz, T. C. Newell, L. F. Lester, and K. J. Malloy, *Ground-State Emission and Gain in Ultralow-Threshold InAs–InGaAs Quantum-Dot Lasers*, J. Sel. Top. Quantum El. **7**, 135 (2001).
- ⁵⁹ R. Krebs, F. Klopff, J. P. Reithmaier, and A. Forchel, *High Performance 1.3 μm Quantum-Dot Lasers*, Jpn. J. Appl. Phys. (1) **41**, 1158 (2002).
- ⁶⁰ H. Zellmer, S. Buteau, A. Tünnermann, and H. Welling, *All fibre laser system with 0.1 W output power in blue spectral range*, El. Lett. **33**, 1383 (1997).
- ⁶¹ E. B. Mejía, A. N. Starodumov, and Y. O. Barmenkov, *Blue and infrared up-conversion in Tm^{3+} -doped fluorozirconate fiber pumped at 1.06, 1.117, and 1.18 μm* , Appl. Phys. Lett. **74**, 1540 (1999).
- ⁶² F. Klopff, J. P. Reithmaier, and A. Forchel, *980 nm Quantum Dot Lasers with Very Small Threshold Current Densities*, phys. stat. sol. (b) **3**, 845 (2001).
- ⁶³ S. S. Mikhlin, A. E. Zhukov, A. R. Kovsh, N. A. Maleev, V. M. Ustinov, Y. M. Shernyakov, I. P. Soshnikov, D. A. Livshits, I. S. Tarasov, D. A. Bedarev, B. V. Volovik, M. V. Maximov, A. F. Tsatsul'nikov, N. N. Ledentsov, and P. S. Kop'ev, *0.94 μm diode lasers based on Stranski-Krastanow and sub-monolayer quantum dots*, Semicond. Sci. Technol. **15**, 1061 (2000).
- ⁶⁴ J. Porsche, M. Ost, F. Scholz, A. Fantini, F. Phillipp, T. Riedl, and A. Hangleiter, *Growth of self-assembled InP quantum islands for red-light-emitting injection lasers*, J. Sel. Top. Quantum El. **6**, 482 (2000).
- ⁶⁵ T. Riedl, A. Hangleiter, J. Porsche, and F. Scholz, *Small-signal modulation response of InP/GaInP quantum-dot lasers*, Appl. Phys. Lett. **80**, 4015 (2002).
- ⁶⁶ P. Borri, S. Schneider, W. Langbein, U. Woggon, A. E. Zhukov, N. N. Ledentsov, Z. I. Alferov, D. Ouyang, and D. Bimberg, *Ultrafast carrier dynamics and dephasing in InAs quantum dot amplifiers emitting near 1.3 μm -wavelength at room temperature*, Appl. Phys. Lett. **79**, 2633 (2001).
- ⁶⁷ P. Borri, *Ultrafast Optical Properties of Quantum Dot Amplifiers in Nano-Optoelectronics*, ed. by M. Grundmann (Springer, Berlin, Heidelberg, 2002), p. 411.
- ⁶⁸ P. Bhattacharya and S. Ghosh, *Tunnel injection $\text{In}_{0.4}\text{Ga}_{0.6}\text{As}/\text{GaAs}$ quantum dot lasers with 15 GHz modulation bandwidth at room temperature*, Appl. Phys. Lett. **80**, 3482 (2002).

- ⁶⁹ C. Ribbat, R. Sellin, I. Kaiander, F. Hopfer, N. N. Ledentsov, D. Bimberg, A. R. Kovsh, V. M. Ustinov, A. E. Zhukov, and M. V. Maximov, *Complete suppression of filamentation and superior beam quality in quantum-dot lasers*, Appl. Phys. Lett. **82**, 952 (2003).
- ⁷⁰ N. Kirstaedter, O. G. Schmidt, N. N. Ledentsov, D. Bimberg, V. M. Ustinov, A. Y. Egorov, A. E. Zhukov, M. V. Maximov, P. S. Kop'ev, and Z. I. Alferov, *Gain and differential gain of single layer InAs/GaAs quantum dot injection lasers*, Appl. Phys. Lett. **69**, 1226 (1996).
- ⁷¹ K. Haberland, *Optical in-situ Studies during Metal-Organic Vapor Phase Epitaxy with respect to III-V-Device Production in Berlin Studies in Solid State Physics*, ed. by C. Thomsen, D. Bimberg, M. Dähne, and W. Richter (Wissenschaft & Technik Verlag, Berlin, 2002).
- ⁷² F. Heinrichsdorff, A. Krost, D. Bimberg, A. O. Kosogov, and P. Werner, *Self organized defect free InAs/GaAs and InAs/InGaAs/GaAs quantum dots with high lateral density grown by MOCVD*, Appl. Surf. Sci. **123/124**, 725 (1998).
- ⁷³ R. Sellin, F. Heinrichsdorff, C. Ribbat, M. Grundmann, U. W. Pohl, and D. Bimberg, *Surface flattening during MOCVD of thin GaAs layers covering InGaAs quantum dots*, J. Crystal Growth **221**, 581 (2000).
- ⁷⁴ M. Grundmann, O. Stier, S. Bognár, C. Ribbat, F. Heinrichsdorff, and D. Bimberg, *Optical Properties of Self-Organized Quantum Dots: Modeling and Experiments*, phys. stat. sol. (a) **178**, 255 (2000).
- ⁷⁵ V. A. Haisler, F. Hopfer, R. L. Sellin, A. Lochmann, K. Fleischer, N. Esser, W. Richter, N. N. Ledentsov, D. Bimberg, C. Möller, and N. Grote, *Micro-Raman studies of vertical-cavity surface-emitting lasers with Al_xO_y /GaAs distributed Bragg reflectors*, Appl. Phys. Lett. **81**, 2544 (2002).
- ⁷⁶ F. Hopfer, *Oberflächenemittierende Quantenpunktlaser*, Ph.D. thesis (Technische Universität Berlin), to be published.
- ⁷⁷ W. Stolz, *Alternative N-, P- and As-precursors for III/V-epitaxy*, J. Crystal Growth **209**, 272 (2000).
- ⁷⁸ G. B. Stringfellow, *Organometallic Vapor-Phase Epitaxy* (Academic Press, 2nd edition, 1999).
- ⁷⁹ F. Höhnsdorf, J. Koch, C. Agert, and W. Stolz, *Investigations of (GaIn)(NAs) bulk layers and (GaIn)(NAs)/GaAs multiple quantum well structures grown using tertiarybutylarsine (TBAs) and 1,1-dimethylhydrazine (UDMH₂)*, J. Crystal Growth **195**, 391 (1998).
- ⁸⁰ M. P. Chase, M. D. Deal, and J. D. Plummer, *Diffusion modeling of zinc implanted into GaAs*, J. Appl. Phys. **81**, 1670 (1997).
- ⁸¹ F. Brunner, T. Bergunde, E. Richter, P. Kurpas, M. Achouche, A. Maaßdorf, J. Würfl, and M. Weyers, *Carbon doping for the GaAs*

- base layer of Heterojunction Bipolar Transistors in a production scale MOVPE reactor, *J. Crystal Growth* **221**, 53 (2000).
- 82 K. Tateno, Y. Kohama, and C. Amano, *Carbon doping and etching effects of CBr_4 during metalorganic chemical vapor deposition of GaAs and AlAs*, *J. Crystal Growth* **172**, 5 (1997).
- 83 U. W. Pohl, K. Knorr, C. Möller, U. Gernert, W. Richter, J. Bläsing, J. Christen, J. Gottfriedsen, and H. Schumann, *Low-Temperature Metalorganic Vapor Phase Epitaxy (MOVPE) of GaN using Tertiarybutylhydrazine*, *Jpn. J. Appl. Phys. (2)* **38**, L105 (1999).
- 84 D. K. Maude, *DX centres in GaAs in Properties of Gallium Arsenide*, ed. by M. R. Brozel (INSPEC, London, 1996), Vol. XXVII, p. 250.
- 85 Y.-M. Houn and T. S. Low, *Te doping of GaAs and $Al_xGa_{1-x}As$ using diethyltellurium in low pressure OMVPE*, *J. Crystal Growth* **77**, 272 (1986).
- 86 L. G. Salmon and I. J. D'Haenens, *The effect of aluminum composition on silicon donor behavior in $Al_xGa_{1-x}As$* , *J. Vac. Sci. Technol. B* **2**, 197 (1984).
- 87 S. Z. Sun, E. A. Armour, K. Zheng, and C. F. Schaus, *Zinc and tellurium doping in GaAs and $Al_xGa_{1-x}As$ grown by MOCVD*, *J. Crystal Growth* **113**, 103 (1991).
- 88 S. Leu, H. Protzmann, F. Höhnsdorf, W. Stolz, J. Steinkirchner, and E. Hufgard, *Si-doping of MOVPE grown InP and GaAs by using the liquid Si source ditertiarybutyl silane*, *J. Crystal Growth* **195**, 91 (1998).
- 89 W. Stolz and T. Whitaker, *TBAs and TBP - Improved Group V Sources for MOVPE*, *Compound Semiconductors* **5**, 29 (1999).
- 90 P. Kurpas, *Untersuchungen zur Eignung alternativer Phosphor- und Arsen-Ausgangsstoffe für die Metallorganische Gasphasenepitaxie (MOVPE)* (Shaker Verlag, Aachen, 1995).
- 91 R. M. Lum, J. K. Klingert, D. W. Kisker, D. M. Tennant, M. D. Morris, D. L. Malm, J. Kovalchick, and L. A. Heimbrook, *Investigation of carbon incorporation in GaAs using ^{13}C -enriched trimethylarsenic and $^{13}CH_4$* , *J. Electron. Mat.* **17**, 101 (1988).
- 92 R. M. Lum, J. K. Klingert, and M. G. Lamont, *Comparison of alternate As-sources to arsine in the MOCVD growth of GaAs*, *J. Crystal Growth* **89**, 137 (1988).
- 93 T. Kobayashi and N. Inoue, *Carbon-doped GaAs grown by metalorganic vapor phase epitaxy using TMAs and TEG*, *J. Crystal Growth* **102**, 183 (1990).
- 94 G. Haacke, S. P. Watkins, and H. Burkhard, *Metalorganic chemical vapor deposition of high-purity GaAs using tertiarybutylarsine*, *Appl. Phys. Lett.* **54**, 2029 (1989).

- ⁹⁵ R. Beccard, G. Lengeling, D. Schmitz, Y. Gigase, and H. Jürgensen, *Replacements of hydrides by TBAs and TBP for the growth of various III-V materials in production scale MOVPE reactors*, J. Crystal Growth **170**, 97 (1997).
- ⁹⁶ G. B. Stringfellow, *Novel precursors for organometallic vapor phase epitaxy*, J. Crystal Growth **128**, 503 (1993).
- ⁹⁷ J. Mimila-Arroyo, A. Lusson, J. Chevallier, M. Barbé, B. Theys, F. Jomard, and S. W. Bland, *Carbon acceptor doping efficiency in GaAs grown by metalorganic chemical vapor deposition*, Appl. Phys. Lett. **79**, 3095 (2001).
- ⁹⁸ K. Watanabe and H. Yamazaki, *Characterization of annealed heavily C-doped p^+ -AlGaAs*, J. Appl. Phys. **74**, 5587 (1993).
- ⁹⁹ S. Krishna, S. Raghavan, A. L. Gray, A. Stintz, and K. J. Malloy, *Characterization of rapid-thermal-annealed InAs/In_{0.15}Ga_{0.85}As dots-in-well heterostructure using double crystal x-ray diffraction and photoluminescence*, Appl. Phys. Lett. **80**, 3898 (2002).
- ¹⁰⁰ F. Heinrichsdorff, M. Grundmann, O. Stier, A. Krost, and D. Bimberg, *Influence of In/Ga intermixing on the optical properties of In-GaAs/GaAs quantum dots*, J. Crystal Growth **195**, 540 (1998).
- ¹⁰¹ R. Leon, S. Fafard, P. G. Piva, S. Ruvimov, and Z. Liliental-Weber, *Tunable intersublevel transitions in self-forming semiconductor quantum dots*, Phys. Rev. B **58**, R4262 (1998).
- ¹⁰² H. Kakinuma, M. Mohri, and M. Akiyama, *Characterization of Oxygen and Carbon in Undoped AlGaAs Grown by Organometallic Vapor-Phase Epitaxy*, Jpn. J. Appl. Phys. (1) **36**, 23 (1997).
- ¹⁰³ S. Leu, F. Höhnsdorf, W. Stolz, R. Becker, A. Salzmann, and A. Greiling, *C- and O-incorporation in (AlGa)As epitaxial layers grown by MOVPE using TBAs*, J. Crystal Growth **195**, 98 (1998).
- ¹⁰⁴ F. Reinhardt, B. Dwir, and E. Kapon, *Oxidation of GaAs/AlGaAs heterostructures studied by atomic force microscopy in air*, Appl. Phys. Lett. **68**, 3168 (1996).
- ¹⁰⁵ F. Reinhardt, B. Dwir, G. Biasiol, and E. Kapon, *Atomic force microscopy of III-V nanostructures in air*, Appl. Surf. Sci. **104-105**, 529 (1996).
- ¹⁰⁶ A. Krost, G. Bauer, and J. Woitok, *High Resolution X-Ray Diffraction in Optical Characterization of Epitaxial Semiconductor Layers*, ed. by G. Bauer and W. Richter (Springer, Berlin, 1996), p. 287.
- ¹⁰⁷ S. A. Furman and A. V. Tikhonravov, *Optics of Multilayer Systems* (Editions Frontières, 1992).
- ¹⁰⁸ R. Westphalen, G. Landgren, B. Stalnacke, and R. Beccard, *Improved homogeneity of LP-MOVPE grown InP/GaInAsP heterostructure for DBR using an optimized liner and susceptor arrangement*, Proc. of the

- 11th Int. Conf. Ind. Phosph. Rel. Mat. (IPRM), Davos, Switzerland, May 16-20 (1999), p. 139.
- ¹⁰⁹ K. D. Choquette, K. M. Geib, C. I. H. Ashby, R. D. Twisten, O. Blum, H. Q. Hou, D. M. Follstaedt, B. E. Hammons, D. Mathes, and R. Hull, *Advances in Selective Wet Oxidation of AlGaAs Alloys*, J. Sel. Top. Quantum El. **3**, 916 (1997).
- ¹¹⁰ K. D. Choquette, K. M. Geib, H. C. Chui, B. E. Hammons, H. Q. Hou, T. J. Drummond, and R. Hull, *Selective oxidation of buried AlGaAs versus AlAs layers*, Appl. Phys. Lett. **69**, 1385 (1996).
- ¹¹¹ H. Q. Jia, H. Chen, W. C. Wang, W. X. Wang, W. Li, Q. Huang, J. Zhou, and Q. K. Xue, *Improved thermal stability of wet-oxidized AlAs*, Appl. Phys. Lett. **80**, 974 (2002).
- ¹¹² S. Ruvimov, P. Werner, K. Scheerschmidt, U. Gösele, J. Heydenreich, U. Richter, N. N. Ledentsov, M. Grundmann, D. Bimberg, V. M. Ustinov, A. Y. Egorov, P. S. Kop'ev, and Z. I. Alferov, *Structural characterization of (In,Ga)As quantum dots in a GaAs matrix*, Phys. Rev. B **51**, 14766 (1995).
- ¹¹³ J. Oshinowo, M. Nishioka, S. Ishida, and Y. Arakawa, *Highly uniform InGaAs/GaAs quantum dots (15 nm) by metalorganic chemical vapor deposition*, Appl. Phys. Lett. **65**, 1421 (1994).
- ¹¹⁴ J. Márquez, L. Geelhaar, and K. Jacobi, *Atomically resolved structure of InAs quantum dots*, Appl. Phys. Lett. **78**, 2309 (2001).
- ¹¹⁵ D. Leonard, M. Krishnamurthy, C. M. Reaves, S. P. Denbaars, and P. M. Petroff, *Direct formation of quantum-sized dots from uniform coherent islands of InGaAs on GaAs surfaces*, Appl. Phys. Lett. **63**, 3203 (1993).
- ¹¹⁶ U. Woggon, W. Langbein, J. M. Hvam, A. Rosenauer, T. Remmele, and D. Gerthsen, *Electron microscopic and optical investigations of the indium distribution in GaAs capped $\text{In}_x\text{Ga}_{1-x}\text{As}$ islands*, Appl. Phys. Lett. **71**, 377 (1997).
- ¹¹⁷ J. W. Gibbs, *Collected Works* (Longmans, London, 1928), Vol. 1 (*Thermodynamics*).
- ¹¹⁸ C. Herring, *Some Theorems on the Free Energies of Crystal Surfaces*, Phys. Rev. **82**, 87 (1951).
- ¹¹⁹ V. A. Shchukin and D. Bimberg, *Spontaneous ordering of nanostructures on crystal surfaces*, Rev. Mod. Phys. **71**, 1125 (1999).
- ¹²⁰ F. C. Frank and J. H. van der Merve, *One-dimensional dislocations*, Proc. Roy. Soc. London A **198**, 205 (1949).
- ¹²¹ M. Volmer and A. Weber, *Keimbildung in übersättigten Gebilden*, Z. Physik. Chem. **119**, 277 (1926).

- ¹²² I. N. Stranski and L. Krastanow, *Zur Theorie der orientierten Ausscheidung von Ionenkristallen aufeinander*, Sitzungsber. Akad. Wiss. Wien, Math.-Naturwiss. Klasse **146**, 797 (1937).
- ¹²³ T. R. Ramachandran, A. Madhukar, I. Mukhametzhanov, R. Heitz, A. Kalburge, Q. Xie, and P. Chen, *Nature of Stranski–Krastanow growth of InAs on GaAs(001)*, J. Vac. Sci. Technol. B **13**, 1330 (1998).
- ¹²⁴ W. Ostwald, *Über die vermeintliche Isomerie des roten und gelben Quecksilberoxyds und die Oberflächenspannung fester Körper*, Z. Physik. Chem. **34**, 495 (1900).
- ¹²⁵ L. G. Wang, P. Kratzer, M. Scheffler, and N. Moll, *Formation and Stability of Self-Assembled Coherent Islands in Highly Mismatched Heteroepitaxy*, Phys. Rev. Lett. **82**, 4042 (1999).
- ¹²⁶ A.-L. Barabási, *Self-assembled island formation in heteroepitaxial growth*, Appl. Phys. Lett. **70**, 2565 (1997).
- ¹²⁷ M. Meixner, E. Schöll, V. A. Shchukin, and D. Bimberg, *Self-Assembled Quantum Dots: Crossover from Kinetically Controlled to Thermodynamically Limited Growth*, Phys. Rev. Lett. **87**, 236101 (2001).
- ¹²⁸ C. Priester and M. Lannoo, *Origin of Self-Assembled Quantum Dots in Highly Mismatched Heteroepitaxy*, Phys. Rev. Lett. **75**, 93 (1995).
- ¹²⁹ V. A. Shchukin, N. N. Ledentsov, A. Hoffmann, D. Bimberg, I. P. Soshnikov, B. V. Volovik, V. M. Ustinov, D. Litvinov, and D. Gerthsen, *Entropy-Driven Effects in Self-Organized Formation of Quantum Dots*, phys. stat. sol. (b) **224**, 503 (2001).
- ¹³⁰ A. Rosenauer, T. Remmele, and D. Gerthsen, *Atomic scale strain measurements by the digital analysis of transmission electron microscopic lattice images*, Optik **105**, 99 (1997).
- ¹³¹ R. Leon, C. Lobo, X. Z. Liao, J. Zou, D. J. H. Cockayne, and S. Fafard, *Island shape instabilities and surfactant-like effects in the growth of InGaAs/GaAs quantum dots*, Thin Solid Films **357**, 40 (1999).
- ¹³² D. Leonard, K. Pond, and P. M. Petroff, *Critical layer thickness for self-assembled InAs islands on GaAs*, Phys. Rev. B **50**, 11687 (1994).
- ¹³³ G. S. Solomon, J. A. Trezza, and J. S. Harris, *Effects of monolayer coverage, flux ratio, and growth rate on the island density of InAs islands on GaAs*, Appl. Phys. Lett. **66**, 3161 (1995).
- ¹³⁴ R. Leon, C. Lobo, J. Zou, T. Romeo, and D. J. H. Cockayne, *Stable and Metastable InGaAs/GaAs Island Shapes and Surfactantlike Suppression of the Wetting Transformation*, Phys. Rev. Lett. **81**, 2486 (1998).

- ¹³⁵ R. E. Welser and L. J. Guido, *Evidence of two-species nucleation of InAs islands on (100) and (111)B GaAs substrates*, Appl. Phys. Lett. **68**, 912 (1996).
- ¹³⁶ M. Sopanen, H. Lipsanen, and J. Ahopelto, *Self-organized InP islands on (100) GaAs by metalorganic vapor phase epitaxy*, Appl. Phys. Lett. **67**, 3768 (1995).
- ¹³⁷ J. Johansson and W. Seifert, *Kinetics of self-assembled island formation: Part I - Island density*, J. Crystal Growth **234**, 132 (2002).
- ¹³⁸ P. B. Joyce, T. J. Krzyzewski, G. R. Bell, T. S. Jones, S. Malik, D. Childs, R. Murray, and S. Den Baars, *Growth rate effects on the size, composition and optical properties of InAs/GaAs quantum dots grown by molecular beam epitaxy*, J. Crystal Growth **227-228**, 1000 (2001).
- ¹³⁹ P. B. Joyce, T. J. Krzyzewski, G. R. Bell, T. S. Jones, E. C. Le Ru, and R. Murray, *Optimizing the growth of 1.3 μm InAs/GaAs quantum dots*, Phys. Rev. B **64**, 235317 (2001).
- ¹⁴⁰ I. Mukhametzhanov, Z. Wei, R. Heitz, and A. Madhukar, *Punctuated island growth: An approach to examination and control of quantum dot density, size, and shape evolution*, Appl. Phys. Lett. **75**, 85 (1999).
- ¹⁴¹ E. Steimetz, W. Richter, F. Schienle, D. Fischer, M. Klein, and J.-T. Zettler, *The Effect of Different Group V Precursors on the Evolution of Quantum Dots Monitored by Optical In Situ Measurements*, Jpn. J. Appl. Phys. (1) **37**, 1483 (1998).
- ¹⁴² F. Heinrichsdorff, *MOCVD growth and laser applications of In(Ga)As/GaAs Quantum Dots* (Mensch & Buch Verlag, Berlin, 1998).
- ¹⁴³ R. Sellin, N. N. Ledentsov, and D. Bimberg, *Verfahren zur Verbesserung der Effizienz von epitaktisch hergestellten Quantenpunkt-Halbleiterbauelementen mit einer oder mehreren Quantenpunktschichten*, Patent pending, ref. no. 10044040 (DE) (2000).
- ¹⁴⁴ K. Scheerschmidt and P. Werner, *TEM Characterization of Quantum Dots in Nano-Optoelectronics*, ed. by M. Grundmann (Springer, Berlin, Heidelberg, 2002), p. 67.
- ¹⁴⁵ M. Kasu and N. Kobayashi, *Equilibrium multiautomic step structure of GaAs(001) vicinal surfaces grown by metalorganic chemical vapor deposition*, Appl. Phys. Lett. **62**, 1262 (1993).
- ¹⁴⁶ N. N. Ledentsov, G. M. Gurianov, G. E. Tsyrlin, V. N. Petrov, Y. B. Samsonenko, A. O. Golubok, and S. Y. Tipisev, *Effect of heat-treatment conditions on the surface morphology of gallium arsenide grown on vicinal GaAs (100) substrates by molecular-beam epitaxy*, Semiconductors **28**, 526 (1994).

- ¹⁴⁷ M. Kasu and N. Kobayashi, *Surface kinetics of metalorganic vapor-phase epitaxy: surface diffusion, nucleus formation, sticking at steps*, J. Crystal Growth **174**, 513 (1997).
- ¹⁴⁸ T. Ito and K. Shiraishi, *A Theoretical Investigation of Migration Potentials of Ga Adatoms near Step Edges on GaAs(001)-c(4×4) Surface*, Jpn. J. Appl. Phys. (2) **35**, L1016 (1996).
- ¹⁴⁹ E. J. Heller and M. G. Lagally, *In-situ scanning tunneling microscopy observation of surface morphology of GaAs(001) grown by molecular beam epitaxy*, Appl. Phys. Lett. **60**, 2675 (1992).
- ¹⁵⁰ A. Kley, P. Ruggerone, and M. Scheffler, *Novel Diffusion Mechanism on the GaAs(001) Surface: The Role of Adatom-Dimer Interaction*, Phys. Rev. Lett. **79**, 5278 (1997).
- ¹⁵¹ V. Holý, G. Springholz, M. Pinczolits, and G. Bauer, *Strain Induced Vertical and Lateral Correlations in Quantum Dot Superlattices*, Phys. Rev. Lett. **83**, 356 (1999).
- ¹⁵² M. M. Sobolev, I. V. Kochnev, V. M. Lantratov, N. A. Bert, N. A. Cherkashin, N. N. Ledentsov, and D. A. Bedarev, *Thermal annealing of Defects in InGaAs/GaAs Heterostructures with Three-Dimensional Islands*, Semiconductors **34**, 195 (2000).
- ¹⁵³ P. D. Dapkus, H. M. Manasevit, K. L. Hess, T. S. Low, and G. E. Stillman, *High purity GaAs prepared from trimethylgallium and arsine*, J. Crystal Growth **55**, 10 (1981).
- ¹⁵⁴ N. N. Ledentsov, M. V. Maximov, D. Bimberg, T. Maka, C. M. S. Torres, I. V. Kochnev, I. L. Krestnikov, V. M. Lantratov, N. A. Cherkashin, Y. M. Musikhin, and Z. I. Alferov, *1.3 μm luminescence and gain from defect-free InGaAs–GaAs quantum dots grown by metal-organic chemical vapour deposition*, Semicond. Sci. Technol. **15**, 604 (2000).
- ¹⁵⁵ I. L. Krestnikov, N. A. Cherkashin, D. S. Sizov, D. A. Bedarev, I. V. Kochnev, V. M. Lantratov, and N. N. Ledentsov, *InGaAs Nanodomains Formed in situ on the Surface of (Al,Ga)As*, Tech. Phys. Lett. **27**, 233 (2001).
- ¹⁵⁶ R. L. Sellin, C. Ribbat, M. Grundmann, N. N. Ledentsov, and D. Bimberg, *Close-to-ideal device characteristics of high-power InGaAs/GaAs quantum dot lasers*, Appl. Phys. Lett. **78**, 1207 (2001).
- ¹⁵⁷ R. L. Sellin, C. Ribbat, D. Bimberg, F. Rinner, H. Konstanzer, M. T. Kelemen, and M. Mikulla, *High-reliability MOCVD-grown quantum dot laser*, El. Lett. **38**, 883 (2002).
- ¹⁵⁸ R. Leon, C. Lobo, A. Clark, R. Bozek, A. Wyszomolek, A. Kurpiewski, and M. Kaminska, *Different paths to tunability in III–V quantum dots*, J. Appl. Phys. **84**, 248 (1998).

- ¹⁵⁹ N. Moll, A. Kley, E. Pehlke, and M. Scheffler, *GaAs equilibrium crystal shape from first principles*, Phys. Rev. B **54**, 8844 (1996).
- ¹⁶⁰ E. Pehlke, N. Moll, A. Kley, and M. Scheffler, *Shape and stability of quantum dots*, Appl. Phys. A **65**, 525 (1997).
- ¹⁶¹ R. L. Sellin, I. Kaiander, D. Ouyang, T. Kettler, and D. Bimberg, *Alternative-precursor metalorganic chemical vapor deposition and laser application of self-organized InGaAs/GaAs quantum dots*, Appl. Phys. Lett. **82**, 841 (2003).
- ¹⁶² A. Y. Egorov, D. Bedarev, D. Bernklau, G. Dumitras, and H. Riechert, *Self-Assembled InAs Quantum Dots in an InGaAsN Matrix on GaAs*, phys. stat. sol. (b) **224**, 839 (2001).
- ¹⁶³ H. Saito, T. Makimoto, and N. Kobayashi, *MOVPE growth of strained InGaAsN/GaAs quantum wells*, J. Crystal Growth **195**, 416 (1998).
- ¹⁶⁴ W. J. Fan, S. F. Yoon, T. K. Ng, S. Z. Wang, W. K. Loke, R. Liu, and A. Wee, *Comparison of nitrogen compositions in the as-grown GaN_xAs_{1-x} on GaAs measured by high-resolution x-ray diffraction and secondary-ion mass spectroscopy*, Appl. Phys. Lett. **80**, 4136 (2002).
- ¹⁶⁵ W. Li, M. Pessa, and J. Likonen, *Lattice parameter in GaNAs epilayers on GaAs: Deviation from Vegard's law*, Appl. Phys. Lett. **78**, 2864 (2001).
- ¹⁶⁶ G. T. Liu, A. Stintz, H. Li, T. C. Newell, A. L. Gray, P. M. Varangis, K. J. Malloy, and L. F. Lester, *The Influence of Quantum-Well Composition on the Performance of Quantum Dot Lasers Using InAs/InGaAs Dots-in-a-Well (DWELL) Structures*, J. Quantum El. **36**, 1272 (2000).
- ¹⁶⁷ F. Guffarth, R. Heitz, A. Schliwa, O. Stier, N. N. Ledentsov, A. R. Kovsh, V. M. Ustinov, and D. Bimberg, *Strain engineering of self-organized InAs quantum dots*, Phys. Rev. B **64**, 85305 (2001).
- ¹⁶⁸ N.-T. Yeh, T.-E. Nee, and J.-I. Chyia, *Matrix dependence of strain-induced wavelength shift in self-assembled InAs quantum-dot heterostructures*, Appl. Phys. Lett. **76**, 1567 (2000).
- ¹⁶⁹ M. V. Maximov, A. F. Tsatsul'nikov, B. V. Volovik, D. A. Bedarev, A. E. Zhukov, A. R. Kovsh, N. A. Maleev, V. M. Ustinov, P. S. Kop'ev, Z. I. Alferov, R. Heitz, N. N. Ledentsov, and D. Bimberg, *Quantum dots formed by activated spinodal decomposition of InGa(Al)As alloy on InAs stressors*, Physica E **7**, 326 (2000).
- ¹⁷⁰ H. Y. Liu, X. D. Wang, B. Xu, D. Ding, W. H. Jiang, J. Wu, and Z. G. Wang, *Effect of In-mole-fraction in InGaAs overgrowth layer on self-assembled InAs/GaAs quantum dots*, J. Crystal Growth **213**, 193 (2000).
- ¹⁷¹ R. Heitz, I. Mukhametzhanov, A. Madhukar, A. Hoffmann, and D. Bimberg, *Temperature Dependent Optical Properties of Self-*

- Organized InAs/GaAs Quantum Dots*, J. Electron. Mat. **28**, 520 (1999).
- ¹⁷² O. Stier, M. Grundmann, and D. Bimberg, *Electronic and optical properties of strained quantum dots modeled by 8-band k - p theory*, Phys. Rev. B **59**, 5688 (1999).
- ¹⁷³ X. Z. Liao, J. Zou, D. J. H. Cockayne, R. Leon, and C. Lobo, *Indium Segregation and Enrichment in Coherent $\text{In}_x\text{Ga}_{1-x}\text{As}/\text{GaAs}$ Quantum Dots*, Phys. Rev. Lett. **82**, 5148 (1999).
- ¹⁷⁴ P. B. Hirsch, A. Howie, R. B. Nicholson, D. W. Pashley, and M. J. Whelan, *Electron Microscopy of Thin Crystals* (Butterworths, London, 1965), p. 161.
- ¹⁷⁵ J. A. Ibers and W. C. Hamilton (Ed.), *International Tables for X-Ray Crystallography* (Kynoch Press, Birmingham, Vol. IV, 1974), p. 155.
- ¹⁷⁶ A. E. Zhukov, A. R. Kovsh, N. A. Maleev, S. S. Mikhlin, V. M. Ustinov, A. F. Tsatsul'nikov, M. V. Maximov, B. V. Volovik, D. A. Bedarev, Y. M. Shernyakov, P. S. Kop'ev, and Z. I. Alferov, *Long-wavelength lasing from multiply stacked InAs/InGaAs quantum dots on GaAs substrates*, Appl. Phys. Lett. **75**, 1926 (1999).
- ¹⁷⁷ Q. Xie, P. Chen, and A. Madhukar, *InAs island-induced-strain driven adatom migration during GaAs overlayer growth*, Appl. Phys. Lett. **65**, 2051 (1994).
- ¹⁷⁸ M. Grundmann, O. Stier, and D. Bimberg, *InAs/GaAs pyramidal quantum dots: Strain distribution, optical phonons, and electronic structure*, Phys. Rev. B **52**, 11969 (1995).
- ¹⁷⁹ A. Lenz, R. Timm, H. Eisele, C. Hennig, S. K. Becker, R. L. Sellin, U. W. Pohl, D. Bimberg, and M. Dähne, *Reversed truncated cone composition distribution of $\text{In}_{0.8}\text{Ga}_{0.2}\text{As}$ quantum dots overgrown by an $\text{In}_{0.1}\text{Ga}_{0.9}\text{As}$ layer in a GaAs matrix*, Appl. Phys. Lett. **81**, 5150 (2002).
- ¹⁸⁰ W. Wu, J. R. Tucker, G. S. Solomon, and J. S. Harris, *Atom-resolved scanning tunneling microscopy of vertically ordered InAs quantum dots*, Appl. Phys. Lett. **71**, 1083 (1997).
- ¹⁸¹ B. Grandidier, Y. M. Niquet, B. Legrand, J. P. Nys, C. Priester, D. Stiévenard, J. M. Gérard, and V. Thierry-Mieg, *Imaging the Wave-Function Amplitudes in Cleaved Semiconductor Quantum Boxes*, Phys. Rev. Lett. **85**, 1068 (2000).
- ¹⁸² H. Eisele, *Cross-Sectional Scanning Tunneling Microscopy of InAs/GaAs Quantum Dots* in *Berlin Studies in Solid State Physics*, ed. by C. Thomsen, D. Bimberg, M. Dähne, and W. Richter (Wissenschaft & Technik Verlag, Berlin, 2002), Vol. 10.
- ¹⁸³ W. Barvosa-Carter, M. E. Twigg, M. J. Yang, and L. J. Whitman, *Microscopic characterization of $\text{InAs}/\text{In}_{0.28}\text{GaSb}_{0.72}/\text{InAs}/\text{AlSb}$ laser structure interfaces*, Phys. Rev. B **63**, 245311 (2001).

- ¹⁸⁴ R. M. Feenstra, J. A. Stroscio, J. Tersoff, and A. P. Fein, *Atom-selective imaging of the GaAs(110) surface*, Phys. Rev. Lett. **58**, 1192 (1987).
- ¹⁸⁵ P. Ebert, B. Engels, P. Richard, K. Schroeder, S. Blügel, C. Domke, M. Heinrich, and K. Urban, *Contribution of Surface Resonances to Scanning Tunneling Microscopy Images: (110) Surfaces of III-V Semiconductors*, Phys. Rev. Lett. **77**, 2997 (1996).
- ¹⁸⁶ O. Flebbe, H. Eisele, T. Kalka, F. Heinrichsdorff, A. Krost, D. Bimberg, and M. Dähne-Prietsch, *Atomic structure of stacked InAs quantum dots grown by metal-organic chemical vapor deposition*, J. Vac. Sci. Technol. B **17**, 1639 (1999).
- ¹⁸⁷ N. Grandjean, J. Massies, and O. Tottereau, *Surface segregation in (Ga,In)As/GaAs quantum boxes*, Phys. Rev. B **55**, R10189 (1997).
- ¹⁸⁸ K. Muraki, S. Fukatsu, Y. Shiraki, and R. Ito, *Surface segregation of In atoms during molecular beam epitaxy and its influence on the energy levels in InGaAs/GaAs quantum wells*, Appl. Phys. Lett. **61**, 557 (1992).
- ¹⁸⁹ H. Toyoshima, T. Niwa, J. Yamazaki, and A. Okamoto, *In surface segregation and growth-mode transition during InGaAs growth by molecular-beam epitaxy*, Appl. Phys. Lett. **63**, 821 (1993).
- ¹⁹⁰ H. Eisele, O. Flebbe, T. Kalka, F. Heinrichsdorff, A. Krost, D. Bimberg, and M. Dähne-Prietsch, *The Stoichiometry of InAs Quantum Dots Determined by Cross-Sectional Scanning Tunneling Microscopy*, phys. stat. sol. (b) **215**, 865 (1999).
- ¹⁹¹ H. Eisele, O. Flebbe, T. Kalka, C. Preinesberger, F. Heinrichsdorff, A. Krost, D. Bimberg, and M. Dähne-Prietsch, *Cross-sectional scanning-tunneling microscopy of stacked InAs quantum dots*, Appl. Phys. Lett. **75**, 106 (1999).
- ¹⁹² H. Eisele, O. Flebbe, T. Kalka, and M. Dähne-Prietsch, *Cross-sectional STM Study of InAs Quantum Dots for Laser Devices*, Surf. Interface Anal. **27**, 537 (1999).
- ¹⁹³ N. Liu, J. Tersoff, O. Baklenov, A. L. Holmes, and C. K. Shih, *Non-uniform Composition Profile in In_{0.5}Ga_{0.5}As Alloy Quantum Dots*, Phys. Rev. Lett. **84**, 334 (2000).
- ¹⁹⁴ P. W. Fry, I. E. Itskevich, D. J. Mowbray, M. S. Skolnick, J. J. Finley, J. A. Barker, E. P. O'Reilly, L. R. Wilson, I. A. Larkin, P. A. Maksym, M. Hopkinson, M. Al-Khafaji, J. P. R. David, A. G. Cullis, G. Hill, and J. C. Clark, *Inverted Electron-Hole Alignment in InAs-GaAs Self-Assembled Quantum Dots*, Phys. Rev. Lett. **74**, 733 (2000).
- ¹⁹⁵ W. Sheng and J.-P. Leburton, *Electron-hole alignment in InAs/GaAs self-assembled quantum dots: Effects of chemical composition and dot shape*, Phys. Rev. B **63**, R 161301 (2001).

- ¹⁹⁶ S. Sato and S. Satoh, *Metalorganic chemical vapor deposition of GaInNAs lattice matched to GaAs for long-wavelength laser diodes*, J. Crystal Growth **192**, 381 (1998).
- ¹⁹⁷ N. Tansu and L. J. Mawst, *Low-Threshold Strain-Compensated In-GaAs(N) ($\lambda=1.19\text{--}1.31\text{ }\mu\text{m}$) Quantum-Well Lasers*, Phot. Techn. Lett. **14**, 444 (2002).
- ¹⁹⁸ D. A. Livshits, A. Y. Egorov, and H. Riechert, *8 W continuous wave operation of InGaAsN lasers at 1.3 μm* , El. Lett. **36**, 1381 (2000).
- ¹⁹⁹ A. Ramakrishnan, G. Steinle, D. Supper, C. Degen, and G. Ebbinghaus, *Electrically pumped 10 Gbit/s MOVPE-grown monolithic 1.3 μm VCSEL with GaInNAs active region*, El. Lett. **38**, 322 (2002).
- ²⁰⁰ P. R. C. Kent and A. Zunger, *Evolution of III-V Nitride Alloy Electronic Structure: The Localized to Delocalized Transition*, Phys. Rev. Lett. **86**, 2613 (2001).
- ²⁰¹ S. Adachi, *GaAs and Related Materials* (World Scientific, Singapore, 1994).
- ²⁰² I. Vurgaftman, J. R. Meyer, and L. R. Ram-Mohan, *Band parameters for III-V compound semiconductors and their alloys*, J. Appl. Phys. **89**, 5815 (2001).
- ²⁰³ H. P. Hjalmarson, P. Vogel, D. J. Welford, and J. D. Dow, *Theory of Substitutional Deep Traps in Covalent Semiconductors*, Phys. Rev. Lett. **44**, 810 (1980).
- ²⁰⁴ W. Shan, W. Walukiewicz, J. W. Ager, E. E. Haller, J. F. Geisz, D. J. Friedman, J. M. Olson, and S. R. Kurtz, *Band Anticrossing in GaInNAs Alloys*, Phys. Rev. Lett. **82**, 1221 (1999).
- ²⁰⁵ D. Serries, T. Geppert, P. Ganser, M. Maier, K. Köhler, N. Herres, and J. Wagner, *Quaternary GaInAsN with high In content: Dependence of band gap energy on N content*, Appl. Phys. Lett. **80**, 2448 (2002).
- ²⁰⁶ T. Schmidtling, M. Klein, M. Pristovsek, K. Knorr, U. W. Pohl, and W. Richter, *MOVPE of GaAsN on GaAs(001) using tertiarybutylhydrazine*, Ext. Abstr. EWMOVPE VIII, Praha, 433 (1999).
- ²⁰⁷ S. Makino, T. Miyamoto, T. Kageyama, N. Nishiyama, F. Koyama, and K. Iga, *GaInNAs/GaAs quantum dots grown by chemical beam epitaxy*, J. Crystal Growth **221**, 561 (2000).
- ²⁰⁸ S. Makino, T. Miyamoto, T. Kageyama, Y. Ikenaga, F. Koyama, and K. Iga, *Nitrogen Composition and Growth Temperature Dependence of Growth Characteristics for Self-Assembled GaInNAs/GaAs Quantum Dots by Chemical Beam Epitaxy*, Jpn. J. Appl. Phys. (1) **41**, 953 (2002).
- ²⁰⁹ M. Sopanen, H. P. Xin, and C. W. Tu, *Self-assembled GaInNAs quantum dots for 1.3 and 1.55 μm emission on GaAs*, Appl. Phys. Lett. **76**, 994 (2000).

- 210 E. V. K. Rao, A. Ougazzaden, Y. L. Bellego, and M. Juhel, *Optical properties of low band gap GaAs_{1-x}N_x layers: Influence of post-growth treatments*, Appl. Phys. Lett. **72**, 1409 (1998).
- 211 H. P. Xin and C. W. Tu, *GaInNAs/GaAs multiple quantum wells grown by gas-source molecular beam epitaxy*, Appl. Phys. Lett. **72**, 2442 (1998).
- 212 M. R. Gokhale, J. Wei, H. Wang, and S. R. Forrest, *Growth and characterization of small band gap (~ 0.6 eV) InGaAsN layers on InP*, Appl. Phys. Lett. **74**, 1287 (1999).
- 213 A. Ougazzaden, S. Bouchoule, A. Mereuta, E. V. K. Rao, and J. Decobert, *Room temperature laser operation of bulk InGaAsN/GaAs structures grown by AP-MOVPE using N₂ as carrier gas*, El. Lett. **35**, 474 (1999).
- 214 E. Tournié, M.-A. Pinault, and A. Guzmán, *Mechanisms affecting the photoluminescence spectra of GaInNAs after post-growth annealing*, Appl. Phys. Lett. **80**, 4148 (2002).
- 215 J. M. Gérard, J. B. Génin, J. Levebre, J. M. Moison, N. Lebouché, and F. Barthe, *Optical investigation of the self-organized growth of InAs/GaAs quantum boxes*, J. Crystal Growth **150**, 351 (1995).
- 216 G. B. Stringfellow, J. K. Shurtle, R. T. Lee, C. M. Fetzer, and S. W. Jun, *Surface processes in OMVPE - the frontiers*, J. Crystal Growth **221**, 1 (2000).
- 217 N. N. Ledentsov, J. Böhrer, D. Bimberg, I. V. Kochnev, M. V. Maximov, P. S. Kop'ev, Z. I. Alferov, A. O. Kosogov, S. S. Ruvimov, P. Werner, and U. Gösele, *Formation of coherent superdots using metal-organic chemical vapor deposition*, Appl. Phys. Lett. **69**, 1095 (1996).
- 218 C. Ribbat, *Hochleistungs-Quantenpunkt-Halbleiterlaser* (Ph.D. thesis, Technical University of Berlin, http://edocs.tu-berlin.de/diss/2002/ribbat_christian.htm, Berlin, 2003).
- 219 L. V. Asryan, M. Grundmann, N. N. Ledentsov, O. Stier, R. A. Suris, and D. Bimberg, *Effect of excited-state transitions on the threshold characteristics of a quantum dot laser*, J. Quantum El. **37**, 418 (2001).
- 220 C. Ribbat, R. Sellin, M. Grundmann, and D. Bimberg, *High Power Quantum Dot Lasers at 1160 nm*, phys. stat. sol. (b) **224**, 819 (2001).
- 221 R. Heitz, H. Born, F. Guffarth, O. Stier, A. Schliwa, A. Hoffmann, and D. Bimberg, *Existence of a phonon bottleneck for excitons in quantum dots*, Phys. Rev. B **64**, 241305(R) (2001).
- 222 R. Heitz, *Optical Properties of Self-Organized Quantum Dots in Nano-Optoelectronics*, ed. by M. Grundmann (Springer, Berlin, Heidelberg, 2002), p. 239.
- 223 A. Al-Muhanna, L. J. Mawst, D. Botez, D. Z. Garbuzov, R. U. Martinnelli, and J. C. Connolly, *High-power (> 10 W) continuous-wave op-*

- eration from 100- μm -aperture 0.97- μm -emitting Al-free diode lasers, *Appl. Phys. Lett.* **73**, 1182 (1998).
- 224 X. He, S. Srinivasan, S. Wilson, C. Mitchell, and R. Patel, *10.9 W continuous wave optical power from 100 μm aperture InGaAs/AlGaAs (915 nm) laser diodes*, *El. Lett.* **34**, 2126 (1998).
- 225 D. A. Livshits, I. V. Kochnev, V. M. Lantratov, N. N. Ledentsov, T. A. Nalyot, I. S. Tarasov, and Z. I. Alferov, *Improved catastrophic optical mirror damage level in InGaAs/AlGaAs laser diodes*, *El. Lett.* **36**, 1848 (2000).
- 226 O. B. Shchekin, G. Park, D. L. Huffaker, and D. G. Deppe, *Discrete energy level separation and the threshold temperature dependence of quantum dot lasers*, *Appl. Phys. Lett.* **77**, 466 (2000).
- 227 Y. Q. Wei, S. M. Wang, F. Ferdos, J. Vukusic, A. Larsson, and Q. X. Zhao, *Large ground-to-first-excited-state transition energy separation for InAs quantum dots emitting at 1.3 μm* , *Appl. Phys. Lett.* **81**, 1621 (2002).
- 228 H. Jiang and J. Singh, *Strain distribution and electronic spectra of InAs/GaAs self-assembled dots: An eight-band study*, *Phys. Rev. B* **56**, 4696 (1997).
- 229 O. B. Shchekin and D. G. Deppe, *The role of p-type doping and the density of states on the modulation response of quantum dot lasers*, *Appl. Phys. Lett.* **80**, 2758 (2002).
- 230 W. T. Tsang, *A new current-injection heterostructure laser: The double-barrier double-heterostructure laser*, *Appl. Phys. Lett.* **38**, 835 (1981).
- 231 A. R. Kovsh, N. A. Maleev, A. E. Zhukov, S. S. Mikhlin, A. P. Vasil'ev, Y. M. Shernyakov, M. V. Maximov, D. A. Lvshits, V. M. Ustinov, Z. I. Alferov, N. N. Ledentsov, and D. Bimberg, *InAs/InGaAs/GaAs quantum dot lasers of 1.3 μm range with high (88%) differential efficiency*, *El. Lett.* **38**, 1104 (2002).
- 232 O. B. Shchekin and D. G. Deppe, *1.3 μm InAs quantum dot laser with $T_0 = 161\text{ K}$ from 0 to 80°C*, *Appl. Phys. Lett.* **80**, 3277 (2002).
- 233 S. Rapp, F. Salomonsson, K. Streubel, S. Mogg, F. Wennekes, J. Bentell, and M. Hammar, *All-Epitaxial Single-Fused 1.55 μm Vertical Cavity Laser Based on an InP Bragg Reflector*, *Jpn. J. Appl. Phys.* (1) **38**, 1261 (1999).
- 234 J. M. Dallesasse, J. N. Holonyak, A. R. Sugg, T. A. Richard, and N. El-Zein, *Hydrolyzation oxidation of $\text{Al}_x\text{Ga}_{1-x}\text{As}$ -AlAs-GaAs quantum well heterostructures and superlattices*, *Appl. Phys. Lett.* **57** (1990).
- 235 F. Hopfer, *Oberflächenemittierende Quantenpunktlaser* (Diploma thesis, Technische Universität Berlin, 1998).

- ²³⁶ V. M. Ustinov, A. Y. Egorov, V. A. Odnoblyudov, N. V. Kryzhanovskaya, Y. G. Musikhin, A. F. Tsatsul'nikov, and Z. I. Alferov, *InAs/InGaAsN quantum dots emitting at 1.55 μm grown by molecular beam epitaxy*, J. Crystal Growth **251**, 388 (2003).
- ²³⁷ D. S. Sizov, M. V. Maksimov, A. F. Tsatsul'nikov, N. A. Cherkashin, N. V. Kryzhanovskaya, A. B. Zhukov, N. A. Maleev, S. S. Mikhlin, A. P. Vasil'ev, R. Sellin, V. M. Ustinov, N. N. Ledentsov, D. Bimberg, and Z. I. Alferov, *The Influence of Heat Treatment Conditions on the Evaporation of Defect Regions in Structures with InGaAs Quantum Dots in the GaAs Matrix*, Semiconductors **36**, 1020 (2002).
- ²³⁸ M. Kondow, B. Shi, and C. W. Tu, *In situ etching using a novel precursor of tertiarybutylchloride (TBCl)*, J. Crystal Growth **209**, 263 (2000).
- ²³⁹ P. Wolfram, W. Ebert, J. Kreissl, and N. Grote, *MOVPE-based in situ etching of In(GaAs)P/InP using tertiarybutylchloride*, J. Crystal Growth **221**, 177 (2000).
- ²⁴⁰ N. Tansu and L. J. Mawst, *High-Performance Strain-Compensated InGaAs–GaAsP–GaAs ($\lambda = 1.17 \mu\text{m}$) Quantum-Well Diode Lasers*, Phot. Techn. Lett. **13**, 179 (2001).
- ²⁴¹ C. Ellmers, S. Leu, R. Rettig, M. Hofmann, W. W. Rühle, and W. Stolz, *GaAs-based VCSEL-structures with strain-compensated (GaIn)As/Ga(PAs)-MQWH active regions grown by using TBAs and TBP*, J. Crystal Growth **195**, 630 (1998).
- ²⁴² C. Ellmers, F. Höhnsdorf, J. Koch, C. Agert, S. Leu, D. Karaiskaj, M. Hofmann, W. Stolz, and W. W. Rühle, *Ultrafast (GaIn)(NAs)/GaAs vertical-cavity surface-emitting laser for the 1.3 μm wavelength regime*, Appl. Phys. Lett. **74**, 2271 (1999).